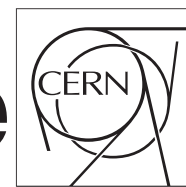


The Compact Muon Solenoid Experiment

CMS Draft Note

Mailing address: CMS CERN, CH-1211 GENEVA 23, Switzerland



2012/09/28

Head Id: 149293

Archive Id: 149674

Archive Date: 2012/09/26

Archive Tag: trunk

Search for the standard model Higgs boson in the decay channel $H \rightarrow ZZ \rightarrow 4\ell$ in pp collisions

N. Amapane¹, I. Anderson², P. Avery³, M. Bachtis⁴, S. Baffioni⁵, F. Beaudette⁵, D. Benedetti⁶, C. Bernet⁴, P. Bhat⁷, J. Bochenek⁸, S. Bolognesi², D. Bortoletto⁶, C. Botta⁴, D. Bourilkov³, S. Braibant⁹, N. Cartiglia¹, S. Cassaso¹, F.R. Cavallo⁹, C. Charlot⁵, M. Chen³, T. Cheng³, S. Chhibra¹⁰, M. Dalchenko⁵, S. Dasu¹¹, A. Drozdetskiy³, N. De Filippis¹⁰, P. Giacomelli⁹, A. Gritsan², K. Hahn¹², P. Janot⁴, K. Johnson⁸, M. Klute¹², R. Khurana¹³, A. Korytov³, M. Kovac^{5,18}, A. Levin¹², B. Mangano¹⁴, M. Mannelli⁴, E. Di Marco¹⁵, C. Mariotti^{1,4}, K. Matchev³, E. Migliore¹, P. Milenovic³, G. Miniello¹⁰, G. Mitselmakher³, M. Masciovecchio⁹, M. Meneghelli⁹, A. Mohammadi¹⁶, M. Mozer⁴, C. Ochando⁵, C. Paus¹², M. Pelliccioni¹, E. Perez⁴, G. Petrucciani¹⁴, R. Plestina^{5,18}, H. Prosper⁸, I. Puljak^{4,18}, D. Ralph¹², A. Rinkevicius³, I. Ross¹¹, D. Sabes⁵, R. Salerno⁵, A. Savin¹¹, V. Sharma¹⁴, G. Singh¹⁰, Y. Sirois⁵, J. Smith¹⁷, M. Snowball³, K. Sung¹², J. Swanson¹¹, S. Tentindo⁸, N. Tran⁷, N. Tritto¹⁰, A. Vartak¹⁴, A. Whitbeck², and S. Xie^{12,15}

¹ Torino University² John Hopkins University³ University of Florida⁴ CERN⁵ Laboratoire Leprince-Ringuet⁶ Purdue University⁷ FNAL⁸ Florida State University⁹ Bologna University¹⁰ Bari University¹¹ University of Wisconsin¹² Massachusetts Institute of Technology¹³ Saha Institute of Nuclear Physics and Visva-Bharati University¹⁴ University of California, San Diego¹⁵ California Institute of Technology¹⁶ Universit libre de Bruxelles¹⁷ University of California, Davis¹⁸ University of Split

Abstract

A search for a Higgs boson in the $H \rightarrow ZZ$ four-lepton decay channel, with each Z boson decaying to an electron or a muon is reported. The search covers Higgs boson mass hypotheses in the range $110 < m_H < 600$ GeV. The analysis uses pp collision data recorded by the CMS detector at the LHC, and corresponding to integrated luminosities of 5.05 fb^{-1} at $\sqrt{s} = 7\text{ TeV}$ and 5.26 fb^{-1} at $\sqrt{s} = 8\text{ TeV}$. The mass distributions measured with four-lepton invariant masses $m_{4\ell} > 100$ GeV is found globally consistent with the expectation of standard model background production of ZZ pairs for invariant mass above 180 GeV. Upper limits at 95% confidence level exclude the standard model Higgs boson in the range 131–162 and 172–525 GeV, while the expected range is 121–570 GeV. An excess of events is observed in the mass range $120 < m_{4\ell} < 130$ GeV making the observed limits weaker than expected in the absence of a signal. These events cluster around a mass $m_{4\ell} \simeq 125.5$ GeV, giving rise to a local excess with respect to the background expectation, with a significance of 3.2σ . This result constitutes evidence for a new massive state.

This box is only visible in draft mode. Please make sure the values below make sense.

PDFAuthor:

The HZZ4l team

PDFTitle:

Search for the standard model Higgs boson in the decay channel H to ZZ to 4l in pp collisions

PDFSubject:

CMS

PDFKeywords:

CMS, physics, Higgs

Please also verify that the abstract does not use any user defined symbols

1 Contents

2	1	Introduction	2
3	1.1	Overview of the PRL Analysis	4
4	1.2	Main Changes Since PRL Analysis	6
5	2	General Analysis Strategy	7
6	2.1	Blinding policy	8
7	3	Datasets and Triggers	9
8	3.1	Experimental Data	9
9	3.2	Simulated Samples	9
10	4	Leptons Observables	15
11	4.1	Electron Reconstruction and Identification	15
12	4.2	Muon Reconstruction and Identification	21
13	4.3	Primary and Secondary Leptons	22
14	4.4	Lepton Isolation	23
15	5	Leptons Measurements	30
16	5.1	T&P methodology	30
17	5.2	Electrons	30
18	5.3	Muons	39
19	6	Photon Observables and FSR recovery	44
20	6.1	Photon Reconstruction and Identification	44
21	6.2	Photon Isolation	45
22	6.3	Building Z's with FSR Photon Recovery	45
23	6.4	Studies on $H \rightarrow ZZ$, SM ZZ MC	46
24	6.5	Studies on data	47
25	7	Event Selection	49
26	7.1	Selection Performance and Control	50
27	8	Signal Model and uncertainties	57
28	8.1	Signal model	57
29	8.2	Signal model uncertainties	61
30	8.3	Four-lepton mass: scale and resolution	69
31	9	Irreducible ZZ Background Model and uncertainties	83
32	9.1	$ZZ^{(*)}$ yields	83
33	9.2	$ZZ^{(*)}$ Background Model	83
34	9.3	$ZZ^{(*)}$ model uncertainties	86
35	10	Irreducible Z+DY double parton interaction background	90
36	11	Reducible Background Model and Systematic Uncertainties	92
37	11.1	Reducible background prediction	92
38	11.2	Reducible Backgrounds Uncertainties	105
39	11.3	Summary	106
40	12	Kinematic Discriminant (MELA)	109
41	12.1	Introduction of the methodology	109
42	12.2	Construction of the MELA discriminant	111
43	12.3	Parameterization of the MELA discriminant	115

44	13	Summary of Selection and Systematic Uncertainties	121
45	13.1	Event yields and errors	121
46	13.2	Distributions of events	121
47	13.3	FSR performances	128
48	13.4	Differences with respect to the 2011 PRL analysis	129
49	13.5	Summary of systematic uncertainties	130
50	14	Statistical Analysis	132
51	14.1	Methodology using 2D distributions ($m_{4\ell}$, KD)	132
52	14.2	Limits	132
53	14.3	Significance of excesses	132
54	14.4	Approach to Higgs Boson Mass Measurements	139
55	14.5	Approach to Higgs Boson Spin and Property Measurements	139
56	14.6	Measurement of ZZ cross section	146
57	15	Summary and Conclusions	149
58	A	Appendix #1 Event Properties	155
59	B	Appendix #2 Control of lepton efficiencies from data, tables	170
60	C	Appendix #3 Cross checks	177
61	C.1	Cross-check with a 1D fit of $m_{\ell\ell}$	177
62	C.2	Cross-check with a cut on KD and a 1D fit of $m_{\ell\ell}$	179
63	C.3	Cross-check without FSR recovery	181
64	D	Appendix #4 Some events from the PRL analysis not in the current analysis	182

65 1 Introduction

66 The standard model (SM) of electroweak interactions [1–3] relies on the existence of the Higgs
 67 boson, a scalar particle of mass m_H associated with the field responsible for the spontaneous
 68 electroweak symmetry breaking [4–9]. The mass m_H is not fixed by the theory and the existence
 69 of the scalar boson has not yet been established experimentally. The Higgs boson production
 70 followed by the decay $H \rightarrow ZZ$ is expected to be one of the main discovery channels at the
 71 CERN proton-proton (pp) Large Hadron Collider (LHC) for a wide range of m_H values.

72 Direct searches for the SM Higgs bosons have been performed by the ATLAS and CMS exper-
 73 iments using each about 4.7 fb^{-1} of pp data from the LHC collected in 2010 and 2011 at $\sqrt{s} =$
 74 7 TeV. Searches for the SM Higgs boson in the $H \rightarrow ZZ \rightarrow 4\ell$ channel ($\ell = e, \mu$), have been
 75 carried by ATLAS [10] and CMS [11]. Search results combining these with various production
 76 and decay channels were obtained by both collaborations [12, 13]. The results from CMS ex-
 77 clude the SM Higgs boson in the mass range 127–600 GeV at 95% confidence level (CL). Direct
 78 searches for the SM Higgs boson at the LEP e^+e^- collider and the Tevatron $p\bar{p}$ collider have
 79 led, respectively, to a lower mass bound of $m_H > 114.4 \text{ GeV}$ [14], and to an exclusion in the
 80 range 162–166 GeV [15], at 95% CL. Indirect constraints from precision measurements favour
 81 the mass range $m_H < 158 \text{ GeV}$ [16, 17] at 95% CL.

82 In this paper, a search in the four-lepton decay channels $H \rightarrow 4\ell$ and $H \rightarrow 2\ell 2\tau$, with $\ell = e$
 83 or μ , is presented. The analysis is designed for a Higgs boson in the mass range $110 < m_H <$
 84 600 GeV. It re-uses the data collected by CMS in 2011, combined with the new data collected
 85 in 2012 at $\sqrt{s} = 8 \text{ TeV}$ which corresponds to an additional integrated luminosity of $X.X \text{ fb}^{-1}$.

The search essentially relies on the reconstruction, identification and isolation of leptons. Compared to previous CMS analyses [11, 18], it profits from improved lepton reconstruction and isolation efficiencies, combined with the usage of a discriminant exploiting the production and decay kinematics expected for the signal events. The analysis achieves high lepton reconstruction efficiencies for a ZZ system composed of two pairs of same-flavour and opposite-charge isolated leptons, e^+e^- , $\mu^+\mu^-$, or $\tau^+\tau^-$, in the measurement range $m_{4\ell}, m_{2\ell 2\tau} > 110$ GeV. One or both of the Z bosons can be off-shell. The single-resonant four-lepton production ($Z \rightarrow 4\ell$) is used as a standard candle in the mass range $70 < m_{4\ell} < 110$ GeV. The background sources include an irreducible four-lepton contribution from direct ZZ (or $Z\gamma^*$) production via $q\bar{q}$ annihilation and gg fusion. Reducible contributions arise from Zbb and $t\bar{t}$ where the final states contain two isolated leptons and two b jets producing secondary leptons. Additional background of instrumental nature arises from $Z +$ jets events where jets are misidentified as leptons.

The analysis and results described in this note represent an extension of a similar analysis previously published by the CMS Collaboration with collected data in 2010 and 2011. It accompanies the paper HIG-12-016 in preparation. A comparable note (AN-11-123, version 7) accompanied the HIG-11-004 PAS released for the EPS HEP 2011 conference, then (AN-11-123, version 9) accompanied the HIG-11-015 PAS released for the Lepton-Photon 2011 conference and finally AN-11-386 accompanied the HIG-11-025 and PRL paper. A full independent cross-check analysis as also been performed and is documented in the note.

The reader being familiar with the CMS detector, we give here only a short summary for completeness. A detailed description of the can be found elsewhere [19]. The detector comprises a superconducting solenoid providing a uniform magnetic field of 3.8 T. The bore of the solenoid is instrumented with various particle detection systems. The inner tracking system is composed of a pixel detector with three barrel layers and a silicon strip tracker with 10 barrel detection layers. Each system is completed by two end caps, extending the acceptance up to $|\eta| < 2.5$. The pseudorapidity η is defined as $\eta = -\ln \tan(\theta/2)$ where θ is the polar angle with respect to the direction of the proton beam. A lead tungstate crystal electromagnetic calorimeter (ECAL) with fine transverse ($\Delta\eta, \Delta\phi$) granularity and a brass-scintillator hadronic calorimeter (HCAL) surround the tracking volume and cover the region $|\eta| < 3$. The steel return yoke outside the solenoid is in turn instrumented with gas detectors which are used to identify muons in the range $|\eta| < 2.4$. The barrel region is covered by drift tube chambers and the end cap region by cathode strip chambers, each complemented by resistive plate chambers.

Table 1: The number of candidates observed, compared to background and signal rates for each final state for $100 < m_{4\ell} < 600$ GeV for the baseline selection. For the $Z + X$ background, the estimations are based on data.

Channel	4e	4 μ	2e2 μ
ZZ background	12.27 ± 1.16	19.11 ± 1.75	30.25 ± 2.78
Z+X	1.67 ± 0.55	1.13 ± 0.55	2.71 ± 0.96
All background	13.94 ± 1.28	20.24 ± 1.83	32.96 ± 2.94
$m_H = 120$ GeV	0.25	0.62	0.68
$m_H = 140$ GeV	1.32	2.48	3.37
$m_H = 350$ GeV	1.95	2.61	4.64
Observed	12	23	37

1.1 Overview of the PRL Analysis

The number of candidates observed, as well as the estimated background in the signal region, are reported in Table 1 for the baseline selection. The reconstructed four-lepton invariant mass distribution for the combined $4e$, 4μ , and $2e2\mu$ channels with the baseline selection is shown in Fig. 1a and compared to expectations from the backgrounds. The shape of the mass distribution below $m_H = 180$ GeV reflects the shape of the dominant $q\bar{q}$ annihilation process [20]. The low

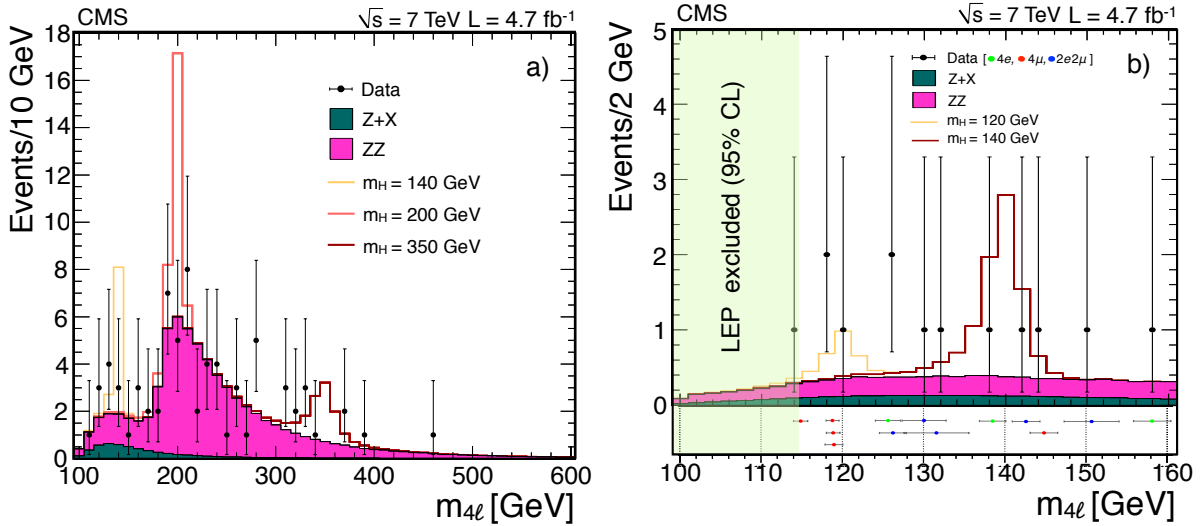


Figure 1: a) Distribution of the four-lepton reconstructed mass for the sum of the $4e$, 4μ , and $2e2\mu$ channels. b) Expansion of the low mass range with existing exclusion limits at 95% CL; also shown are the central values and individual candidate mass measurement uncertainties. Points represent the data, shaded histograms represent the background and unshaded histogram the signal expectations.

mass range is shown in Fig. 1b together with the mass of each candidate and its uncertainty. The reducible and instrumental background rates are small. These rates have been obtained from data and the corresponding $m_{4\ell}$ distributions are obtained from MC samples. The measured distribution is compatible with the expectation from SM direct production of ZZ pairs. We observe 72 candidates, 12 in $4e$, 23 in 4μ , and 37 in $2e2\mu$, while 67.1 ± 6.0 events are expected from standard model background processes. No hard photon ($p_T^\gamma > 5$ GeV) was found, outside the isolation veto cone that surrounds each lepton, that could be unambiguously identified as FSR. Thirteen candidates are observed within $100 < m_{4\ell} < 160$ GeV while 9.5 ± 1.3 background events are expected. We observe 53 candidates for the high-mass selection compared to an expectation of 51.3 ± 4.6 events from background. This high-mass event selection is used to provide a measurement of the total cross section $\sigma(pp \rightarrow ZZ + X) \times \mathcal{B}(ZZ \rightarrow 4\ell) = 28.1^{+4.6}_{-4.0}(\text{stat.}) \pm 1.2(\text{syst.}) \pm 1.3(\text{lumi.}) \text{ fb}$. The measurement agrees with the SM prediction at NLO [21] of 27.9 ± 1.9 fb and is consistent with previous measurements at the LHC [22]. The local p -values, representing the significance of local excesses relative to the background expectation, are shown as a function of m_H in Fig. 2a, obtained either taking into account or not the individual candidate mass measurement uncertainties, for the combination of the three channels. Excesses are observed for masses near 119 GeV and 320 GeV. The small $\approx 2\sigma$ excess near 320 GeV includes three events with $p_T^{4\ell} > 50$ GeV. The most significant excess near 119 GeV corresponds to about 2.5σ significance. The significance is less than 1.0σ (about 1.6σ) when the look-elsewhere effect [23] is accounted for over the full mass range (for the low-mass

range $100 < m_{4\ell} < 160$ GeV). The local significances change only slightly when including candidate mass uncertainties, instead of using the average mass resolution, e.g. rising to 2.7σ around 119 GeV and reaching 1.5σ around 126 GeV.

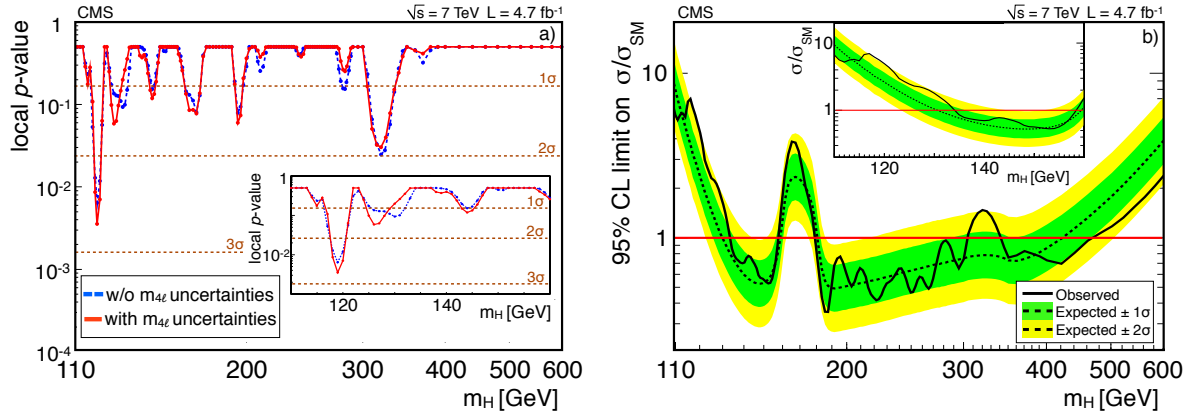


Figure 2: a) The significance of the local excesses with respect to the standard model expectation as a function of the Higgs boson mass, without (blue) or with (red) individual candidate mass measurement uncertainties. b) The observed and the median expected upper limits at 95% CL on $\sigma = \sigma(pp \rightarrow H + X) \times \mathcal{B}(H \rightarrow 4\ell)$, relative to their standard model prediction σ_{SM} , for a Higgs boson in the mass range 110–600 GeV, using the CL_s approach. The insets expand the low mass range.

146

147 In absence of a significant clustering of candidates at any given mass, we derive exclusion lim-
 148 its. The exclusion limits for a SM-like Higgs boson are computed for a large number of mass
 149 points in the range 110–600 GeV, using the predicted signal and background mass distribution
 150 shapes. The choice of the step size in the scan between Higgs mass hypotheses is driven by
 151 either detector resolution, or the natural width of the Higgs boson. The signal mass distri-
 152 butions shapes are determined using simulated samples for 27 values of m_H covering the full
 153 mass range. The shapes are fit using a function obtained from a convolution of a Breit-Wigner
 154 probability density function to describe the theoretical resonance line shape and a Crystal Ball
 155 function to account for the detector effects. The parameters of the Crystal Ball function are
 156 interpolated for the m_H points where there is no simulated sample available. The shapes of
 157 the background mass distributions are determined by fits to the simulated sample of events,
 158 while the normalization is taken from estimates of overall event yields as described above. For
 159 each mass hypothesis, we perform an unbinned likelihood fit using the statistical approach
 160 discussed in Ref. [24]. We account for systematic uncertainties in the form of nuisance parame-
 161 ters with a log-normal probability density function. The observed and median expected upper
 162 limits on $\sigma(pp \rightarrow H + X) \times \mathcal{B}(H \rightarrow 4\ell)$ at 95% CL are shown in Fig. 2b. The limits are calcu-
 163 lated relative to their expected SM Higgs boson prediction σ_{SM} , using the modified frequentist
 164 method CL_s [25, 26]. The bands represent the 1σ and 2σ probability intervals around the ex-
 165 pected limit. These upper limits exclude the standard model Higgs boson at 95% CL in the m_H
 166 ranges 134–158 GeV, 180–305 GeV and 340–465 GeV. The limits reflect the dependence of the
 167 branching ratio $\mathcal{B}(H \rightarrow ZZ)$ on m_H . The worsening of the limits at high mass arises from the
 168 decreasing cross section for the $H \rightarrow 4\ell$ signal. By virtue of the excellent mass resolution and
 169 low background, the structure in the measured limits follows the fluctuations of the number of
 170 observed events.

1.2 Main Changes Since PRL Analysis

Two main area of improvements have been explored with respect to the 2011 analysis: 1) improving efficiency of lepton reconstruction, identification and isolation (through the text we often use "reconstruction" meaning "reconstruction+identification+isolation") and 2) using more kinematical variables together with higher level statistical methods like using the 2D instead of the 1D fit. All the changes will be explained and demonstrated later in the text, here we outline the main motivation and main results.

Figure 3 shows the efficiencies of final selection in PRL analysis with respect to the generator acceptance, for all three channels. The efficiency reaches a plateau at about 200 GeV, and is steeply falling towards the low masses. The efficiency reduction in the low mass region is caused by two effects: larger fraction of low p_T leptons and lower efficiency of leptons reconstruction for low p_T leptons. This is demonstrated in Figure 4 where p_T distribution of four leptons in $4e$ and 4μ is shown just after the generator acceptance and after the full selection, for the 120 GeV Higgs boson. From the figure one can see that the largest area for the possible improvement is in improving the efficiency of electron reconstruction, with smaller gain from improving muon reconstruction and lowering the lepton p_T cuts.

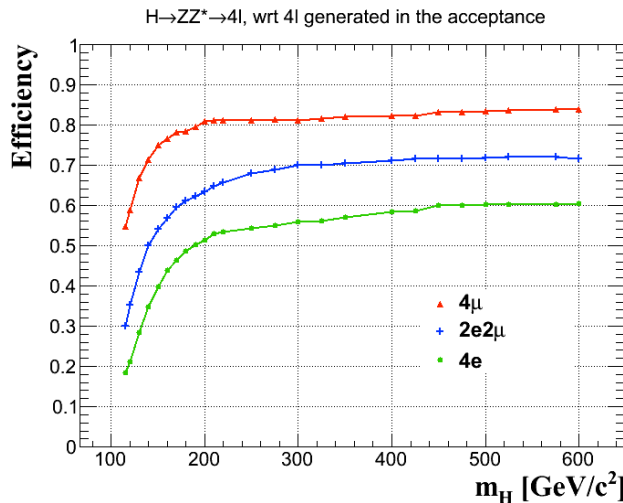


Figure 3: Efficiency of final selection with respect to the generator acceptance in all three analysis channels, in the PRL analysis.

In recent months lot of effort was invested, together with the egamma and muon POGs, to improve electron and muons reconstruction. BDT multivariate technique has been used to improve the electron identification, while for muons reconstruction and identification PF muons show improved efficiency with respect to global muons used in 2011 analysis, for the same lepton fake rates for both electrons and muons. Lepton isolation is also improved using the PF isolation algorithm, resulting in increased selection efficiency and local significance summarized in Table 2. Overall gain in local significance from improving electron and muon objects only, combining all channels, is 12%.

The PRL analysis employed cuts on the two $Z^{(*)}$ invariant masses m_1 and m_2 with the shape-based fit of the $m_{4\ell}$ distribution. In the current approach, we expand information used and construct a kinematic discriminant KD from the seven mass and angular observables $KD = F\{m_1, m_2, \theta^*, \Phi_1, \theta_1, \theta_2, \Phi\}$ and perform a 2D shape fit with the two observables $(m_{4\ell}, KD)$. The KD discriminant combines this power in a single observable using full correlation of all input

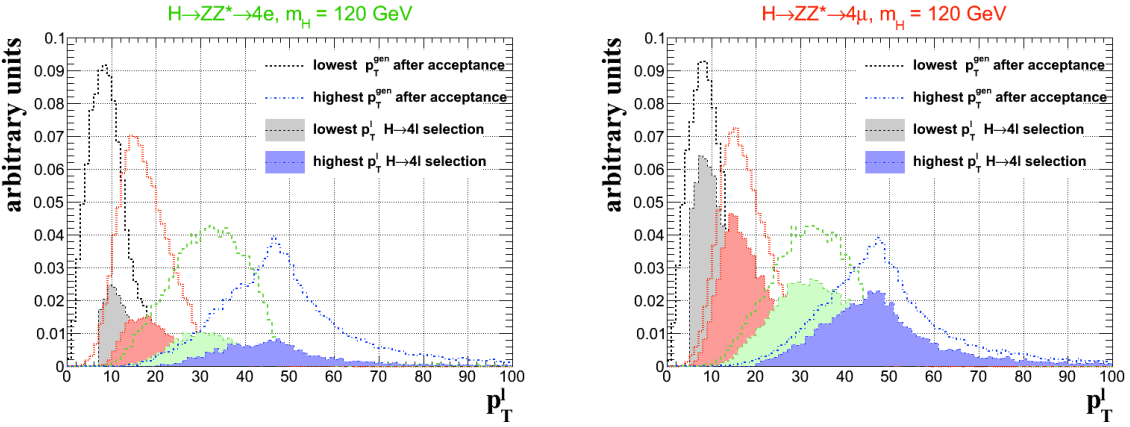


Figure 4: P_T distribution of four leptons in $4e$ (left) and 4μ (right) channel in the PRL 2011 analysis, after generator acceptance (empty histograms) and after full selection (full histograms) for the 120 GeV Higgs boson.

Channel	Efficiency increase			Local significance		
	Signal $m_H = 120$ GeV	ZZ bckgd [100-135] GeV	Z + X bckgd [100-600] GeV	PRL analysis	Improved objects	Gain
$4e$	51%	56%	36%	0.68	0.92	35%
4μ	10%	7%	11%	1.53	1.61	5%
$2e2\mu$	28%	21%	26%	1.38	1.61	16%

Table 2: Efficiency increase and local significance gain when improving objects in the PRL analysis. Overall gain in local significance, combining all channels is 12%.

200 observables in the most optimal way.

201 In Fig. 5 we show expected limits obtained with a PRL analysis, and compare them to the
202 new baseline analysis with 2D fit of the $(m_{4\ell}, \text{KD})$ distribution and with a 1D fit of the $m_{4\ell}$
203 distribution. Improvements in upper limits are of the order of 15% in the low mass region with
204 the new selection (1D fit) and of about 25% total improvements across the whole mass range
205 (using new selection and kinematics).

206 The size of expected improvements from new objects, kinematical discriminant and 2D fit jus-
207 tifies the reanalysis of 2011 data, together with the analysis of 2012 data.

208 2 General Analysis Strategy

209 We use data collected with the di-electron and di-muon triggers and select events with well-
210 reconstructed four leptons: $e^+e^-e^+e^-$, $\mu^+\mu^-\mu^+\mu^-$, $e^+e^-\mu^+\mu^-$. An optimal analysis in the 4ℓ
211 channel must preserve the highest possible reconstruction efficiency for the Higgs boson signal.

212 The sample of events with reconstructed 4ℓ receives an irreducible contribution from $ZZ^{(*)}$ pro-
213 duction via $q\bar{q}$ and gluon-induced processes. It further receives the main reducible background
214 contributions from Zbb and $t\bar{t} \rightarrow W^+bW^-\bar{b}$, with W undergoing leptonic decays, where the fi-
215 nal states contain two isolated leptons and two b jets possibly giving rise to secondary leptons.
216 Reconstructed 4ℓ events can also arise from instrumental background such as $Z+jets$ or $WZ +$
217 jet(s) where jets are misidentified as leptons.

218 It has been shown in previous studies that an optimal working point can be found where the
219 contribution from the reducible and instrumental backgrounds are quasi-eliminated. This is
220 achieved by applying cuts on the maximum allowed energy flow in the isolation cones around

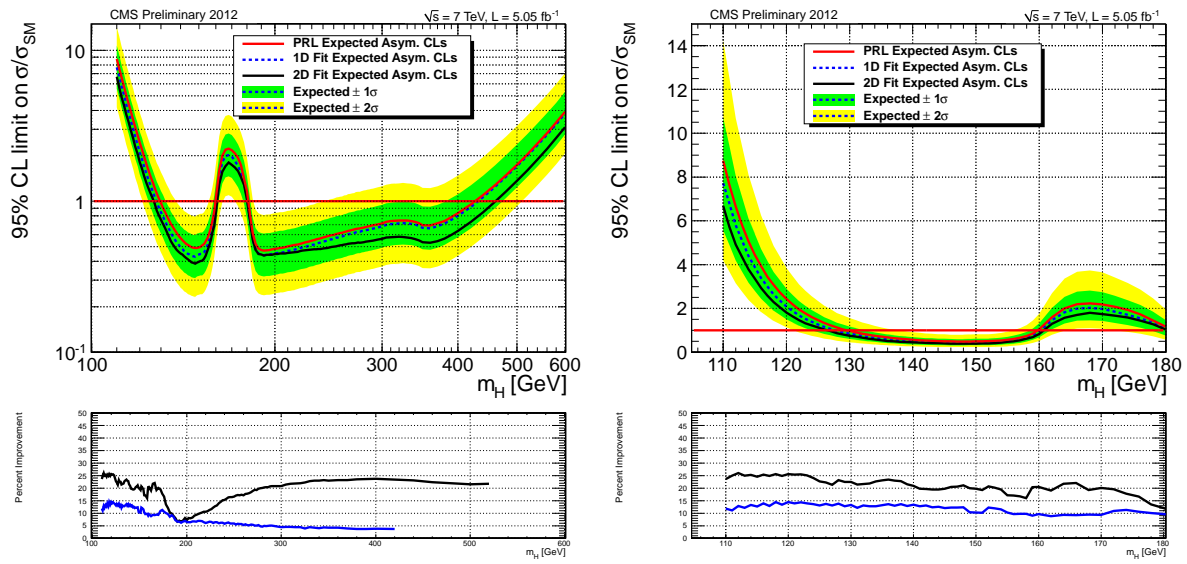


Figure 5: Expected 95% CL upper limit on the ratio of the production cross section to the SM expectation with the PRL analysis fit (dashed), new baseline analysis with new selection and 2D fit (blue solid), and with new selection and 1D fit (red solid) and with 5/fb of data. The 68% and 95% ranges of expectation with PRL analysis for the background-only model are also shown with green and yellow bands, respectively. Also show is the ratio of 1D fit and 2D fit expectation with respect to the PRL analysis.

leptons and on the maximum impact parameter of lepton tracks with respect to the primary interaction vertex. The analysis aims at the highest possible lepton reconstruction, identification and isolation efficiencies, that are compatible with a quasi-negligible reducible and instrumental background, in the acceptance range used for this analysis, i.e. with transverse momentum and pseudorapidity for electrons of $p_T^e > 7 \text{ GeV}/c$, $|\eta^e| < 2.5$, and for muons of $p_T^\mu > 5 \text{ GeV}/c$, $|\eta^\mu| < 2.4$.

The statistical analysis of selected events is based on their four-lepton mass ($m_{4\ell}$) distribution. The presence of the Higgs boson is expected to manifest itself as a resonance over the continuum $m_{4\ell}$ distribution of the $pp \rightarrow ZZ \rightarrow 4\ell$ origin. The width of the peak for a SM Higgs boson with a low mass ($m_H < 250 \text{ GeV}$) is expected to be defined by the detector resolution. For higher masses, SM Higgs boson's intrinsic width quickly overtakes the detector resolution.

The $pp \rightarrow ZZ \rightarrow 4\ell$ background prediction relies fully on the theory. All instrumental uncertainties associated with selecting four prompt leptons (trigger, reconstruction, isolation and impact parameter cuts) are derived directly from data.

The remaining contribution of reducible backgrounds is evaluated using data driven techniques. This includes the overall rates of 4ℓ events, passing all selection cuts, and their mass distributions.

2.1 Blinding policy

In the channel with low background and high resolution, $H \rightarrow ZZ \rightarrow 4l$, do not look (either make no plots with such events or exclude events at ntuple level) at m_{4l} between 110 and 140, and above 300 GeV. The m_{4l} distribution can be checked in the full mass range either in the control regions (with no signal expected) or with significantly relaxed cuts (when signal cannot be seen under about 100 larger background).

²⁴⁴ The blinding procedure applies both to the analysis of 2011 (if any change with respect to
²⁴⁵ published analysis is done) and 2012 data.

²⁴⁶ 3 Datasets and Triggers

²⁴⁷ 3.1 Experimental Data

²⁴⁸ The data sample used in this analysis was recorded by the CMS experiment during 2011 for the
²⁴⁹ run range from 160431 to 180252 and during 2012 for the run range from 190645 to 196509. The
²⁵⁰ CMS standard selection of runs and luminosity sections is applied which requires high quality
²⁵¹ data with a good functioning of the different sub-detectors. Thus, similar detector operation
²⁵² conditions are imposed for the validation of the data to be used for the analysis of the $4e$, 4μ
²⁵³ and $2e2\mu$ channels.

²⁵⁴ Of the total integrated luminosity \mathcal{L} of 46.67 pb^{-1} , a sample corresponding to $\mathcal{L} = 5.05 \text{ fb}^{-1}$ in
²⁵⁵ 2011 at 7 TeV and $\mathcal{L} = 5.26 \text{ fb}^{-1}$ in 2012 at 8 TeV. The absolute pp luminosity is known with a
²⁵⁶ precision of 2.2% [27] in 2011 and 4.4% in 2012 (ref).

²⁵⁷ The analysis relies on primary datasets (PDs) produced centrally and which combine various
²⁵⁸ collections of High Level Triggers (HLT). The detailed content of the PDs evolves in phase
²⁵⁹ with the evolution of the trigger menu to cope with ever increasing instantaneous luminosity.
²⁶⁰ For the 2011 data, the analysis relies on the so-called "DoubleElectron" and "DoubleMuon"
²⁶¹ PDs [28]. These latter PDs are formed by a "OR" between various triggers with symmetric
²⁶² or asymmetric trigger thresholds for the two leptons, with or without additional identification
²⁶³ and isolation requirements. They also include triggers requiring three leptons above a low p_T
²⁶⁴ threshold. In 2012 cross-triggers are added to recover few percent of inefficiency in the $2e2\mu$
²⁶⁵ channel at low Higgs boson masses, forming the so-called "MuEG" PD.

²⁶⁶ The PDs and trigger paths used for this analysis are summarized in Table 3.

²⁶⁷ Some comments:

- ²⁶⁸ • In 2011, when applying double muon triggers other than `HLT_Mu17_Mu8` one
²⁶⁹ has to require 2 offline recoMuons to be matched with L3Muons $p_T > 8 \text{ GeV}$ and
²⁷⁰ $p_T > 17 \text{ GeV}$.
- ²⁷¹ • When running on data we get: 4μ channel from DoubleMu datasets, $4e$ channel
²⁷² from DoubleElectron datasets and $2e2\mu$ channel from DoubleElectron and from Dou-
²⁷³ bleMu vetoing DoubleElectrons triggers for 2011 data, while for 2012 we use in ad-
²⁷⁴ dition MuEG dataset vetoing DoubleElectrons and DoubleMuons triggers.
- ²⁷⁵ • Only a subset of runs from June08 re-reco are used. These are runs where the ecal
²⁷⁶ laser corrections were recovered and not present in PromptReco.
- ²⁷⁷ • In 2012, a small quantity of data were taken with low pile-up special conditions. As
²⁷⁸ the triggers we are using were turned off, we rejected these runs.

²⁷⁹ In Table 4 we list all the triggers used with 2012 data.

²⁸⁰ 3.2 Simulated Samples

²⁸¹ SM Higgs boson signal samples, as well as samples for a large variety of electroweak and
²⁸² QCD-induced SM background processes, have been obtained using detailed Monte Carlo (MC)
²⁸³ simulations. All datasets were subject to full reconstruction and skimming. The signal and
²⁸⁴ background samples have been used for the optimization of the event selection strategy prior to

Datasets	
2011	2012
/DoubleElectron/Run2011A-16Jan2012-v1 /DoubleMu/Run2011A-16Jan2012-v1 /DoubleElectron/Run2011B-16Jan2012-v1 /DoubleMu/Run2011B-16Jan2012-v1	/DoubleElectron/Run2012A-PromptReco-v1 /DoubleMu/Run2012A-PromptReco-v1 /MuEG/Run2012A-PromptReco-v1 /DoubleElectron/Run2012B-PromptReco-v1 /DoubleMu/Run2012B-PromptReco-v1 /MuEG/Run2012B-PromptReco-v1 /DoubleMu/Run2012A-23May2012-v2/AOD /DoubleElectron/Run2012A-23May2012-v2/AOD /MuEG/Run2012A-23May2012-v1/AOD /MuEG/Run2012A-08Jun2012-v3/AOD /DoubleElectron/Run2012A-08Jun2012-v2/AOD /DoubleMu/Run2012A-08Jun2012-v2/AOD
Muon triggers	
HLT_DoubleMu7 OR HLT_Mu13_Mu8 OR HLT_Mu17_Mu8	HLT_Mu17_Mu8
Electron triggers	
HLT_Ele17_CaloTrk_Ele8_CaloTrk OR HLT_Ele17_CaloTrk_Ele8_CaloTrk	HLT_Ele17_CaloTrk_Ele8_CaloTrk
Cross triggers	
	HLT_Mu17_TkMu8 OR HLT_Mu8_Ele17_CaloTrk OR HLT_Mu17_Ele8_CaloTrk
Integrated luminosity	
5.05 fb ⁻¹	5.26 fb ⁻¹

Table 3: Datasets and triggers used in the analysis. CaloTrk = CaloIdT_CaloIsoVL_TrkIdVL_TrkIsoVL

# Channel	Purpose	HLT path	L1 seed	prescale
4e	main	HLT_Ele17_CaloTrk_Ele8_CaloTrk	L1_DoubleEG_13_7	1
4 μ	main	HLT_Mu17_Mu8 OR HLT_Mu17_TkMu8	L1_Mu10_MuOpen L1_Mu10_MuOpen	1 1
2e2 μ	main	HLT_Ele17_CaloTrk_Ele8_CaloTrk OR HLT_Mu17_Mu8 OR HLT_Mu17_TkMu8 OR HLT_Mu8_Ele17_CaloTrk OR HLT_Mu17_Ele8_CaloTrk	L1_DoubleEG_13_7 L1_Mu10_MuOpen L1_Mu10_MuOpen L1_MuOpen_EG12 L1_Mu12_EG6	1 1 1 1 1
4e	backup	HLT_Ele15_Ele8_Ele5_CaloIdL_TrkIdVL	L1_TripleEG_12_7_5	1
4 μ	backup	HLT_TripleMu5	L1_TripleMu0	1
4e and 2e2 μ	Z T&P	HLT_Ele17_CaloTrkVT_Ele8_Mass50	L1_DoubleEG_13_7	5
4e and 2e2 μ	Z T&P low pT	HLT_Ele20_CaloTrkVT_SC4_Mass50_v1	L1_SingleIsoEG18er	10
4 μ and 2e2 μ	Z T&P	HLT_IsoMu24_eta2p1	L1_SingleMu16er	
4 μ and 2e2 μ	J/psi T&P	HLT_Mu7_Track7_Jpsi HLT_Mu5_Track3p5_Jpsi HLT_Mu5_Track2_Jpsi		

Table 4: Triggers in 2012 data analysis. CaloTrk = CaloIdT_CaloIsoVL_TrkIdVL_TrkIsoVL, CaloTrkVT = CaloIdVT_CaloIsoVT_TrkIdT_TrkIsoVT

the analysis of the experimental data. They are further used in this analysis for the comparisons with the measurements, the evaluation of acceptance corrections and systematics, and for the background evaluation procedure where measurements in a “background control” region are extrapolated to the “signal” region.

The backgrounds include indistinguishable 4ℓ contributions from di-boson production, via $q\bar{q} \rightarrow ZZ^{(*)}$ and $gg \rightarrow ZZ^{(*)}$, as well as instrumental backgrounds in which hadronic jets or secondary leptons from heavy meson decays are misidentified as primary leptons. Here and henceforward, Z stands for Z, Z^* , and γ^* (where possible). For the event generation, ℓ is to be understood as being any charged lepton, e , μ or τ . The analysis will focus on reconstructed final states with electrons or muons. The main possible sources of instrumental background contributions, are the Z + jets production with Z $\rightarrow \ell^+\ell^-$ decays, the Z $b\bar{b}$ (and Z $c\bar{c}$) associated

296 production with $Z \rightarrow \ell^+ \ell^-$ decays, and the production of top quark pairs in the decay mode
 297 $t\bar{t} \rightarrow WbW\bar{b} \rightarrow \ell^+ \ell^- \nu\bar{\nu} b\bar{b}$. Multiple jet production from QCD hard interactions can also con-
 298 tribute in early stages of the analysis, as well as other di-boson (WW, WZ, $Z\gamma$) and single top
 299 backgrounds.

Table 5 summarizes the Monte Carlo simulation datasets used for this analysis.

Process	MC generator	$\sigma_{(N)NLO}$	Comments and sample name
		7 TeV	8 TeV
Higgs boson $H \rightarrow ZZ \rightarrow 4\ell$			
$gg \rightarrow H$	POWHEG	[1-20] fb	$m_H = 110-1000 \text{ GeV}/c^2$
$VV \rightarrow H$	POWHEG	[0.2-2] fb	$m_H = 110-1000 \text{ GeV}/c^2$
ZZ continuum			
$q\bar{q} \rightarrow ZZ \rightarrow 4e(4\mu, 4\tau)$	POWHEG	15.34 fb	ZZTo4e(4mu,4tau)
$q\bar{q} \rightarrow ZZ \rightarrow 2e2\mu$	POWHEG	30.68 fb	ZZTo2e2mu
$q\bar{q} \rightarrow ZZ \rightarrow 2e(2\mu)2\tau$	POWHEG	30.68 fb	ZZTo2e(2mu)2tau
$gg \rightarrow ZZ \rightarrow 2\ell 2\ell'$	ggZZ	3.48 fb	GluGluToZZTo2L2L
$gg \rightarrow ZZ \rightarrow 4\ell$	ggZZ	1.74 fb	GluGluToZZTo4L
Other di-bosons			
$WW \rightarrow 2\ell 2\nu$	Madgraph	4.88 pb	WWJetsTo2L2Nu
$WZ \rightarrow 3\ell\nu$	Madgraph	0.868 pb	WZJetsTo3LNu
$t\bar{t}$ and single t			
$t\bar{t} \rightarrow \ell^+ \ell^- \nu\bar{\nu} b\bar{b}$	POWHEG	17.32 pb	TTTo2L2Nu2B
t (s-channel)	POWHEG	3.19 pb	T_TuneXX_s-channel
\bar{t} (s-channel)	POWHEG	1.44 pb	Tbar_TuneXX_s-channel
t (t-channel)	POWHEG	41.92 pb	T_TuneXX_t-channel
\bar{t} (t-channel)	POWHEG	22.65 pb	Tbar_TuneXX_t-channel
t (tW-channel)	POWHEG	7.87 pb	T_TuneXX_tW-channel-DR
\bar{t} (tW-channel)	POWHEG	7.87 pb	Tbar_TuneXX_tW-channel-DR
$Z/W + jets$ ($q = d, u, s, c, b$)			
$W + jets$	MadGraph	31314 pb	WJetsToLNu
$Z + jets, m_{\ell\ell} > 50$	MadGraph	3048 pb	DYJetsToLL*M-50
$Z + jets, 10 < m_{\ell\ell} < 50$	MadGraph	12782.63 pb	DYJetsToLL*M-10To50

Table 5: Monte Carlo simulation datasets used for the signal and background processes; Z stands for Z, Z^*, γ^* ; ℓ means e, μ or τ ; V stands for W and Z; \hat{p}_T is the transverse momentum for $2 \rightarrow 2$ hard processes in the rest frame of the hard interaction. Comment: $qq \rightarrow ZZ$ samples at 8 TeV have lower cut in m_{ll} , 4 GeV instead of 12 GeV at 7 TeV. TuneZ2 is used for 7 TeV, while TuneZ2star is used for 8 TeV analysis. The low mass Drell-Yann was produced with a filter for the 8 TeV analysis.

300

301 All the signal and background processes cross sections are re-weighted to NLO. In the case of
 302 Higgs production via the gluon fusion mechanism, the most recent NNLO+NNLL calculations
 303 of the cross sections are included [29].

304 The general multi-purpose Monte Carlo event generator PYTHIA [30] is used for several pro-
 305 cesses including QCD multijet production. It serves either to generate a given hard process at
 306 leading order (LO), or, in cases where the hard processes are generated at higher orders, only
 307 for the showering, hadronization, decays, and for adding the underlying event. This is the case
 308 for the MadGraph (MadEvent) Monte Carlo [31] event generators which are used to generate

309 multi-parton amplitudes and events for some important background processes. This is also
 310 the case for POWHEG NLO generator [32] which is used for the Higgs boson signal and for the
 311 ZZ and $t\bar{t}$ background. For the latter the $t\bar{t}$ decays are handled, exceptionally, within POWHEG.
 312 Finally, this is also the case for the dedicated tool GG2ZZ [33] used to generate the $gg \rightarrow ZZ$
 313 contribution to the ZZ cross section. For the underlying event, the so-called “PYTHIA tune Z2”
 314 in 2011 and “PYTHIA tune Z2 star” in 2012, which relies on p_T -ordered showers is used. For
 315 the parton density functions in the colliding protons, the CTEQ6M set is used except for the
 316 POWHEG samples from the “Fall11 and Summer12” which makes use of CT10.

317 More details on the event generators and the background samples used in this analysis, as well
 318 as indications on the procedures used to re-weight the MC events where needed, are provided
 319 in the following section 3.2.1.

320 3.2.1 Signal: $H \rightarrow ZZ^{(*)} \rightarrow 4\ell$

321 The Higgs boson samples used in the current analysis are generated with POWHEG [32] which
 322 incorporates NLO gluon fusion ($gg \rightarrow H$) and weak-boson fusion $q\bar{q} \rightarrow q\bar{q}H$. The CTEQ6M
 323 parton distribution (PDF) set is used for generation with the Higgs boson widths taken from
 324 Ref. [29]. Additional samples with WH, ZH and $t\bar{t}H$ associated production are produced with
 325 PYTHIA. The Higgs boson is forced to decay to two Z-bosons, which are allowed to be off-shell,
 326 and both Z-bosons are forced to decay via $Z \rightarrow 2\ell$.

327 Generator level events are re-weighted according to the total cross section $\sigma(pp \rightarrow H)$ which
 328 comprises the gluon fusion contribution up to NNLO and NNLL taken from Ref. [29, 34–42]
 329 and the weak-boson fusion contribution at NNLO computed in Ref. [29, 43–47]. The total cross
 330 section is scaled by the $BR(H \rightarrow 4\ell)$ [29, 48–51]. Figure 6 (a) shows the $H \rightarrow 4\ell$ cross-section
 331 as a function of the Higgs mass m_H for $\sqrt{s} = 7$ TeV.

332 For the Fall11 production, a total of 28 Monte Carlo samples were produced in the range 115
 333 to $600 \text{ GeV}/c^2$, with a step of $10 \text{ GeV}/c^2$ up to $230 \text{ GeV}/c^2$, and then steps of $25 \text{ GeV}/c^2$ up to
 334 $600 \text{ GeV}/c^2$. In Summer12 production additional samples were produced from $650 \text{ GeV}/c^2$ to
 335 $1000 \text{ GeV}/c^2$, with a step of $50 \text{ GeV}/c^2$, as well as additional low mass samples with finer granularities.
 336

337 In comparison to $\sigma(pp \rightarrow H) \cdot BR(H \rightarrow ZZ^{(*)} \rightarrow 2e2\mu)$, the 4μ and $4e$ channel cross-sections
 338 are enhanced in the case of off-shell Z boson due to an interference of amplitudes with permutations
 339 of identical leptons originating from different Z-bosons, as shown in Fig. 6 (b). This is
 340 correctly taken into account by Prophecy4f [29, 48, 49].

341 The POWHEG MC program used to simulate the $gg \rightarrow H$ process results in a Higgs Boson
 342 p_T spectrum that differs significantly from the best theoretical calculation which is available
 343 at NNLL+NLO. A theoretical estimate of this p_T spectrum is computed using the HqT [52]
 344 program, which implements such NNLL+NLO calculation. A re-weighting procedure has been
 345 studied to be applied to the simulated events (see Section 8.2.1). But the effect is very small for
 346 this analysis in which no direct constraints are imposed on the transverse momentum of the
 347 4ℓ system, or on the hadronic recoil against this system (e.g. no jet veto or missing transverse
 348 momentum cut).

349 In the current analysis we use only samples for gluon fusion production mechanism and rescale
 350 them to the total cross section including all other production processes (weak-boson fusion,
 351 WH, ZH and $t\bar{t}H$ associated production).

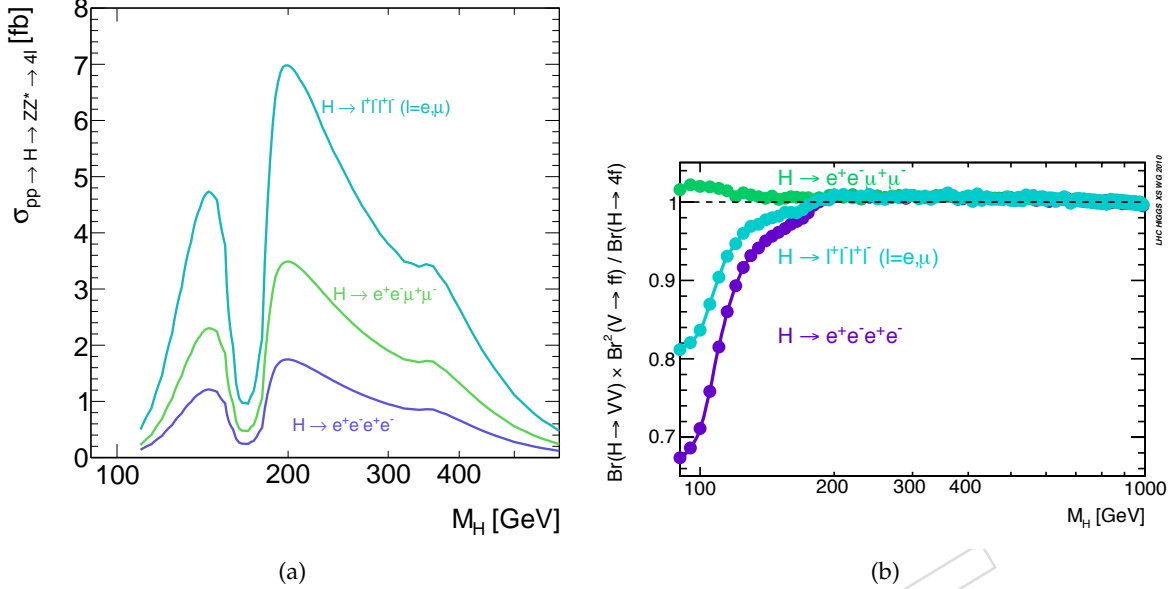


Figure 6: (a) Cross-section for SM Higgs in $H \rightarrow 4\ell$, $H \rightarrow 2e2\mu$ and $H \rightarrow 4e$ (or 4μ) as a function of m_H in pp collisions at $\sqrt{s} = 7$ TeV. (b) Cross-section enhancement due to the interference of amplitudes with permutations of identical leptons originating from different Z -bosons, as a function of m_H .

3.2.2 Background: $q\bar{q} \rightarrow ZZ^{(*)} \rightarrow 4\ell$

For the current analysis we use the samples $q\bar{q} \rightarrow ZZ^{(*)} \rightarrow 4\ell$ produced with `POWHEG`, that include the complete NLO simulation, interfaced to `PYTHIA` for showering, hadronization, decays and the underlying event.

3.2.3 Background: $gg \rightarrow ZZ^{(*)} \rightarrow 4\ell$

The gluon-induced ZZ background, although technically of NNLO compared to the first order Z -pair production, amounts to a non-negligible fraction of the total irreducible background at masses above the $2M_Z$ threshold. A full NNLO calculation for the ZZ production which would also take these gluon-induced diagrams into account is not available. Therefore the contributions are estimated by using the dedicated tool `gg2ZZ` [33], which computes the $gg \rightarrow ZZ$ at LO, which is of order α_s^2 , compared to α_s^0 for the LO $q\bar{q} \rightarrow ZZ$. The hard scattering $gg \rightarrow ZZ^{(*)} \rightarrow 4\ell$ events are then showered and hadronized using `PYTHIA`.

The `gg2ZZ` tools provide the functionality to compute the cross-section after applying a cut on the minimally generated invariant mass of the same-flavour lepton pairs (which can be interpreted as the Z/γ invariant mass) $m_{\ell\ell}^{\min} = 10$ GeV/c². This number is computed by using the LO PDF set `CTEQ6L1`, and the central renormalization and factorization scales $\mu_R = \mu_F = m_Z$, where $m_Z = 91.188$ GeV/c² is the nominal Z -boson mass. To estimate the accuracy of this number the renormalization and factorization scales were varied in the range $\mu \in [\mu_0/2, 2\mu_0]$; therefore an error of $^{+28\%}_{-20\%}$ is computed. The large uncertainty is expected, since the calculation is only LO, and only at NLO the scale dependencies start to cancel. It is thus very hard to estimate the accuracy of the convergence of the perturbative series (which contains only the first coefficient here), thus an uncertainty of $\pm 50\%$ on this number is proposed.

The `gg2ZZ` generator gives the contribution for final states with unlike flavours of the lepton

³⁷⁵ pairs, but it was also used to estimate the like-flavour background. This is an approximation
³⁷⁶ which is only strictly valid when $m_{4\ell} \geq 2m_Z$. Below this threshold the relative amount of
³⁷⁷ like-flavour events increases compared to unlike-flavour events.

³⁷⁸ The differential cross-section for $gg \rightarrow ZZ^{(*)}$ as a function of the four lepton invariant mass for
³⁷⁹ different flavour lepton pairs was provided in Ref [53].

³⁸⁰ 3.2.4 Background: Z+jets $\rightarrow 2\ell+\text{jets}$

³⁸¹ Z+jets $\rightarrow 2\ell+\text{jets}$ samples was generated with MadGraph, with a statistics of $\approx 40\text{M}$ events
³⁸² representing an equivalent integrated luminosity well above $\mathcal{O}(10)\text{fb}^{-1}$. Both light ($q = d, u, s$)
³⁸³ and heavy-flavor ($q = c, b$) jets are included in the sample. A generation cut on two-lepton
³⁸⁴ invariant mass of $m_{2\ell} > 50\text{ GeV}/c^2$ is imposed in the simulation. A total NNLO cross section of
³⁸⁵ 3048 (3503.7) pb is used at 7 (8) TeV.

³⁸⁶ To separate the contribution from heavy-flavor jets (from now on referred to as the $Zb\bar{b}$ sample)
³⁸⁷ the Madgraph Z+jets sample was partitioned in Z+light jets and Z+heavy flavor jets using a
³⁸⁸ filter selecting events with two b-jets or two c-jets in the final state.

³⁸⁹ 3.2.5 Background: $t\bar{t} \rightarrow 2\ell 2\nu 2b$

³⁹⁰ A $t\bar{t} \rightarrow 2\ell 2\nu 2b$ sample is generated with POWHEG event generator using CTEQ6M. The theoretical
³⁹¹ NLO cross-section for the process is $\sigma_{NLO}(pp \rightarrow t\bar{t} \rightarrow 2\ell 2\nu 2b) = 17.32$ (23.64) pb at 7 (8)
³⁹² TeV [54].

³⁹³ A sample of about 10 milion events corresponding to an integrated luminosity of more than
³⁹⁴ 600 fb^{-1} is simulated.

DRAFT

395 4 Leptons Observables

396 The reconstruction of the SM Higgs boson in the decay chain $H \rightarrow ZZ^{(*)} \rightarrow 4\ell$ imposes
 397 high-performance lepton reconstruction, identification and isolation as well as excellent lep-
 398 ton energy-momentum measurements. The identification of isolated leptons emerging from
 399 the event primary vertex allows for a drastic reduction of QCD-induced sources of misidenti-
 400 fied (“fake”) leptons. The precision energy-momentum measurements translates in a precision
 401 Higgs boson mass measurement $m_{4\ell}$, the most discriminating observable for the Higgs boson
 402 search.

403 With four leptons in the final state, and in view of the modest fraction of the total produc-
 404 tion cross-section observable in the 4ℓ channels, a very high lepton reconstruction efficiency
 405 is mandatory. For Higgs bosons with masses $m_H < 2m_Z$, one lepton pair at least couples to
 406 an off-shell Z^* boson. The softest lepton in that pair typically has $p_T^\ell < 10 \text{ GeV}/c$ for masses
 407 $m_H < 140 \text{ GeV}/c^2$. Preserving the highest possible reconstruction efficiency while ensuring
 408 sufficient discrimination against hadronic jets is especially challenging for the reconstruction
 409 for leptons at very low p_T^ℓ . Such very low p_T^ℓ values lie at the extreme edge of the domain which
 410 is controlled at the LHC using tag-and-probe methods in inclusive single Z production. In the
 411 case of the muons, this can be complemented by tag-and-probe using J/Ψ production. In the
 412 low p_T range, a full combination of information provided by the tracker and electromagnetic
 413 calorimetry (for electrons) or by the tracker and muon spectrometer (for muons) becomes es-
 414 sential for the reconstruction, identification and isolation of leptons. Otherwise, the single Z
 415 production is an ideal candle for this analysis, covering leptons in the p_T range from $\mathcal{O}(10)$ to
 416 $\mathcal{O}(100) \text{ GeV}/c$.

417 4.1 Electron Reconstruction and Identification

418 4.1.1 Reconstruction

419 The electron reconstruction [55] combines ECAL and tracker information. Electron candidates
 420 are reconstructed from clusters of energy deposits in the ECAL, which are then matched to hits
 421 in the silicon tracker. The standard CMS electron reconstruction algorithm is used [56–58] for
 422 this analysis. The energy deposited in the electromagnetic calorimeter (ECAL) is measured in
 423 clusters of clusters (superclusters) which collect Bremsstrahlung photons emitted in the tracker
 424 volume. Superclusters are used to search for hits in the innermost tracker layers which are used
 425 to seed electron tracks. This procedure is complemented by a tracker-driven approach allow-
 426 ing to improve the reconstruction efficiency at low p_T . Trajectories in the tracker volume are
 427 reconstructed using a dedicated modeling of the electron energy loss and fitted with a Gaus-
 428 sian Sum Filter. A cleaning is performed to resolve ambiguous cases where several tracks are
 429 reconstructed due to the conversion of radiated photons in the tracker material. Electron candi-
 430 dates are preselected using loose cuts on track-cluster matching observables so to preserve the
 431 highest possible efficiency while removing part of the QCD background. The four-momenta
 432 for an electron is obtained by taking angles from the associated Gaussian Sum Filter (GSF)
 433 track, and the energy from a combination of tracker and ECAL information [56]. The informa-
 434 tion from the track is measured at the distance-of-closest approach to the beam spot position
 435 in the transverse plane. Electron tracks are not re-fitted to the common primary vertex. For the
 436 physics analysis, the electron candidates are required to have transverse momentum p_T^e larger
 437 than $7 \text{ GeV}/c$ and a reconstructed $|\eta^e| < 2.5$. The reconstruction efficiency for isolated electron
 438 is expected to be above $\approx 90\%$ over the full ECAL acceptance, apart from some narrow “crack”
 439 regions. Integrated over the acceptance, the reconstruction efficiency for basic electron objects

steeply rises to reach $\approx 90\%$ at $p_T = 10 \text{ GeV}/c$, and then more slowly to reach a plateau of $\approx 95\%$ for $p_T^e = 30 \text{ GeV}/c$. More on electron reconstruction efficiency and control from 2011 and 2012 data will be discussed below in section 5.

Electron charge mis-identification has been measured on 2010 data using Z events and a charge mis-ID of 0.004 ± 0.001 (0.028 ± 0.003) was measured in the ECAL barrel (ECAL endcaps) in very good agreement with the simulation [59]. No significant p_T dependency was observed in the range of on-shell Z boson decays, also in agreement with the expectation.

The electron momentum scale and resolution can be controlled using Z boson decays to electrons. Fits to the Z line-shape selecting electrons with $E_T > 25 \text{ GeV}$ show differences in scale between data and MC of 0.3% (0.4%)¹ in the ECAL barrel (ECAL endcap), thus significantly improved with respect to previous 2010 results [60]. The electron classification also allows for the identification electrons accompanied by low bremsstrahlung with smallest measurement error [55, 58] on which the intrinsic energy resolution is checked. Scale factors on the data and additional smearing on the MC as obtained by fits to the Z line-shape [61] are applied on reconstructed electrons so to correct for the measured differences between the data and MC. Detailed comparisons between data and MC, after e-scale corrections on DATA and smearing on MC, will be shown in Section 8.2.2.

4.1.2 Identification

The purity of the sample of electron candidates is enhanced for the analysis by applying identification requirements on top of the basic collection of reconstructed electron objects. Electron candidates are selected using the newly developed electron identification tool using multivariate techniques [62]. It makes use of three main categories of variables: observables that match the information of the calorimeters and the tracker including the preshower, purely-calorimetric and purely-tracking observables.

The complete list of track-ECAL matching variables is presented below:

- E_{tot} / p_{in} , where E_{tot} is the supercluster energy and p_{in} the track momentum at the innermost track position;
- E_e / p_{out} , where E_e is the energy of the cluster closest to the electron track extrapolation to ECAL and p_{out} the track momentum at the outermost track position;
- $|\Delta\eta_{in}| = |\eta_{sc} - \eta_{in}^{extrap.}|$, where $|\eta_{sc}|$ is the energy weighted position in η of the supercluster and $\eta_{in}^{extrap.}$ is the η coordinate of the position of the closest approach to the supercluster position, extrapolating from the innermost track position and direction;
- $|\Delta\phi_{in}| = |\phi_{sc} - \phi_{in}^{extrap.}|$, where $|\Delta\phi_{in}|$ is a quantity similar to the former one but in azimuthal coordinates.
- $|\Delta\eta_{out}| = |\eta_e - \eta_{out}^{extrap.}|$, where $|\eta_e|$ is the η position of the cluster closest to the electron track extrapolation to ECAL ($\eta_{out}^{extrap.}|$).
- $1./E_{tot} - 1./p_{4-mom}$ which measures the deviation of the supercluster energy and electron momentum obtained by combining the tracker and ECAL information p_{4-mom} [ADDREF].

In order to improve the electron-pion discrimination the energy measured in the HCAL and in the preshower (ES) is also compared with the supercluster energy by using the ratios: E_{HCAL}/E_{tot}

¹numbers for the 03Oct ReReco sample; numbers for 05Jul and 05Aug ReReco are respectively 0.4% (0.2%) and 0.6% (0.8%)

481 and E_{ES}/E_{tot} .

482 In addition, several shower shapes variables are used:

- 483 • $\sigma_{i\eta i\eta}$ the width of the ECAL cluster along the η direction computed in the 5×5 block
484 of crystals centered on the highest energy crystal of the seed cluster;
- 485 • $\sigma_{i\phi i\phi}$ as the former but in azimuthal coordinates;
- 486 • $\eta - width$ supercluster η width.
- 487 • $\phi - width$ supercluster ϕ width.
- 488 • $(E_{5x5} - E_{5x1})/E_{5x5}$: where E_{5x5} is the energy computed in block of crystals and E_{5x1}
489 is the energy computed in the strip of crystals containing the cluster seed.
- 490 • $R9 = E_{3x3}/E_{tot}$ energy sum of 3×3 crystal centered on the most energetic, divided by
491 the supercluster energy

492 Finally, to further improve the separation between electrons and charged hadrons, pure track-
493 ing observables are also used, both using the dedicated CMS electron tracking (GSF) or the
494 standard KF tracks:

- 495 • $f_{brem} = (p_{in} - p_{out})/p_{in}$ with the GSF track, which measures very well the Bremsstrahlung
496 emission which helps in discriminating against charged-hadron particles.
- 497 • χ^2_{GSF}
- 498 • $hits_{KF}$
- 499 • χ^2_{KF}

500 The information carried out by these variables is maximized by using a multivariate analysis
501 (Boosted Decision Trees or BDT) where the signal and background samples for the training
502 have been carefully chosen.

503 The training of the BDTs was performed on a $W + 1$ -fake electron sample, directly taken from
504 DATA, for the background, while for signal, a mixture of Monte Carlo $Higgs \rightarrow ZZ \rightarrow 4e$
505 samples (with masses: 115-120-130-140 GeV/ c^2) was used.

506 The training of the multivariate analysis was performed in three different bins of η : $|\eta| < 0.8$,
507 $0.8 \leq |\eta| < 1.479$ and $1.479 \leq |\eta| < 2.5$ in order to take into account the different material
508 budget in the tracker. Moreover due to the dependencies of the electron observables on p_T
509 it was found that the final signal to background separation was improved when dividing the
510 sample in two bins of p_T : $5 \text{ GeV} \leq p_T \leq 10 \text{ GeV}$ and $p_T \geq 10 \text{ GeV}$.

511 The output of the BDT is presented in Fig. 7 for each of the six bins used for the training. Very
512 good separation between signal and background and very good agreement between fakes in
513 DATA and MC are observed.

514 In addition, all electrons must have 0 or 1 expected missing inner hits in order to reject con-
515 versions. Henceforward **eID** designates electron candidates selected among the basic electron
516 objects according to the technique and cuts just described.

517 A detailed study and control from 2011 and 2012 data of the efficiency for electron identification
518 with respect to the electron reconstruction is reported in section 5.

519 4.1.2.1 Working point optimization

520 An optimization procedure was performed in order to find the BDT working point to be used
521 in this analysis. A Monte Carlo $Higgs \rightarrow ZZ \rightarrow 4e$ sample (with $m_H = 120 \text{ GeV}/c^2$) was used

522 as signal, while background was modeled by a $Z + 1$ -fake electron sample, directly taken from
 523 DATA. The Z selection closely follow the selection used in the PRL published analysis (see
 524 section 1.1). The additional electron is a *loose electron* as defined in section 7. In addition, the
 525 missing transverse energy (as reconstructed by the particle flow algorithm) was required to
 526 be less than 25 GeV in order to suppress contamination from WZ events containing three real
 527 leptons.

528 In each of the six p_T and η bins described above, the cut value on the BDT output was chosen so
 529 as to obtain the same background efficiency as the cut-based electron identification algorithm
 530 used in the PRL analysis ("Cuts-In-Categories"). As it can be appreciated on the figure 8, in
 531 each tested bins, the BDT is performing much better than the cut-based electron identification
 532 used before. In particular, for $p_T < 10$ GeV, the electron identification efficiency is increase by
 533 30 % for the same per-lepton background efficiency as in PRL.

534 The cut values on the BDT output resulting from the optimization procedure are summarized
 535 below:

- 536 • $5 < p_T < 10$ GeV:
 - 537 • $|\eta| < 0.8 : BDT > 0.47$
 - 538 • $0.8 < |\eta| < 1.479 : BDT > 0.004$
 - 539 • $|\eta| > 1.479 : BDT > 0.295$
- 540 • $p_T > 10$ GeV
 - 541 • $|\eta| < 0.8 : BDT > 0.5$
 - 542 • $0.8 < |\eta| < 1.479 : BDT > 0.12$
 - 543 • $|\eta| > 1.479 : BDT > 0.6$

DRAFT

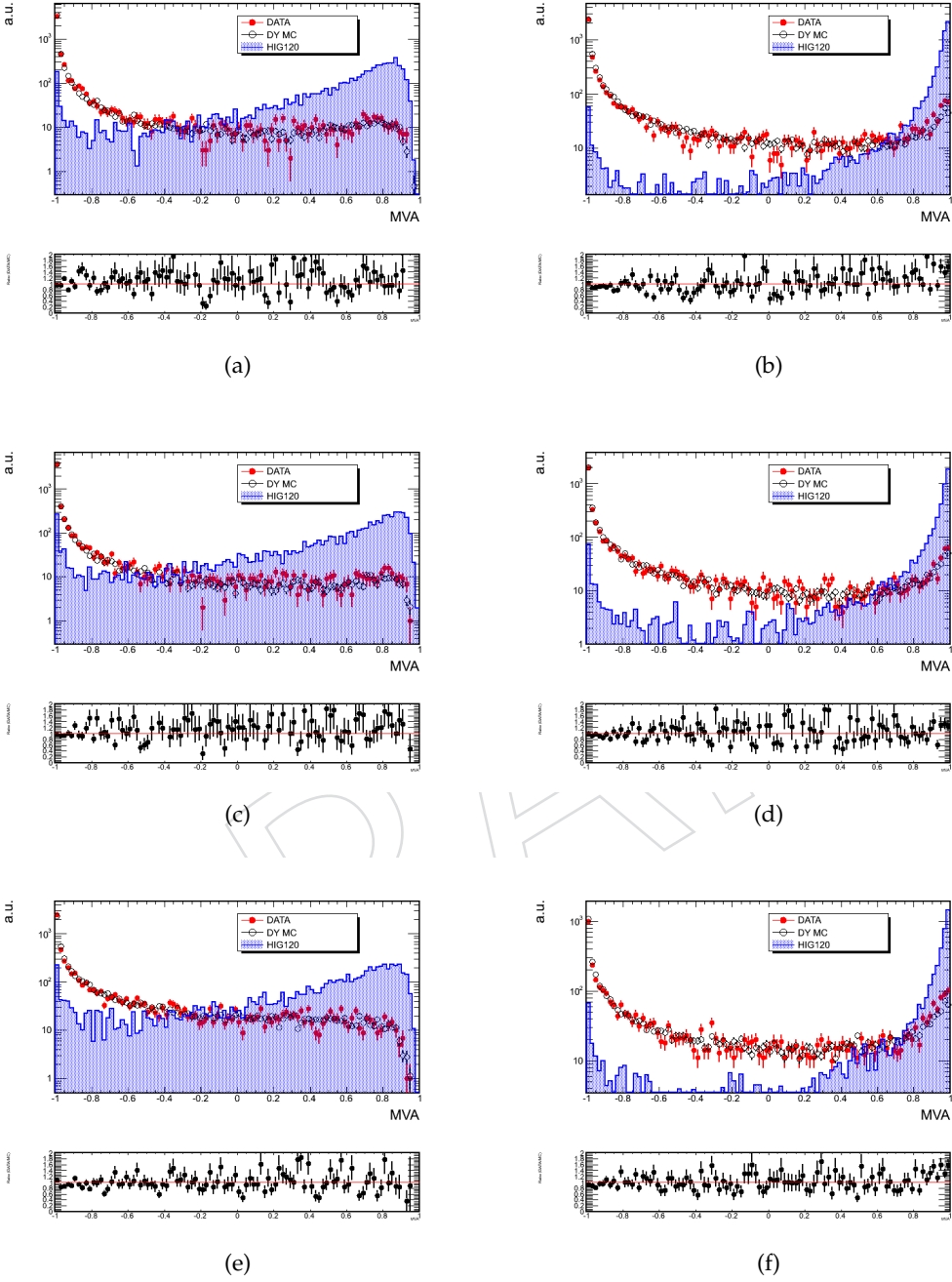


Figure 7: BDT output for each of the six categories used in the training. (a) $|\eta| < 0.8$, $p_T < 10$ GeV (b) $|\eta| < 0.8$, $p_T > 10$ GeV, (c) $0.8 \leq |\eta| \leq 1.479$, $p_T < 10$ GeV, (d) $0.8 \leq |\eta| \leq 1.479$, $p_T > 10$ GeV, (e) $1.479 \leq |\eta| \leq 2.5$, $p_T < 10$ GeV, (f) $1.479 \leq |\eta| \leq 2.5$, $p_T > 10$ GeV, for a Higgs signal with $m_H=120$ GeV (blue), for fake electrons in DATA (red points) and in MC (open circles). Ratio of fake electron between DATA and MC is also shown.

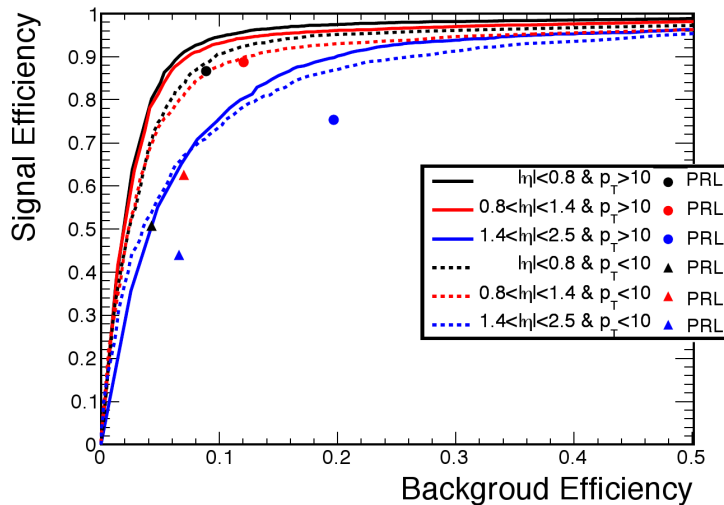


Figure 8: Higgs Signal Efficacy (MC) vs Background Efficiency from $Z + 1$ -fake electron sample (DATA). Solid lines represent results for the BDT, while single points show the corresponding ones for the "Cut-In-Categories" electron identification used in the PRL analysis. Results are shown for various bins in p_T and η .

544 4.2 Muon Reconstruction and Identification

545 4.2.1 Reconstruction

546 In the standard CMS reconstruction for pp collisions, muon tracks are first reconstructed inde-
 547 pendently in the inner tracker (*tracker track*) and in the muon system (*standalone-muon track*).
 548 Based on these objects, two reconstruction approaches are used [63]:

- 549 • *Global Muon reconstruction (outside-in)*. For each standalone-muon track, a matching
 550 tracker track is found by comparing parameters of the two tracks propagated onto
 551 a common surface, and a *global-muon track* is fitted combining hits from the tracker
 552 track and standalone-muon track, using the Kalman-filter technique [64]. At large
 553 transverse momenta, $p_T \gtrsim 200 \text{ GeV}/c$, the global-muon fit can improve the momen-
 554 tum resolution compared to the tracker-only fit [65, 66].
- 555 • *Tracker Muon reconstruction (inside-out)*. In this approach, all tracker tracks with $p_T >$
 556 $0.5 \text{ GeV}/c$ and the total momentum $p > 2.5 \text{ GeV}/c$ are considered as possible muon
 557 candidates and are extrapolated to the muon system taking into account the mag-
 558 netic field, the average expected energy losses, and multiple scattering in the detec-
 559 tor material. If at least one muon segment (i.e., a short track stub made of DT or CSC
 560 hits) matches the extrapolated track, the corresponding tracker track qualifies as a
 561 Tracker Muon. Track-to-segment matching is performed in a local (chamber) coor-
 562 dinate system, where local x is the best-measured coordinate (in the $r\phi$ plane) and
 563 local y is the coordinate orthogonal to it. The extrapolated track and the segment
 564 are considered to be matched if the distance between them in local x is less than
 565 3 cm or if the value of the pull for local x is less than 4, where the pull is defined as
 566 the difference between the position of the matched segment and the position of the
 567 extrapolated track, divided by their combined uncertainties.

568 Tracker Muon reconstruction is more efficient than the Global Muon reconstruction at low mo-
 569 mента, $p \lesssim 5 \text{ GeV}/c$, because it requires only a single muon segment in the muon system,
 570 whereas Global Muon reconstruction is designed to have high efficiency for muons penetrat-
 571 ing through more than one muon station and typically requires segments in at least two muon
 572 stations.

573 Thanks to the high tracker-track efficiency [67] and a very high efficiency of reconstructing
 574 segments in the muon system, about 99% of muons produced in pp collisions and having suffi-
 575 ciently high momentum are reconstructed either as a Global Muon or a Tracker Muon, and very
 576 often as both. Candidates found both by the Global Muon and the Tracker Muon approaches
 577 that share the same tracker track are merged into a single candidate. Muons reconstructed
 578 only as standalone-muon tracks have worse momentum resolution and less favourable colli-
 579 sion muon to cosmic-ray muon ratio than the Global and Tracker Muons and are usually not
 580 used in physics analyses.

582 4.2.2 Identification

583 The combination of different algorithms provides a robust and efficient muon reconstruction.
 584 A given physics analysis can achieve the desired balance between identification efficiency and
 585 purity by applying a selection based on various muon identification variables. For this analysis
 586 we choose the *Particle Flow Muon selection*: the CMS particle-flow event reconstruction [68] com-
 587 bines the information from all subdetectors to identify and reconstruct individually particles
 588 produced in the collision. The resulting list of particles is then used to construct higher-level
 589 particle-based objects and quantities, such as jets and missing transverse energy. To identify

590 Particle-Flow Muons, a selection is performed on all the muon candidates reconstructed with
 591 the standard algorithms described above (Tracker and Global Muons). This selection has been
 592 optimized to identify muons in jets with high efficiency, keeping the misidentification rate from
 593 charged hadrons low. This is needed to avoid biases in jet and E_T^{miss} measurements coming
 594 from non-identified or misidentified muons. As a consequence, the Particle-Flow Muon selec-
 595 tion has been designed to retain non-isolated muons, including the muons from hadron decays
 596 in flight, usually considered as a background in typical muon analyses. This is achieved by ap-
 597 plying selection criteria, which differ in strictness depending on whether the muon candidate
 598 is isolated or not, and whether its momentum is compatible with the energy deposition in the
 599 calorimeters assigned to the candidate by the particle-flow event reconstruction. The results
 600 is that the identification criteria on prompt isolated muons can be relaxed, without paying the
 601 price of an increase in fake reconstruction probability.

602 The details of the Particle-Flow Muon selection are described in Ref. [69].

603
 604 In the 2011 analysis the identification selection based only on the Global Muon reconstruction
 605 was used. In comparison with the 2011 choice the *Particle Flow Muon selection* is more efficient
 606 on prompt isolated muons as can be seen in Fig. 9. The fake rate (probability to mis-identify
 607 particle other than muons) has been measured to be compatible with that one expected with
 the 2011 identification selection.

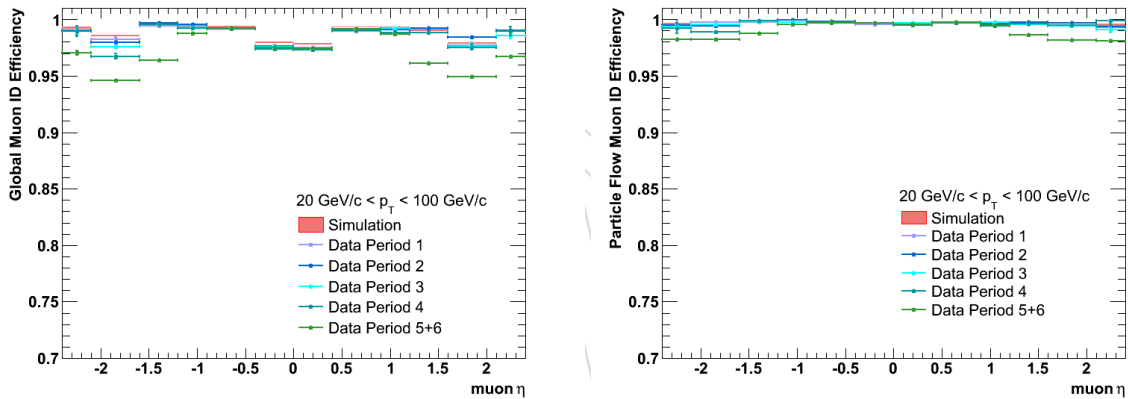


Figure 9: Muon reconstruction and identification efficiency for Global muons (left) and Particle Flow muons (right), measured with the tag-ang-probe method (Sec. 5) on different 2011 data periods as function of muon η .

608

609 4.2.3 Sensitivity to PU

610 The identification efficiency as a function of the number of reconstructed primary vertices in
 611 the pile-up scenario of 2012 data taking is shown to be stable in Fig. 10.

612 4.3 Primary and Secondary Leptons

613 The notion of leptons originating from a “common primary vertex” is taken throughout the
 614 analysis a meaning that each individual lepton as an associated track with a small impact
 615 parameter with respect to the event primary vertex. In practice for the event selection (see
 616 section 7), the significance of the impact parameter to the event vertex, $|\text{SIP}_{3D} = \frac{\text{IP}}{\sigma_{\text{IP}}}|$ is used
 617 where IP is the lepton impact parameter in three dimensions at the point of closest approach
 618 with respect to the primary interaction vertex, and σ_{IP} the associated uncertainty. Hereafter, a
 619 “primary lepton” is a lepton satisfying $|\text{SIP}_{3D}| < 4$.

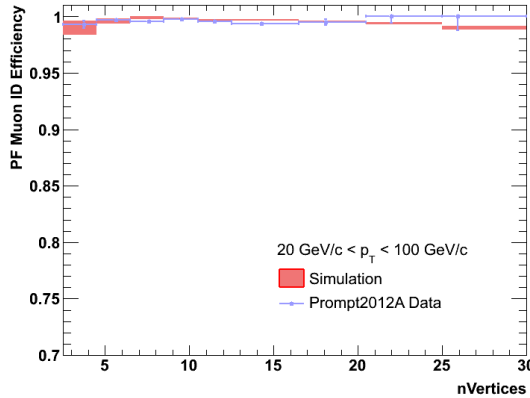


Figure 10: Muon reconstruction and identification efficiency for Particle Flow muons, measured with the tag-ang-probe method (Sec. 5) on 2012 data as function of the number of reconstructed primary vertices.

4.4 Lepton Isolation

Standard tools provided by CMS are used in the following manner. The isolation is defined by performing the scalar sum of the transverse momentum of the particle flow candidates reconstructed in a ΔR cone of 0.4, defined as:

$$\text{RelPFiso} = \frac{\sum_{\text{lepton}}^{\text{chargedhadron}} p_T + \sum_{\text{lepton}}^{\text{neutralhadron}} p_T + \sum_{\text{lepton}}^{\text{photon}} p_T}{p_T} \quad (1)$$

Because of the multiple interactions per bunch-crossing in ideal LHC conditions, the isolation can get worsened from the extra energy from pileup entering the isolation cone. The charged particle flow candidates are filtered through the algorithm *pfNoPileup* that does primary vertex association, while the neutral part is corrected according the method described in Sec. 4.4.1.

In case of electrons, the optimal efficiency in the barrel of the association of the brem clusters particle flow photons to the reconstructed particle flow electrons make possible to exploit the full cone area, while in the endcap some inefficiency in the particle flow electron id (to be corrected) makes necessary the usage of some internal vetoes to remove the electron footprint. Then, the particle-based isolation of a GSF electron requires the following vetoes on the candidates in the cone:

- barrel and endcap:

1. veto all the reconstructed particle flow electrons (in the most of the cases, this requirement removes the pf-electron correspondent to the GSF electron, with all its brem clusters)
2. veto all the charged hadrons that share the same GSF track or the closest CTF track with the electron

- endcap:

1. veto all the charged hadrons in a cone $\Delta R=0.015$ around the electron
2. veto all the photons in a cone $\Delta R=0.08$ around the electron

with these vetoes the footprint of the electron in both barrel and endcap is reduced to less than 1% (see [62]). To isolate leptons, the PRL analysis was exploiting the information that come

from the energy deposits in the calorimeters (*ECAL and HCAL detector-based isolation*) by performing the scalar sum of the transverse energy of rechits inside a cone $\Delta R = \sqrt{\Delta\eta^2 + \Delta\phi^2}$ (0.3) and the scalar sum of the transverse momentum of the tracks in the same cone (*tracker isolation*). The Figures 11 to 13 are showing background efficiency as a function of signal efficiency (ie, ROC curves) for various cuts on the isolation algorithms and in several η and p_T bins.

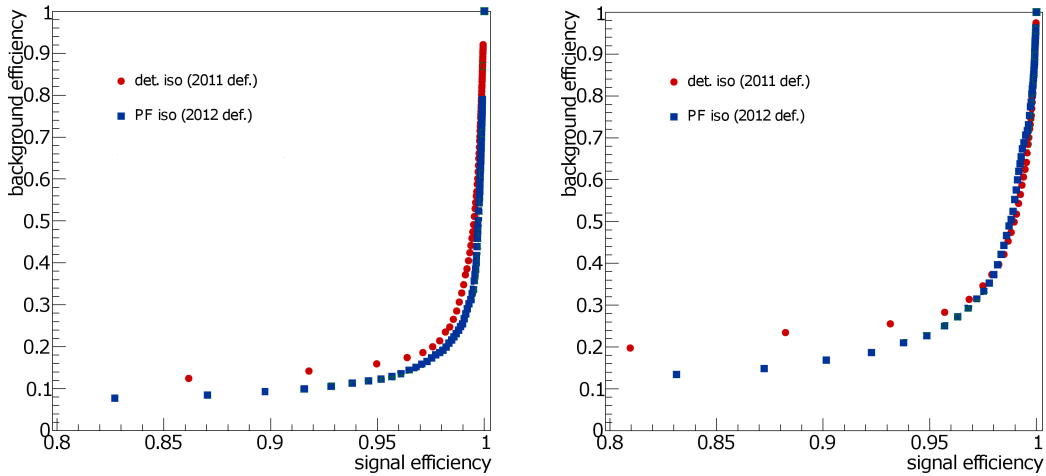


Figure 11: Background (electron fakes in $Z+1$ fake data control sample) versus signal efficiency (electrons MC-truth matched in $H \rightarrow ZZ \rightarrow 4l$ signal MC) for electrons with $p_T > 20$ GeV in the barrel (left) and in the endcap (right). Background samples is selected 2011 data sample

649

650 In the high p_T region all the algorithms give approximatively the same performances, while the
 651 gain using particle-based isolation is increasing as the electron p_T lowers, justifying the choice
 652 to use it in this analysis.

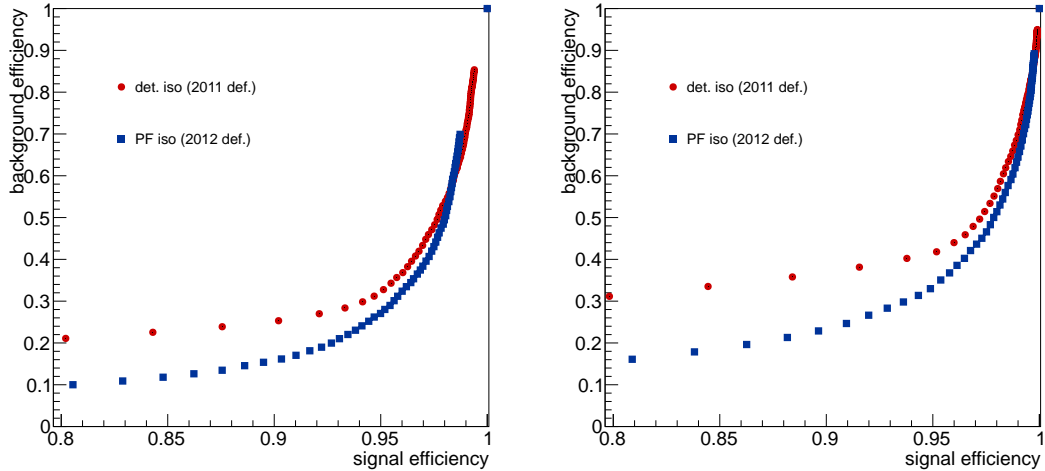


Figure 12: Background (electron fakes in $Z+1$ fake data control sample) versus signal efficiency (electrons MC-truth matched in $H \rightarrow ZZ \rightarrow 4l$ signal MC) for electrons with $10 < p_T < 20$ GeV in the barrel (left) and in the endcap (right). Background samples is selected 2011 data sample

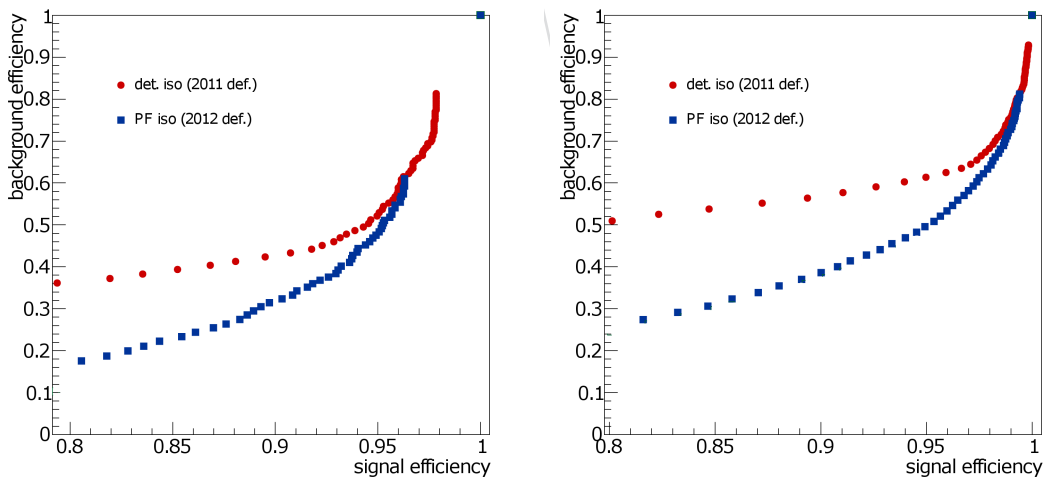


Figure 13: Background (electron fakes in $Z+1$ fake data control sample) versus signal efficiency (electrons MC-truth matched in $H \rightarrow ZZ \rightarrow 4l$ signal MC) for electrons with $5 < p_T < 10$ GeV in the barrel (left) and in the endcap (right). Background samples is selected 2011 data sample

653 **4.4.1 Pile-up corrections**

654 Isolation variables are among the most pile-up sensitive variables in this analysis. Pile-up
 655 causes the mean energy deposited in the detector to increase, leading to the rise of the mean
 656 isolation values. Thus, the efficiency of a cut on isolation variables strongly depends on pile-up
 657 conditions. In order to have a pile-up robust analysis, the isolation variable has to be corrected.

658 The degradation of isolation performances due to pile-up can be partly mitigated associating
 659 the charged particle flow candidates to the primary vertices. We do this through this association
 660 with `pfNoPileup` association, which consists in filtering the sample of charged particle flow
 661 candidates associated with the other primary vertices excluding the one with the highest $\sum p_T^2$
 662 of the associated tracks.

However, the neutral component (neutral hadron and photons), for which this association cannot be trivially done, need a special treatment. Among several correction methods, the one using `FastJet` [70, 71] energy density (ρ) in the event has been chosen to estimate the mean pile-up contribution within the isolation cone of a lepton. A ρ variable is defined for each jet in a given event and the median of the ρ distribution for each event is taken. The correction to the neutral component of the isolation variable is then applied according to the formula :

$$\sum_{\text{neutral}}^{\text{corr}} p_T = \max\left(\sum_{\text{neutral}}^{\text{uncorr}} p_T - \rho \cdot A_{\text{eff}}, 0 \text{ GeV}\right) \quad (2)$$

663 where the *effective area* (A_{eff}) of a given component is defined as the ratio between the slope of
 664 the average isolation *iso* and ρ as a function of number of vertices.

665 We are currently using the ICHEP recommendation from the e/g and muon POGs regarding
 666 ρ computation and A_{eff} . However, while work is in progress to align the slightly different
 667 approaches followed for electrons and muons, we take as a reference for ICHEP what has been
 668 proposed by POGs and describe them in what follows.

669 **ρ computation**

670 For 2011, the energy density ρ is calculated using jets reconstructed with k_T algorithm (with
 671 $D = 0.6$), taking as input all particles built with the particle-flow algorithm². For 2012, the
 672 same ρ definition was taken from muons, except that the charged particles were removed when
 673 building jets. For electrons, all particles were considered, up to $|\eta| < 3$.

674 **Effective Areas**

675 It was noticed that the A_{eff} are increasing with the η of the lepton, and this is mainly due to
 676 increasing pileup and with the fact that the geometrical isolation cone gets truncated at the end
 677 of the tracker acceptance.

678 As a consequence, A_{eff} for the neutral isolation component was calculated in fine bins in η ,
 679 especially in the endcap. In Table 6 we report the effective areas measured in 1.6 fb^{-1} of the
 680 first 2012 data and in the full 2011 dataset (5.05 fb^{-1}), on the $Z \rightarrow ee$ sample.

681 For the muons, the Table 7 summarizes the numbers derived for both 2011 and 2012 data periods.

Summary

Since the charged hadron isolation is already not dependent on the number of vertices, the total

²From the technical point of view, *rho* was not stored in Fall11 AOD's used for the 7 TeV analysis and need to be computed on the fly. `Rho_EtaMax` and `Ghost_EtaMax` are set to 2.5

η range	2012 data (5.26 fb^{-1})	2011 data (5.05 fb^{-1})
$ \eta < 1.0$	0.19 ± 0.006	0.18 ± 0.002
$1.0 < \eta < 1.479$	0.25 ± 0.006	0.20 ± 0.003
$1.479 < \eta < 2.0$	0.12 ± 0.004	0.15 ± 0.002
$2.0 < \eta < 2.2$	0.21 ± 0.007	0.19 ± 0.003
$2.2 < \eta < 2.3$	0.27 ± 0.02	0.21 ± 0.006
$2.3 < \eta < 2.4$	0.44 ± 0.03	0.22 ± 0.007
$ \eta > 2.4$	0.52 ± 0.05	0.29 ± 0.008

Table 6: Effective areas calculated on 2012 data (5.26 fb^{-1}) and 2011 data (5.05 fb^{-1}) for electrons in different η bins, for isolation cone of $\Delta R = 0.4$.

η range	2012 data (5.26 fb^{-1})	2011 data (5.05 fb^{-1})
$ \eta < 1.0$	0.674	0.132
$1.0 < \eta < 1.479$	0.565	0.120
$1.479 < \eta < 2.0$	0.442	0.114
$2.0 < \eta < 2.2$	0.515	0.139
$2.2 < \eta < 2.3$	0.821	0.168
$ \eta > 2.3$	0.660	0.189

Table 7: Effective areas calculated on 2012 data (5.26 fb^{-1}) and 2011 data (5.05 fb^{-1}) for muons in different η bins, for isolation cone of $\Delta R = 0.4$.

corrected isolation sum is the following:

$$\sum_{\text{corr}} p_T = \sum_{\text{charged}} p_T + \left(\sum_{\text{neutral}}^{\text{uncorr}} p_T - \rho \cdot A_{\text{eff}} \right) \quad (3)$$

We validate that the corrections are flattening the average isolation \sum_{corr} in the same dataset where we calibrated the effective areas. The figure 14 is showing the average energy flow before and after the corrections for electrons and for two selected η bins. While the average energy flow was growing as the number of vertices increases before the pile-up corrections, a flat distribution is obtained after applying the recipe described in this section.

Moreover, the isolation efficiencies for single electrons in the bin $7 < p_T < 100 \text{ GeV}$ as a function of the number of vertices is shown in Figure 15, together with MC efficiencies. They were calculated with the tag and probe method. After the pile-up correction treatment, the efficiency shows moderate decrease with increasing number of vertices.

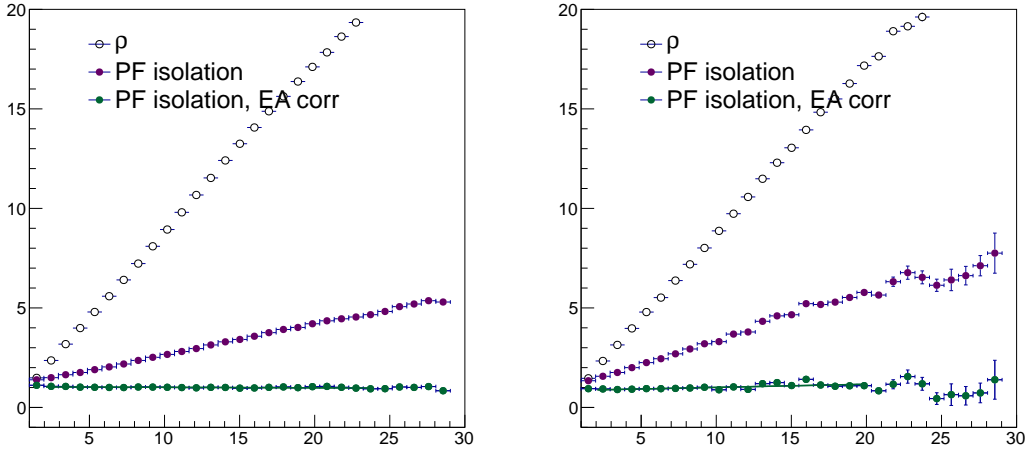


Figure 14: Average energy flow in electron isolation cone of $\Delta R=0.4$, before and after the pileup corrections, for identified electrons with a $Z \rightarrow \ell\ell$ selection in 2011 data in two η bins. Left: $|\eta| < 1.0$; right: $2.2 < |\eta| < 2.3$.

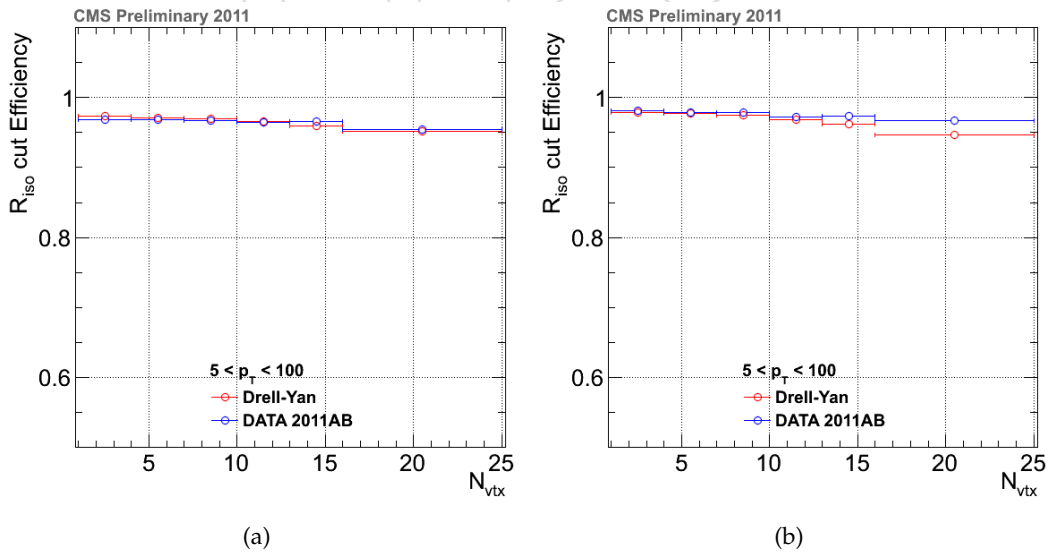


Figure 15: Electron isolation efficiencies computed with the tag-and-probe method in the bin $7 < p_T < 100$ GeV as a function of the number of vertices for electrons in ECAL barrel (a) and ECAL endcap (b)

692 4.4.2 Working Point optimization

693 In order to find the best working point for isolation, we followed an optimization done in the
 694 phase space of the analysis, with kinematic cuts close to the final ones. Various isolation cuts
 695 were tried: simple cut on each lepton leg (1D cut), cut on the sum of isolation of lepton pairs
 696 (2D cut, as in PRL). Two types of backgrounds were considered: irreducible ZZ (taken from
 697 MC) and reducible. For the latter, the estimation was done on DATA, following the procedure
 698 used for the PRL analysis (see Section 1.1). In short:

- 699 • select a sample with $Z + \text{two same-sign, same-flavor loose leptons}$ with $|\text{SIP}| < 4$.
- 700 • for each cut value, compute the corresponding fake rate. Apply it on the two legs
 701 with *loose leptons* to obtain the number of reducible background events.

702 The optimial cut value was choosen so as to maximize the significance of a signal, calculated
 703 from a Poisson statistics. The figure 16 (left) shows the ratio between the significance and the
 704 maximal significance as a function of the cut value on RelPFiso, for both 1D and 2D cut, for
 705 the 4μ channel and for a $m_H=120$ GeV MC signal sample. For simplicity, the 1D cut option was
 706 chosen, since the 2D cut configuration was only bringing 1% more significance.

707 Moreover, it was shown that the optimum cut value had almost no dependance with the
 708 mass of the Higgs signal sample tested. Finally, having a different cut for barrel and endcap
 709 has been considered. The figure 16 (right) is showing the significance obtained scanning dif-
 710 ferent cuts for muons in the barrel or in the endcap. As it can be appreciated, the maximum
 711 significance only differs by 0.5% from the configuration where a single cut (< 0.4) s used irre-
 712 spective of the muon η localisation.

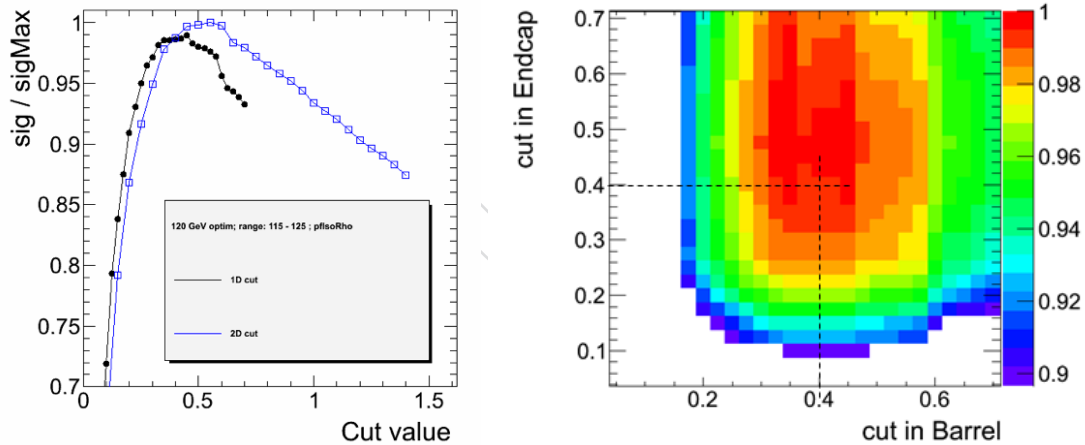


Figure 16: Left: ratio between the significance and the maximal significance as a function of the cut value on RelPFiso, for both 1D and 2D cut, for the 4μ channel and for a $m_H=120$ GeV MC signal sample. Right: significance obtained scanning different cuts for muons in the barrel or in the endcap.

713 Similar results were also found for the electron cases. We therefore decided to use RelPFiso
 714 < 0.4 for both electrons and muons, over the whole η range.

5 Leptons Measurements

5.1 T&P methodology

The efficiencies for reconstruction, identification and trigger for electrons and muons is measured with data based on a selection of events of inclusive single Z production. The well-known tag-and-probe technique [63, 72] combines the requirements of a mass constraint from a pair of basic objects (e.g. tracks for muons, or clusters of calorimetry cells for electrons) with a tight lepton selection applied on one leg (the "tag"), so to ensure sufficient purity. The other leg (the "probe") is used to measure the efficiency of a given reconstruction algorithm or identification criterium. The efficiency is defined as the ratio of the number of passing probes to the total number of probes before the cut.

It is important to perform such a measurement with the exact electron and muon objects as used in this analysis. By using appropriate definitions for probes, the overall efficiency per lepton can be factorized in a series of terms, that can be measured independently:

$$\epsilon = \epsilon_{\text{RECO}|\text{trackorclustering}} \times \epsilon_{\text{ID}|\text{RECO}} \times \epsilon_{\text{ISO}|\text{ID}} \times \epsilon_{\text{SIP}|\text{ISO}} \quad (4)$$

where each terms represents the efficiency for the probe to pass a given selection or reconstruction step, given that it passes the criteria for the previous one. The clustering efficiency for electrons is assumed to be 100% efficient which is checked by MC to be the case within few per mille in the p_T range of interest for this analysis. The efficiency to reconstruct a muon in the inner tracker has been measured separately and found to be 99% or higher in the whole tracker acceptance, in good agreement with the expectations from simulations [73].

By applying the method to both data and simulation we derive data to simulation scale factors. These scale factors are later used to either correct the signal efficiency in the simulation (using in this case their uncertainty as systematic error) or to provide systematic uncertainties (cf. section 8.2.2). Statistical uncertainties on the efficiencies are estimated using Clopper-Pearson confidence intervals [74, 75]. In the computation of the final systematics on the signal efficiency the systematics on the tag-and-probe method are also considered; they are evaluated varying the signal and background modeling.

The tables with all numbers for the efficiencies measured with the Tag and Probe technique on data, MC and the data/MC ratio are collected in Appendix B.

5.2 Electrons

In the case of electrons, tags are defined as an electron fulfilling the following criteria:

- $p_T > 20 \text{ GeV}/c$ and $|\eta| < 2.5$
- passing the VBF Simple Cuts, Working Point 60% (WP60) which involves cuts on pure identification variables ($|\Delta\eta_{\text{in}}|$, $|\Delta\phi_{\text{in}}|$, H/E and $\sigma_{i\eta i\eta}$), track and calorimeter isolation as well as conversion removal [76].
- being matched geometrically to the leg of the double object trigger used for the study that has requirement on the electron ID at trigger level.

5.2.1 Electron Reconstruction and Identification

Electron reconstruction efficiency has been measured on 2011 data following the methodology described in [74] and the results reported in [77] are used in this analysis for the 7 TeV Analysis.

Following the same methodology, the reconstruction (for 2012 data) and identification efficiency (for both 2011 and 2012 data) are measured in several p_T and η bins by performing an extended likelihood fit of the passing and failing samples in each bin. A Breit-Wigner convoluted with a Crystall-Ball function, with an exponential to describe the tails, is used to model the signal (cf Figure 17). The functional forms where chosen after careful Monte Carlo studies. The background is described by an Error function times an exponential.

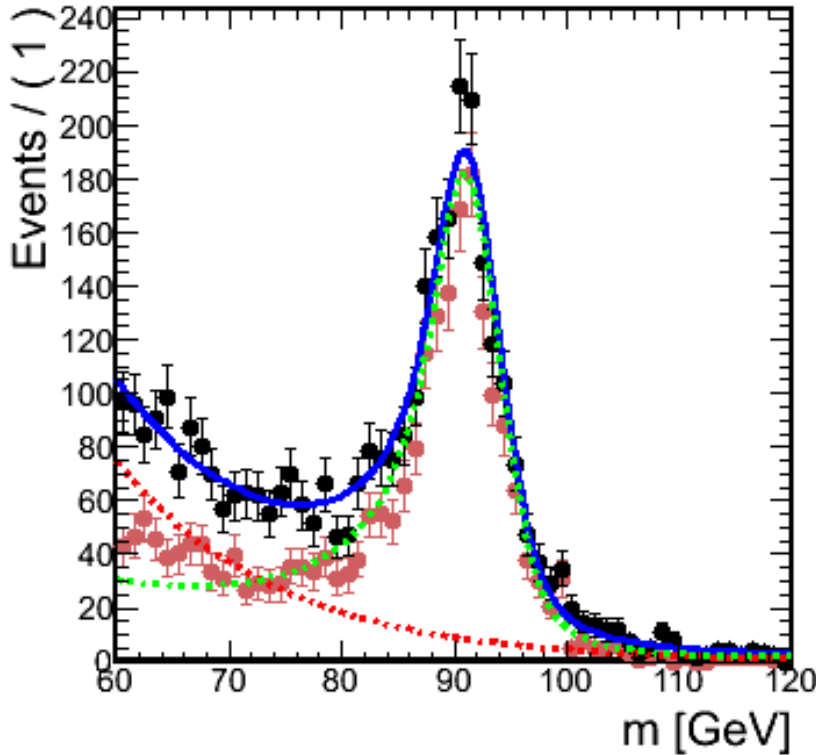


Figure 17: Example of the $m_{\ell\ell}$ distributions from MC and fit for passing probes used for the electron identification efficiency measurement. Black points are after T&P selection, red for events for which the reconstructed probe is matched with a generated electron. Green dashed line is the signal model, red is the background model and blue is signal+background.

The measured reconstruction efficiencies for single electrons as a function of the SuperCluster probe E_T (with $E_T > 10 \text{ GeV}/c$) are shown in Figure 18 for 8 TeV data, for electrons in ECAL barrel and in ECAL endcaps.

The measured identification efficiencies for single electrons as a function of the electron probe p_T (with $p_T > 7 \text{ GeV}/c$) are shown in Figure 19 for 7 TeV data and in Figure 20 for 8 TeV data, together with MC efficiencies. The latter were obtained fitting signal simulation, where the probe electron is matched with a generated electron. In addition, the tail in data is constrained by what is obtained from MC. The efficiencies are computed in bins of η coverage and all data taking periods are considered together. Given the limited statistics available for 8 TeV, only two η bins are currently shown. All numerical values are tabulated in Appendix B.

There is a overall good data/MC agreement in the barrel and the endcaps. Only statistical errors are reported on the plots. The differences observed at low p_T and in the endcaps between data and MC are mostly due to the background estimation (with higher background in the low p_T and high η regions) and the known discrepancies between data and MC of some of the variables used in the electron ID.

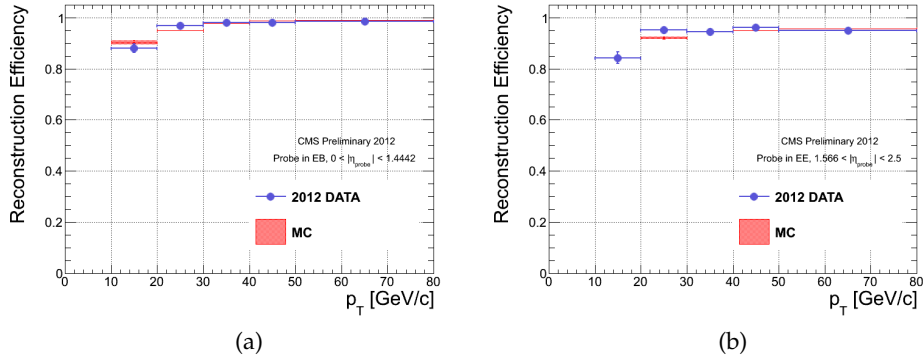


Figure 18: Electron reconstruction efficiencies computed with the tag-and-probe method as a function of the SuperCluster probe E_T in two different η bins: (a) $|\eta| < 1.442$, (b) $1.442 < |\eta| < 2.5$. Results are for 8 TeV data.

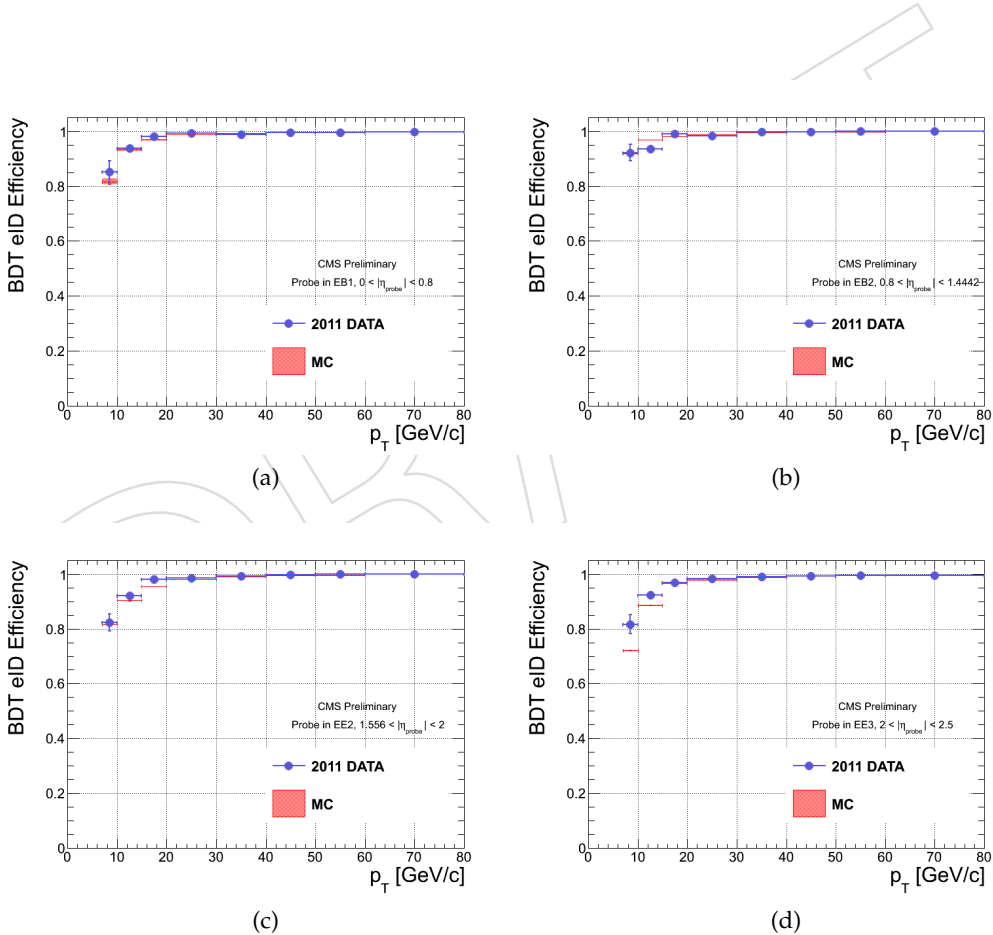


Figure 19: Electron identification efficiencies computed with the tag-and-probe method as a function of the probe p_T in four different η bins: (a) $|\eta| < 0.78$, (b) $0.78 \leq |\eta| \leq 1.442$, (c) $1.566 \leq |\eta| < 2$ and (d) $2 \leq |\eta| < 2.5$. Results are for 7 TeV data.

775 As an example, the $m_{\ell\ell}$ distributions for passing and failing probes used for the measurement of the electron identification efficiency in the $(10 - 15)$ GeV/c p_T bin and for $1.566 \leq |\eta| <$

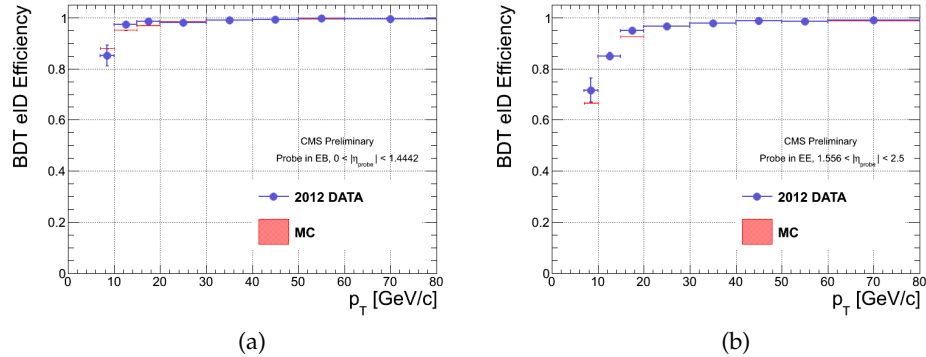


Figure 20: Electron identification efficiencies computed with the tag-and-probe method as a function of the probe p_T in two different η bins: (a) $|\eta| < 1.442$, (b) $1.442 < |\eta| < 2.5$. Results are for 8 TeV data.

777 2 in 2011 data is shown in Figure 21.

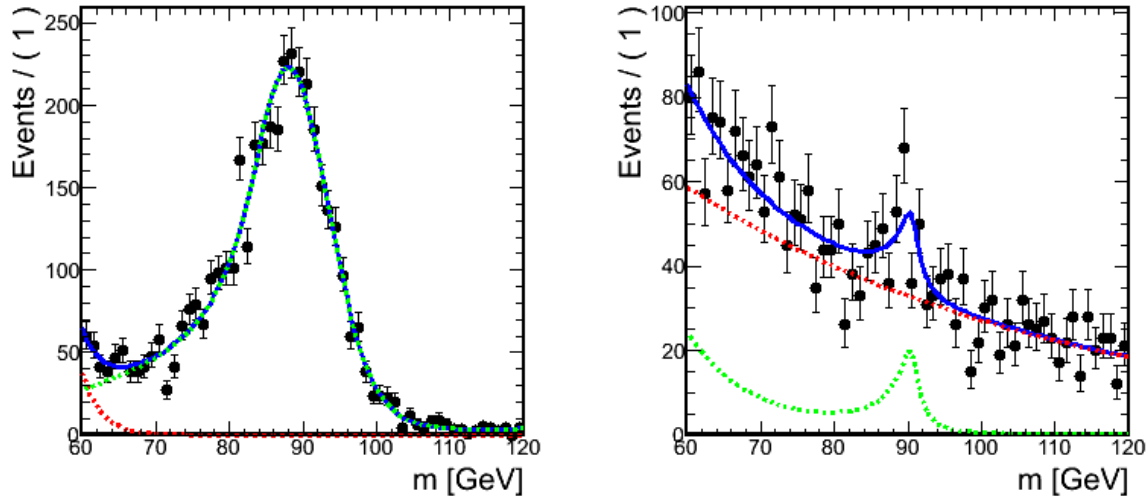


Figure 21: The $m_{\ell\ell}$ distributions and fits for passing and failing probes used for the electron identification efficiency measurement in the $(10 - 15)$ GeV/ c p_T bin and for $1.566 \leq |\eta| < 2$. Black points are 2011 data, green line is signal model, red line is background model and blue line is signal+background.

778 5.2.2 Electron Isolation and |SIP3D|

779 For electron isolation and $|SIP3D|$ efficiencies measurement are done simultaneously. The
 780 probes are identified electrons satisfying the BDT requirements described above. The tag re-
 781 quirement was slightly changed, moving from WP60 to WP80, and using particle-based isolat-
 782 ion. The passing criterium for probes is $R_{iso} < 0.4$ and $|SIP3D| < 4$. The isolation+—SIP—
 783 efficiency relative to the identified electrons is measured by requiring the probe electron to ful-
 784 fil the identification criteria, thus reducing significantly the amount of background events in
 785 the sample. In the low pT ($pT < 20\text{ GeV}$) and high pT ($pT > 50\text{ GeV}$) bins for the probe, the Drell-
 786 Yan content of the sample is enhanced, creating a tail in the low mass and high mass region

respectively. An additional Err x Exp function is added to the function describing the signal to model this tail made of genuine signal electrons. The Drell-Yan over Z ratio is taken from the simulation. Especially in the low p_T bin, this procedure ensures that the Drell-Yan signal and background contributions are disentangled without introducing a pdf taken from the simulation. In addition, for the low p_T bins (below 20 GeV), the identification criteria has been tightened on the probe in order to reject more background, under the assumption that the small correlation between the identification and the isolation and impact parameter is either fully negligible or correctly reproduced by the simulation so that the data/MC scale factors remain unchanged.

Some examples of $m_{\ell\ell}$ distributions for passing and failing probes used for the measurement of the electron isolation+ $|SIP3D|$ efficiency in the $(10 - 15)$ GeV/c p_T bin and for $1.566 \leq |\eta| < 2$ in 2011 data is shown in Figure 22.

The measured identification+isolation+ $|SIP3D|$ efficiencies for single electrons as a function of the probe p_T , together with MC efficiencies, are shown in Figure 23 for 2011 data and Figure 24 for 2012 data. In 2011, the measurement in the ECAL Barrel-Endcap transition region has been performed in a single bin, integrated over the whole p_T range. The agreement overall is very good. Only statistical errors are reported on the plots.

The tables 42 and 43 (in Appendix B) are summarizing the numerical values for the efficiencies measured in both data and MC for the full electron selection requirement (ID+Iso+SIP). Systematics errors are also reported. They have two origins:

- signal tail: the number of events under the tail are varied by two times, up and down, and the efficiency is re-computed. The difference wrt nominal measurement is taken as systematic error.
- peak modeling: a 1% is assigned, based on past studies [74], changing the signal function to a Voigtian.

5.2.3 Electron trigger

The Tag & Probe technic was used on 2012 data to measure the trigger efficiency for the Double Electron trigger used in the analysis:

HLT_Ele17_CaloIdT_CaloIsoVL_TrkIdVL_TrkIsoVL_Ele8_CaloIdT_CaloIsoVL_TrkIdVL_TrkIsoVL

This HLT path is composed by three HLT filters:

- hltEle17TightIdLooseIsoEle8TightIdLooseIsoTrackIsoFilter (*Ele17* in the following),
- hltEle17TightIdLooseIsoEle8TightIdLooseIsoTrackIsoDoubleFilter (*Ele17Ele8* in the following),
- hltEle17TightIdLooseIsoEle8TightIdLooseIsoTrackIsoDZ (*Ele17Ele8dZ* in the following).

An event fired the trigger if the three filters are satisfied. To measure the trigger efficiency, events should satisfy the following selection:

- T&P trigger: HLT_Ele20_CaloIdVT_CaloIsoVT_TrkIdT_TrkIsoVT_SC4_Mass50_v1
- Tag: electron with $p_T > 20$ GeV, passing "Tight Trigger Working Point 2012" (tighter than trigger requirements), and spatially matched ($\Delta R < 0.1$) with an online HLT electron passing the HLTFilter hltEle20CaloIdVTCaloIsoVTTrkIdTTrkIsoVTSC4TrackIsoFilter.
- Probe: electron passing the analysis selection (BDT eID, PFIso and SIP) and spatially matched ($\Delta R < 0.1$) with an online HLT electron passing the HLTFilter hltEle20CaloIdVTCaloIsoVTTrkIdTTrkIsoVTSC4PMMassFilter.
- Tag and Probe electrons must have opposite sign and their invariant mass must be reconstructed between 60 and 120 GeV.

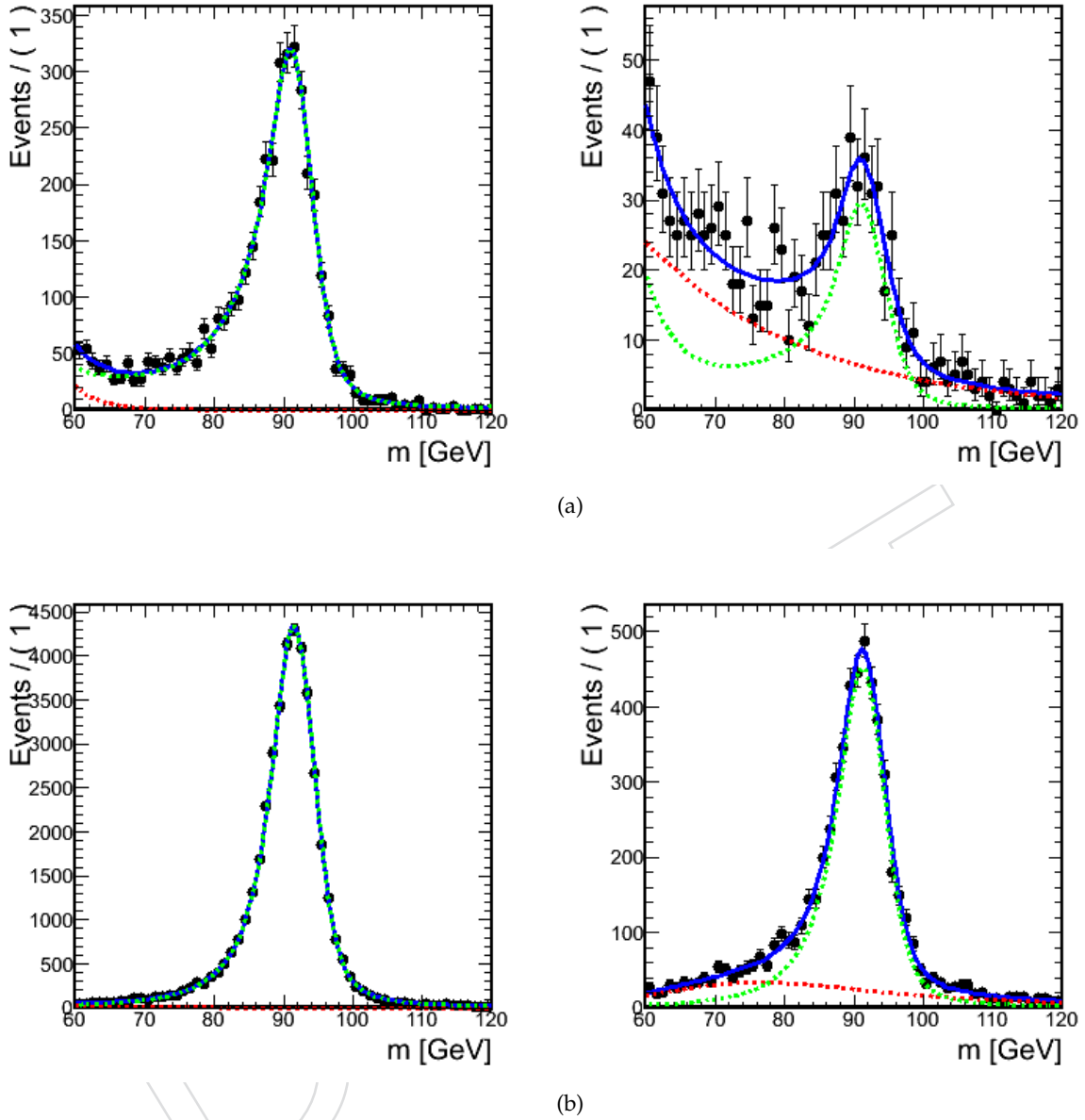


Figure 22: The m_{ee} distributions and fits for passing and failing probes used for the electron isolation and $|SIP3D|$ efficiency measurement in a) the $(10 - 15)$ GeV/c p_T bin in the barrel and b) the $(30-40)$ GeV/c p_T bin for $2 \leq |\eta| < 2.5$. Black points are 2011 data, green line is signal model, red line is background model and blue line is signal+background.

832 It's not possible to directly measure the efficiency to pass the Ele8 leg. Indeed, the second (and third)
 833 filter are requiring two electrons: one with $E_T > 17$ GeV and one with $E_T > 8$ GeV . In the following,
 834 we make the assumption that all electrons passing 17 GeV threshold are passing the 8 GeV one. The
 835 efficiency to pass the Ele8 leg is therefore computed from electrons passing these filters.
 836

837 The efficiency to pass Ele17 is calculated as the number of probes passing Ele17 and Ele17Ele8dZ over the
 838 total number of probes. The efficiency to pass Ele17Ele8dZ is calculated as the number of probes passing
 839 Ele17Ele8dZ over the total number of probes.
 840

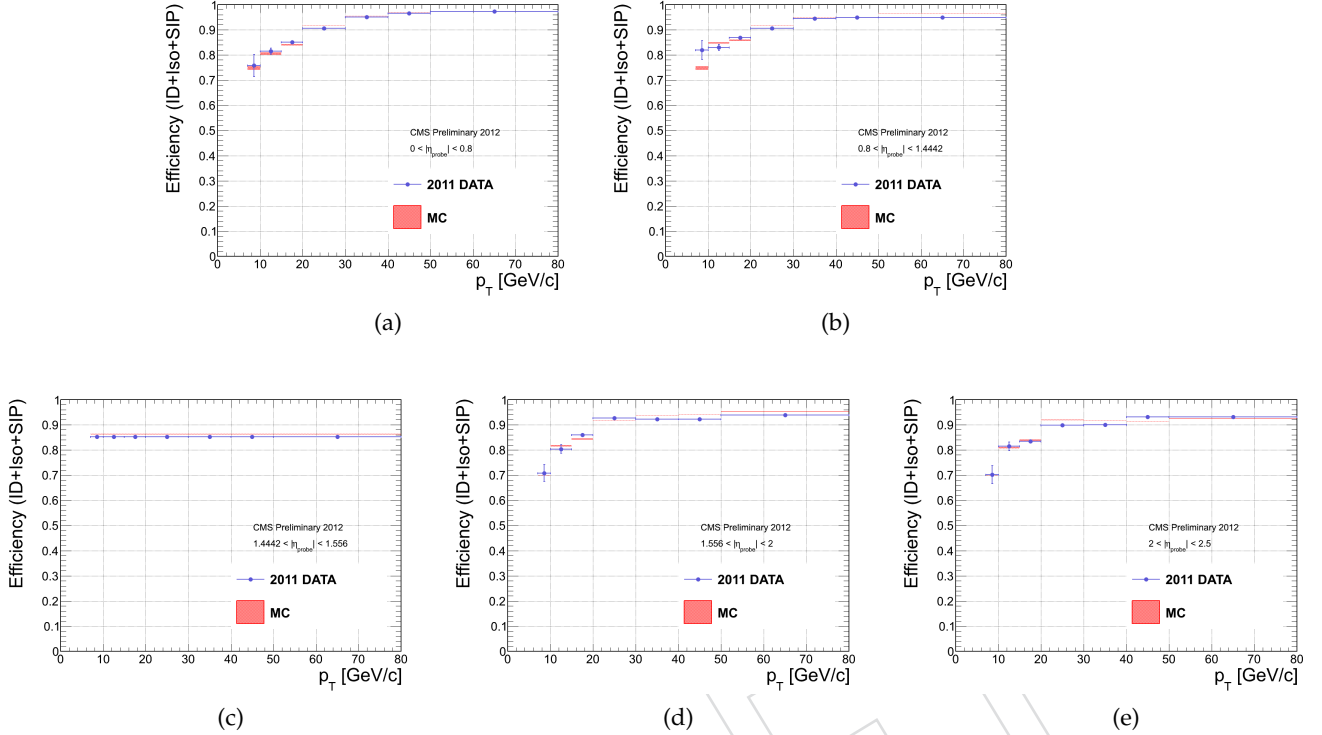


Figure 23: Electron identification+isolation+ $|SIP3D|$ efficiencies computed with the tag-and-probe method as a function of the probe p_T in five different η bins: (a) $0 \geq \eta < 0.78$, (b) $0.78 \geq \eta \leq 1.442$, (c) $1.442 \geq \eta \leq 1.566$, (d) $1.566 \geq \eta < 2$ and (e) $2 \geq \eta < 2.5$. The measurement in (c) has been performed in a single bin, integrated over the whole p_T range. Results are shown for 7 TeV data.

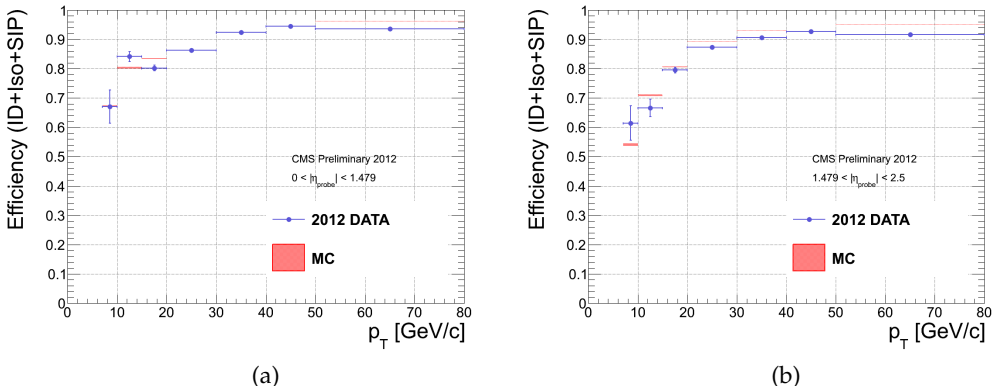


Figure 24: Electron identification+isolation+ $|SIP3D|$ efficiencies computed with the tag-and-probe method as a function of the probe p_T in two different η bins: (a) $|\eta| < 1.442$, (b) $1.442 < |\eta| < 2.5$. Results are for 8 TeV data.

841 The Figure 25 is showing the comparison between data and MC of the trigger efficiency for the filters
 842 $Ele17$ and $Ele17Ele8dZ$ for electrons in ECAL barrel and endcaps.

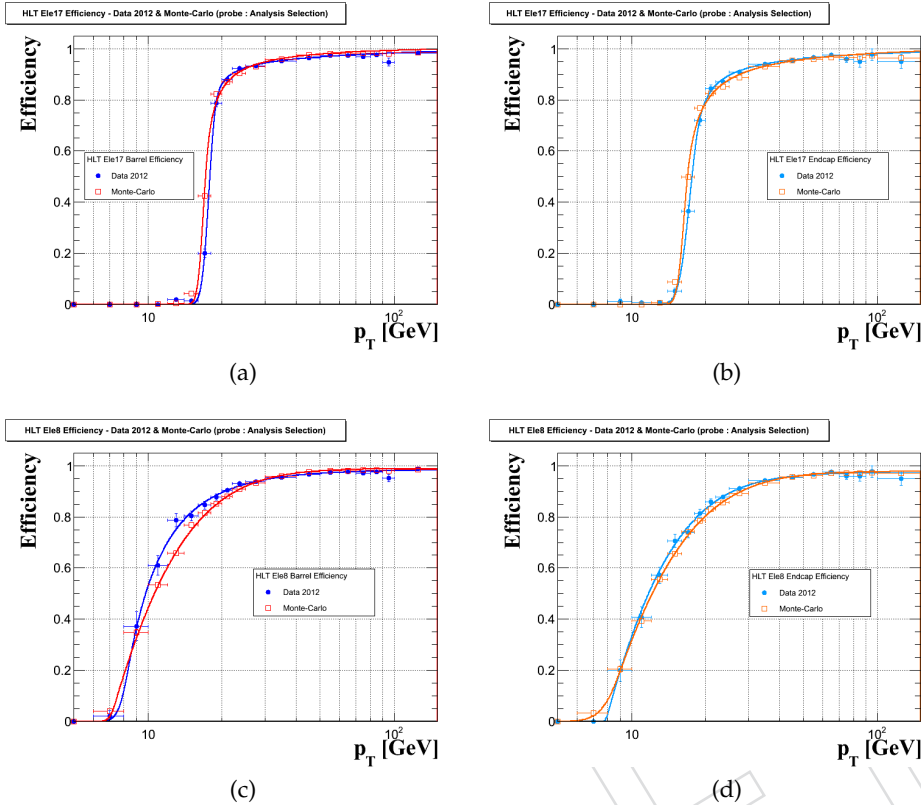


Figure 25: Electron HLT Trigger efficiency for the *Ele17* (resp. *Ele17Ele8dZ*) filter as a function of the probe p_T for electrons in ECAL barrel (a) and endcaps (b) (resp. (c) and (d)). Results are shown for 8 TeV data (blue) and Summer12 MC (red), with parameterizations superimposed. Probes are asked to pass ID, Isolation and SIP requirements of the analysis.

843 Data and MC are in fair agreement for the *Ele17* leg. The differences are less than 0.3% for the plateau
 844 and 0.5% for the turn-on. Discrepancies are slightly higher for the *Ele17Ele8dZ* leg with a difference of
 845 about 1 GeV in the plateau for electrons in the ECAL barrel (0.5 GeV in the endcaps) and a difference of
 846 1-2 GeV in the turn-on.

847 These turn-ons have been used to compute the efficiency of signal events to pass the trigger require-
 848 ments. The following prescription was used for each of the four electron candidates on an event-by-
 849 event basis. For each electron, with a given p_T and η , the probability to pass a given filter is computed
 850 from the turnon-ons. A random number is thrown between 0 and 1. If the number is below the proba-
 851 bility, the electron is passing the filter considered. If at least 2 electrons are passing *Ele17Ele8dZ* and at
 852 least one electron is passing *Ele17*, the event fired the trigger. The trigger efficiency has been computed
 853 after all other analysis cuts and has been compared to the direct measurement, requiring the trigger bit.

854 As can be seen from the Figure 26 (left), the efficiency computed with turn-ons (red or blue curves) are
 855 higher than the ones computed requiring the trigger bit. This is understood as being an effect due to the
 856 different algorithms used at HLT and offline levels for the electron isolation. Particle-based isolation is
 857 indeed used at offline level, vetoing other leptons in the isolation cone, while detector-based isolation is
 858 used at HLT level, without any veto on additional leptons. Events with nearby electrons therefore tend
 859 to fail the trigger requirements.

860 The turn-ons computed on single electrons don't allow to compute the "real" trigger efficiency. How-
 861 ever, comparing the trigger efficiency obtained this way with turn-ons measured on data and MC allows
 862 to estimate a possible correction to apply to the direct measurement with the trigger bit. It can be ap-
 863 preciated on Figure 26 (left) that there are little differences between data (blue) and MC (red). As a

consequence, we don't apply any correction on the MC related to trigger.

The trigger efficiency is not 100%, especially at low mass. It has been shown that the usage of a OR between the Double Electron and a Tri-Electrons trigger permits to recover 3.3% efficiency for $m_H = 125$ GeV (see Figure 26, right). The Tri-Electron trigger is not used in the current analysis but will be considered for the next iterations.

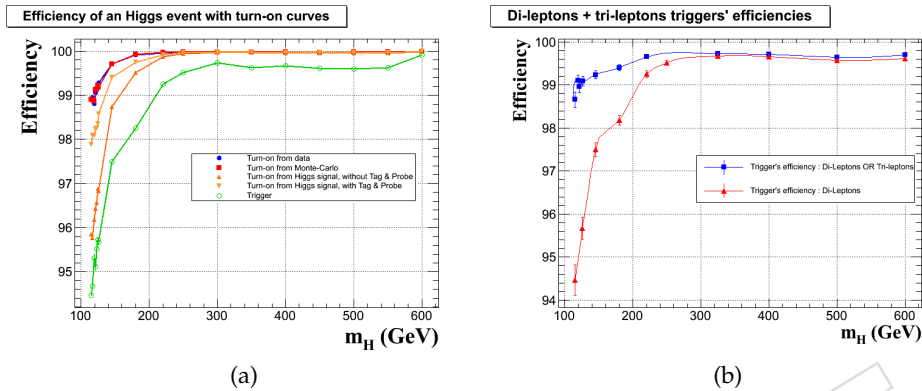


Figure 26: As a function of the Higgs mass (a), Electron HLT Trigger efficiency of the Double Electron Trigger computed with turn-ons measured on $Z \rightarrow ee$ data (red), $Z \rightarrow ee$ MC (blue), Higgs events with (orange), without (dark orange) Tag & Probe techniques and with the trigger bit (green). As a function of the Higgs mass (b), Electron HLT trigger efficiency of the Double Electron trigger (red) and of a OR between the Double and Tri-Electrons triggers, computed with the trigger bit. The trigger efficiencies are computed after all other analysis cuts.

5.3 Muons

The overall offline selection efficiency for muons is factorized as the product of:

- the efficiency to reconstruct a track in the inner detector (ϵ_{trk}),
- the efficiency of the Particle Flow muon reconstruction and identification for muons that have been successfully reconstructed in the inner tracker ($\epsilon_{\text{id}|\text{tk}}$),
- the efficiency of the impact parameter requirement, for muons passing the identification ($\epsilon_{\text{sip}_{3d}|\text{id}}$),
- the efficiency of the isolation requirement, for muons passing all other selection criteria ($\epsilon_{\text{iso}|\text{sip}_{3d}}$).

The efficiency to reconstruct the track from a muon in the inner tracker has been measured on 2010 and 2011 data[78], and found to be in close to 100%, and in agreement with the predictions from simulation to better than 0.2%.

5.3.1 Reconstruction and identification

For muons that are successfully reconstructed as a track in the inner tracker, the performance of the reconstruction in the muon system and the identification criteria for Particle Flow muons has been measured in 2011 and 2012 data using the tag-and-probe method using dimuons from Z (for $p_T > 15$ GeV) and J/ Ψ decays (for $p_T < 15$ GeV). A detailed description of the method, and results on 2010 data, can be found elsewhere[63]. The efficiencies measured from data, and the corresponding values obtained applying the same procedure on simulated Z and J/ Ψ events are shown in Fig. 27, and the numerical values of the efficiencies and data-to-simulation correction factors are reported in the appendix (Tab. ??). The simulated events used for comparisons in the two datataking periods have been reconstructed with the same software algorithms as the data, and are weighted as function of the number of reconstructed primary vertices to match the multiplicity observed in data.

For the 2011 data taking period, in the barrel region ($|\eta| < 1.2$) the results of the measurement on data are in very good agreement with the predictions from simulations for p_T above 5 GeV relevant for the analysis³, and the plateau value of the efficiency is reproduced within 0.3% or better. In the endcaps, the plateau value of the efficiency is about 0.8% lower in data than in the simulation, due to some issues in the CSC readout system during the second part of the data taking.

Good agreement is likewise observed in 2012 data, although the statistical accuracy of the measurement at low transverse momenta is currently limited.

5.3.2 SIP3D

The same tag-and-probe method has been used also to measure the efficiency of the requirement on the significance of the 3D impact parameter, for muons passing the Particle Flow identification requirements. In this context, only muons from Z decays can be used, as the J/ Ψ decays contain a significant contamination of non-prompt J/ Ψ 's from B hadron decays.

The efficiency of the $|\text{SIP3D}| < 4$ criteria is found to be above 99.5% in the barrel, and decreasing slightly down to about 99% in the forward part of the detector (Fig. 28). In the latter region, the efficiency in data about 0.4% lower than in simulations (Tab. ??).

5.3.3 Isolation

The isolation efficiency, the last component of the offline selection efficiency, has been measured on data using the tag-and-probe method for muons passing the Particle Flow identification and the $|\text{SIP3D}| < 4$ criteria. Similarly to the efficiency measurement of impact parameter requirements, only muons from Z decays can be used, since muons from J/ Ψ 's are not expected to be isolated, especially for non-prompt J/ Ψ mesons. The measurement is statistically limited in the 5–10 GeV p_T region on 2012 data, but otherwise an excellent agreement is observed between data and expectations from simulation (Fig. 29).

³The higher efficiency in data with respect to simulations for p_T below 5 GeV is due to the more conservative uncertainty estimates used in the track-to-segment matching in data.

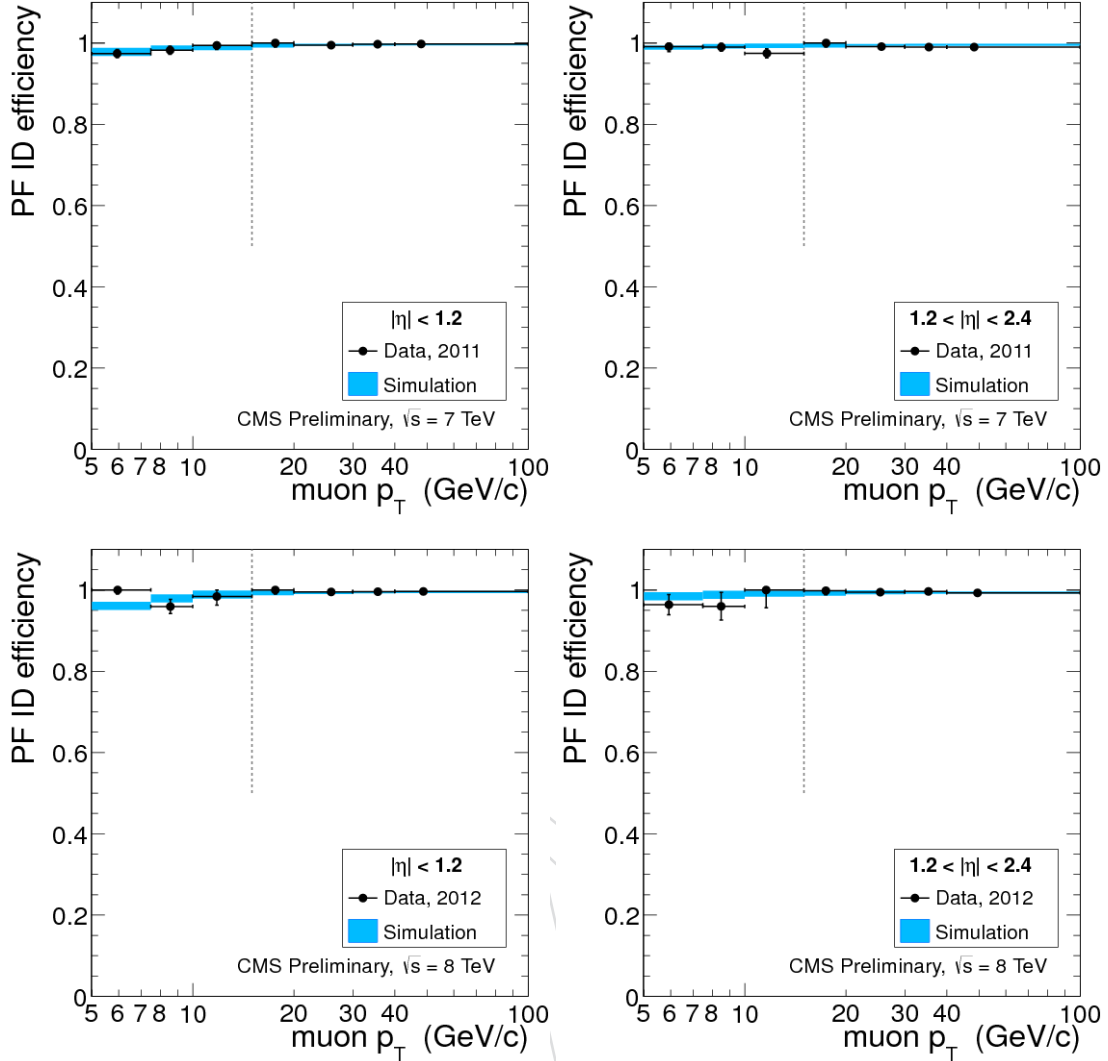


Figure 27: Muon reconstruction and identification efficiency for Particle Flow muons, measured with the tag-ang-probe method on 2011 data (top) and 2012 data (bottom) as function of muon p_T , in the barrel (left) and endcaps (right).

5.3.4 Trigger

The tag-and-probe method has also been used to measure the per-muon efficiency for double muon triggers: as the requirements for either leg of the double muon trigger are always looser than the single muon trigger used to select the tags, the tag+probe pair will satisfy a given double muon trigger requirement whenever the probe satisfies the requirements of a leg of that muon trigger. The double muon trigger requirements are not symmetric for the two legs, but the information about the HLT objects can be used to determine if the probe leg satisfies the requirements only of the loose leg or also of the tight one.

The measurement has been performed in 2011, both inclusively and separately for the “Run2011A” and “Run2011B” periods, for the dimuon trigger with p_T thresholds of 17 and 8 GeV (`HLT_Mu17_Mu8`); as in the rest of the analysis, for the earlier part of the data taking this trigger is emulated by requiring the events to fire a dimuon trigger with lower thresholds but whose associated HLT objects have p_T above the 17 and 8 GeV. For the 2012 running period, measurements have been performed both for the dimuon triggers with only L3 muons as in 2011 (`HLT_Mu17_Mu8`) and for the one exploiting also tracker muon reconstruction (`HLT_Mu17_TkMu8`), and for the logical OR of the two.

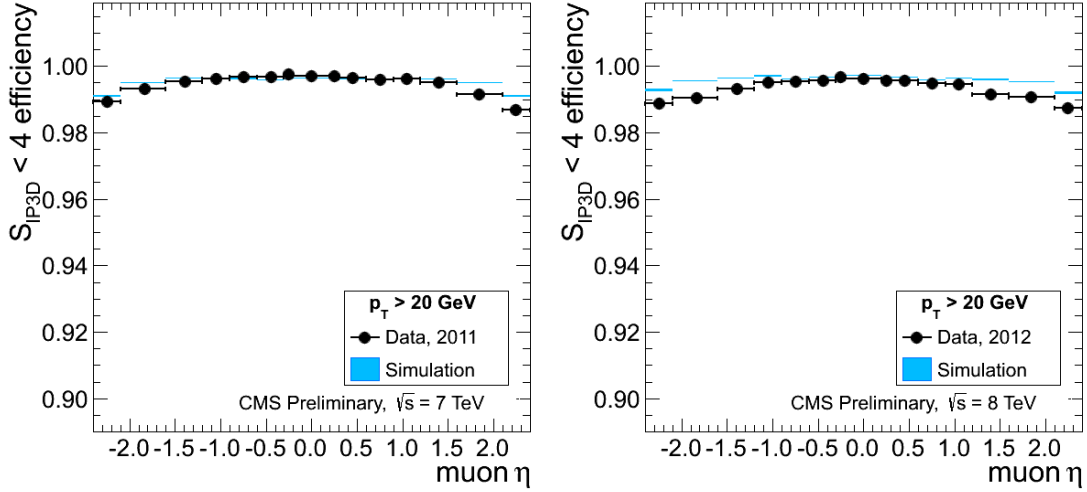


Figure 28: Efficiency for the requirement on the 3D impact parameter significance $|S_{IP3D}| < 4$, as function of muon pseudorapidity, for 2011 data (left) and 2012 data (right). Muons with $p_T > 20$ GeV and satisfying the Particle Flow identification requirements are used.

928 The position and sharpness of the turn-on curve of the trigger efficiency as function of p_T measured on
 929 data is in very good agreement with the expectations from simulation for all the triggers considered; two
 930 representative results are shown in the top panels of Fig. 30. A measurement of the trigger efficiency on
 931 the plateau as function of pseudorapidity η reveals a lower efficiency in data compared to simulation in
 932 the endcaps and in the narrow transition between the two wheels of the barrel (Fig. 30, lower panels).
 933 The effect of this inefficiency is however mitigated by the fact that multiple leptons in the event can fire
 934 the trigger, resulting in per-event inefficiencies of only FIXME for μ and FIXME for $2e2\mu$ events, and so
 935 no correction factor is applied at present in the analysis.

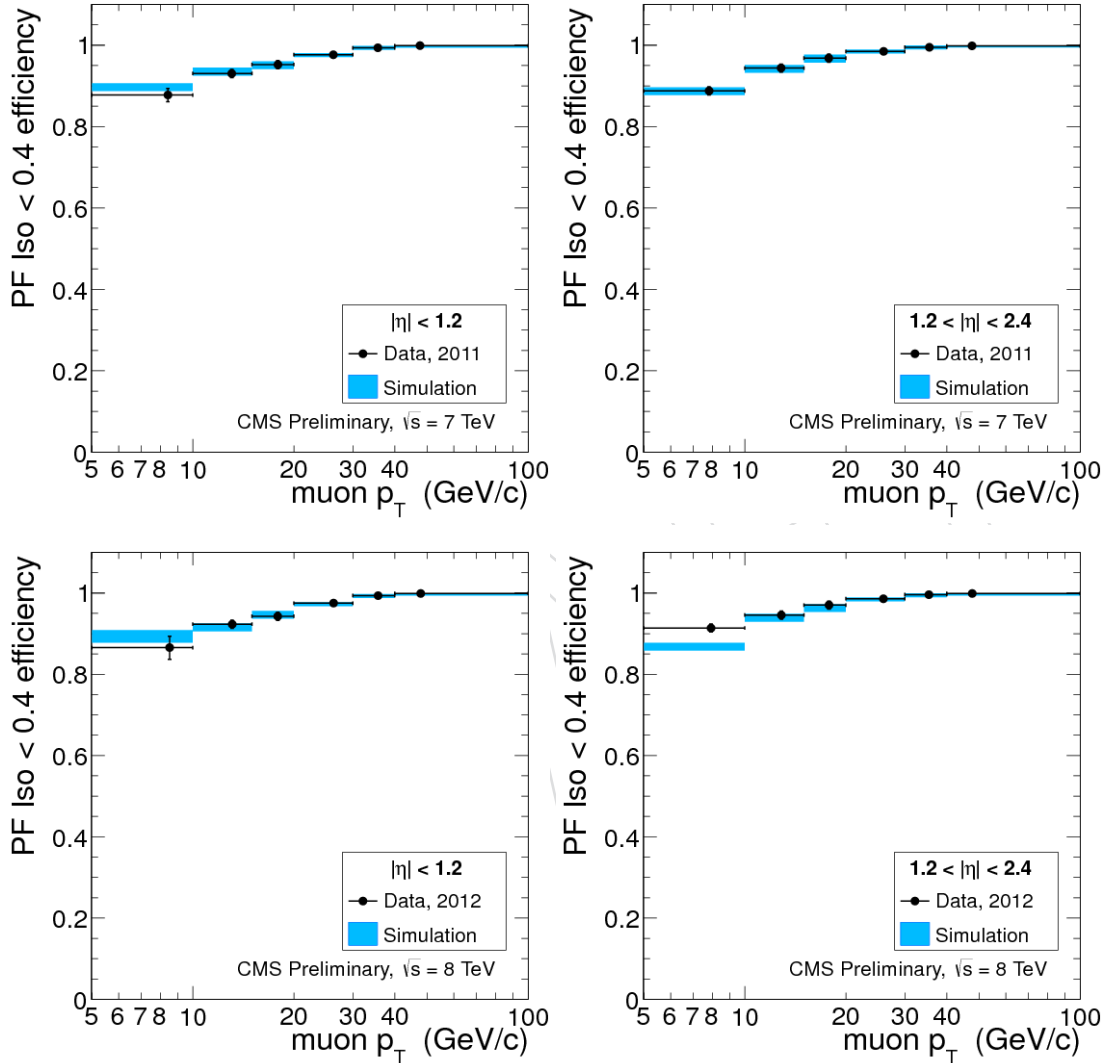


Figure 29: Muon isolation efficiency for Particle Flow muons passing the impact parameter requirements, measured with the tag-ang-probe method on 2011 data (top) and 2012 data (bottom) as function of muon p_T , in the barrel (left) and endcaps (right). FIXME plots of 2012 to be updated with more data.

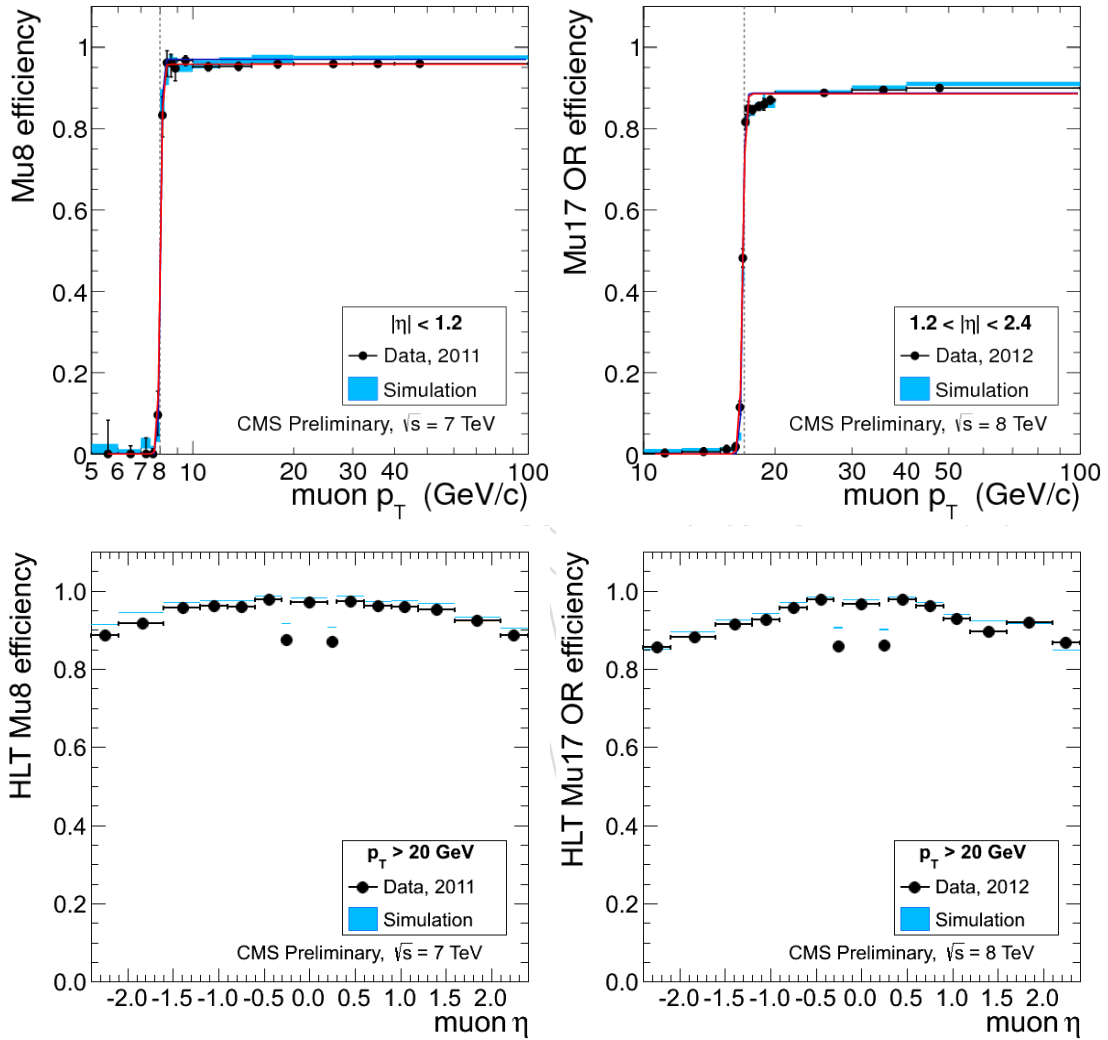


Figure 30: Muon HLT Trigger efficiency for the Mu8 leg (on the left), the Mu17 leg (right), as a function of the muon p_T (top), of the muon η (bottom). Muons are asked to pass ID, Isolation and SIP requirements of the analysis.

936 6 Photon Observables and FSR recovery

937 A Z decay into a lepton pair can be accompanied by final state radiation (FSR), $Z \rightarrow \ell^+ \ell^- \gamma$. If the
 938 photon transverse momentum, p_T^γ , is required to exceed 2 GeV/c, about 8% (15%) of the decays into
 939 muons (electrons) are affected. As the photon emission is most often collinear with one of the leptons,
 940 electron measured energies automatically include the energy of a large fraction of the emitted photons
 941 in the associated electromagnetic super-cluster. On the other hand, muon measured momenta do not
 942 include the emitted photons. Final state radiation is therefore expected to degrade the Z mass resolution
 943 when measured with the sole muon pairs, and in turn degrade the Higgs boson mass resolution when
 944 measured with the four leptons momenta, especially in the 4μ and in the $2e2\mu$ final states and, to a lesser
 945 extent, in the $4e$ final state. It is also expected to reduce the efficiency of the lepton isolation cut when
 946 the emitted photon is in the lepton isolation cone

947 Both an excellent Higgs boson mass resolution and a large selection efficiency are essential ingredients
 948 in view of the small production cross section in the 4ℓ channels, in particular to discriminate the Higgs
 949 boson signal with the background continuum. It is the purpose of this analysis to recover the FSR
 950 photons with large efficiency and purity, to remove the energy of the recovered photons from the lepton
 951 isolation cones, and to measure the mass of the Higgs boson candidate from the momenta of the leptons
 952 and the recovered photons.

953 In addition to being collinear with the leptons, final state radiation also tends to favour low energy
 954 photon emission collinear to the lepton. An efficient recovery thus requires photon identification and
 955 reconstruction in the vicinity of other particles, down to photon transverse momenta of the order of
 956 the Higgs mass core resolution, *i.e.*, down to a couple GeV/c. Less energetic photons are expected to
 957 degrade the mass resolution in an insignificant manner, and are increasingly difficult to reconstruct and
 958 separate from the background.

959 6.1 Photon Reconstruction and Identification

960 Identifying low energy photons overlapping with other particles is included in the particle-flow concept
 961 developed in CMS [?].

962 Photons (type 1) are identified and reconstructed with the particle-flow reconstruction with a specific
 963 clustering algorithm, efficient down to an energy of 230 MeV in the ECAL barrel and 600 MeV in the
 964 ECAL end-caps. The determination of the photon energies and directions is monitored in the data with
 965 $\pi^0 \rightarrow \gamma\gamma$ decays, and is shown to be accurate, reliable, and in agreement with the predictions from
 966 simulation [? ?].

967 The particle-flow reconstruction includes an identification of showering muons, tuned for energetic
 968 muons. In the rare cases in which such a showering muon is identified, the energies of the particle-
 969 flow clusters linked to the muon do not give rise to separate particles. For the transverse momenta of
 970 interest in the low-mass Higgs boson search, however, the showering probability is vanishingly small,
 971 which leads to the loss of a not entirely negligible fraction of collinear FSR photons. Particle-Flow ECAL
 972 clusters linked to identified showering muons are therefore identified as photons (type 2) in this analysis.
 973 Specifically, the energy of these photons is set to `pfmuon.ecalEnergy()`, and its direction is chosen
 974 to be that of the muon.

975 In rare occurrences, the particle-flow reconstruction may identify a photon although it is already included
 976 in the electron super-cluster, due to imperfect cross cleaning. It is therefore required that photons be
 977 further away from the direction of any electron by 0.05 in pseudo-rapidity, and by 2.0 rad in azimuth.

978 The last two points are clear area of improvement in the particle-flow reconstruction algorithm logic,
 979 improvements that are beyond the scope of this note.

980 In the four-muon final state, the total efficiency of the photon reconstruction for $p_T^\gamma > 2$ GeV/c and
 981 $|\eta_\gamma| < 2.4$, determined by matching reconstructed photons to generated photons from FSR with a match-
 982 ing cut $\Delta R < 0.10$, is shown in Fig. 31a as a function of p_T^γ . The expected energy resolution for the two

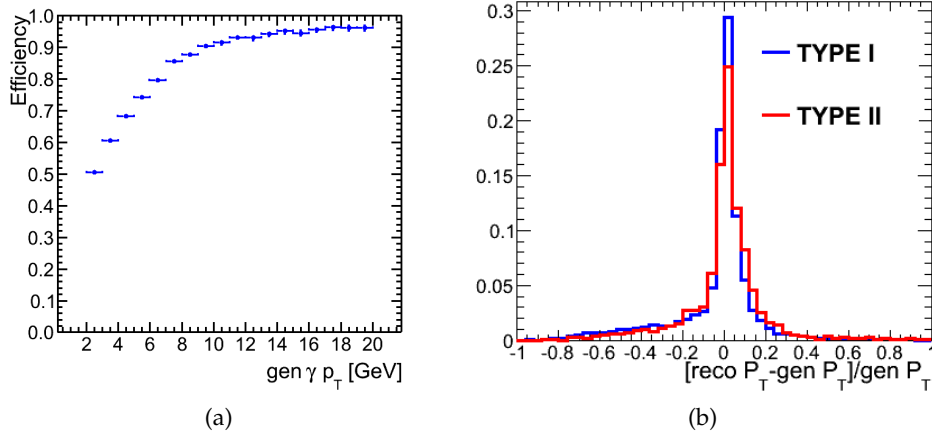


Figure 31: Reconstruction efficiency (a) and transverse energy resolution (b) for photons produced by final state radiation in $H \rightarrow ZZ \rightarrow 4\mu$ events

983 types of photons is displayed in Fig. 31b. In the four-muon final state, about 20% of the FSR photons are
 984 of type 2.

985 6.2 Photon Isolation

986 The photon isolation is determined from the charged hadrons, photons and neutral hadrons identified
 987 by the particle-flow reconstruction in a cone of size $\Delta R = 0.30$ around the photon direction. In this cone,
 988 all charged hadrons compatible with originating from the signal primary vertex (in the `pfPileUp.cc`
 989 meaning) and with a p_T larger than 200 MeV/c, all photons and neutral hadrons with a p_T larger than
 990 500 MeV/c are included in the iso-deposits.

991 The absolute photon isolation is defined as the sum of the transverse momenta of all these iso-deposits.
 992 To discriminate against photons that are produced in pileup interactions, an additional isolation deposit
 993 is defined that corresponds to the charged particle sum from the vertices other than the primary vertex.

994 Finally, the pileup-corrected relative isolation is obtained by dividing the absolute isolation by the photon
 995 transverse momentum, p_T^γ , and is given by:

$$I_\gamma = \frac{I_{\text{ch}} + I_\gamma + I_{\text{neut}} + I_{\text{PU}}}{p_T} \quad (5)$$

996 6.3 Building Z's with FSR Photon Recovery

997 The way to build Z candidates is defined in section 7. It uses leptons passing all selectoin criteria,
 998 including isolation. In case a FSR photon candidate is selected in the event, the isolation sum may have
 999 to be modified. This section describes how the building of Z candidates is made in presence of an FSR
 1000 photon. In the present analysis, only photons with p_T^γ in excess of 2 GeV/c and well in the tracker
 1001 acceptance ($|\eta| < 2.4$) are considered, and tentatively assigned to a lepton and to a Z from the candidate
 1002 Higgs boson decay. The association to a lepton goes as follows.

- 1003 (i) Photons are considered only if the minimum ΔR distance wrt any of the Z leptons is smaller
 1004 than $\Delta R < 0.5$.
- 1005 (ii) If the distance of the photon to the closest lepton is between 0.07 and .50, the probablity that
 1006 this photon arise from pile-up or, to a lesser extent, from the underlying event, becomes ap-
 1007 preciable, because of the large annulus area. To enrich the photon sample in genuine FSR

1008 photons, the p_T^γ cut is tightened to 4 GeV/c and the photon is required to be somewhat isolated from other particles: the relative PF isolation including pileup contribution is required
 1009 to be smaller than 1.0.

1011 (iii) For both Z candidates, only the photons that make a mass with a lepton pair closer to the
 1012 nominal Z mass (taken here to be 91.2 GeV/c²) but with a maximum $m_{ll\gamma} < 100$ GeV are
 1013 kept.

1014 (iv) After the photons have been selected with the above criteria the best photon is selected as
 1015 following:

- 1016 • If there is at least one photon with $p_T > 4$ GeV the one with the highest transverse
 1017 momentum is associated to the Z boson
- 1018 • If there is no photon with $p_T > 4$ GeV the closest photon to any of the leptons is
 1019 associated to the Z

1020 The invariant mass criteria defined in section 7 are applied using the four-vector defined by the sum of
 1021 the four-vectors of the two leptons and the photon.

1022 An event can therefore have zero, one or two selected FSR photon candidates. If no candidate is se-
 1023 lected, the default four lepton analysis applies. Otherwise, the selected photons are removed from the
 1024 corresponding lepton isolation cones (if in the isolation cones), and the default four lepton analysis flow
 1025 proceeds with the modified lepton isolations, and with the Z candidate masses determined with the
 1026 corresponding lepton pair and the associated photon.

1027 Finally, the Higgs boson candidate mass is determined from the momenta of the four leptons and those
 1028 of all FSR photon candidates. The performance of the FSR identification algorithm is quantified using
 1029 samples from simulation and data. The gain of the FSR algorithm is two fold

- 1030 • Events with associated photons move to the nominal reconstructed mass improving the res-
 1031 olution.
- 1032 • New events migrate into the sample by the higher isolation efficiency and the improved def-
 1033 inition of the mass of the Z.

1034 The following performance metrics are used to quantify the performance of FSR reconstruction:

- 1035 • **Efficiency:** Number of Identified FSR photons matched to generated FSR photons with $p_T >$
 1036 2 GeV and $|\eta| < 2.4$ divided by the number of generated FSR photons with $p_T > 2$ GeV and
 1037 $|\eta| < 2.4$
- 1038 • **Rate:** Number of Events with Identified FSR photons divided by the total number of events
 1039 after all selection requirements
- 1040 • **Purity:** Number of Events with Identified FSR photons where the mass of the system consist-
 1041 ing of the leptons and the photons is nearer to the nominal mass of the studied resonance wrt
 1042 the mass of the leptons alone.
- 1043 • **Yield Gain:** Number of events after all selection requirements after applying the FSR recovery
 1044 algorithm divided by the number of events after all selection requirements without applying
 1045 the FSR recover algorithm.

1046 The performance of the algorithm in the signal and irreducible background has been quantified using
 1047 simulated $H \rightarrow ZZ$ and SM ZZ samples with an average PU of 20 interactions. Addiitonal studies have
 1048 been performed in data exploiting decays of $Z \rightarrow ll, Z \rightarrow 4l$. In addition, studies of the shapes and
 1049 rates of the reducible backgrounds have been performed in signal free control regions.

1050 6.4 Studies on $H \rightarrow ZZ, SM ZZ$ MC

1051 The FSR identification algorithm is tested on simulated Higgs signal events with a mass of 125 GeV with
 1052 an average PU of 20 interactions. The total efficiency is compared by running the full selection with and
 1053 without the FSR algorithm applied. Figure 32 shows the comparison of the invariant mass distribution
 1054 before and after FSR recovery for events with an identified FSR photon and overall events. The FSR
 1055 algorithm recovers performance by moving the events from the FSR tail back to the Higgs peak bulk

distribution. In addition, due to the isolation requirements and the new definition of the masses of the Z

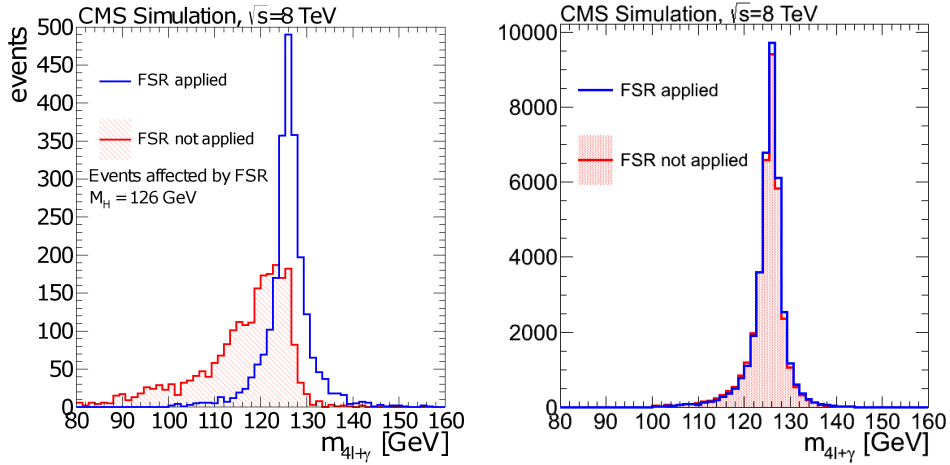


Figure 32: Invariant mass reconstruction of the Higgs candidate of the events with an identified FSR photon (left) and all events (right) for Higgs signal with $m_H = 126 \text{ GeV}$

1056
1057
1058
1059
1060
1061 bosons more events are introduced in the final selection after FSR recovery. In the case of Higgs signal, the tails are reduced and the arithmetic RMS is improved from 7.1% to 6.9% while the Gaussian RMS is not modified showing that the effect on the width distribution due to the impurity is negligible. In the case of the ZZ continuum the performance is expected to be similar. The rate, efficiency and purity for Higgs signal and SM ZZ is presented in table 8

final state	rate (%)	purity (%)	gain (%)
$H \rightarrow ZZ(\text{all})$	6.0	80	2.0
$H \rightarrow ZZ \rightarrow 4\mu$	9.1	82	3.0
$H \rightarrow ZZ \rightarrow 2e2\mu$	5.0	78	0.6
$H \rightarrow ZZ \rightarrow 4e$	1.4	72	1.8
SM ZZ(all)	6.7	81	2.1
SM ZZ $\rightarrow 4\mu$	10.1	83	3.0
SM ZZ $\rightarrow 2e2\mu$	6.5	77	0.6
SM ZZ $\rightarrow 4e$	1.8	72	1.8

Table 8: Rate, purity and efficiency gain for signal and ZZ background

1062
1063
1064
1065
1066 The effect of FSR on electrons is much smaller due to the absorption of nearby FSR photons in the electromagnetic super-cluster, therefore the four muon final state is affected the most. An increase in the total efficiency of 2% is expected and this is mainly attributed to the subtraction of the photon from the isolation annulus of the leptons and to the increased efficiency of the di-lepton mass requirements after including the photon.

6.5 Studies on data

1068
1069
1070
1071
1072
1073 The FSR algorithm is studied in detail in Z decays in two or four leptons and in topologies compatible with the $Z + X$ reducible background hypothesis. The performance of the FSR recovery algorithm in Z decays is presented in figure 33. Excellent performance is observed in Z data as the Z peak becomes steeper. The observed rate on $Z \rightarrow ll$ events is 1.9% while the efficiency gain is 0.9%. The $Z \rightarrow 4l$ final state is reconstructed with loose criteria to increase the event yield and demonstrate the performance of the algorithm. Significant improvement is observed in the reconstruction of the Z peak.

1074
1075 To study the effect of FSR in the reducible background shape a background enriched region is selected by requiring that the Z_2 leptons have same sign, and by dropping ID and isolation requirements. Figure 34

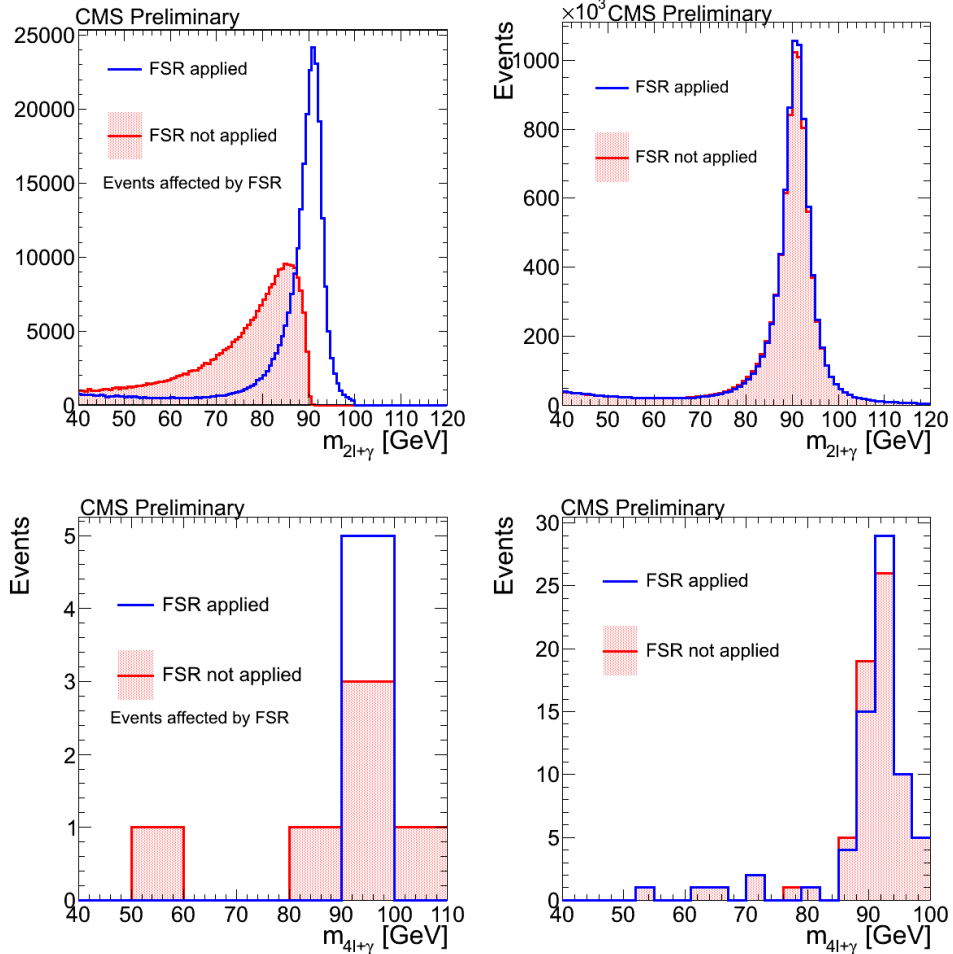


Figure 33: Invariant mass of the Z before and after FSR recovery for events with an identified FSR photon(left) and overall number of events for $Z \rightarrow \ell\ell$ decays (top) and $Z \rightarrow 4\ell$ decays (bottom)

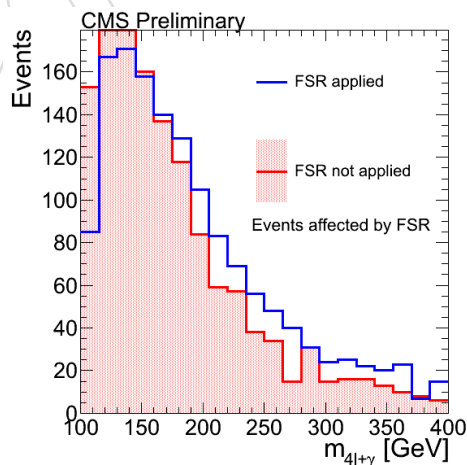


Figure 34: Invariant mass of the four lepton system for the background enriched region for events affected by FSR(left) and all events(right)

1076 shows the FSR effect on this control region. The effect on the background shape is explained by the result
 1077 of the FSR algorithm in jets. If a lepton is inside a jet, a possible π^0 can be attributed to FSR therefore
 1078 the rate is much higher than in the case of isolated leptons and corresponds to a total of 60%. The
 1079 fake photons associated as FSR result into a flattening of the background shape that results to reduced
 1080 background in the region of interest.

1081 7 Event Selection

1082 A "skimming" common to all 4ℓ channels was first applied on PDs for data reduction. It requires:

- 1083 • at least one good primary vertex (PV) fullfilling the following criteria: high number of degree
 1084 of freedom ($N_{PV} > 4$), collisions restricted along the z -axis ($z_{PV} < 24$ cm) and small radius
 1085 of the PV ($r_{PV} < 2$ cm).
- 1086 • at least 2 reconstructed lepton candidates, either a electron basic track-supercluster object or
 1087 global muon object, or a tracker muon object;
- 1088 • $p_{T,1} > 20$ GeV/ c , $p_{T,2} > 10$ GeV/ c for electron (muon) objects;
- 1089 • an invariant mass $M > 40$ GeV/ c^2 between two same flavor leptons;

1090 Only leptons with $p_T^e > 5$ GeV/ c , $p_T^\mu > 3$ GeV/ c and $|\eta^e| < 2.5$, $|\eta^\mu| < 2.4$ are considered in the skim
 1091 definition.

1092 Two flavors of leptons on which the selection steps act on are defined:

- 1093 1. *loose leptons*: electrons within the geometrical acceptance of $|\eta^e| < 2.5$, with $p_T^e > 7$ GeV/ c and
 1094 having 0 or 1 expected missing inner hits, muons (global or tracker) satisfying $|\eta^\mu| < 2.4$, $p_T^\mu >$
 1095 5 GeV/ c . Both electrons and muons should satifsy loose requirements on the transverse ($d_{xy} < 0.5$
 1096 cm) and longitudinal ($d_z < 1$ cm) impact parameter with respect to the primary vertex. Non-
 1097 global tracker muons must be arbitrated. In addition, it is required that $\Delta R > 0.02$ between the
 1098 leptons. The *loose leptons* are used in the estimation of reducible background (see section 11).

- 1099 2. *good leptons*: these are *loose leptons* on which additional criteria are imposed. Namely:

- 1100 • electrons should pass the electron identification criteria as described in section 4.1.2.1,
 1101 muons should meet the Particle Flow Muons requirements (see section 4.2.3);
- 1102 • Relative PFIso < 0.4 (see section 4.4);
- 1103 • the significance of the impact parameter to the event vertex, SIP_{3D}, is required to satisfy
 1104 $|SIP_{3D}| = \frac{IP}{\sigma_{IP}} < 4$ for each lepton, where IP is the lepton impact parameter in three
 1105 dimensions at the point of closest approach with respect to the primary interaction
 1106 vertex, and σ_{IP} the associated uncertainty.

1107 Before building *good leptons* candidates, an e/μ cross cleaning procedure is applied. *Loose electrons* are
 1108 discarded if they satisfy: $\Delta R(e, \mu) < 0.05$, where the muons considered are *loose muons* passing Particle
 1109 Flow or Global muons criteria.

1110 The events are then requested to have fired the relevant electron and muon triggers, consistently in data
 1111 and MC (see section 3.1).

1112 We therefore impose the following sequence of selection requirements:

- 1113 1. *First Z*: a pair of *good lepton* candidates of opposite charge and matching flavour (e^+e^- , $\mu^+\mu^-$)
 1114 with reconstructed mass $m_{1,2}$ closest to the nominal Z boson mass is retained and denoted Z_1 . The
 1115 selected pair should satisfy $40 < m_{Z_1} < 120$ GeV/ c^2 .
- 1116 2. *Three or more leptons*: at least another *good lepton* candidate of any flavour or charge.
- 1117 3. *Four or more leptons and a matching pair*: a fourth *good lepton* candidate with the flavour of the third
 1118 lepton candidate from the previous step, and with opposite charge.

- 1119 4. *Choice of the “best 4ℓ ” and Z_1, Z_2 assignments:* retain a second lepton pair, denoted Z_2 , among all the
 1120 remaining $\ell^+\ell^-$ combinations. If more than one Z_2 combination satisfies all the criteria, the one
 1121 built from leptons of highest p_T is chosen. The selected pair should satisfy $4 < m_{Z1} < 120 \text{ GeV}/c^2$
 1122 . At this stage, it is required that any two leptons from the four selected have $p_{T,i} > 20 \text{ GeV}/c$ and
 1123 $p_{T,j} > 10 \text{ GeV}/c$.
- 1124 5. *QCD suppression:* the reconstruction mass of opposite-sign and same-flavor lepton pair must sati-
 1125 fisy $m_{\ell\ell} > 4 \text{ GeV}/c^2$.
- 1126 6. *$m_{4\ell}, Z$ and $Z^{(*)}$ kinematics:* with $m_{4\ell} > m_{4\ell}^{\min}, m_{Z1}^{\min} < m_{Z1} < 120 \text{ GeV}/c^2$ and $m_{Z2}^{\min} < m_{Z2} <$
 1127 $120 \text{ GeV}/c^2$, where m_{Z2}^{\min} and m_{Z2}^{\min} are defined below.

1128 The first step ensures that the leptons in the preselected events are on the high efficiency plateau for
 1129 the trigger. Control samples for the Z +jet, $Zb\bar{b}/c\bar{c}$ and $t\bar{t}$ backgrounds are obtained as subsets of the
 1130 event sample that remain after the first step. The second step allows for control of the three-lepton event
 1131 rates which include WZ di-boson production events. The first four steps are designed to reduce the
 1132 contribution of the instrumental backgrounds from QCD multi-jets and Z + jets, whilst preserving the
 1133 maximal signal efficiency and the phase space for the evaluation of background systematics. By reduc-
 1134 ing the number of jets misidentified as leptons, fewer combinatorial ambiguities arise when assigning
 1135 the leptons to candidate Z bosons. The choice of the best combination of four leptons completes the four
 1136 first steps. Low mass resonances as well as multiple hadron decays are killed by step five. Three sets
 1137 of kinematic cuts are therefore introduced to allow studies of the s -channel contribution or to maximize
 1138 the sensitivity in different ranges of Higgs boson mass hypothesis:

- 1139 • **$Z \rightarrow 4\ell$ phase space** analysis defined by requiring $m_{Z2}^{\min} \equiv 4 \text{ GeV}/c^2$ and $m_{Z1}^{\min} \equiv 40 \text{ GeV}/c^2$
 1140 $m_{4\ell}^{\min} \equiv 70 \text{ GeV}/c^2$ and $m_{4\ell}^{\max} \equiv 110 \text{ GeV}/c^2$.
- 1141 • **baseline Higgs phase space** analysis defined by requiring $m_{Z2}^{\min} \equiv 12 \text{ GeV}/c^2$ and $m_{Z1}^{\min} \equiv$
 1142 $40 \text{ GeV}/c^2$ and $m_{4\ell}^{\min} \equiv 100 \text{ GeV}/c^2$. This provides a best sensitivity for masses $m_H <$
 1143 $130 \text{ GeV}/cc$
- 1144 • **High-mass phase space** analysis is defined by requiring $m_{Z2}^{\min} \equiv 60 \text{ GeV}/c^2$ and $m_{Z1}^{\min} \equiv$
 1145 $60 \text{ GeV}/c^2$. It is used to measure the ZZ cross-section.

1146 The events satisfying the high-mass selection are a subset of those satisfying the baseline selection. The
 1147 enlarge phase space of the baseline selection for the Higgs boson signal is needed at very low masses
 1148 given the very small cross section \times branching ratio, at the price of a larger background. The increased
 1149 acceptance for the signal becomes small for mass ($< 10\%$ in relative compared to the baseline selection)
 1150 above $\approx 130 \text{ GeV}/cc$ where reducing the phase space to better suppress the background become ad-
 1151 vantageous. For Higgs boson masses above $\approx 2 \times m_Z$, further restricting the phase space of the pair of
 1152 Z boson can be made without significant loss of acceptance for the signal, with the benefit of a slight
 1153 reduction of the ZZ^* background.

1154 7.1 Selection Performance and Control

1155 The signal detection efficiencies from MC for a 4ℓ system within the geometrical acceptance⁴ as a func-
 1156 tion of Higgs boson mass hypothesis are shown in Fig. 35 for the baseline selection. It rises from
 1157 about 28% / 58% / 40% at $m_H = 125 \text{ GeV}/c^2$ to about 60% / 85% / 72% at $m_H = 400 \text{ GeV}/c^2$ for the
 1158 $4e / 4\mu / 2e2\mu$ channels.

1159 The invariant mass of two good leptons (Z_1) as built in the first step of the selection is shown in Fig. 36
 1160 for both electron and muon channels and for both 7 and 8 TeV data. A nice agreement can be appreciated
 1161 between data and Monte Carlo expectations.

1162 The events yields as a function of the selection steps are shown in Fig. 37 and Fig. 38 for the baseline
 1163 selection in the $4e, 4\mu$ and $2e2\mu$ channels and for 7 and 8 TeV analysis.

⁴In this case the geometrical acceptance is defined having the generated electrons satisfying $|\eta^e| < 2.5$ and generated muons satisfying $|\eta^\mu| < 2.4$, no p_T cut is requested.

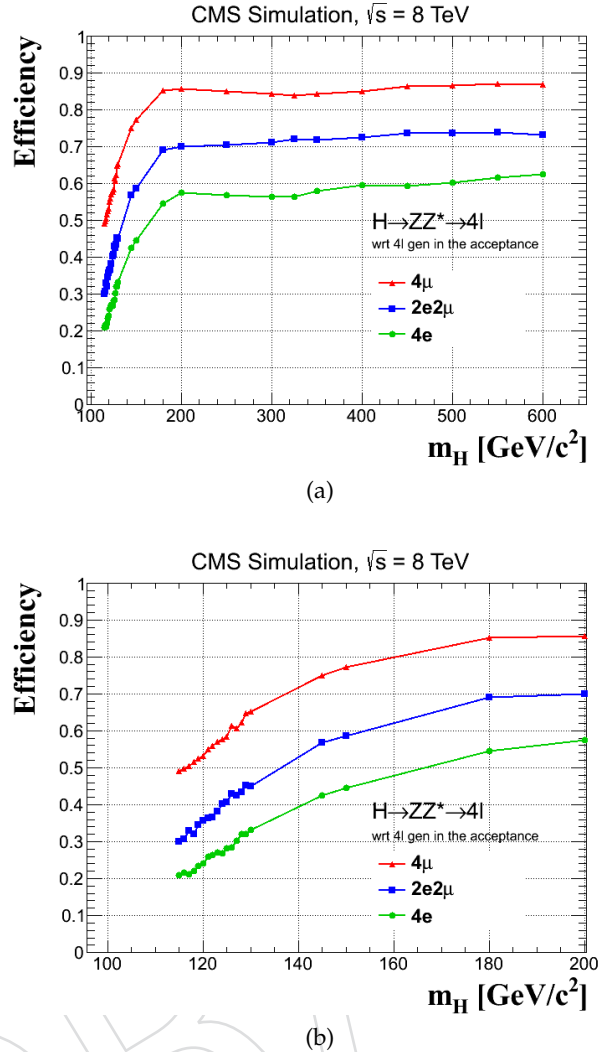


Figure 35: Signal detection efficiencies from MC for a 4ℓ system within the geometrical acceptance in the $4e$ (green), 4μ (red) and $2e2\mu$ (blue) channels as a function of Higgs boson mass hypothesis, for the full range (a) and a zoom on the low mass range (b).

1164 Figure 39 and Figure 40 show a comparison between data and MC at an early stage of the event selection
 1165 where four or more leptons are reconstructed and where a pair of leptons have been assigned to the Z_1
 1166 for both 7 and 8 TeV analysis. The comparison is made here relaxing the flavour and sign requirements
 1167 on the second pair of leptons such that the sample contains signal-like and background-like events. Note
 1168 that we don't necessarily expect a perfect DATA to MC agreement as this sample is dominated by
 1169 fake leptons and that no additional scale factors is applied. In the analysis, the reducible background is
 1170 ultimately taken from DATA; Monte Carlo is only used to check the background composition. Moreover,
 1171 in 2012, the current low Monte Statistics available for $Z+jets$ events prevent to draw firm conclusions.
 1172 The situation should improve after ICHEP.

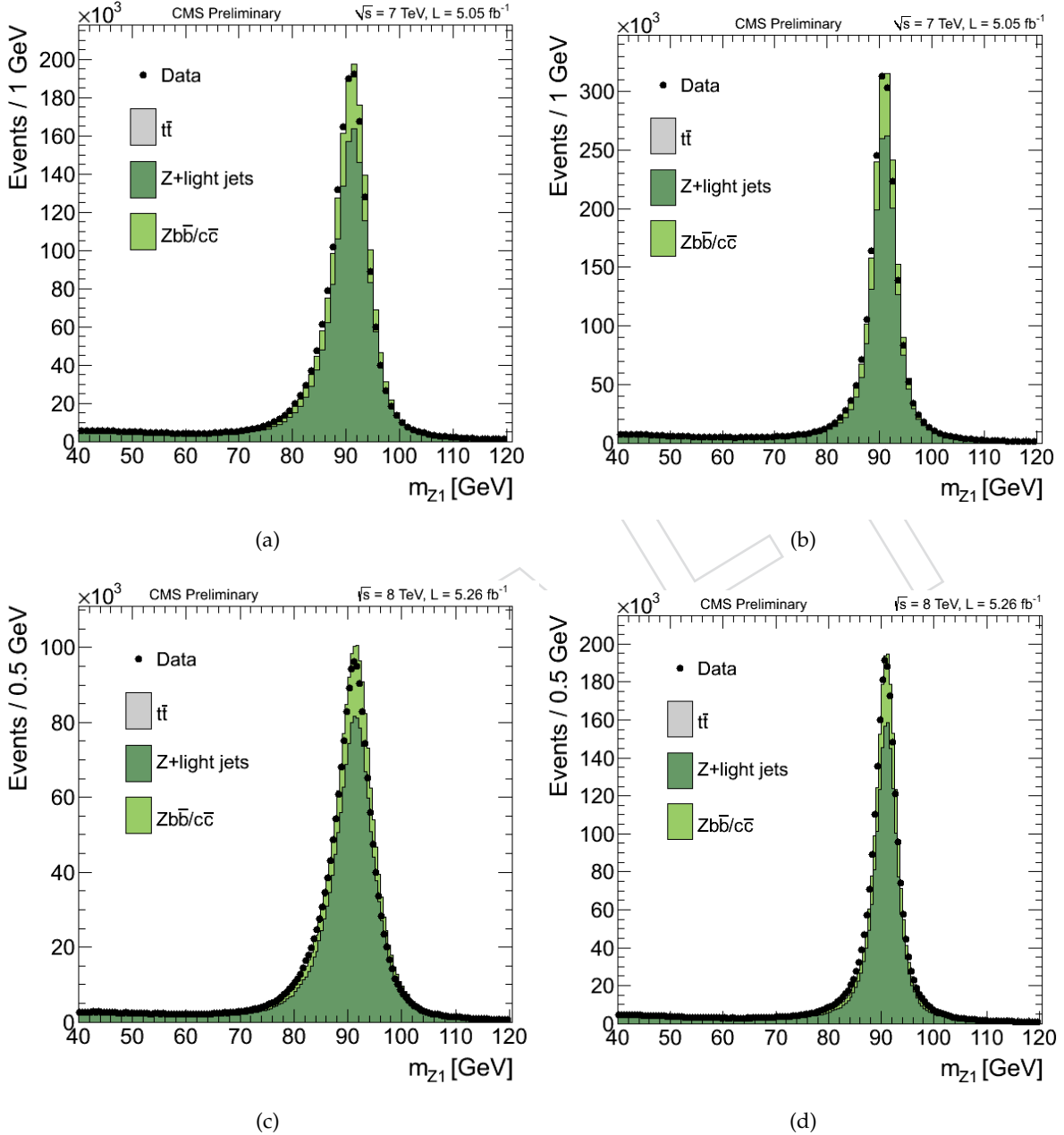


Figure 36: Comparison of Z_1 invariant mass in (a) ee 7TeV, (b) $\mu\mu$, 7TeV (c) ee 8TeV, (d) $\mu\mu$, 8 TeV, between data and MonteCarlo expectations. The samples correspond to an integrated luminosity of $\mathcal{L} = 5.05 \text{ fb}^{-1}$ for the 7 TeV data, and 5.26 fb^{-1} for the 8 TeV data.

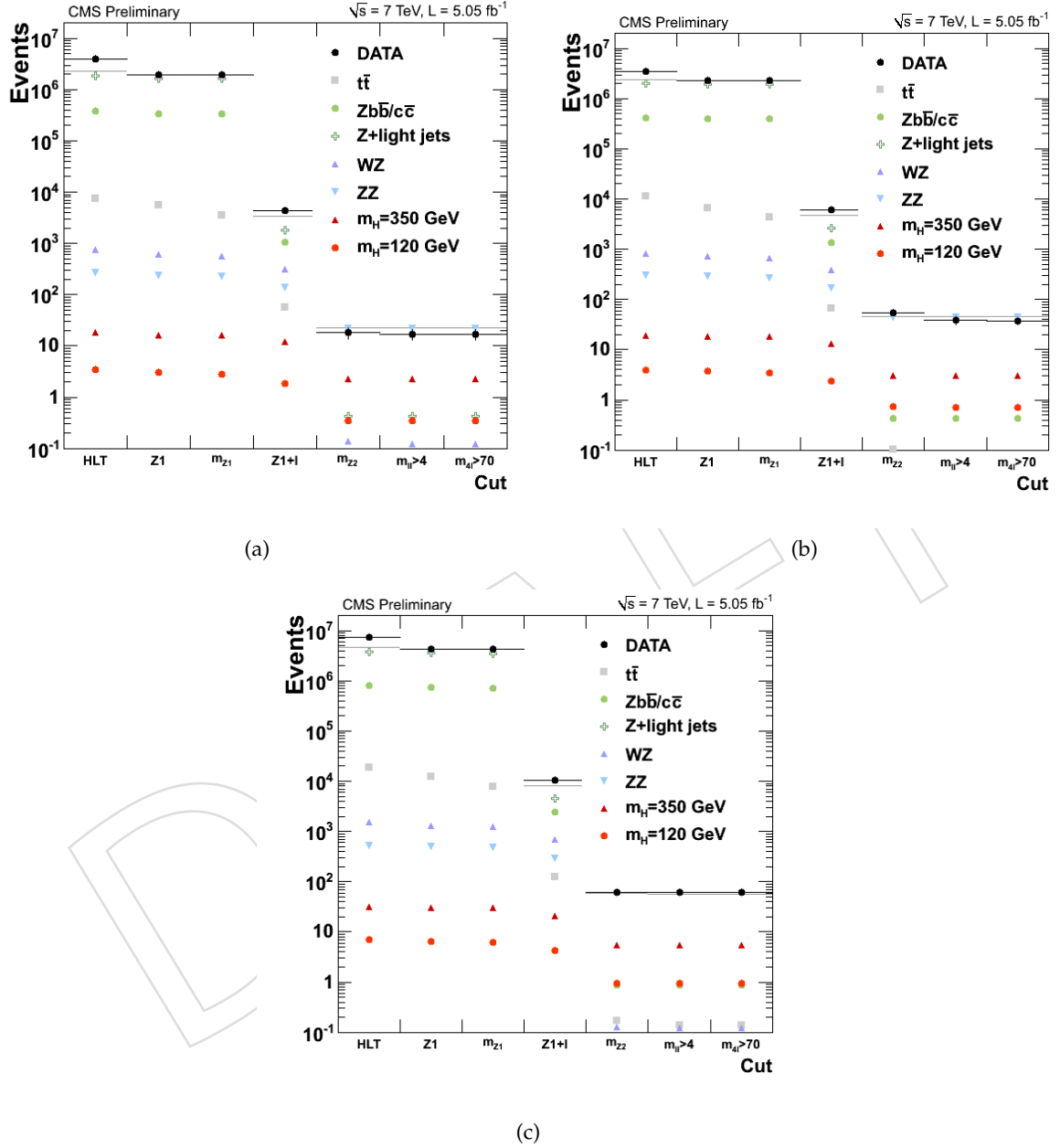


Figure 37: Event yields in the (a) 4 e , (b) 4 μ and (c) 2 e 2 μ channels as a function of the event selection steps. The MC yields are not corrected for background expectation. The samples correspond to an integrated luminosity of $\mathcal{L} = 5.05\ fb^{-1}$ of 7 TeV data.

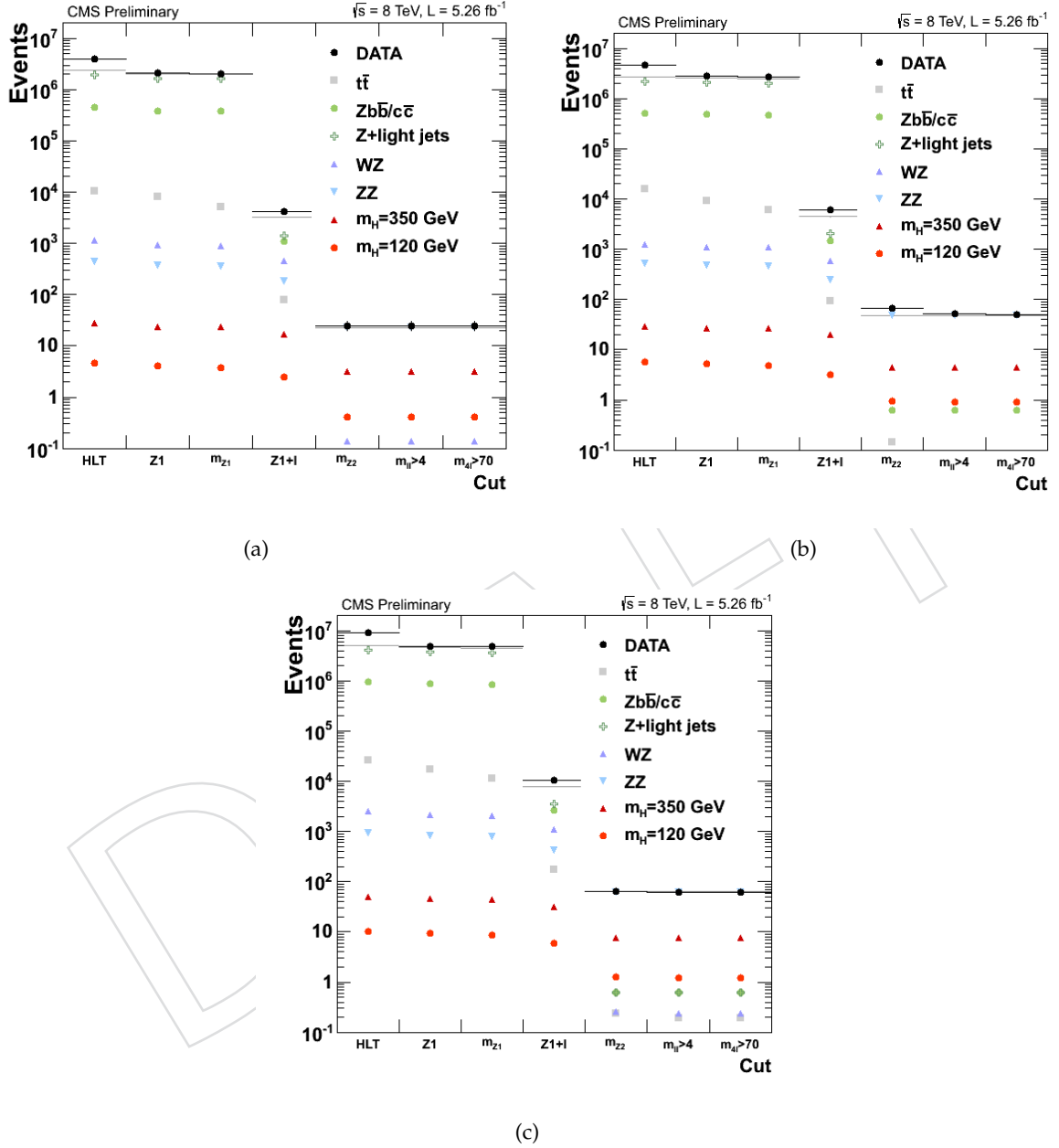


Figure 38: Event yields in the (a) 4e, (b) 4 μ and (c) 2e2 μ channels as a function of the event selection steps. The MC yields are not corrected for background expectation. The samples correspond to an integrated luminosity of $\mathcal{L} = 5.26 \text{ fb}^{-1}$ of 8 TeV data.

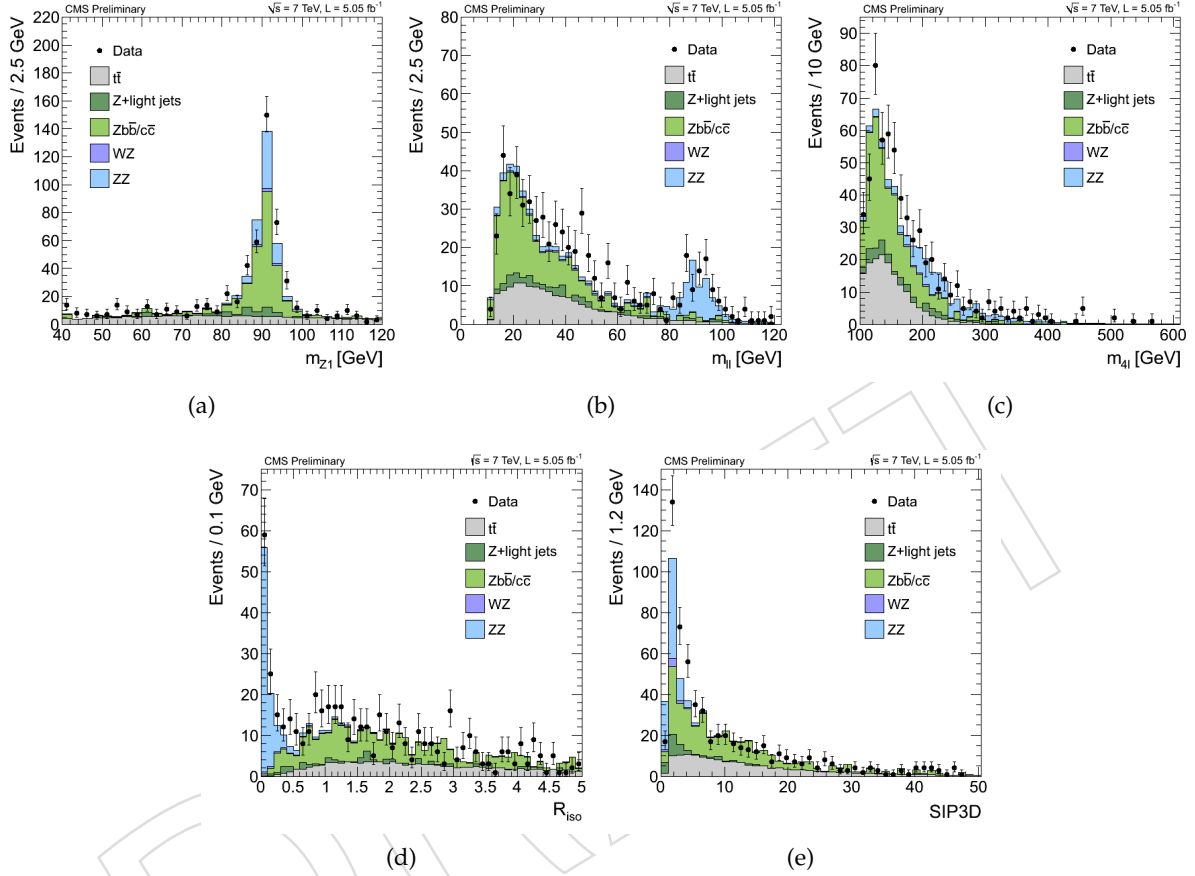


Figure 39: Comparison between data and MC at an early stage of the event selection where four or more leptons are reconstructed and where a pair of leptons have been assigned to the Z_1 . The comparison is made here relaxing the flavour and sign requirements on the second pair of leptons such that the sample contains signal-like and background-like events. The plots show (a) the reconstructed mass m_{Z_1} , (b) the reconstructed mass m_{ll} , (c) the reconstructed four-lepton invariant mass m_{4l} , (d) the combined relative isolation $R_{iso,\ell}$ for the second pair of leptons with largest isolation, (e) the significance of the impact parameter to the event vertex for the leptons of the second pair with largest SIP_{3D} . Points with statistical uncertainties represent the data. Shaded histograms represent the MC expectations, corrected for background expectation. The samples correspond to an integrated luminosity of $\mathcal{L} = 5.05 \text{ fb}^{-1}$.

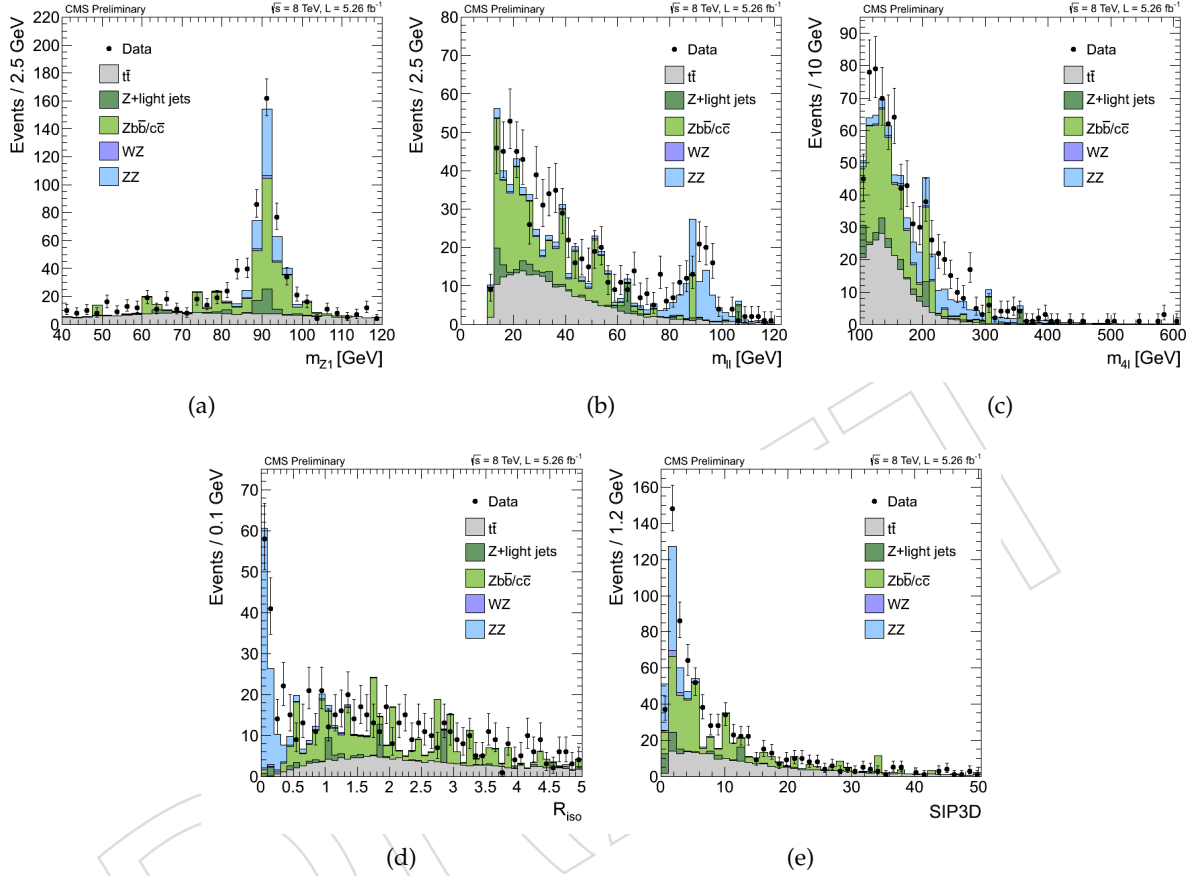


Figure 40: Comparison between data and MC at an early stage of the event selection where four or more leptons are reconstructed and where a pair of leptons have been assigned to the Z_1 . The comparison is made here relaxing the flavour and sign requirements on the second pair of leptons such that the sample contains signal-like and background-like events. The plots show (a) the reconstructed mass m_{Z_1} , (b) the reconstructed mass $m_{\ell\ell}$, (c) the reconstructed four-lepton invariant mass $m_{4\ell}$, (d) the combined relative isolation $R_{iso,\ell}$ for the second pair of leptons with largest isolation, (e) the significance of the impact parameter to the event vertex for the leptons of the second pair with largest SIP_{3D} . Points with statistical uncertainties represent the data. Shaded histograms represent the MC expectations, corrected for background expectation. The samples correspond to an integrated luminosity of $\mathcal{L} = 5.26 \text{ fb}^{-1}$.

1173 8 Signal Model and uncertainties

1174 8.1 Signal model

1175 The model for the differential signal event yield is written as follows:

$$\frac{dN}{dm_{4\ell}} = C(m_H) \cdot N^{MC}(m_H) \cdot F_H(m_{4\ell} | m_H). \quad (6)$$

1176 In this equation, $N^{MC}(m_H)$ is the event yield predicted from the MC used, $C(m_H)$ is the cumulative
1177 data-to-MC correction factor for all instrumental efficiencies (trigger, reco/ID, impact parameter cut,
1178 isolation cut) to be described below. Data-to-MC corrections for 7 TeV and 8 TeV will be discussed in
1179 Sec. 8.2.2.

1180 The *pdf* $F_H(m_{4\ell} | m_H)$ is the convolution of the virtual Higgs boson mass distribution $pdf_1(m_{H^*} | m_H)$
1181 introduced in Ref. [79] and the Crystal Ball function $CB(m_{4\ell} | m_{H^*})$ also described in Ref. [79]:

$$F_H(m_{4\ell} | m_H) = CB(m_{4\ell} | m_{H^*}) \otimes pdf_1(m_{H^*} | m_H) \quad (7)$$

1182 The MC event yields, correction factors, and signal shape are tracked separately for $4e$, 4μ , and $2e2\mu$
1183 events. The MC event yields are tracked separately for all five production mechanisms $gg \rightarrow H$, qqH ,
1184 WH , ZH and $t\bar{t}H$, while the data-to-MC efficiency corrections and signal shapes are assumed to be the
1185 same.

1186 The $pdf_1(m_{H^*} | m_H)$ function is based on the relativistic Breit-Wigner shape for $gg \rightarrow H$. The func-
1187 tion is written via the running total Higgs boson width $\Gamma_{TOT}(m_{H^*})$, gg and ZZ couplings (expressed
1188 via $\Gamma_{gg}(m_{H^*})$ and $\Gamma_{ZZ}(m_{H^*})$), and the partonic luminosity profile $L(m_{H^*})$. All parameters used for
1189 $pdf_1(m_{H^*} | m_H)$ function are fixed:

$$pdf_1(m_{H^*} | m_H) = \frac{1}{NormConst} \cdot \frac{\Gamma_{gg}(m_{H^*}) \Gamma_{ZZ}(m_{H^*})}{(m_{H^*}^2 - m_H^2)^2 + m_{H^*}^2 \Gamma_{TOT}^2(m_{H^*})} \cdot L_{gg}(m_{H^*}) \cdot m_{H^*} \quad (8)$$

1190 Currently we don't reweight the Powheg events in order to give the "proper" Higgs boson mass line-
1191 shape due to time constraints. We use the approach from PRL analysis, i.e. assigning 30% uncertainties
1192 for this source of nuisance.

1193 The Crystal Ball function $CB(m_{4\ell} | m_{H^*})$ has four independent parameters and is intended to capture the
1194 Gaussian core (σ_m) of the four-lepton mass resolution function, systematic mass shift Δm_{H^*} of the peak,
1195 and the left-hand tail originating from leptons emitting bremsstrahlung in the tracker material, present for both
1196 electrons and muons, and from the non-Gaussian mis-measurements specific to interactions of electrons
1197 with the detector material (two parameters, n and α):

$$CB(\xi) = N \cdot \begin{cases} A \cdot (B + |\xi|)^{-n}, & \text{for } \xi < \alpha \\ \exp(-\xi^2/2), & \text{for } \xi \geq \alpha \end{cases} \quad (9)$$

1198 where $\xi = (m_{4\ell} - m_{H^*} - \Delta m_{H^*})/\sigma_m$. The prominence of the left-hand tail is defined by the power n . The
1199 parameter α defines where the splicing of the tails and the core are made. Parameters A and B are not
1200 independent; they are defined by requiring the continuity of the function itself and its first derivatives.
1201 N is the normalizing constant.

1202 Fits for the three final 4ℓ states and four representative Higgs boson masses are shown in Fig. 41. One
1203 can see no discernible difference in shapes for 7 TeV and 8 TeV simulations. The Crystal Ball func-
1204 tion parameters show a reasonably stable evolution vs four-lepton invariant mass, which allows us to
1205 parametrise them with simple functions (see Fig. 42):

1206 The functional form for the dependence of the CB parameters on m_H $f(m_H, a)$ are listed in Table 9 and
1207 10.

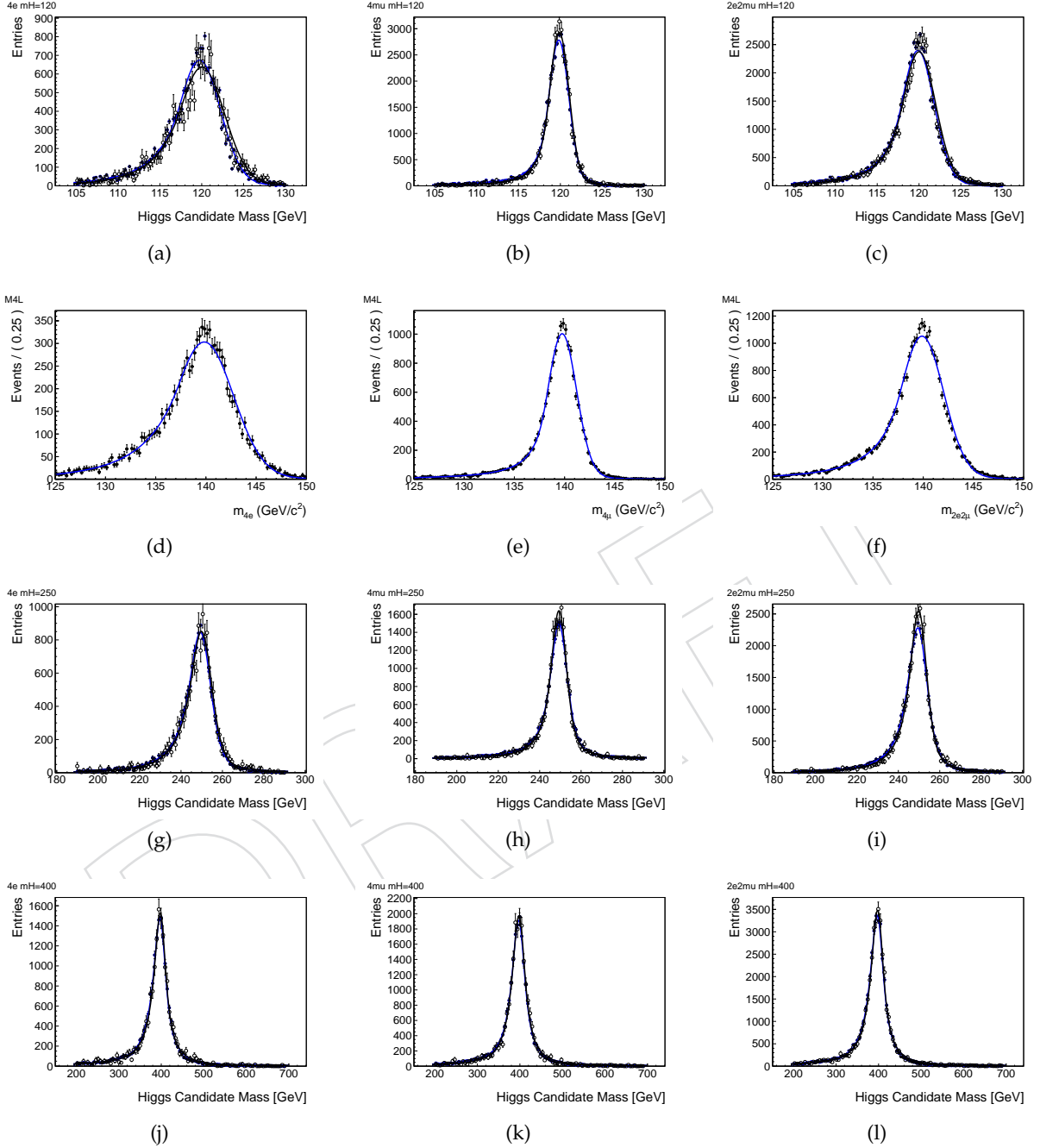


Figure 41: Probability density functions $f(m_{4\ell} | m_H)$ describing the Higgs boson mass shape at reconstruction level for for $4e$ (left), 4μ (middle), and $2e2\mu$ (right) final states. Blue solid points and blue curves are for 7 TeV samples, and black open points and black curves are for 8 TeV. Four rows correspond to different Higgs boson masses: $m_H = 120$ GeV (a-c), $m_H = 140$ GeV (d-f), $m_H = 250$ GeV (g-i), $m_H = 400$ GeV (j-l).

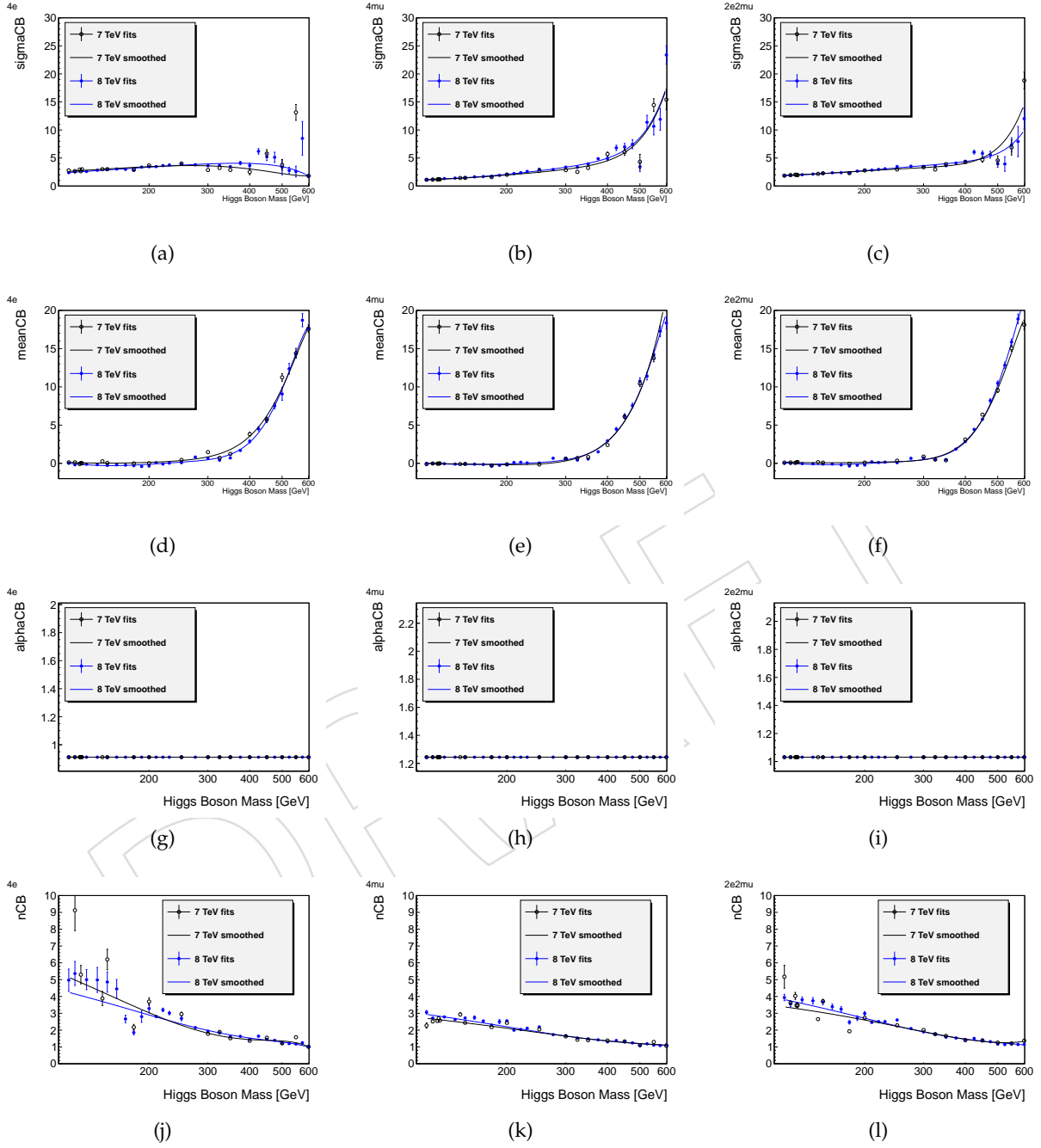


Figure 42: Dependence of Crystal Ball function parameters on the Higgs boson mass $f(m_{4\ell} | m_H)$ for for $4e$ (left), 4μ (middle), and $2e2\mu$ (right) final states: $\sigma m / m_H$ (a-c), mean / m_H (d-f), α (g-i), n (j-l). Blue solid points and blue curves are for 7 TeV samples, and black open points and black curves are for 8 TeV.

Table 9: $ggH \rightarrow 4l$ parameterization for the $4e$, 4μ and $2e2\mu$ final states for 7 TeV.

Parameter mean	
$4e$	$12.4 - 2.6 \cdot 10^{-1} * m + 2.0 \cdot 10^{-3} * m^2 - 7.0 \cdot 10^{-6} * m^3 + 1.2 \cdot 10^{-8} * m^4 - 7.2 \cdot 10^{-12} * m^5$
4μ	$5.6 - 1.2 \cdot 10^{-1} * m + 9.0 \cdot 10^{-4} * m^2 - 3.3 \cdot 10^{-6} * m^3 + 5.7 \cdot 10^{-9} * m^4 - 3.4 \cdot 10^{-12} * m^5$
$2e2\mu$	$10.1 - 2.1 \cdot 10^{-1} * m + 1.6 \cdot 10^{-3} * m^2 - 5.7 \cdot 10^{-6} * m^3 + 9.5 \cdot 10^{-9} * m^4 - 5.7 \cdot 10^{-12} * m^5$
Parameter σ	
$4e$	$0.1 + 2.7 \cdot 10^{-2} * m - 7.5 \cdot 10^{-5} * m^2 + 1.2 \cdot 10^{-7} * m^3 - 1.0 \cdot 10^{-10} * m^4$
4μ	$1.7 - 2.4 \cdot 10^{-2} * m + 2.3 \cdot 10^{-4} * m^2 - 6.3 \cdot 10^{-7} * m^3 + 6.5 \cdot 10^{-10} * m^4$
$2e2\mu$	$1.6 - 8.4 \cdot 10^{-3} * m + 1.4 \cdot 10^{-4} * m^2 - 4.1 \cdot 10^{-7} * m^3 + 4.0 \cdot 10^{-10} * m^4$
Parameter α	
$4e$	0.9
4μ	1.2
$2e2\mu$	1.0
Parameter n	
$4e$	$7.2 - 3.2 \cdot 10^{-2} * m + 6.3 \cdot 10^{-5} * m^2 - 4.4 \cdot 10^{-8} * m^3$
4μ	$4.4 - 1.6 \cdot 10^{-2} * m + 2.8 \cdot 10^{-5} * m^2 - 1.7 \cdot 10^{-8} * m^3$
$2e2\mu$	$6.1 - 2.5 \cdot 10^{-2} * m + 4.3 \cdot 10^{-5} * m^2 - 2.6 \cdot 10^{-8} * m^3$

Table 10: $ggH \rightarrow 4l$ parameterization for the $4e$, 4μ and $2e2\mu$ final states for 8 TeV.

Parameter mean	
$4e$	$4.8 - 10.0 \cdot 10^{-2} * m + 7.8 \cdot 10^{-4} * m^2 - 3.0 \cdot 10^{-6} * m^3 + 5.4 \cdot 10^{-9} * m^4 - 3.4 \cdot 10^{-12} * m^5$
4μ	$0.1 + 2.1 \cdot 10^{-3} * m - 2.7 \cdot 10^{-5} * m^2 + 8.5 \cdot 10^{-9} * m^3 + 2.3 \cdot 10^{-10} * m^4 - 2.1 \cdot 10^{-14} * m^5$
$2e2\mu$	$5.4 - 1.2 \cdot 10^{-1} * m + 9.5 \cdot 10^{-4} * m^2 - 3.7 \cdot 10^{-6} * m^3 + 6.8 \cdot 10^{-9} * m^4 - 4.3 \cdot 10^{-12} * m^5$
Parameter σ	
$4e$	$0.4 + 2.4 \cdot 10^{-2} * m - 3.9 \cdot 10^{-5} * m^2 - 4.8 \cdot 10^{-8} * m^3 + 8.7 \cdot 10^{-11} * m^4$
4μ	$0.8 - 8.7 \cdot 10^{-3} * m + 1.4 \cdot 10^{-4} * m^2 - 4.5 \cdot 10^{-7} * m^3 + 5.3 \cdot 10^{-10} * m^4$
$2e2\mu$	$1.3 - 3.4 \cdot 10^{-3} * m + 1.2 \cdot 10^{-4} * m^2 - 4.5 \cdot 10^{-7} * m^3 + 5.3 \cdot 10^{-10} * m^4$
Parameter α	
$4e$	0.9
4μ	1.2
$2e2\mu$	1.0
Parameter n	
$4e$	$10.2 - 5.7 \cdot 10^{-2} * m + 1.2 \cdot 10^{-4} * m^2 - 9.1 \cdot 10^{-8} * m^3$
4μ	$3.8 - 1.2 \cdot 10^{-2} * m + 1.8 \cdot 10^{-5} * m^2 - 9.8 \cdot 10^{-9} * m^3$
$2e2\mu$	$4.7 - 1.3 \cdot 10^{-2} * m + 1.2 \cdot 10^{-5} * m^2 + 8.7 \cdot 10^{-10} * m^3$

8.2 Signal model uncertainties

Systematic errors on signal model can be factorized into (a) those affecting the overall event yield and (b) uncertainties affecting the shape of signal event distributions:

The uncertainties affecting the overall event yields are as follows:

- Theoretical total cross section uncertainties;
- Theoretical uncertainties on the $H \rightarrow ZZ$ branching fraction;
- Theoretical uncertainties on signal event acceptance within kinematic cuts on leptons;
- Instrumental uncertainties on data-to-MC corrections $C(m_H)$.

The uncertainties affecting the shape of event distributions are as follows:

- Theoretical uncertainties on the distribution $pdf(m_{H^*} | m_H)$ (Eq. 8);
- Instrumental uncertainties on the detector response function $CB(m_{4\ell} | m_{H^*})$ (Eq. 9);
- Theoretical uncertainties on Kinematic Discriminant (KD) distribution $pdf(KD | m_H)$ to be introduced later in Sec. 12;
- Instrumental uncertainties on the KD distributions (these are currently assumed negligible).

The next sub-sections discuss all these systematic errors, except for uncertainties on KD distributions, which is discussed in Sec. 12.

8.2.1 Theoretical uncertainties on the signal model

Total signal cross section

Systematic errors on the signal total cross section for *each* production mechanism and for all Higgs boson masses are fully defined elsewhere [80]. They come from PDF+ α_s systematic errors and from theoretical uncertainties evaluated by varying QCD renormalization and factorization scales (μ_R and μ_F).

Per Ref. [81], the PDF+ α_s and QCD scale uncertainties are treated as uncorrelated. The 7 TeV and 8 TeV uncertainties are assumed to be 100% correlated.

Branching ratio BR($H \rightarrow 4l$)

The uncertainty on $BR(H \rightarrow 4l)$ is taken to be 2% [82] and assumed to be m_H -independent.

Signal acceptance

Depending on the Higgs boson mass, the lepton kinematic cuts restrict the signal acceptance to $\mathcal{A} \sim 0.6 - 0.9$ [79]. The acceptance uncertainties $\delta\mathcal{A}/\mathcal{A}$ are evaluated by using MCFM. For calculations, we used the $pp \rightarrow H \rightarrow ZZ \rightarrow ee\mu\mu$ process at 7 TeV with the following cuts: $m_{ee} > 12$, $m_{\mu\mu} > 12$, electrons' $p_T > 7$ and $|\eta| < 2.5$, and muons' $p_T > 5$ and $|\eta| < 2.4$. The minimal jet-lepton and lepton-lepton ΔR_{min} -distance were relaxed, i.e. set to zero. The cross sections are calculated inclusively in the number of jets found at NLO.

We assume that uncertainties on acceptance at 8 TeV are the same as at 7 TeV and are 100% correlated.

The sensitivity of the signal acceptance to the renormalization and factorization scales is evaluated by varying them by a factor of two up and down. The results are shown in Table 11. We find that the acceptance errors are very small (0.1-0.2%) and, therefore, can be neglected.

For estimation of the PDF+ α_s systematic errors, we use the PDF4LHC prescription [83]. The three PDF sets used are CT10 [84], MSTW08 [85], NNPDF [86]. The results, the envelope containing all variations for the three sets of PDFs, is shown in Fig. 43. We assign a 2% mass-independent error to account for these uncertainties.

Per Ref. [?], the general recommendation is to treat the acceptance and total cross section uncertainties as uncorrelated. Figure 44 shows the level of correlations between the acceptance and cross sections for $m_H = 120$ and 400 GeV. Indeed, we see a very little correlation for the low Higgs boson mass. For

Table 11: Signal acceptance \mathcal{A} for different QCD scales.

Higgs boson mass m_H (GeV)	120	200	400	500	600
Default \mathcal{A}_0 ($\mu_R = \mu_F = m_H/2$)	0.5421	0.7318	0.8120	0.8421	0.8637
\mathcal{A}_{up} ($\mu_R = \mu_F = m_H$)	0.5417	0.7317	0.8128	0.8427	0.8644
\mathcal{A}_{down} ($\mu_R = \mu_F = m_H/4$)	0.5430	0.7328	0.8119	0.8418	0.8632
$\delta\mathcal{A}/\mathcal{A} = \max \Delta\mathcal{A} /\mathcal{A}_0$	0.17%	0.14%	0.11%	0.07%	0.08%

the high mass, the negative correlations seem to develop, which implies that by leaving these correlations out we make our results more conservative. For simplicity, we assign the exact same error to all production mechanisms and assume that they are 100% correlated, which is also conservative.

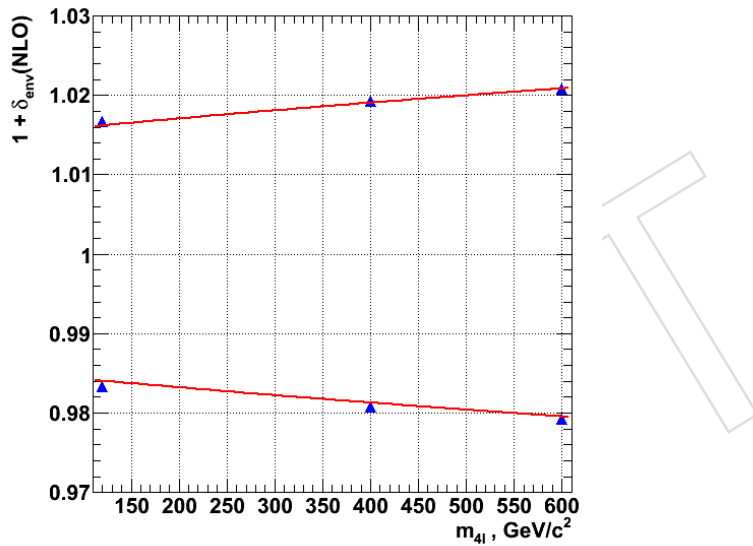


Figure 43: PDF+ α_s uncertainties for $pp \rightarrow H \rightarrow ZZ \rightarrow 4\ell$ vs. Higgs boson mass at $\sqrt{s} = 7$ TeV. The points are evaluated uncertainties. The curves are the fit.

The Higgs p_T distribution in the POWHEG $gg \rightarrow H$ MC is harder than what the most recent NLO+NNLL calculations predict (HqT [87]), as shown in Fig. 45. Therefore, the $H \rightarrow 4\ell$ leptons in the POWHEG sample get an additional boost and the signal acceptance may be somewhat overestimated.

To estimate the scale of the effect, we re-weight Higgs boson events $H \rightarrow 2e2\mu$ in MC to make their p_T spectrum match the one obtained in HqT and then evaluate the change in the signal acceptance arising from the lepton kinematic cuts used in the analysis ($p_T > 5$ GeV and $|\eta| < 2.4$ for muons; $p_T > 7$ GeV and $|\eta| < 2.5$ for electrons). We find that the relative change in the $H \rightarrow 4\ell$ acceptance, shown in Fig. 46, is $< 2\%$. Since the change is so small, we do not correct for it, but rather assign an additional systematic error on acceptance which depends on the Higgs boson mass as shown in Fig. 46.

1263 Theoretical uncertainties on the distribution $pdf_1(m_{H^*}|m_H)$

When the Higgs boson total width Γ_H becomes very large, there are additional uncertainties related to the theoretical treatment of running Higgs width and due to non-negligible effects of the signal-background interference between $gg \rightarrow H \rightarrow ZZ$ and $gg \rightarrow ZZ$. Following the prescription given in Ref. [88], we add one more uncertainty on the Higgs boson cross sections (all sub-channels), $150\% \times (m_H/\text{TeV})^3$, intended to cover for all systematic errors specific to high mass Higgs bosons.

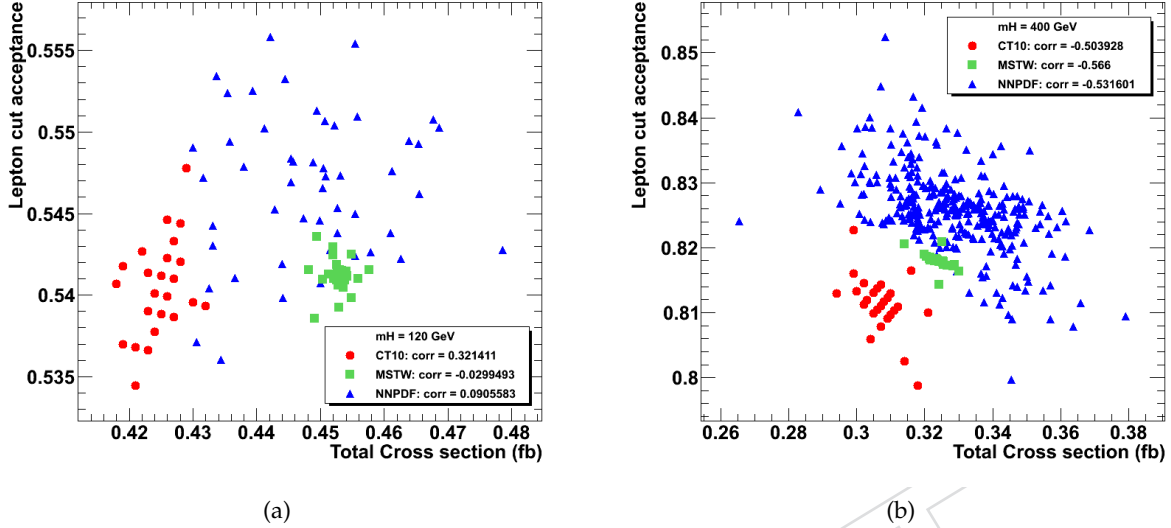


Figure 44: Scatter plots of the signal four-lepton acceptance vs. the total cross section for different eigenvectors of the three PDF sets, for $m_H = 120 \text{ GeV}$ (left) and $m_H = 400 \text{ GeV}$ (right). The three PDF sets are shown in different colors/symbols. The center-of-mass energy is 7 TeV.

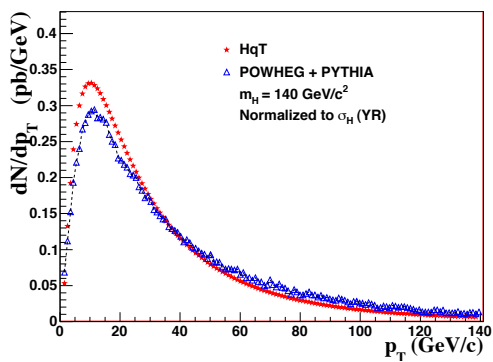


Figure 45: The Higgs boson p_T^H distributions in the POWHEG sample and HqT calculations. The center-of-mass energy is 7 TeV.

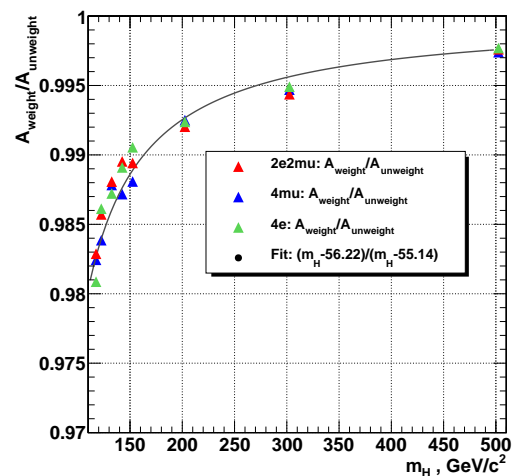


Figure 46: The change in the $H \rightarrow 4\ell$ acceptance due to the Higgs p_T^H reweighting in POWHEG to match the HqT calculations. Center of mass energy is 7 TeV.

1269 **8.2.2 Data-to-MC efficiency scale factors**

1270 Leptons in the signal $H \rightarrow ZZ \rightarrow 4\ell$ are prompt and their trigger and reconstruction/ID efficiencies
 1271 as well as the impact parameter and isolation cut efficiencies can be readily evaluated directly from
 1272 data by invoking the tag-and-probe (T&P) method applied to $Z \rightarrow \ell\ell$ events. The results of these
 1273 measurements are reported in Sec. 5. In this section, we describe results of propagating the measured
 1274 per-lepton efficiencies (and their errors). Two methods were used. They give comparable results.

1275 **PRL Method: per-lepton**

1276 The observed data/Monte Carlo discrepancy in the lepton reconstruction and identification efficiencies
 1277 measured with the data-driven techniques described in Section 5 is used to correct the Monte Carlo on
 1278 an event-by-event basis. The uncertainties on this efficiency correction are propagated independently to
 1279 obtain a systematic uncertainty on the final yields for signals and ZZ background.

1280 In practice, the per-lepton data/MC ratio is used to weight individual events (to correct yields for
 1281 data/MC differences). For each MC sample, five hundred toy MC experiments are ran. In each experi-
 1282 ment, the data/MC correction are floated once with a gaussian hypothesis, where the gaussian mean is
 1283 the central value of the data/MC ratio and the width the associated error. The total number of events
 1284 is therefore calculated. The systematic uncertainty is taken as the RMS of the distribution of the total
 1285 number of expected events in the five hundred toys.

1286 The resulting systematics are reported in the Figures 47 and 48 for the 7 and 8 TeV analysis respectively.

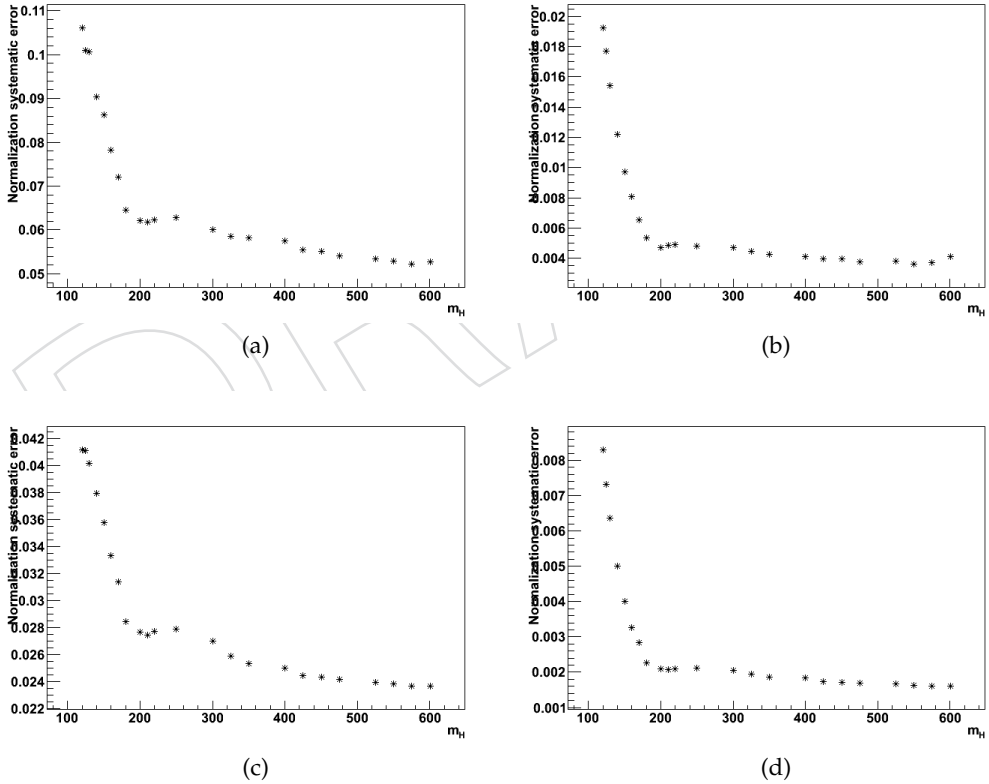


Figure 47: Instrumental Uncertainties related to data/MC differences in efficiencies in recon-
 struction, identification, isolation and $|SIP|$ as a function of m_H , for (a) 4e channel, (b) 4 μ chan-
 nel (c) 2e2 μ channel (electron only uncertainties), (d) 2e2 μ channel (muon only uncertainties).
 Results are for 7 TeV data.

1287 In addition, we had in quadrature a 1.5% uncertainty related to trigger. The errors related to the mo-

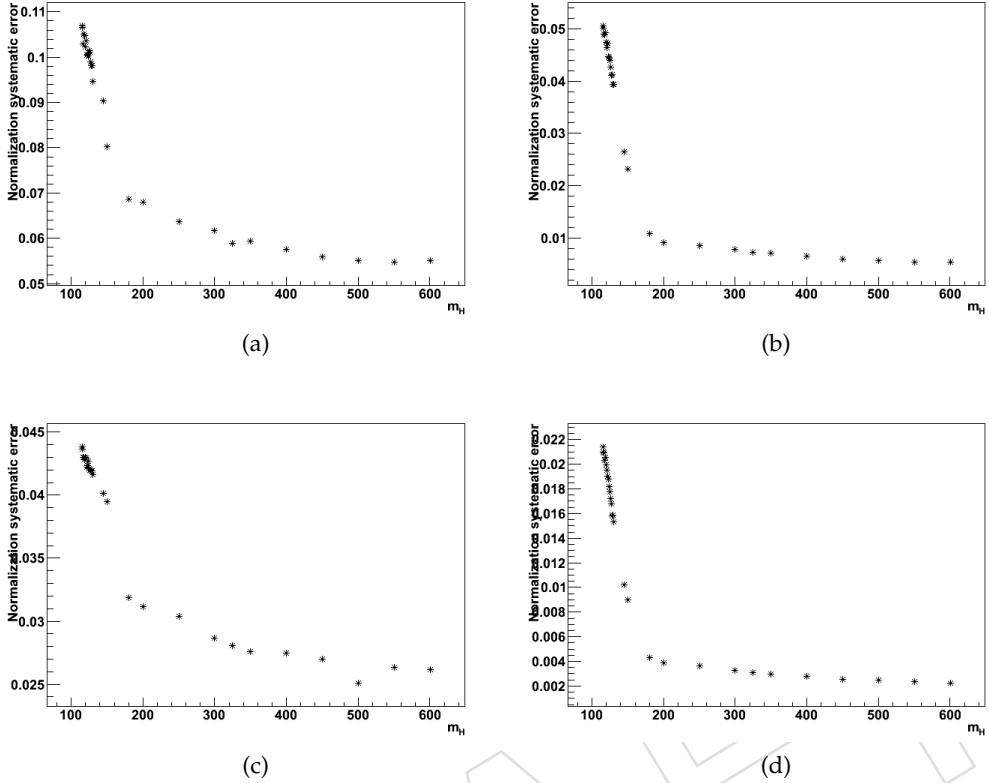


Figure 48: Instrumental Uncertainties related to data/MC differences in efficiencies in reconstruction, identification, isolation and $|SIP|$ as a function of m_H , for (a) 4e channel, (b) 4 μ channel (c) 2e2 μ channel (electron only uncertainties), (d) 2e2 μ channel (muon only uncertainties). Results are for 8 TeV data.

mentum energy scale and resolution will be discussed later in this section.

Alternate Method: per-event

Efficiencies measured in data and simulation using the T&P method in a grid of (p_T, η) -bins are given in Sec. 5. The systematic errors on the absolute efficiencies associated with the method are known to be about 0.5-1% [89]. However, they can be avoided altogether if, instead of calculating the correction factor as a *ratio of the T&P efficiency measured in data to the MC-truth efficiency*:

$$c = \frac{\epsilon_{\text{T\&P}}(\text{data})}{\epsilon_{\text{MCtruth}}}, \quad (10)$$

one defines the correction as the *ratio of two T&P efficiencies, one evaluated in data and another in MC*:

$$c = \frac{\epsilon_{\text{T\&P}}(\text{data})}{\epsilon_{\text{T\&P}}(\text{MC})}. \quad (11)$$

In such a ratio, the systematic errors associated with the technique itself (e.g. arising from a choice of fit functions for Z line shape and substrate background) would tend to cancel since the distributions observed in data and MC are not much different.

By dividing the entire MC samples into several segments according to the various data taking periods, the method properly captures the overall efficiency for prompt leptons averaged over the entire dataset

1300 used for extracting the signal, regardless how much the running conditions during that period were
 1301 changing.

1302 To obtain per-event correction factors $C(m_H)$, we propagate the measured per-lepton correction factors
 1303 $c(p_T, \eta)$ using the method of Lepton Kinematic Templates (LKT). First, using the $gg \rightarrow H \rightarrow 4\ell$ MC, we
 1304 prepare a table listing (p_T^i, η^i) of four signal leptons ($i = 1, 2, 3, 4$) in each MC event. Then, we ran over
 1305 this list multiple times, and give each event a weight

$$C = \prod_i \tilde{c}(p_T^i, \eta^i), \quad (12)$$

1306 where \tilde{c} are drawn as random numbers from the Gaussian *pdf*'s with mean and sigma corresponding
 1307 to the correction factors and their uncertainties as measured with the T&P method for (p_T^i, η^i) -bins. We
 1308 properly take into account the uncorrelation nature of bin-by-bin statistical uncertainties while we also
 1309 preserve the correlation among leptons which belong to the same (pt,eta) bin in a event. The average \bar{C}
 1310 is the data-to-MC correction.

1311 To obtain the statistical uncertainties on the per-event correction factors $\delta C(m_H)$, we ran over again the
 1312 list multiple times, but now the \tilde{c} are drawn as random numbers from the Gaussian *pdf*'s with mean
 1313 = 1 and sigma corresponding to the relative uncertainties as measured with the T&P method for $(p_T^i,$
 1314 $\eta^i)$ -bins. The $\pm 1\sigma$ spread δC is the correction factor uncertainty defined by the statistical precision of
 1315 the T&P measurements. The method can be easily adopted to evaluate correction factors and their
 1316 uncertainties for the di-lepton triggers as well.

1317 We start from the cumulative efficiency measurements (including RECO/ID, ISO and SIP), following the
 1318 above procedure to get overall correction factor for RECO/ID, ISO and SIP selections. This is in practice
 1319 much easier to do and only requires overall T&P measurement instead of three steps for RECO/ID, ISO
 1320 and SIP separately. This is also actually used in the analysis presented here.

1321 In 2011 data taking period, we use only double mu and double electron triggers. There's only muon
 1322 trigger efficiency available so far. As we don't use EMu or MuE cross trigger, the trigger efficiency
 1323 is supposed not to be 100% efficient for the current selection. While for 2012 data, we do use also
 1324 the EMu/MuE cross triggers, so the trigger efficiency is supposed to be very high, one can neglect
 1325 uncertainties on the trigger efficiency.

1326 The uncertainties on the correction factors in this analysis are taken as mass independent by picking the
 1327 largest error from the entire m_H mass range. The results are shown in Figure 49 and 50 for 7 TeV and 8
 1328 TeV separately. These mass-dependent corrections are used to rescale the MC predictions for the Higgs
 1329 boson event yields.

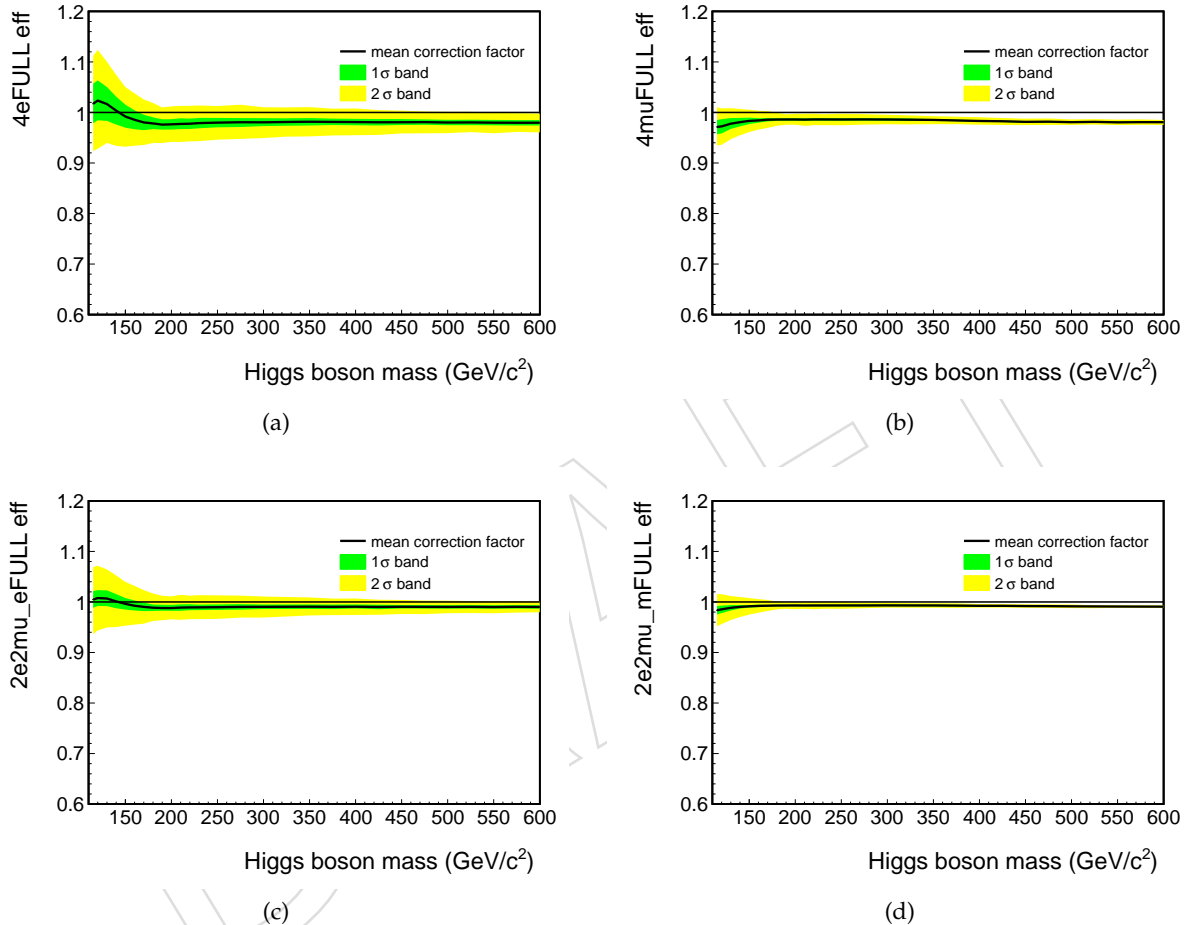


Figure 49: Data-to-MC corrections and their uncertainties for $4e$ (a), 4μ (b) and $2e2\mu$ (c-d) events associated with the electron (left) and muon (right) RECO/ID/ISO/SIP full selection efficiencies for 7 TeV samples.

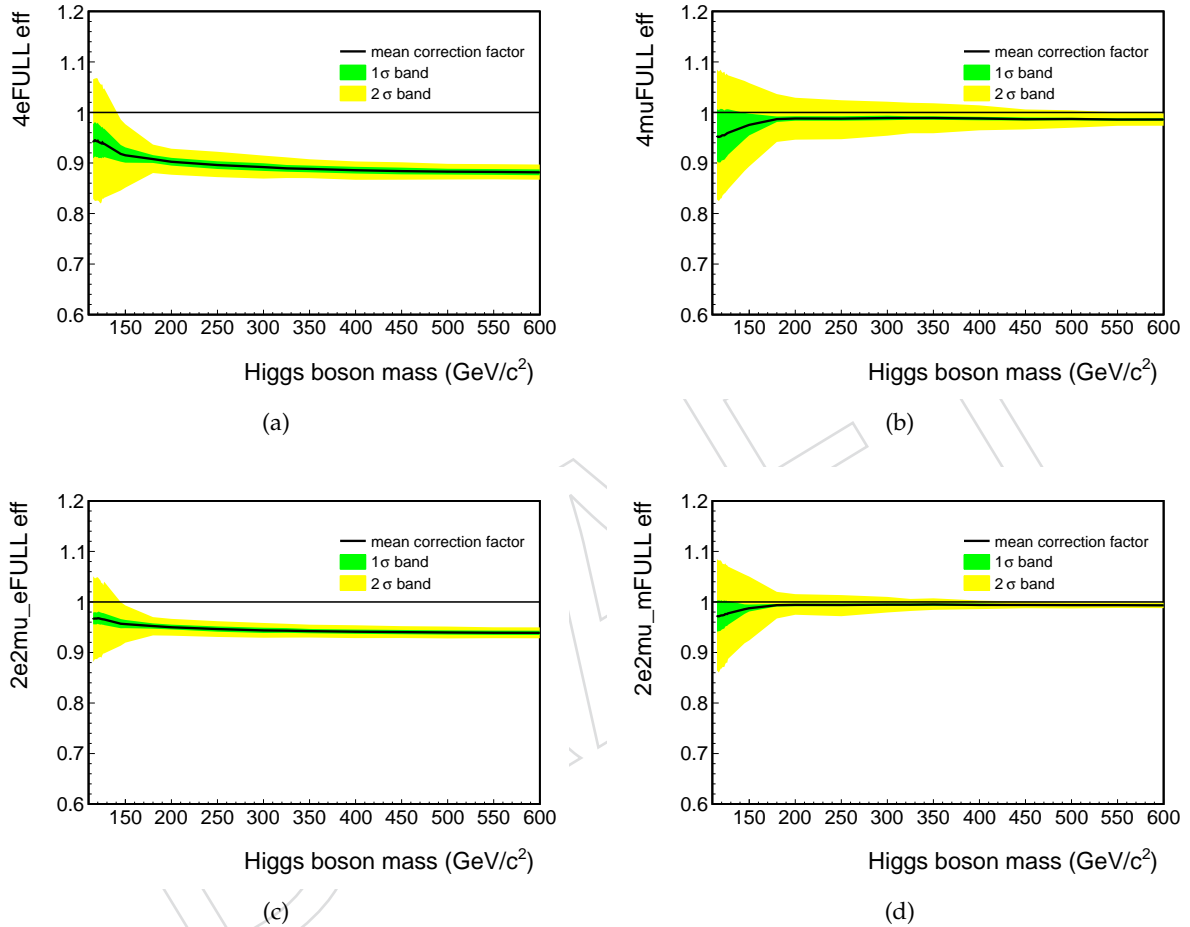


Figure 50: Data-to-MC corrections and their uncertainties for $4e$ (a), 4μ (b) and $2e2\mu$ (c-d) events associated with the electron (left) and muon (right) RECO/ID/ISO/SIP full selection efficiencies for 8 TeV samples.

8.3 Four-lepton mass: scale and resolution

The quality of the momentum measurement of both electrons and muons can substantially vary depending on the leptons characteristics. For electrons, the resolution is dominated by the fluctuations of the measured energy due to bremsstrahlung in the tracker material. For muons the resolution is mainly dependant of the muon p_T and η .

Therefore this entails that the 4ℓ mass resolution varies broadly, by as much as a factor of 2-3, as will be shown in the next section. Therefore, mixing together events with well and poorly measured 4ℓ masses dilutes the Higgs search sensitivity. In this section, we introduce an advanced analysis technique that takes into account mass resolutions assessed on the event-by-event basis.

The gain in sensitivity is not expected to be as much as in $H \rightarrow \gamma\gamma$ search, where events with better $m_{\gamma\gamma}$ resolution have smaller backgrounds. In the case of the $H \rightarrow ZZ \rightarrow 4\ell$ analysis, the $m_{4\ell}$ observable does not help in improving the signal-to-background discrimination. The whole gain comes solely from the proper accounting for the signal mass resolutions for individual events.

8.3.1 Scale and resolution via $Z \rightarrow 2\ell$ and J/ψ

To validate the level of accuracy with which we know the absolute mass scale and resolution, we use $Z \rightarrow \ell\ell$ events.

For electrons, $Z \rightarrow ee$ invariant mass are built in different categories in η and separating well and bad measured electrons using the electron classification. This classification, used for the evaluation of the $E-p$ combined momentum, describes the amount of energy radiated by Bremsstrahlung and the quality of reconstruction, therefore separating different momentum resolutions. Events are looked at in low and high pile-up regimes. The distributions are fitted with a Breit-Wigner (fixed parameters) convoluted with a Crystal Ball (free parameters). Fig 51 and 52 are showing the results obtained this way using 2012 data and comparing to MC expectations.

Systematic uncertainties on electron energy scale can be extracted for these results. It is estimated as the maximum deviation between data and MC of fitted $Z \rightarrow ee$ peak position in different categories of eta and electron classes. This leads to a systematic of 0.4% on the scale at the $Z \rightarrow ee$ peak for 2012 data, consistant with the value determined in 2011. Moreover, the difference in scale due to the different energy used in the derivation of the additional e-scale corrections applied on data is estimated to be 0.2%.

For the resolution, a similar strategy has been adopted, comparing the fitted σ_{CB} between data and MC. The largest relative difference amounts to 22% which we take as systematics on the resolution for 2012 data.

The di-muon invariant mass spectrum with their fits are shown in figure 53 for data (left) and MC Z sample (right). From top to bottom correspond to the four categories which are based on the predicted mass resolution as follows: <1, [1,1.3], [1.3-1.6], [1.6,3.5]. Figure 54 shows the observed mass peak shift and instrumental width (Crystal Ball parameters) for the di-muon Z events. The dashed lines represent the systematic errors we can assign to our ability to predict absolute muon momentum scale ($\pm 0.35\%$) and muon momentum resolution ($\pm 20\%$, or, more accurately, $kappa = 1.2$).

We also categorize Z s according to leptons' pseudorapidity, i.e. Barrel-Barrel, Barrel-Endcap and Endcap-Endcap. In each category, we then further divide them into sub categories according to the predicted mass resolution. As can be seen in figure 55, the observed mass resolution are also within the quoted systematics above.

Further validation can be done on the standard candle $Z \rightarrow 4\ell$ peak region, which is discussed in next section.

8.3.2 Scale and resolution via $Z \rightarrow 4\ell$

The $Z \rightarrow 4\ell$ decays give a clean resonant peak in the four-lepton invariant mass distribution, which can be used as a standard candle in the context of the Higgs boson search in the $H \rightarrow ZZ \rightarrow 4\ell$ decay

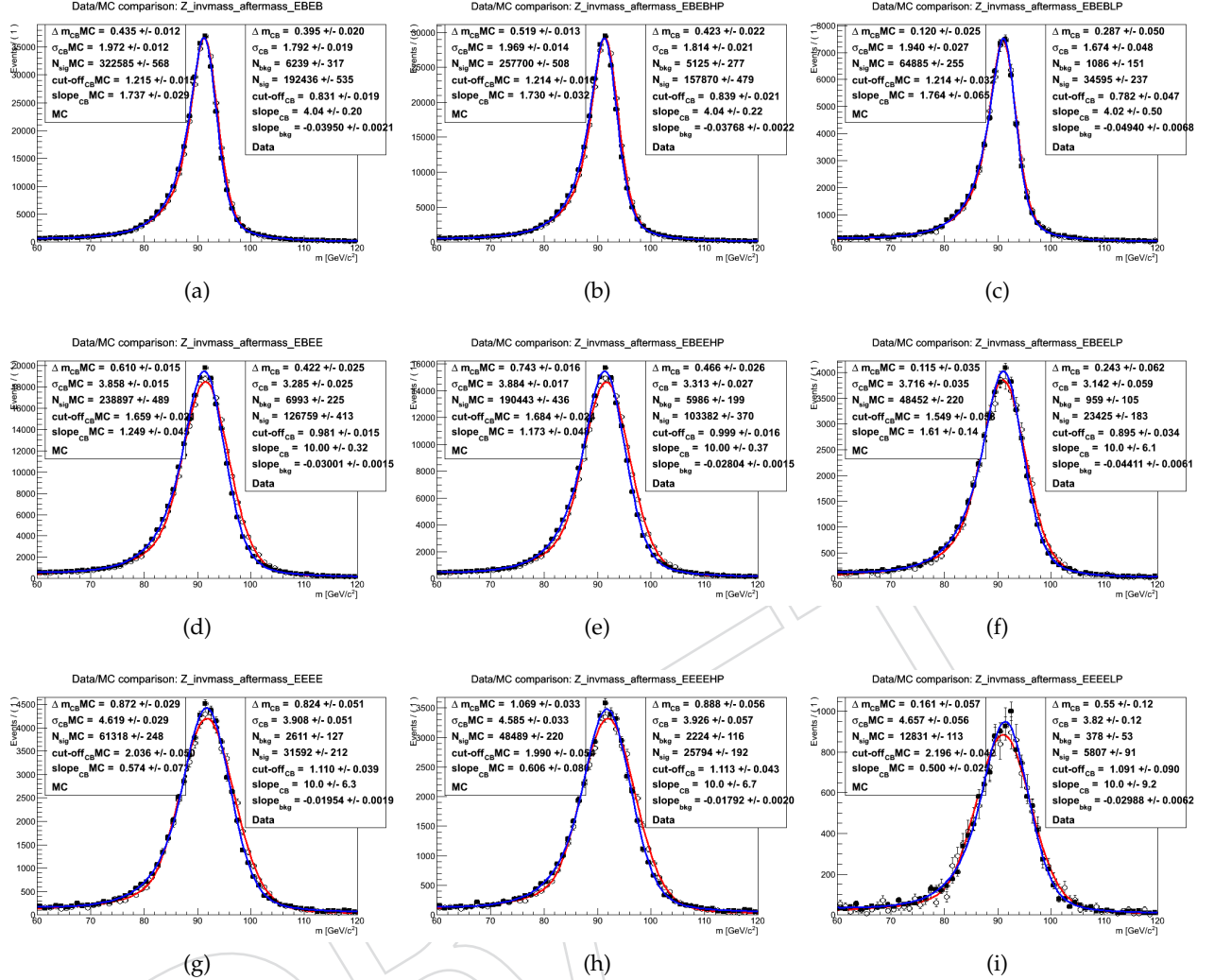


Figure 51: Z to electrons events with both electrons in ECAL barrel (a) and for high (b) and low (c) pile-up regime, with one electron in ECAL Barrel, one in ECAL Endcap (d) and for high (e) and low (f) pile-up regime, with both electrons in ECAL endcaps (g) and for (i) pile-up and low (j) regime. Black points are 2012 data with a fit superimposed (blue line). Open square is MC with a fit superimposed (red line).

mode [90]. The number of events in the $Z \rightarrow 4\ell$ peak at $m_{4\ell} = m_Z$ is an order of magnitude larger than the expected number of events for the SM Higgs boson with a mass m_H anywhere in the remaining allowed range of Higgs boson masses. Therefore, the $Z \rightarrow 4\ell$ peak can be used for a *direct* crosscheck of our understanding of the four-lepton mass scale and the four-lepton mass resolution in the phase space just next to the Higgs boson four-lepton decays. Such a direct calibration using the $Z \rightarrow 4\ell$ peak is complementary to the indirect method of tag-and-probe making use of $Z \rightarrow 2\ell$ events.

Figure 56 shows the fit of the four-lepton mass distribution for the observed events in 7 TeV (left) and 8 TeV (right) data. To enhance the peak, the low end of the m_{Z2} -cut is relaxed from 12 to 4 GeV. The background shape is taken from $pp \rightarrow ZZ \rightarrow 4\ell$ simulation, with the overall normalization floating in the fit. The signal is a convolution of the Breit-Wigner and Crystal Ball functions. The central value and width of the Breit-Wigner function are fixed at the Z boson mass m_Z and width Γ_Z [75]. The Crystal Ball parameters are free in the fit.

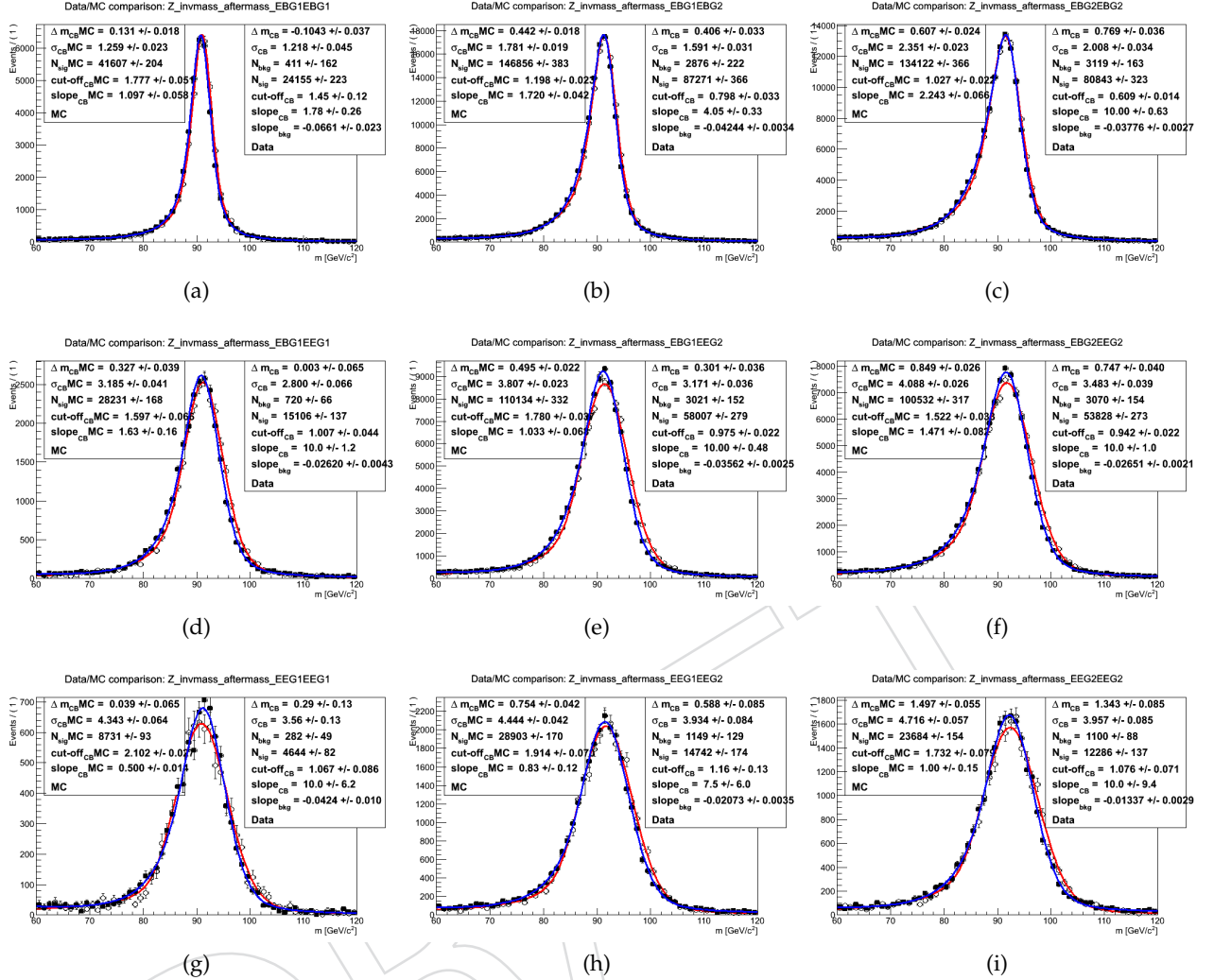


Figure 52: Z to electrons events categorized regarding the electrons classification with both non-showering electrons (golden or big-brem) (a) (d) (g), one non-showering, one showering (showering, bad-track or cracks) (b) (e) (h), both showering electrons (c), (f), (i). First row is for two electrons in ECAL barrel, second row is one electron in ECAL Barrel, the other in the Endcaps, third row is for both electrons in ECAL endcaps. Black points are 2012 data with a fit superimposed (blue line). Open square is MC with a fit superimposed (red line).

One can see that the offset of the peak is 0.38 ± 0.52 GeV ($0.4 \pm 0.6\%$) for the 7 TeV data and 0.65 ± 0.41 GeV ($0.7 \pm 0.5\%$) for the 8 TeV data. These numbers can be used to constrain the possible systematic errors of the four-lepton mass scale. With the current data, we can state that the average four-lepton mass scale does not show any significant bias with the 0.6% statistical uncertainty.

The Crystal Ball width (sigma of the Gaussian core) returned by the fit is 1.55 ± 0.65 GeV ($1.7 \pm 0.7\%$) for the 7 TeV data and 1.89 ± 0.82 GeV ($2.1 \pm 0.9\%$) for the 8 TeV data. With the current data, we can measure the average four-lepton mass resolution with about 50% statistical uncertainty.

With the current amount of data, the number of events in the $Z \rightarrow 4\ell$ peak does not yet constrain the absolute mass scale and resolution with a precision better than we derive in Sec. 8.3.6. Hence, these results can be viewed as a crosscheck, whose advantage is that they are direct measurements made on the four-lepton system.

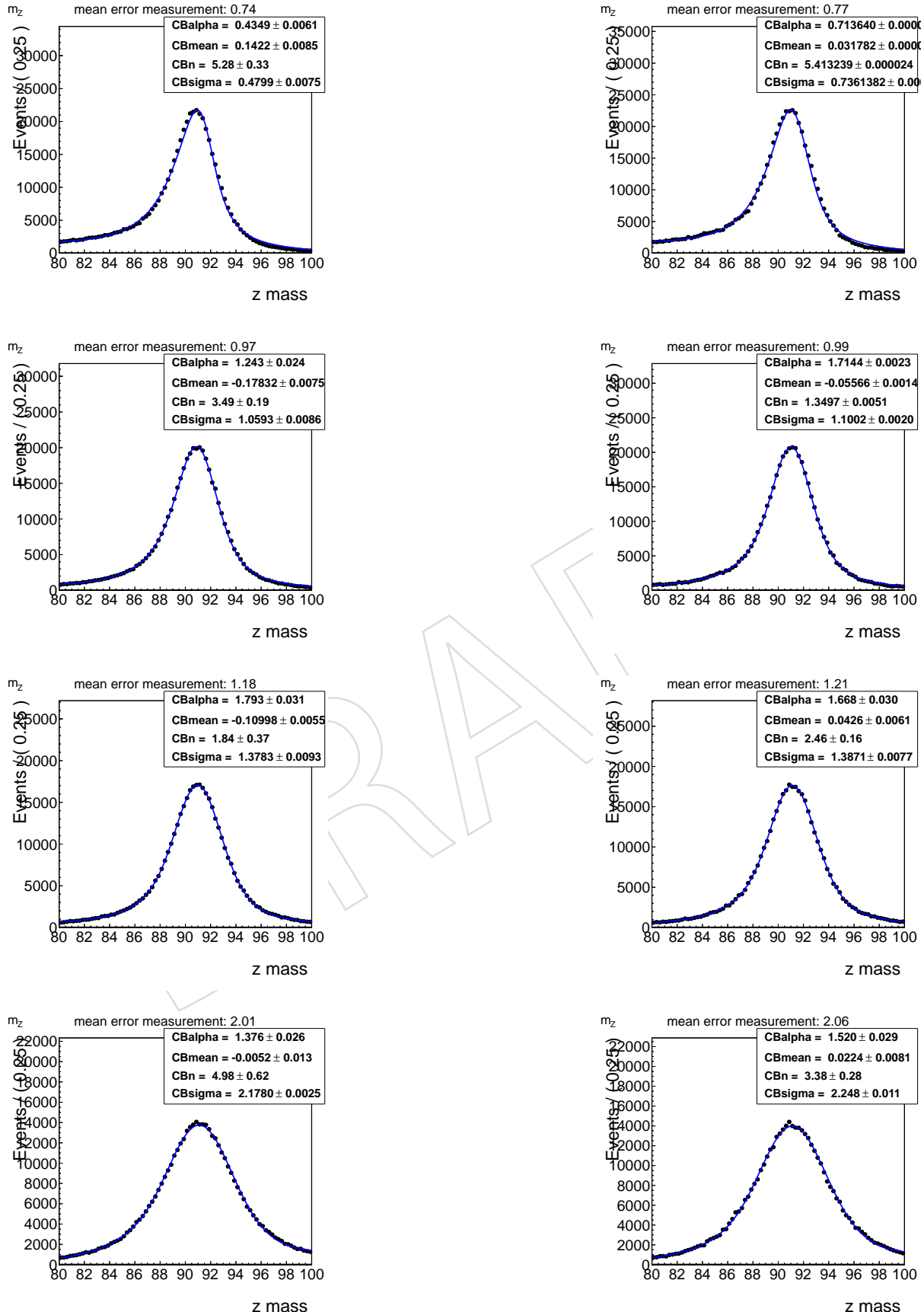


Figure 53: Di-muon invariant mass spectrum (points) and fits with convoluted function of Breit-Wigner and Crystal Ball for data (left) and MC (right) Z events. From top to bottom correspond to the four categories which are based on the predicted mass resolution as follows: < 1 , $[1, 1.3]$, $[1.3-1.6]$, $[1.6, 3.5]$.

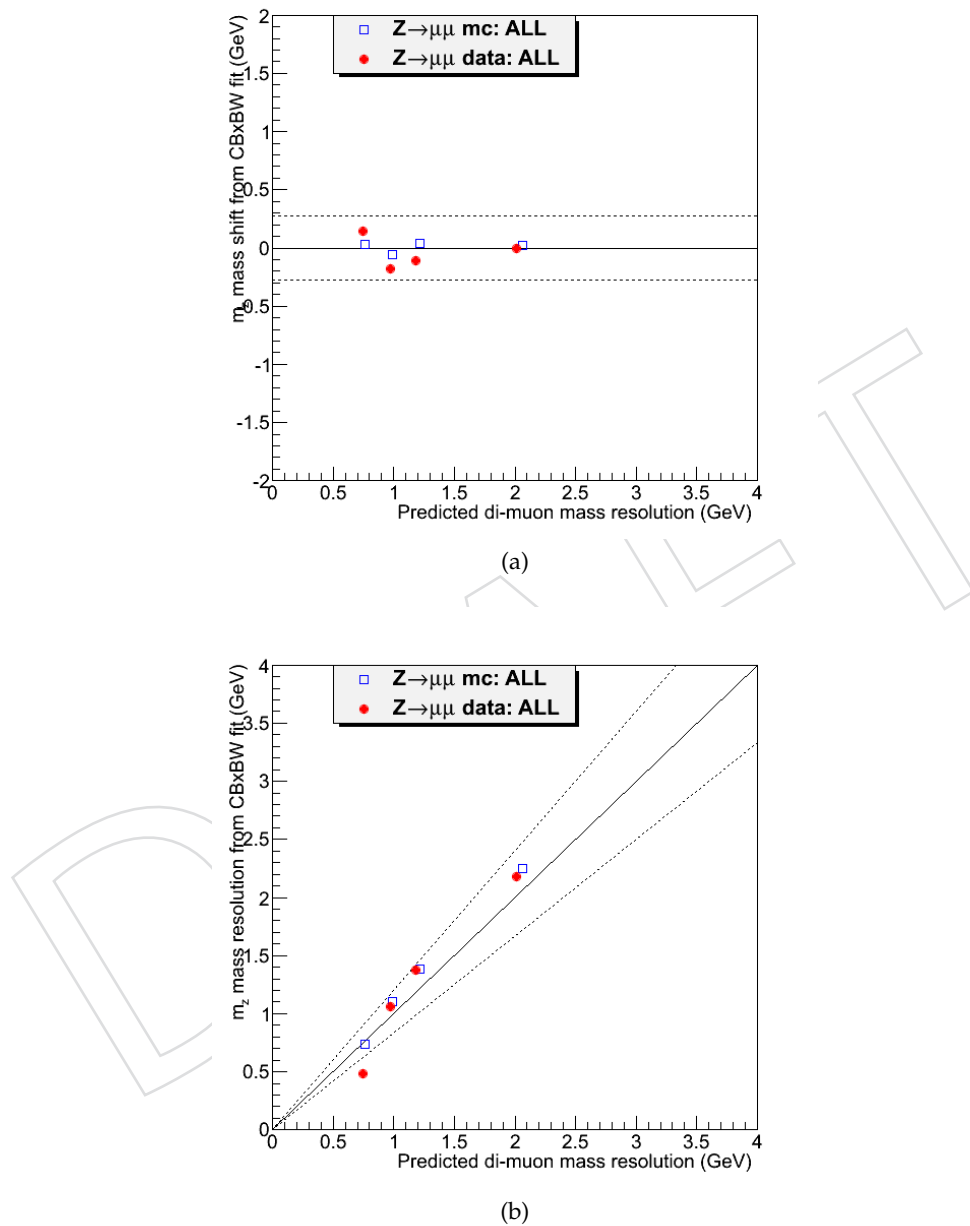


Figure 54: Plots validating our knowledge of the muon momentum scale (a) and resolution (b).

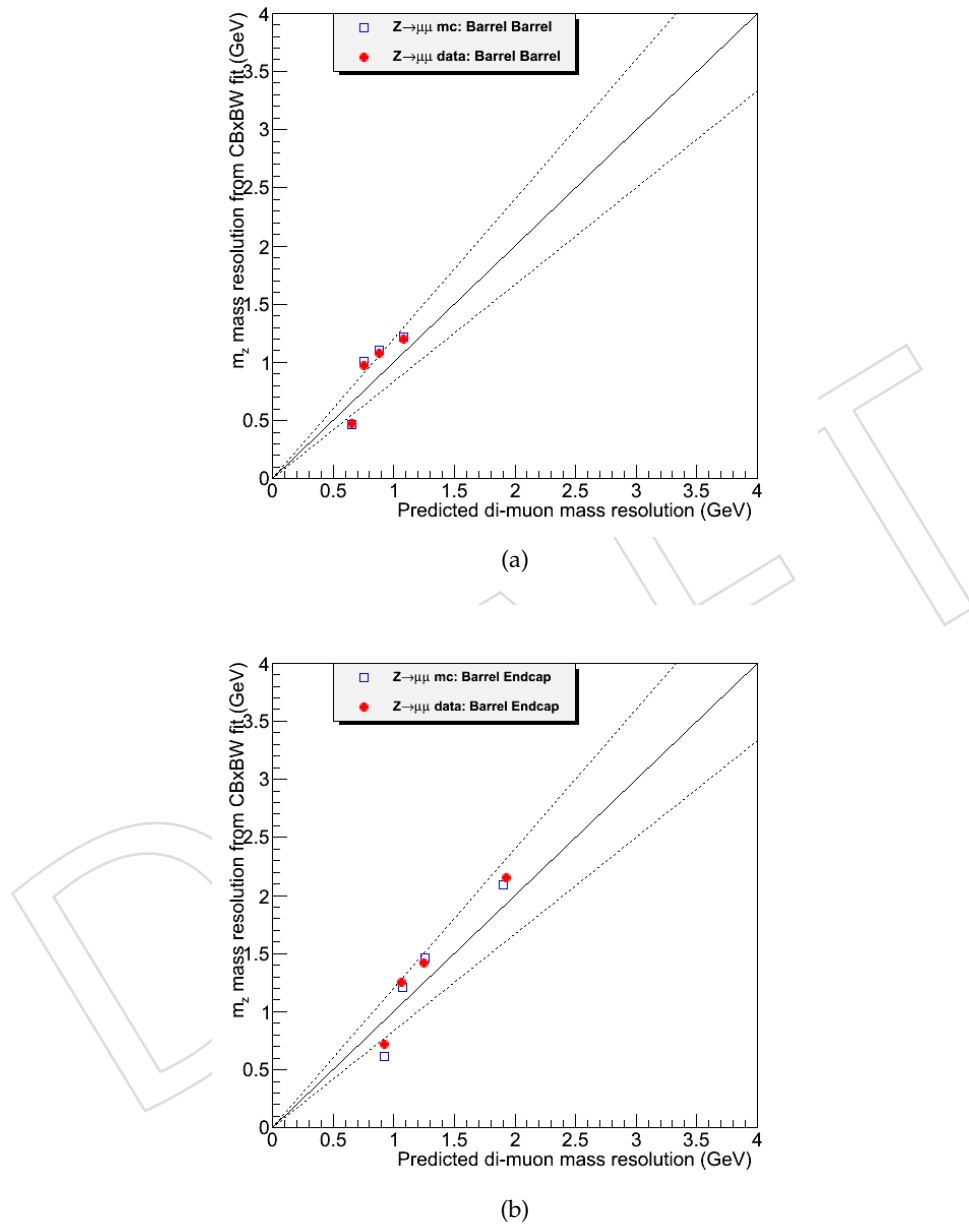


Figure 55: Plots validating our knowledge of the muon momentum resolution for Barrel-Barrel (left) and Barrel-Endcap (right) categories.

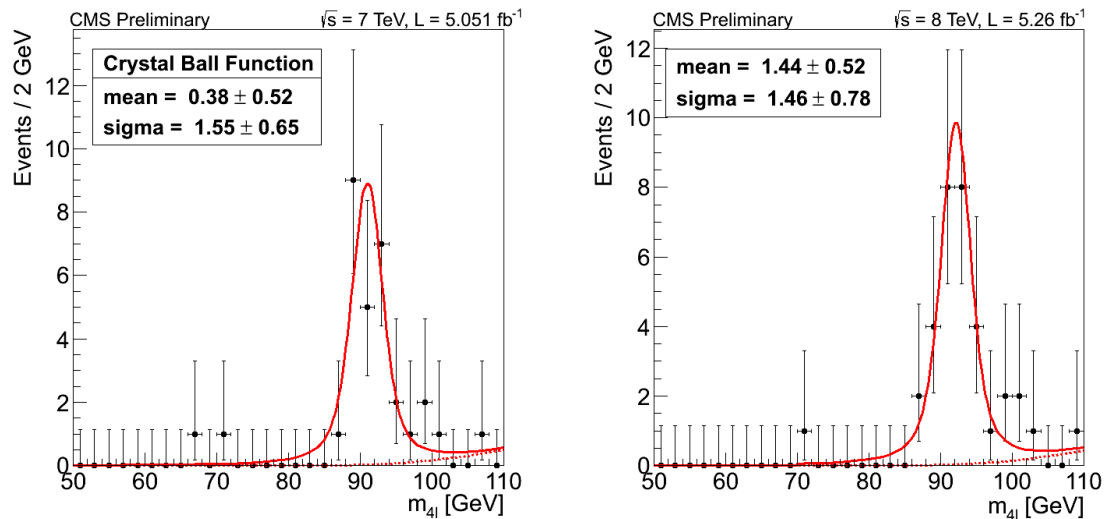


Figure 56: Four-lepton mass distribution in the 7 TeV data (left) and 8 TeV data (right). Data are shown with points. The three final states, $4e$, 4μ , and $2e2\mu$, are added together. The solid line represents a simultaneous fit for the background and Z boson peak (see text for details).

8.3.3 4 ℓ Event-by-Event Error: Error propagation

Event-by-event mass errors can be evaluated starting from the errors on the individual lepton momenta in different ways.

Individual lepton errors are computed on a per-event basis for muons using the full error matrix as obtained from the muon track fit, and for the electrons using the estimated momentum error as obtained from the combination of the ECAL and tracker measurement, neglecting the uncertainty on the track direction from the GSF fit. The error on track angles can be neglected because of their small contribution to the invariant mass error. In addition for electrons, they are small compared to the E measurement (because we have pixels close to the interaction vertex and thus before bremsstrahlung occurs).

In the following we describe two approaches for deriving mass errors. In the first approach the individual lepton momentum measurement errors are propagated to the 4l mass error and to the Z1 and Z2 mass errors using an analytical error propagation including all correlations. In the alternative approach, the directional errors for muons are additionally neglected, and to propagate uncertainties of individual leptons to the uncertainty on the invariant mass, each δm corresponding to individual lepton momentum variation is calculated separately, and then the measured resolution on the invariant mass of the four leptons is taken as the quadrature sum of the four individual δm :

$$\begin{aligned} m_0 &= F(p_{T1}, \phi_1, \eta_1; p_{T2}, \phi_2, \eta_2; p_{T3}, \phi_3, \eta_3; p_{T4}, \phi_4, \eta_4) \\ \delta m_i &= F(\dots; p_{Ti} + \delta p_{Ti}, \phi_i, \eta_i; \dots) - m_0 \\ \delta m &= \sqrt{\delta m_1^2 + \delta m_2^2 + \delta m_3^2 + \delta m_4^2} \end{aligned}$$

At the end, one can see that the two approaches give very similar results (see in results section) which cross checks each other.

8.3.4 MC based expectations

The error evaluation is checked on MC performing pulls distributions. If the errors are correctly evaluated the pull should have a sigma of 1 in the gaussian case. In case of asymmetrical lepton momentum distributions, the RMS of the pull should be one with the errors defined as the RMS of the lepton momentum distributions. It has been demonstrated using toy MC experiments that if the errors are defined as the sigma of the gaussian part of the lepton momentum distribution, the sigma of the gaussian part of the pull should be 1, and if the errors are defined as the effective RMS it is the effective RMS of the pull distribution which should be one.

The Figure 57 shows the MC pull distributions for the 4e channel, for electron momentum and mass measurement. This shows that the individual pull width is different from the Higgs pull width. This effect is understood to be mostly induced by the asymmetry of the electron momentum distribution. When combining asymmetrical distributions from individual leptons to form the m4l distribution, one sees that a pull on individual lepton with an effective RMS at 1 propagates into a pull for the m4l distribution with an effective RMS greater than 1. This means the errors on m4l are underestimated. This has been studied using toy MC experiments, the Figure 58 shows the effective RMS of the m4l pull distributions and of the lepton momentum pull distributions vs asymmetry, defined as the mean-mode of the relative lepton momentum distribution from toy MC experiments.

The Figure 59 shows the MC pull distributions for the (a) 4e, (b) 4 μ and (c) 2e2 μ final states as a function of the m_{4l} reconstructed mass. In the case of electrons, where the momentum distributions show large asymmetries, the errors have been chosen as the effective RMS (effRMS). This choice implies that the effRMS of the pull for the case of electrons is rather shown, together with the σ for comparison.

Errors are seen to be understood from the 20% to the 60% level. The differences observed between muons and electrons are mostly due to the larger asymmetry in electrons $E_e/E_{e,true}$ distributions.

The event-by-event errors are inflated to take into account the pull trend as a function of m_{4l} .

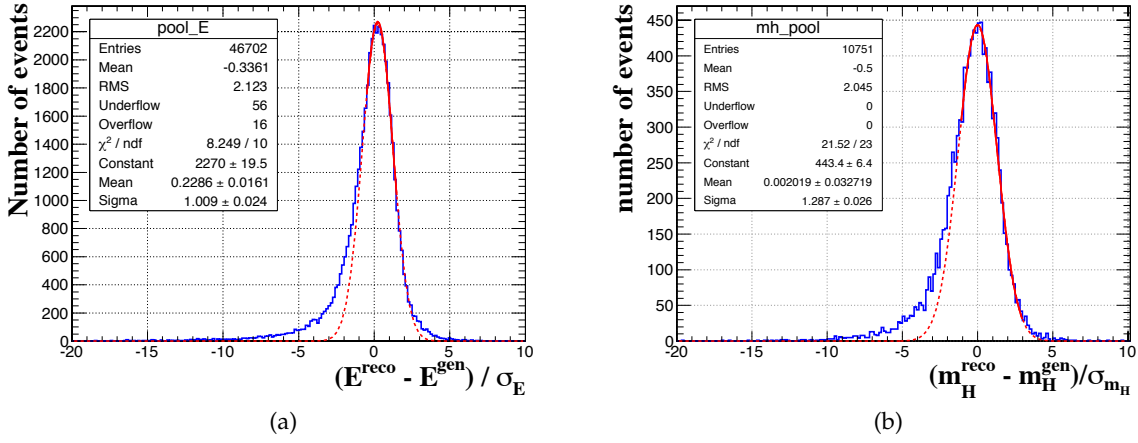


Figure 57: MC pull distributions for a Higgs mass of 120 GeV decaying in the $4e$ channel. (a) pull per electron (b) pull per Higgs event.

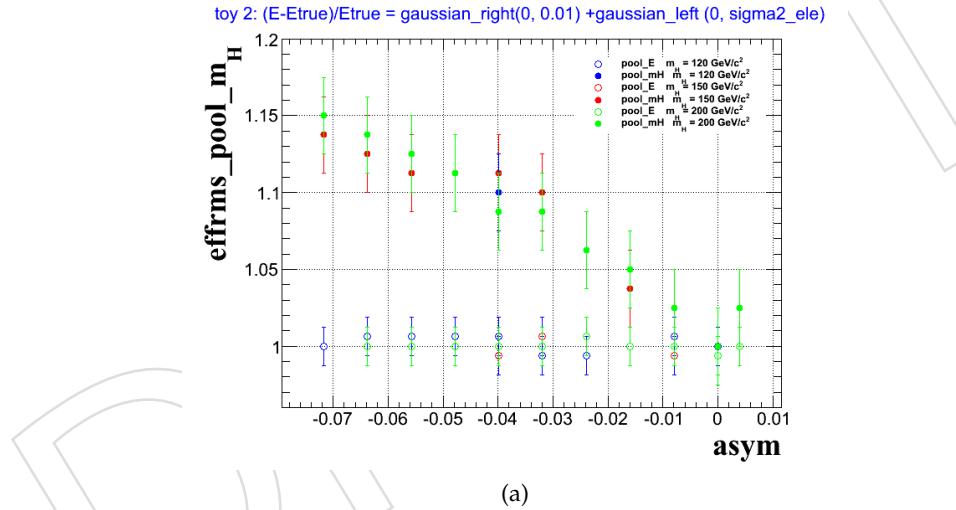


Figure 58: Effective RMS of the $m_{4\ell}$ pull distributions (plain dots) and of the lepton momentum (open dots) pull distributions vs asymmetry for different m_H .

1442 For simplicity, the event-by-event errors are scaled linearly by the factors 1.15 ± 0.06 , 1.30 ± 0.13 and
 1443 1.45 ± 0.07 for 4μ , $2e2\mu$ and $4e$ respectively.

1444 Figure 60 shows the *MC-predicted* $m_{4\ell}$ mass resolution versus reconstructed mass for and $H \rightarrow ZZ \rightarrow 4\ell$
 1445 Monte Carlo samples. The plots are obtained for the CMSSW 4.2 MC samples. The uncertainties on
 1446 lepton p_T used in calculations of $m_{4\ell}$ uncertainties are taken from MC.

1447 8.3.5 Validation of errors

1448 The agreement between data and MC for the evaluation of the estimated lepton errors on event-by-event
 1449 has been studied. The Figure 61 shows the data/MC agreement of the errors for electrons and muons.

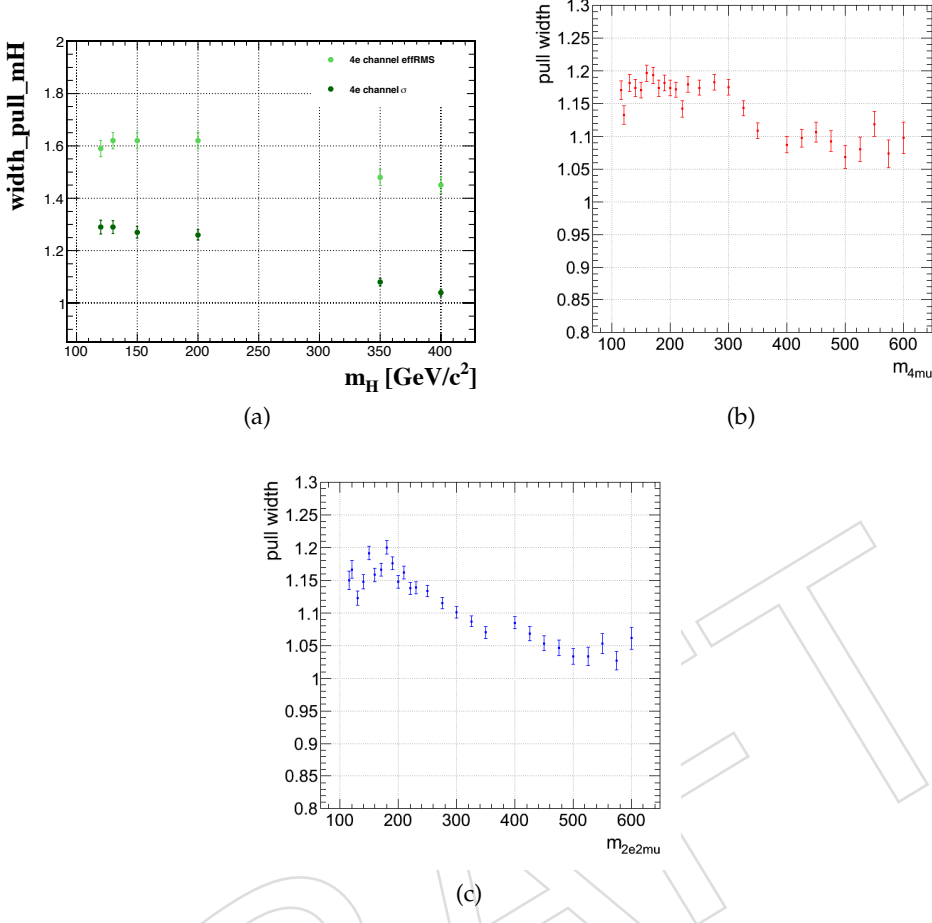


Figure 59: Widths of the MC pull distributions in function of the Higgs mass hypotheses for the (a) $4e$, (b) 4μ and (c) $2e2\mu$ final states.

1450 8.3.6 Results

Figure 62 shows $m_{4\ell}$ mass resolutions for the observed $4e$, 4μ , and $2e2\mu$ events in the low mass region. Figure 63 shows the comparison of errors obtained in data with two approaches separately. Good agreement between two approaches can be seen.

1454 The Figure 64 shows the mass bias for the three channels in function of the Higgs mass hypotheses. This
1455 bias is a result of a convolution of two effects: the calibration and the lepton momentum asymmetries.
1456 It is predicted to be very small, ie less than 0.5 GeV for Higgs mass hypotheses below 200 GeV.

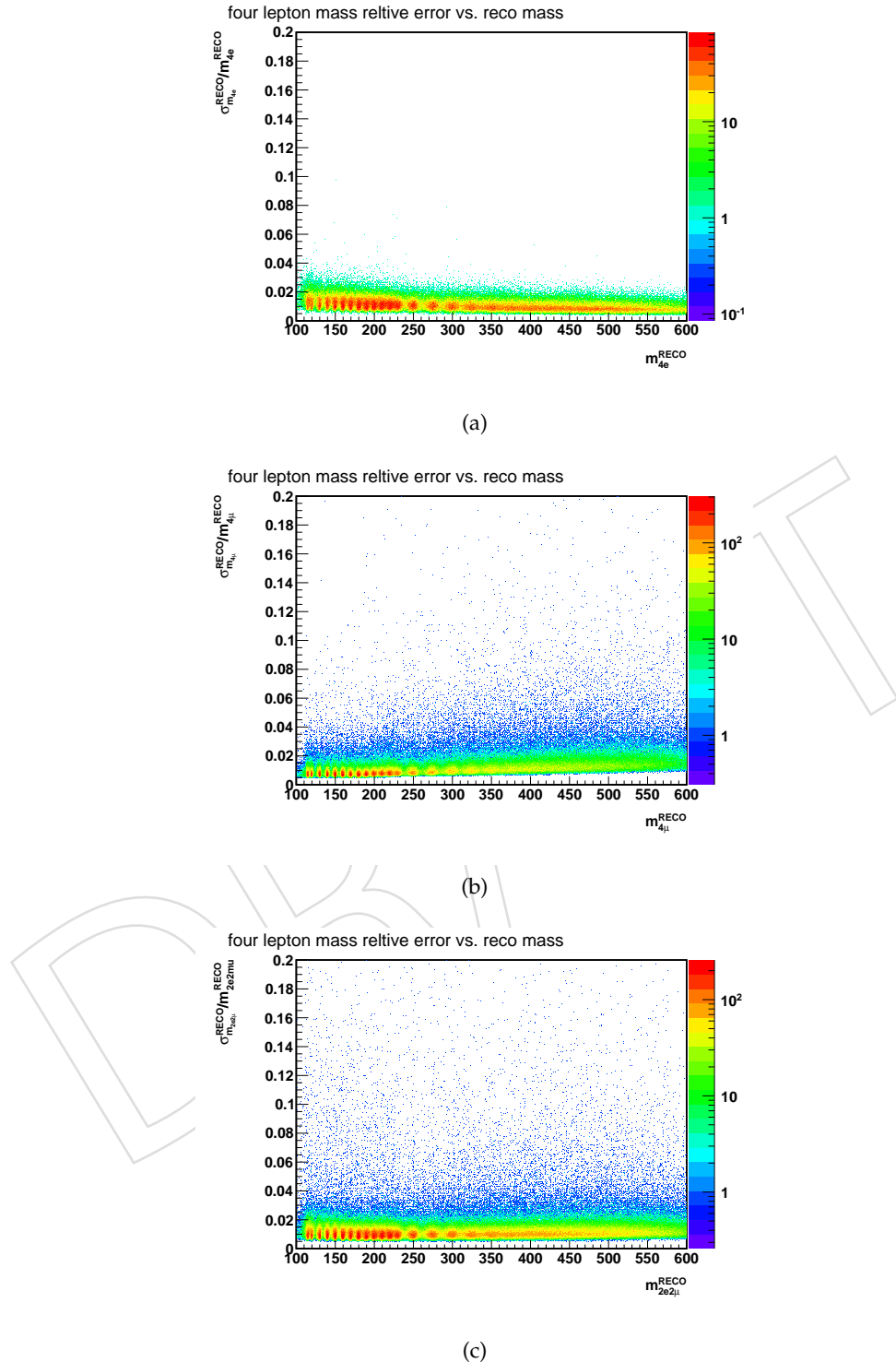


Figure 60: Expected Higgs boson mass resolutions versus Higgs candidates reconstructed mass. Three plots are for the three final states: $4e$ (a), 4μ (b) and $2e2\mu$ (c).

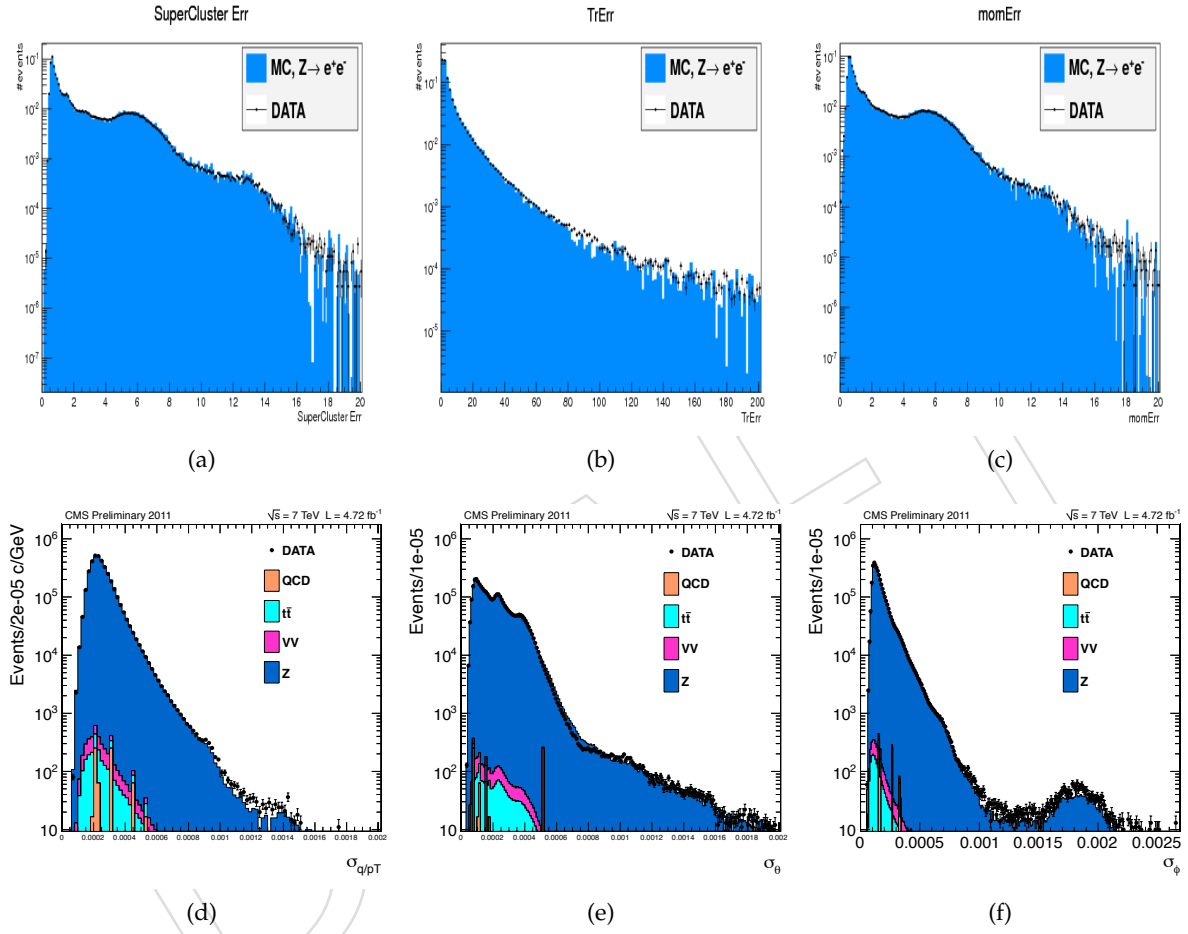


Figure 61: Data/MC agreement for electrons the uncertainties on ECAL measurement (a), tracker measurement (b) and combined momentum (c), for muons the uncertainties on q/p_T (d), θ (e), and ϕ (f). The relative errors have been checked and similar level of agreement is found. MC expectations (blue filled histograms) are superimposed to data (dots). Distributions are shown for 2012 data for electrons and 2011 data for muons.

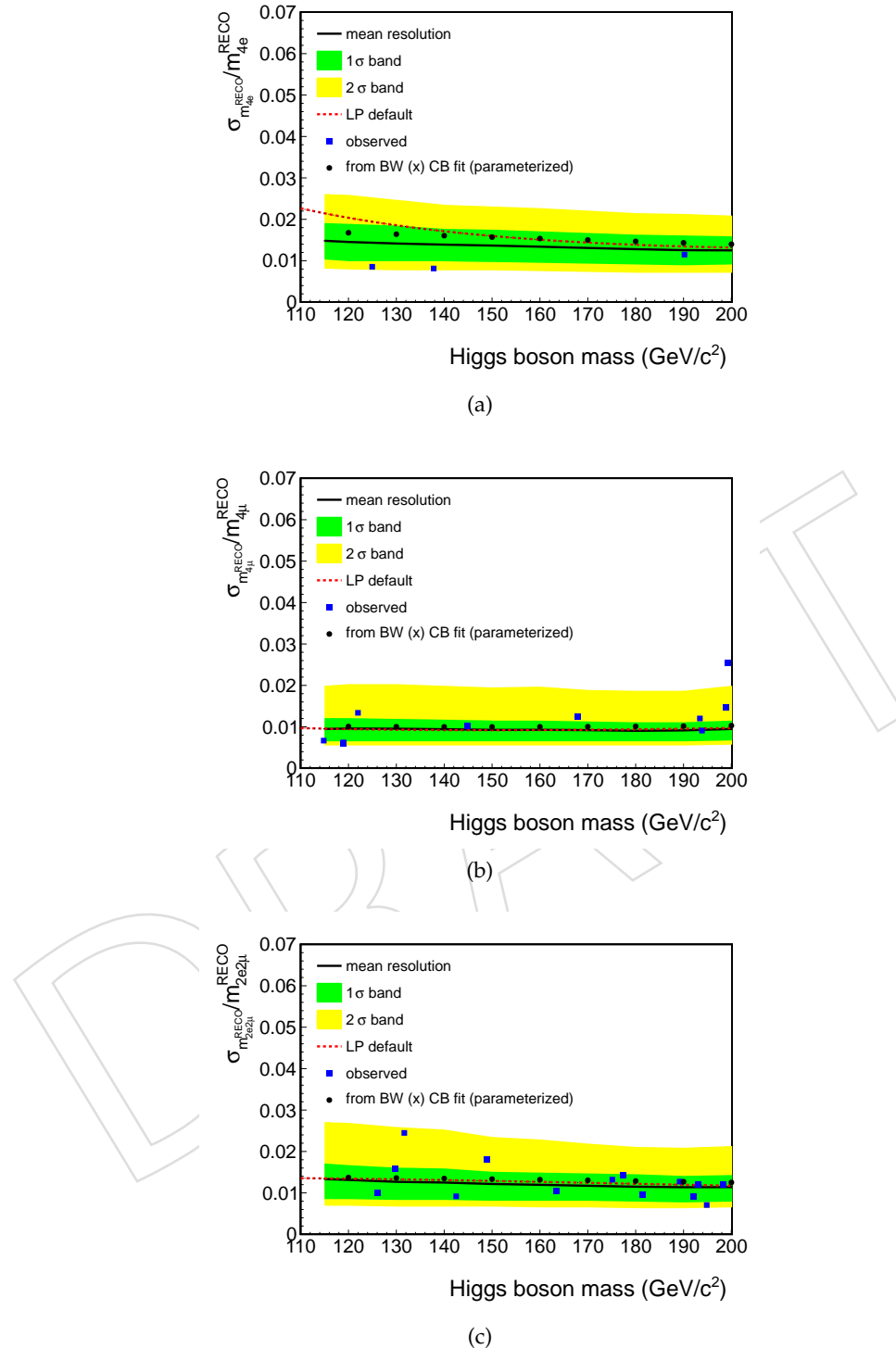
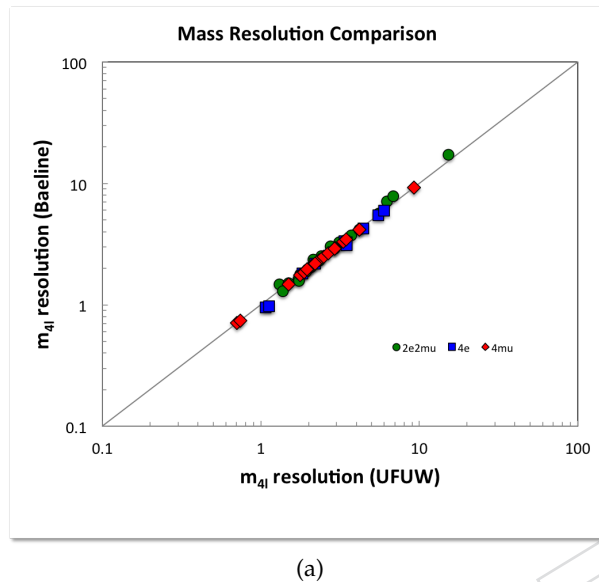
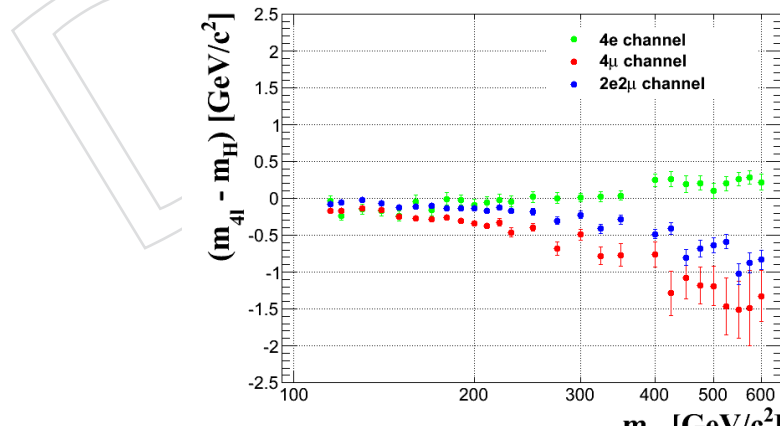


Figure 62: Zoom at the mass resolutions of the observed low mass events (squares). The green (yellow) band indicates the range expected to contain 68% (95%) of all events. The black solid line is the median resolution in MC. **The dotted red line is the resolution used in AN-11-123.** Three plots are for the three final states: 4e (a), 4μ (b) and 2e2μ (c).



(a)

Figure 63: Comparison of mass errors of observed data events between two independent approaches.



(a)

Figure 64: Mass bias for the three channels in function of the Higgs mass hypotheses

1457 9 Irreducible ZZ Background Model and uncertainties

1458 9.1 ZZ^(*) yields

The expected rate in any given mass range $[m_1, m_2]$ is obtained directly from the absolute rate predicted by the MC model simulation:

$$N_{\text{expect}}^{\text{ZZ}} [m_1, m_2] = \int_{m_1}^{m_2} \left(\frac{dN}{dm_{4\ell}} \right)_{\text{MC}} dm_{4\ell} \quad (13)$$

1459 When used for comparisons with data, the method is affected by the full systematics uncertainties on
 1460 the pp integrated luminosity and the theory errors as well as systematic errors on acceptance within
 1461 analysis cuts.

1462 9.2 ZZ^(*) Background Model

The $pp \rightarrow ZZ \rightarrow 4\ell$ backgrounds (NLO and $gg \rightarrow ZZ$) are modeled using the functional form very similar to that of the signal:

$$\text{ZZ@NLO} : \frac{dN}{dm_{4\ell}} = C(m_{4\ell}) \cdot N^{\text{MC}}(m_{4\ell}) \cdot F_{\text{ZZNLO}}(m_{4\ell}), \quad (14)$$

$$gg \rightarrow ZZ : \frac{dN}{dm_{4\ell}} = C(m_{4\ell}) \cdot N^{\text{MC}}(m_{4\ell}) \cdot F_{\text{gg2ZZ}}(m_{4\ell}). \quad (15)$$

1463 where the overall data-to-MC correction factors $C(m_{4\ell})$ are assumed to be the same as for the Higgs
 1464 events with $m_H = m_{4\ell}$. The validity of this assumption is addressed later in section on systematic
 1465 errors.

1466 The functions $F_{\text{ZZNLO}}(m_{4\ell})$ and $F_{\text{gg2ZZ}}(m_{4\ell})$ are parameterized separately for $4e$, 4μ , and $2e2\mu$ using the
 1467 simulated distributions as follows:

$$f_1(m, \vec{a}) = \left(0.5 + 0.5 \text{erf} \left(\frac{m - a_1}{a_2} \right) \right) \cdot \frac{a_4}{1 + e^{(m-a_1)/a_3}} \quad (16)$$

$$f_2(m, \vec{b}) = \left(0.5 + 0.5 \text{erf} \left(\frac{m - b_1}{b_2} \right) \right) \cdot \left(\frac{b_4}{1 + e^{(m-b_1)/b_3}} + \frac{b_6}{1 + e^{(m-b_1)/b_5}} \right) \quad (17)$$

$$f_3(m, \vec{c}) = \left(0.5 + 0.5 \text{erf} \left(\frac{m - c_1}{c_2} \right) \right) \cdot \frac{c_4}{1 + e^{(m-c_1)/c_3}} \quad (18)$$

$$F_{\text{ZZNLO}}(m, \vec{a}, \vec{b}, \vec{c}) = f_1 + f_2 + f_3 \quad (19)$$

$$F_{\text{gg2ZZ}}(m, \vec{a}, \vec{b}, \vec{c}) = f_1 + f_2 \quad (20)$$

1468 The ZZ background shape fits are shown in Fig. 65 and the fit parameters are listed in Tables 12 and 13.
 1469 We do not find any systematic uncertainties that would distort the ZZ $\rightarrow 4\ell$ mass distributions in a
 1470 substantial way over the mass range corresponding to the Higgs boson width. Therefore, all uncertain-
 1471 ties on the ZZ-background are included as uncertainties in normalization, whose absolute scale may
 1472 depend on the Higgs boson mass m_H being probed in the search.

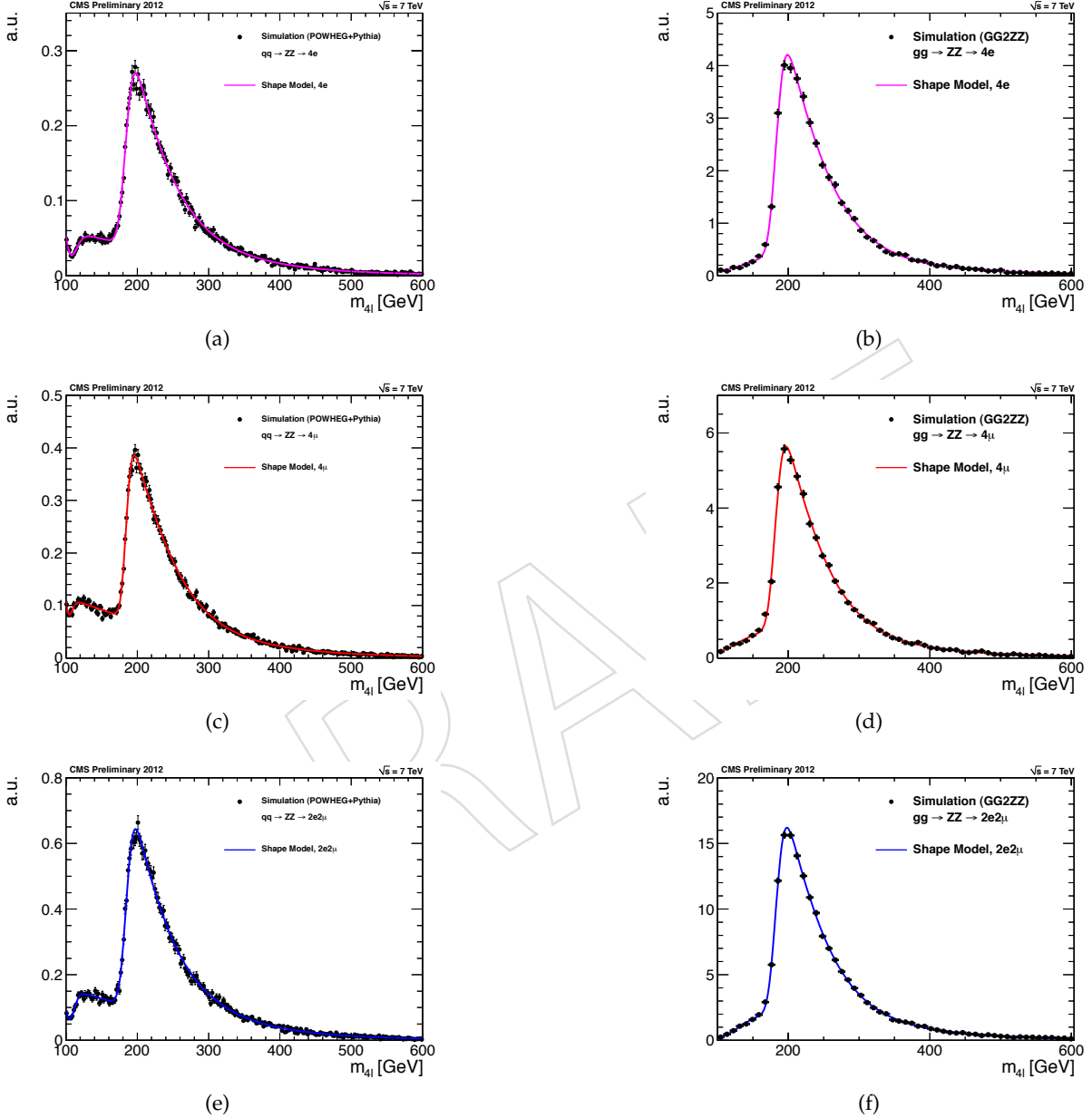


Figure 65: Probability density functions describing the NLO ZZ (left) and $gg \rightarrow ZZ$ (right) background shape for $4e$ (top), 4μ (middle), and $2e2\mu$ (bottom) final states. Center of mass energy is 7 TeV.

Table 12: F_{ZZNLO} parameter values for the $4e$, 4μ and $2e2\mu$ final states NUMBERS NEED TO BE UPDATED

\sqrt{s}		a_1	a_2	a_3	a_4	b_1	b_2	b_3	b_4	b_5	b_6	c_1	c_2	c_3	c_4
7 TeV	$4e$	115.2	21.67	126.9	0.035	185.2	11.7	35.22	0.133	63.13	0.077	98.39	-5.68	88.84	0.029
	4μ	105.2	11.27	117.99	0.0456	185.4	9.57	37.09	0.110	57.88	0.053	96.07	-6.48	1344	0.085
	$2e2\mu$	108.0	14.76	123.4	0.038	185.0	11.00	36.57	0.109	60.56	0.067	83.38	-11.73	930.9	0.472
8 TeV	$4e$	115.2	21.67	126.9	0.035	185.2	11.7	35.22	0.133	63.13	0.077	98.39	-5.68	88.84	0.029
	4μ	105.2	11.27	117.99	0.0456	185.4	9.57	37.09	0.110	57.88	0.053	96.07	-6.48	1344	0.085
	$2e2\mu$	108.0	14.76	123.4	0.038	185.0	11.00	36.57	0.109	60.56	0.067	83.38	-11.73	930.9	0.472

Table 13: F_{gg2ZZ} parameter values for the $4e$, 4μ and $2e2\mu$ final states for 7 TeV NUMBERS NEED TO BE UPDATED

\sqrt{s}		a_1	a_2	a_3	a_4	b_1	b_2	b_3	b_4	b_5	b_6
7 TeV	$4e$	177.9	70.38	113.1	0.041	183.5	11.67	35.24	0.54	28.94	-0.322
	4μ	223.8	108.6	213.7	0.106	184	14.38	47.79	0.323	231.2	-0.104
	$2e2\mu$	155.2	46.3	111.2	0.0475	184.1	12.42	37.75	0.538	34.59	-0.324
8 TeV	$4e$	177.9	70.38	113.1	0.041	183.5	11.67	35.24	0.54	28.94	-0.322
	4μ	223.8	108.6	213.7	0.106	184	14.38	47.79	0.323	231.2	-0.104
	$2e2\mu$	155.2	46.3	111.2	0.0475	184.1	12.42	37.75	0.538	34.59	-0.324

1473 9.3 ZZ^(*) model uncertainties

1474 9.3.1 Theoretical uncertainties

1475 Event yield uncertainties as a function of $m_{4\ell}$

1476 PDF+ α_s and QCD scale uncertainties for $pp \rightarrow ZZ \rightarrow 4\ell$ at NLO and $gg \rightarrow ZZ \rightarrow 4\ell$ are evaluated
 1477 using MCFM [21]. We use the $2e2\mu$ final state and the following fiducial cuts for leptons: $m_{ee} > 12$,
 1478 $m_{\mu\mu} > 12$, electrons' $p_T > 7$ and $|\eta| < 2.5$, and muons' $p_T > 5$ and $|\eta| < 2.4$. The minimal jet-lepton and
 1479 lepton-lepton ΔR_{min} -distance were relaxed, i.e. set to zero. The cross sections are calculated inclusively
 1480 in the number of jets found at NLO. The uncertainties are assessed both for 7 TeV and 8 TeV. Per Ref. [?]
 1481], the PDF+ α_s and QCD scale uncertainties are treated as uncorrelated. However, uncertainties between
 1482 7 TeV and 8 TeV are assumed 100% correlated.

1483 For estimation of the PDF+ α_s systematic errors, we use the PDF4LHC prescription [83]. The three
 1484 PDF sets used are CT10 [84], MSTW08 [85], NNPDF [86]. The obtained results are summarized in
 1485 Figs. 66. The four-lepton mass dependent PDF+ α_s systematic errors, for both 7 TeV and 8 TeV, can be
 1486 parametrized as follows:

$$\text{ZZ@NLO : } \kappa(m_{4\ell}) = 1 + 0.0035\sqrt{(m_{4\ell} - 30)} \quad (21)$$

$$gg \rightarrow ZZ : \kappa(m_{4\ell}) = 1 + 0.0066\sqrt{(m_{4\ell} - 10)} \quad (22)$$

1487 For estimation of QCD scale systematic errors, we calculate variations in the differential cross section
 1488 $d\sigma/dm_{4\ell}$ as we change the renormalization and factorization scales by a factor of two up and down from
 1489 their default setting $\mu_R = \mu_F = m_Z$. The obtained results are summarized in Fig. 67. The four-lepton
 1490 mass dependent QCD scale systematic errors, for both 7 TeV and 8 TeV, can be parametrized as follows:

$$\text{ZZ@NLO : } \kappa(m_{4\ell}) = 1.00 + 0.01\sqrt{(m_{4\ell} - 20)/13} \quad (23)$$

$$gg \rightarrow ZZ : \kappa(m_{4\ell}) = 1.04 + 0.10\sqrt{(m_{4\ell} + 40)/40} \quad (24)$$

1491 Shape uncertainties

1492 The shape uncertainties in $m_{4\ell}$ distribution imply the knowledge of correlations between possible event
 1493 yield variations at different $m_{4\ell}$ points. For simplicity, we assume 100% correlations between errors
 1494 across the entire $m_{4\ell}$ mass range.

1495 For a given test Higgs boson mass M_H , the signal is a localized peak in the $m_{4\ell}$ distribution. We do
 1496 not expect large variations in signal shape in the narrow regions under the Higgs boson peak, which is
 1497 confirmed by looking at the local shape changes due to QCD scale PDF variations. This holds true even
 1498 for the high mass Higgs boson.

1499 The knowledge of correlation of the background under the signal peak and far outside in sidebands is
 1500 relevant for the signal inference only if the sidebands have a sufficient statistical power to constrain the
 1501 prior-to-the-experiment uncertainties. This is not the case in this analysis with the current amount of
 1502 data. With $\mathcal{O}(70)$ observed $ZZ \rightarrow 4\ell$ events, the statistical error is about 12%, which is larger than the
 1503 current theoretical error of 5%.

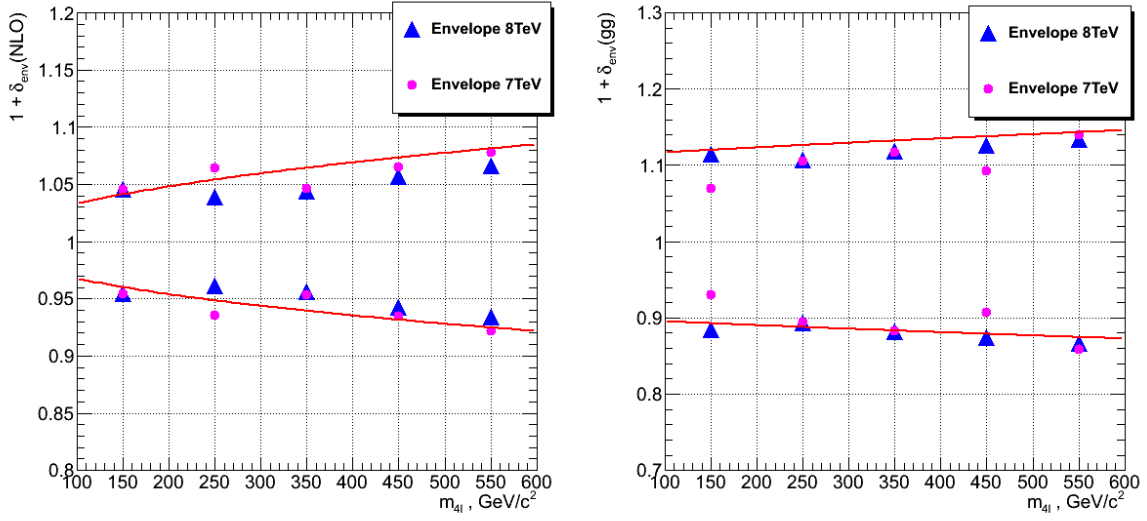


Figure 66: PDF+ α_s uncertainties for (left) $pp \rightarrow ZZ \rightarrow 4\ell$ at NLO and (right) $gg \rightarrow ZZ \rightarrow 4\ell$ processes. The points are evaluated uncertainties. The curves are the fit systematic error $\kappa(m_{4\ell})$ to be used in the statistical analysis. These errors are driven by two independent nuisance parameters pdf_qqbar for $pp \rightarrow ZZ \rightarrow 4\ell$ at NLO and pdf_gg for $gg \rightarrow ZZ \rightarrow 4\ell$.

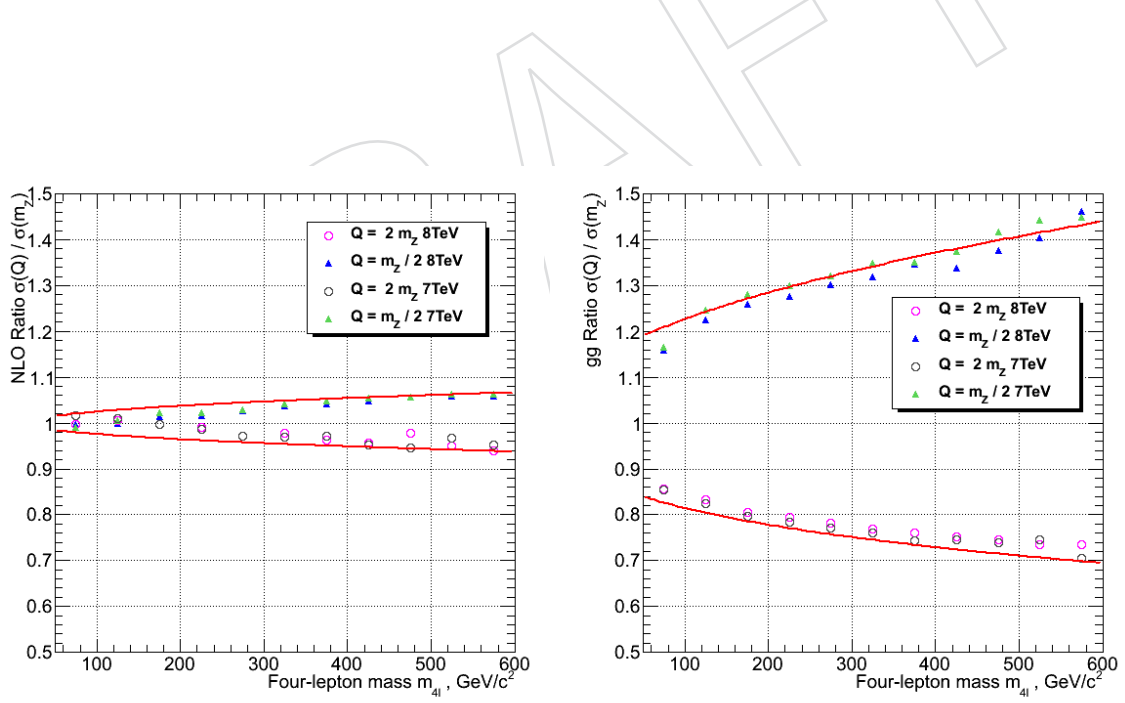


Figure 67: QCD scale uncertainties for (left) $pp \rightarrow ZZ \rightarrow 4\ell$ at NLO and (right) $gg \rightarrow ZZ \rightarrow 4\ell$ processes. The points are evaluated uncertainties. The curves are the fit systematic error $\kappa(m_{4\ell})$ to be used in the statistical analysis. These errors are driven by two independent nuisance parameters $QCDscale_VV$ for $pp \rightarrow ZZ \rightarrow 4\ell$ at NLO and $QCDscale_ggVV$ for $gg \rightarrow ZZ \rightarrow 4\ell$.

1504 **9.3.2 Instrumental uncertainties**1505 **9.3.3 ZZ^(*) results**

1506 The number of events and relative uncertainties from $ZZ^{(*)} \rightarrow 4\ell$ estimated from Monte Carlo simu-
 1507 lation (see section 9.1) for an integrated luminosity of 5.05 fb^{-1} (resp. 2.97 fb^{-1}) of 7 TeV (resp. 8 TeV)
 1508 data in the signal region in the full mass range and in the un-blinded region, with the baseline and high-
 1509 mass selections are shown in Table 14 and 15 for the $q\bar{q}$ annihilation and and for the gluon-gluon fusion
 1510 separately.

Table 14: Number of ZZ background events and relative uncertainties in the signal region estimated from Monte Carlo simulation, for the baseline and high-mass event selections and for the full mass range and the un-blinded region. For details on the errors see Section ???. Results are for the 7 TeV analysis.

baseline		
	channel	Full mass range
$q\bar{q}$	$N^{ZZ \rightarrow 4e}$	14.4 ± 1.2
	$N^{ZZ \rightarrow 4\mu}$	21.9 ± 1.8
	$N^{ZZ \rightarrow 2e2\mu}$	34.7 ± 2.9
gg	$N^{ZZ \rightarrow 4e}$	0.93 ± 0.41
	$N^{ZZ \rightarrow 4\mu}$	1.3 ± 0.56
	$N^{ZZ \rightarrow 2e2\mu}$	2.22 ± 0.96

high-mass		
	channel	Full mass range
$q\bar{q}$	$N^{ZZ \rightarrow 4e}$	11.94 ± 0.92
	$N^{ZZ \rightarrow 4\mu}$	17.08 ± 1.43
	$N^{ZZ \rightarrow 2e2\mu}$	29.06 ± 2.3
gg	$N^{ZZ \rightarrow 4e}$	0.85 ± 0.26
	$N^{ZZ \rightarrow 4\mu}$	1.18 ± 0.37
	$N^{ZZ \rightarrow 2e2\mu}$	2.07 ± 0.63

Table 15: Number of ZZ background events and relative uncertainties in the signal region estimated from Monte Carlo simulation, for the baseline and high-mass event selections and for the full mass range and the un-blinded region. For details on the errors see Section ???. Results are for the 8 TeV analysis.

baseline		
	channel	Full mass range
$q\bar{q}$	$N^{ZZ \rightarrow 4e}$	10.91 ± 0.92
	$N^{ZZ \rightarrow 4\mu}$	17.03 ± 1.43
	$N^{ZZ \rightarrow 2e2\mu}$	27.53 ± 2.3
gg	$N^{ZZ \rightarrow 4e}$	0.9 ± 0.39
	$N^{ZZ \rightarrow 4\mu}$	1.52 ± 0.66
	$N^{ZZ \rightarrow 2e2\mu}$	2.55 ± 1.11
high-mass		
	channel	Full mass range
$q\bar{q}$	$N^{ZZ \rightarrow 4e}$	7.22 ± 1.0
	$N^{ZZ \rightarrow 4\mu}$	10.69 ± 1.4
	$N^{ZZ \rightarrow 2e2\mu}$	17.5 ± 2.3
gg	$N^{ZZ \rightarrow 4e}$	0.64 ± 0.22
	$N^{ZZ \rightarrow 4\mu}$	0.89 ± 0.30
	$N^{ZZ \rightarrow 2e2\mu}$	1.56 ± 0.52

1511 10 Irreducible Z+DY double parton interaction background

1512 Production of $Z \rightarrow \ell\ell$ and $DY \rightarrow \ell\ell$ in double parton interaction (DPI), i.e. simultaneous scattering of
 1513 two pairs of partons within one collision of two protons, leads to an emergence of four prompt leptons
 1514 and constitutes an irreducible background for $H \rightarrow ZZ \rightarrow 4\ell$ search. In this section we estimate the
 1515 contribution of this background using generator-level studies.

1516 The Z+DY DPI cross section $\sigma_{Z+DY}^{\text{DPI}}$ can be evaluated via the following phenomenological relationship:

$$\sigma_{Z+DY}^{\text{DPI}} = \frac{\sigma_Z \cdot \sigma_{\text{DY}}}{\sigma_{\text{eff}}}, \quad (25)$$

1517 where σ_{eff} is a so-called effective cross section. Its value in 7-TeV pp collisions at LHC is 11^{+3}_{-2} mb, as
 1518 recently measured by ATLAS [91], and is consistent with the measurements at Tevatron and by UA2. The
 1519 two DPI sub-processes have approximately independent kinematics; hence, the acceptance of kinematic
 1520 cuts selecting two pairs of leptons is expected to factorize, namely:

$$\mathcal{A}_{Z+DY}^{\text{DPI}} = \mathcal{A}_Z \times \mathcal{A}_{\text{DY}} \quad (26)$$

1521 The top two rows of Table ?? show cross sections and acceptances for $Z \rightarrow \mu\mu$ ($m_{\mu\mu} > 40$ GeV) and
 1522 $DY \rightarrow \mu\mu$ ($m_{\mu\mu} > 12$ GeV) as calculated with Pythia and MCFM at LO. One can see that the MCFM
 1523 DY cross section is 70% higher than what we get using Pythia. Figure 68 (left) shows that the origin
 1524 of the discrepancy is the low mass range. The kinematic acceptances ($p_T > 5$ GeV, $|\eta| < 2.4$ for both
 1525 muons) agree between the two generators ⁵. In the following estimates, we choose to use Pythia cross
 1526 sections with understanding that the systematic error on the estimated $Z + DY \rightarrow 4\mu$ cross section can
 1527 be as large as a factor of two.

1528 The third row in the table shows predicted DPI Z+DY cross sections and four-muon kinematic accep-
 1529 tance, using Eqs. 25 and 26. The last row shows results of a direct simulation of $Z + DY \rightarrow 4\mu$ in Pythia.

1530 One can see that Pythia reproduces the factorisation of acceptances, but gives too small cross section in
 1531 comparison to what one expects according to Eq. 25. ATLAS notes that Pythia does not reproduce by a
 1532 large factor the DPI cross section for W+2jets process [91]. Therefore, in the following estimates we use
 1533 the larger cross section 0.27 fb as obtained from Eq. 25.

1534 The total number of 4μ events within acceptance at $\mathcal{L}=5 \text{ fb}^{-1}$ is, therefore, $(0.27 \text{ fb}) \times 0.16 \times (5 \text{ fb}^{-1}) =$
 1535 0.22. The four-lepton mass distribution for simulated $Z + DY \rightarrow 4\mu$ is shown in Fig. 68 (right). One can
 1536 see that about half of the events contribute to the high mass range (where we expect about 20 $ZZ \rightarrow 4\mu$
 1537 events (Sec. 13) with more than 5% uncertainties. The other half, about 0.1 events, contribute in the low
 1538 mass range, where we expect about $1.2^{+0.6}_{-0.7} 4\mu$ events from reducible backgrounds (Sec. 11). Therefore,
 1539 the expected rate of $Z + DY$ events in all mass ranges, even having large theoretical uncertainties, is well
 1540 covered by the systematic errors associated with irreducible $ZZ \rightarrow 4\ell$ and reducible backgrounds.

Table 16: Cross sections and acceptances for $Z \rightarrow \mu\mu$, $DY \rightarrow \mu\mu$, and $Z + DY \rightarrow 4\mu$ processes
 in pp collisions at $\sqrt{s} = 8$ TeV.

Process	Cross section Pythia (MCFM)	Kinematic acceptance Pythia (MCFM)
Simulated $Z \rightarrow \mu\mu$ ($m_{\mu\mu} > 40$ GeV)	1.03 nb (1.04 nb)	0.47 (0.50)
Simulated $DY \rightarrow \mu\mu$ ($m_{\mu\mu} > 12$ GeV)	2.91 nb (5.09 nb)	0.34 (0.33)
Predicted $Z + DY \rightarrow 4\mu$ using Eqs. 25 and 26	0.27 fb (0.48 fb)	0.16 (0.17)
Simulated $Z + DY \rightarrow 4\mu$	0.07 fb	0.18

⁵ It is worthwhile mentioning that when the mass cut is relaxed to $m_{\mu\mu} > 5$ GeV, the MCFM:Pythia cross section difference becomes more than a factor of three (54 vs 16 fb), while acceptances differ as 0.04:0.08.

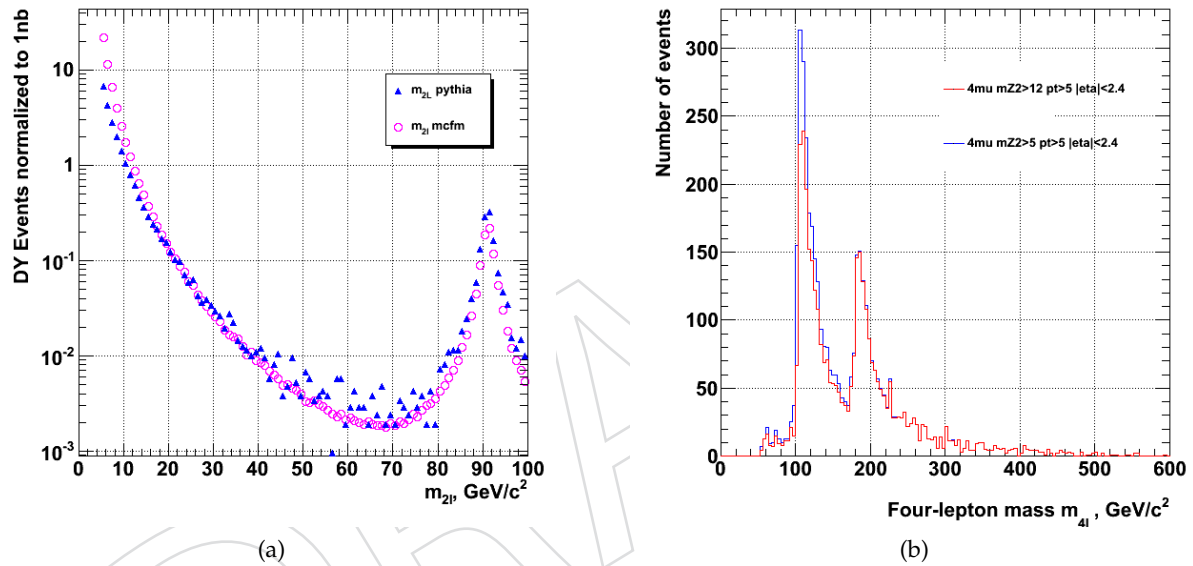


Figure 68: (Left) Generator-level $DY \rightarrow \mu\mu$ differential cross section $d\sigma/dm_{\mu\mu}$ (no muon acceptance cuts applied). (Right) Generator-level four-lepton mass distribution for $Z + DY \rightarrow 4\mu$ events with muon acceptance cuts. Centre of mass energy for both plots is 8 TeV.

1541 11 Reducible Background Model and Systematic Uncertainties

1542 11.1 Reducible background prediction

1543 The reducible backgrounds for the $H \rightarrow ZZ \rightarrow 4\ell$ analysis are processes which contain one or more non-
 1544 prompt leptons in the four-lepton final state. The main sources of non-prompt leptons are non-isolated
 1545 electrons and muons coming from decays of heavy-flavour mesons, mis-reconstructed jets (usually orig-
 1546 inating from light-flavour quarks) and electrons from γ conversions. In the further discussion, we will
 1547 consider “fake lepton” any jet mis-reconstructed as a lepton and any lepton originating from a heavy
 1548 meson decay. In a similar way, any electron originating from a photon conversion will be considered
 1549 “fake electron”.

1550 In the $H \rightarrow ZZ \rightarrow 4\ell$ analysis the rate of these backgrounds processes is estimated by measuring the
 1551 probability for fake electrons f_e and fake muons f_μ which do pass predefined loose selection criteria
 1552 to also pass the final selection criteria. These probabilities are applied in dedicated control samples in
 1553 order to extract the background yield expected in the signal region. We will refer to these probabilities
 1554 as fake ratios. The loose lepton selection criteria are defined in Table 17 and Table 18 and are obtained
 1555 from the final lepton selection criteria by relaxing the identification and isolation criteria. In order to
 1556 fight the “ghost” and “split-track” muons, we require that muons are reconstructed either as global or
 1557 as tracker muons with arbitration, and that no two muons are within the dR cone of 0.02.

Table 17: Definition of loose selection criteria for muon-like objects used for the measurement of muon fake ratio.

#	Parameter	Selection
1	Algorithm	Global OR Tracker (with arbitration)
2	“duplicate” μ cleaning cone ΔR	0.02
3	$ SIP3D $	< 4
4	p_T	$\geq 5 \text{ GeV}/c$
5	$ \eta $	≤ 2.4

Table 18: Definition of loose selection criteria for electron-like objects used for the measurement of electron fake ratio.

#	Parameter	Selection
1	Algorithm	GSF Electrons
2	e/μ cross object cleaning cone ΔR	0.05
3	Missed inner pixel hits	≤ 1
4	$ SIP3D $	< 4
5	p_T	$\geq 7 \text{ GeV}/c$
6	$ \eta $	≤ 2.5

1558 11.1.1 Tight-to-loose ratios in Z+1L

1559 In order to measure the lepton fake ratios f_e, f_μ , we select samples of $Z(\ell\ell) + e$ and $Z(\ell\ell) + \mu$ events
 1560 that are expected to be completely dominated by final states which include a Z boson and a fake lepton.
 1561 These events are required to have two same flavour, opposite charge leptons with $p_T > 20/10 \text{ GeV}$
 1562 passing the tight selection criteria, thus forming the Z candidate. In addition, there is exactly one lepton
 1563 passing the loose selection criteria as defined above. This lepton is used as the probe lepton for the
 1564 fake ratio measurement. The invariant mass of this lepton and the opposite sign lepton from the re-
 1565 constructed Z candidate should satisfy $m_{2l} > 4 \text{ GeV}$. Each event is required to have missing transverse
 1566 energy $E_T^{\text{miss}} < 25 \text{ GeV}$ to suppress contamination due to prompt leptons from WZ and $t\bar{t}$ processes.

1567 Figure 69 shows distributions of the invariant mass of two leptons selected as the ones originating from
 1568 the Z decay: in case of all loose leptons (top) and in case of loose leptons that pass the tight selection
 1569 criteria. The distributions for tight leptons show the presence of (asymmetric) conversion of photons that
 1570 end up with one electron being reconstructed. Figure 70 shows dependance of the electron and muon
 1571 fake ratios on $M_{\text{inv}}(\ell_1, \ell_2)$. In case of the electrons, the increase in fake ratio for $M_{\text{inv}}(\ell_1, \ell_2) < 80 \text{ GeV}$
 1572 can be attributed to photon conversions. With this in mind, there are two complementary approaches
 1573 that are considered while evaluating and applying the fake ratios. In one approach (used in Method A
 1574 described below) the fake ratios are evaluated using a tight requirement of $|M_{\text{inv}}(\ell_1, \ell_2) - M_Z| < 10$

1575 GeV to reduce the bias from photon conversions in the fake ratios. This approach allows measurement
 1576 of the tight-to-loose ratios for the “true” fake leptons. In the second approach (used in Method AA
 1577 described below) the tight-to-loose ratios are measured by using a relaxed invariant mass requirement
 1578 of $40 \text{ GeV} < M_{inv}(\ell_1, \ell_2) < 120 \text{ GeV}$ which is consistent with the dilepton invariant mass requirement
 1579 in the Higgs selection. This is done to have a background composition in the fake rate sample which is
 1580 similar to the expected reducible background composition in the signal region.

1581 The measured differential p_T distributions of the fake ratios using the tight Z mass requirement of
 1582 $|M_{inv}(\ell_1, \ell_2) - M_Z| < 10 \text{ GeV}$ are shown in Figure 71. Figure 72 shows the fake ratios as a func-
 1583 tion of p_T on relaxing the Z mass requirement to $40 \text{ GeV} < M_{inv}(\ell_1, \ell_2) < 120 \text{ GeV}$. It can be observed
 1584 that the fake ratios show dependance on the lepton p_T - in particular, the fake ratios increase in the
 1585 region of high p_T . This effect is in part caused by the fact that the criteria used to suppress the WZ and
 1586 $t\bar{t}$ processes are not efficient in this region of p_T .

1587 The dependance of the fake ratios on the exact composition of background processes in a region of
 1588 interest is one of the main sources of the systematic uncertainties of the method. The procedures to
 1589 estimate these systematic effects in data and simulation will be discussed in the section 11.2.

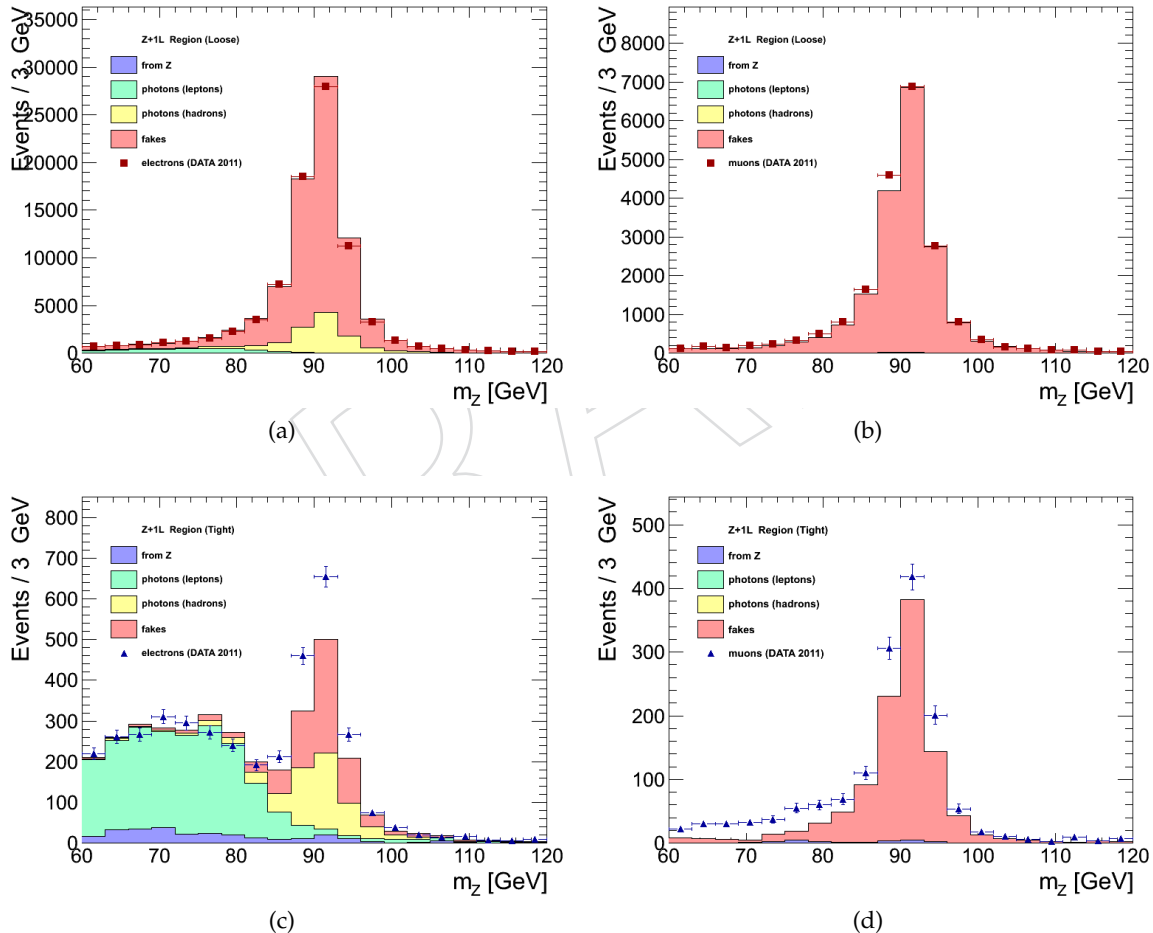


Figure 69: Distribution of the invariant mass of two leptons selected as the ones originating from the Z decay. Distributions are shown for the $Z(\ell\ell) + e$ (left) and $Z(\ell\ell) + \mu$ (right) samples, as defined in the text. The top row corresponds to all the events in these samples, while bottom row shows distributions for events when the loose lepton passes the tight selection criteria.

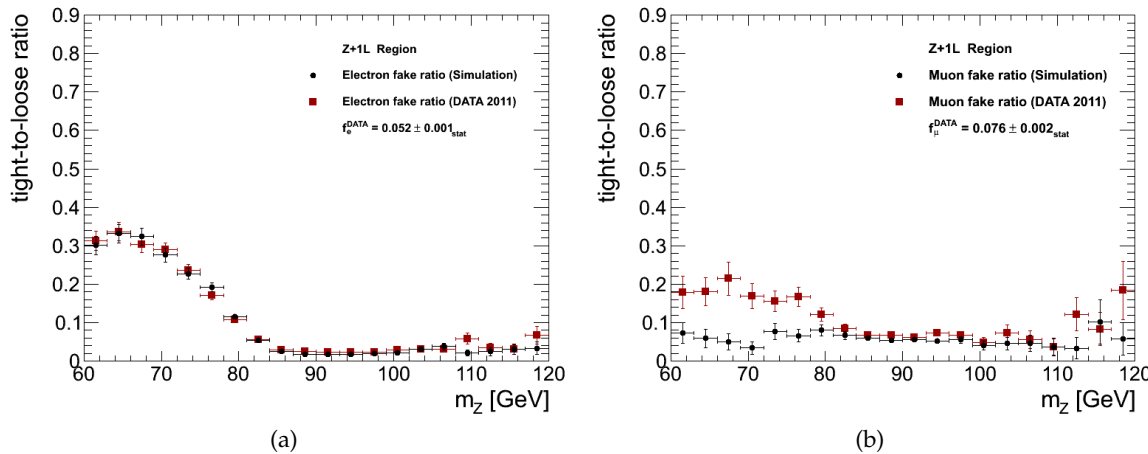


Figure 70: Fake rate measured for a probe lepton which satisfy loose selection, in $Z(\ell\ell) + e$ (left) and $Z(\ell\ell) + \mu$ (right) samples. Plots display the fake ratios before cut on $|M_{inv}(\ell_1, \ell_2)|$ is applied. Distributions of $|M_{inv}(\ell_1, \ell_2)|$ show dependence of the fake ratios in the region below 80 GeV.

11.1.2 Control regions and extrapolation

11.1.2.1 Method A

11.1.2.1 Method A Two control samples are obtained as subsets of four lepton events which pass the “Higgs candidate” selection step, as described in previous sections. First control sample is obtained by requiring two leptons not to pass the final identification and isolation criteria, but to pass the loose lepton requirements as defined in Table 17 and Table 18. The other two leptons should pass the final selection criteria. This sample is denoted as “2 Prompt + 2 Fail” (2P+2F) sample. It is expected to be populated with events that intrinsically have only two prompt leptons (e.g. $DY, t\bar{t}$). Second control sample is obtained by requiring one of the four leptons not to pass the final identification and isolation criteria, but to pass the loose lepton requirements. The other three leptons should pass the final selection criteria. This control sample is denoted as “3 Prompt + 1 Fail” (3P+1F) sample. It is expected to be populated with the type of events that populate the 2P+2F region, as well as with the events that intrinsically have three prompt leptons (e.g. $WZ, Z\gamma^*$).

The control samples obtained in this way are expected to be enriched with the fake leptons and are used to estimate the rate of the reducible background events in the signal region.

The invariant mass distribution of events in the control region 2P+2F is shown for data in Figures 73 and 74. The distributions are shown for $4e$ (a), 4μ (b), $2e2\mu$ (c) and cumulative 4ℓ final states separately. The shape of the observed mass distributions is fitted using the Landau function in a form $n_0 \text{Landau}(\mu, c)$, normalized to the event yield. The fitting is performed for each of the $4e$, $2e2\mu$, 4ℓ channels separately. Due to the limited statistical accuracy in the 4μ final state, the fitting in this channel is performed with the $2e2\mu$ shape and then normalized to the event yield. For the same reasons, the results are shown in Table 19.

Table 19: Mass shape fit parameters. Fitting of the invariant mass is performed in the control region with the $n_0 Landau(\mu, c)$ function. Due to the limited statistical accuracy, the fitting is performed for each of the $4e$, $2e2\mu$, 4ℓ channels separately. In case of the 4μ final state, the fitting is performed with the $2e2\mu$ shape and normalized to the event yield. The parameters are shown for the fitting function normalized to unity.

Parameter	norm. n_0	shift μ	scale c
$4e$, data, 7 TeV	0.0587	140.3	17.9
$2e2\mu$, data, 7 TeV	0.0818	132.8	12.6
$4e$, data, 8 TeV	0.0537	144.3	19.7
$2e2\mu$, data, 8 TeV	0.0677	140.8	15.5

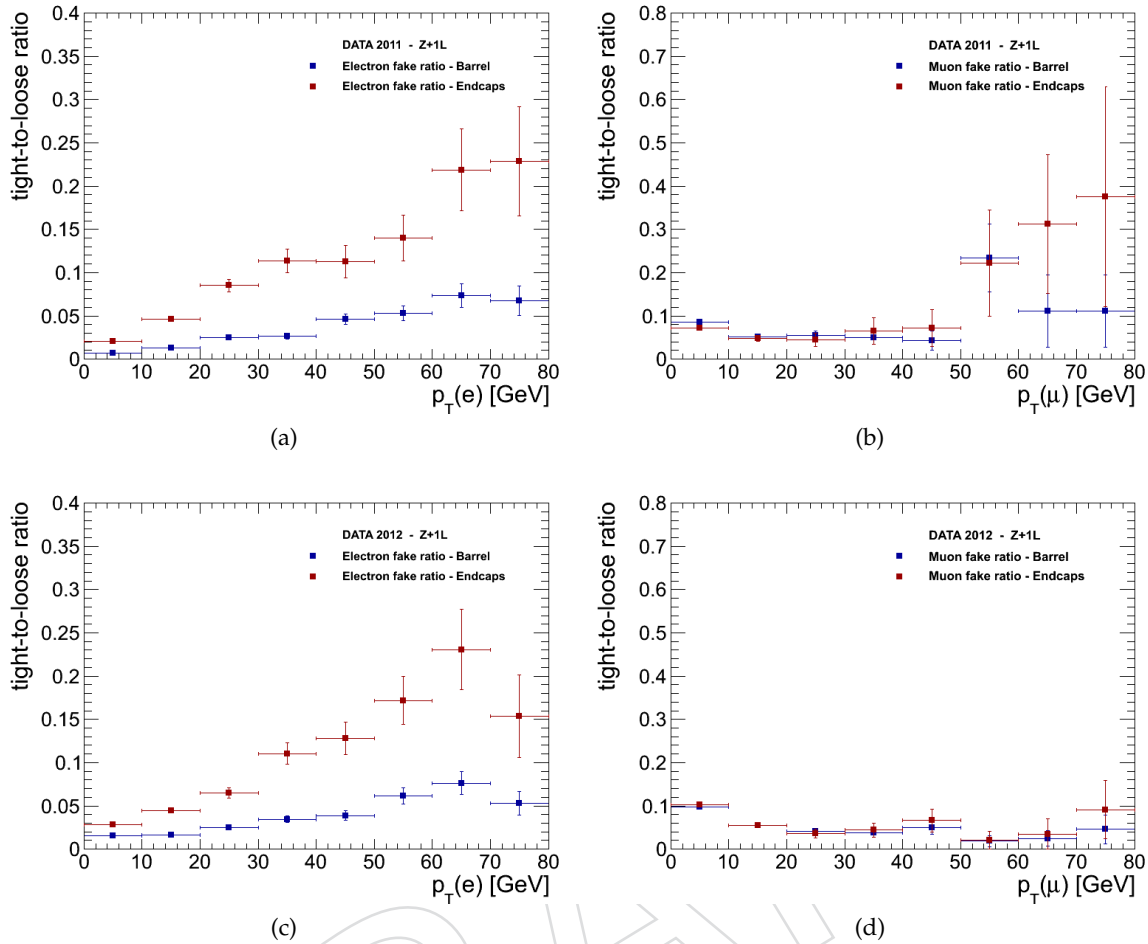


Figure 71: Fake rate measured for a probe lepton which satisfy loose selection, in the $Z(\ell\ell) + e$ (left) and $Z(\ell\ell) + \mu$ (right) samples as defined in the text. Plots show fake ratios measured in data. The distributions at the top correspond to the 7 TeV data, while distributions at the bottom correspond to the 8 TeV data.

1611 The invariant mass distribution of events in the control region 3P+1F is shown for data in Figure 75.
 1612 The distributions are again shown for 4e (a), 4 μ (b), 2e2 μ (c) and cumulative 4 ℓ final states separately.
 1613 The expected number of reducible background events in the 3P+1F region N_{3P1F}^{bkg} can be computed from
 1614 the number of events observed in the 2P+2F control region N_{2P2F} by weighting each of the events in
 1615 the region with the factor $(\frac{f_i}{1-f_i} + \frac{f_j}{1-f_j})$, where f_i and f_j correspond to the fake ratios of the two loose
 1616 leptons in the event:

$$N_{3P1F}^{bkg} = \sum \left(\frac{f_i}{1-f_i} + \frac{f_j}{1-f_j} \right) N_{2P2F} \quad (27)$$

1617 Figure 75 shows distribution of the expected number of reducible background events in this region
 1618 stacked on the distribution of irreducible backgrounds taken from simulation ($ZZ \rightarrow 4\ell$). The difference
 1619 in the distributions of the observed number of events and the expected contribution form the 2P+2P
 1620 region is an indication of the presence of processes with three prompt leptons in this region. It also in
 1621 an agreement with the observation discussed in Figure 69.

1622 The expected contribution of reducible background processes with two fake leptons in the signal region

1623 can be computed from the number of events observed in the 2P+2F control region $N_{2\text{P}2\text{F}}$ by weighting
 1624 each of the events in that region with the factor $\frac{f_i}{1-f_i} \frac{f_j}{1-f_j}$, where f_i and f_j correspond to the fake ratios of
 1625 the two loose leptons. Similarly, the expected contribution of reducible background processes with one
 1626 fake leptons in the signal region can be computed from the difference between the number of observed
 1627 events in the 3P+1F control region $N_{3\text{P}1\text{F}}$ and the expected contribution from the 2P+2F region and ZZ
 1628 processes in the signal region $N_{3\text{P}1\text{F}}^{\text{ZZ}} + N_{3\text{P}1\text{F}}^{\text{bkg}}$. The $N_{3\text{P}1\text{F}}^{\text{bkg}}$ is given by the equation 27 and $N_{3\text{P}1\text{F}}^{\text{ZZ}}$ is the
 1629 contribution from ZZ which is taken from simulation. Therefore, the full expression for the prediction
 1630 can be symbolically written as:

$$N_{\text{SR}}^{\text{bkg}} = \sum \frac{f_i}{(1-f_i)} (N_{3\text{P}1\text{F}} - N_{3\text{P}1\text{F}}^{\text{bkg}} - N_{3\text{P}1\text{F}}^{\text{ZZ}}) + \sum \frac{f_i}{(1-f_i)} \frac{f_j}{(1-f_j)} N_{2\text{P}2\text{F}} \quad (28)$$

1631 The table 20 shows the expected number of events in the signal regions from the reducible background
 1632 processes, both for the 7 TeV and 8 TeV data. Only statistical uncertainties are quoted in the table.
 1633 Systematic uncertainties on these predictions and a procedure to estimate them from measurements in
 1634 data will be discussed in the following chapters.

Table 20: The contribution of reducible background processes in the signal region predicted from measurements in data using the Method A. The quoted predictions correspond to the 5.05fb^{-1} of 7 TeV data and the 5.26fb^{-1} of 8 TeV data.

baseline	4e	4μ	$2e2\mu$
7 TeV	$1.2 \pm 0.0_{\text{stat.}}$	$1.1 \pm 0.1_{\text{stat.}}$	$2.4 \pm 0.1_{\text{stat.}}$
8 TeV	$0.9 \pm 0.1_{\text{stat.}}$	$0.9 \pm 0.1_{\text{stat.}}$	$1.6 \pm 0.1_{\text{stat.}}$
high-mass	4e	4μ	$2e2\mu$
8 TeV	$0.4 \pm 0.1_{\text{stat.}}$	$0.4 \pm 0.1_{\text{stat.}}$	$0.4 \pm 0.0_{\text{stat.}}$

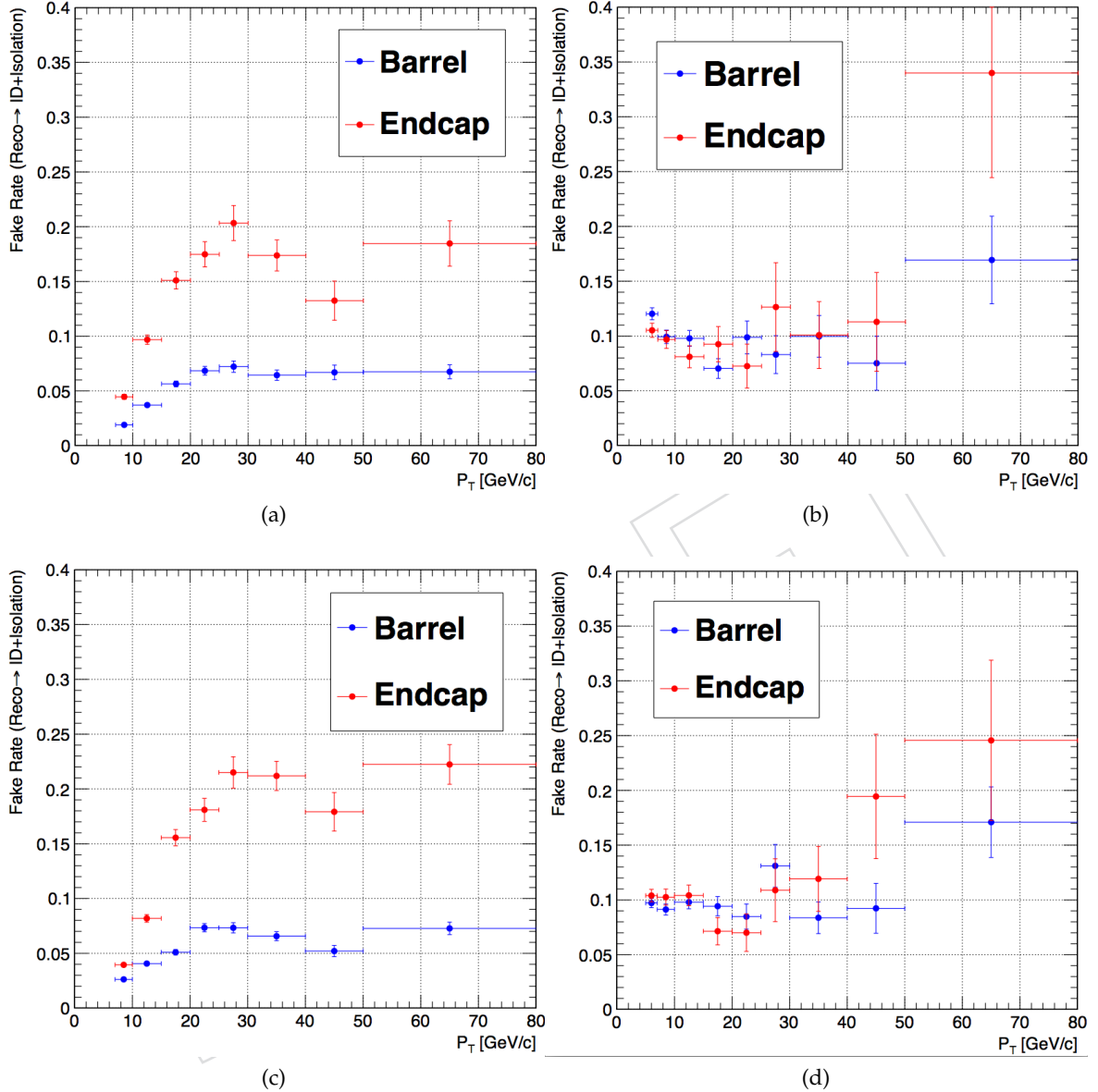


Figure 72: Fake rate measured for a probe lepton which satisfy loose selection, in the $Z(\ell\ell) + e$ (left) and $Z(\ell\ell) + \mu$ (right) samples as defined in the text. The sample of Z events is selected using the same selection criteria for the dilepton invariant mass as in the Higgs selection (see section 7): $40 \text{ GeV} < |M_{inv}(\ell_1, \ell_2)| < 120 \text{ GeV}$. Plots show fake ratios measured in 7 TeV data (top) and 8 TeV data (bottom).

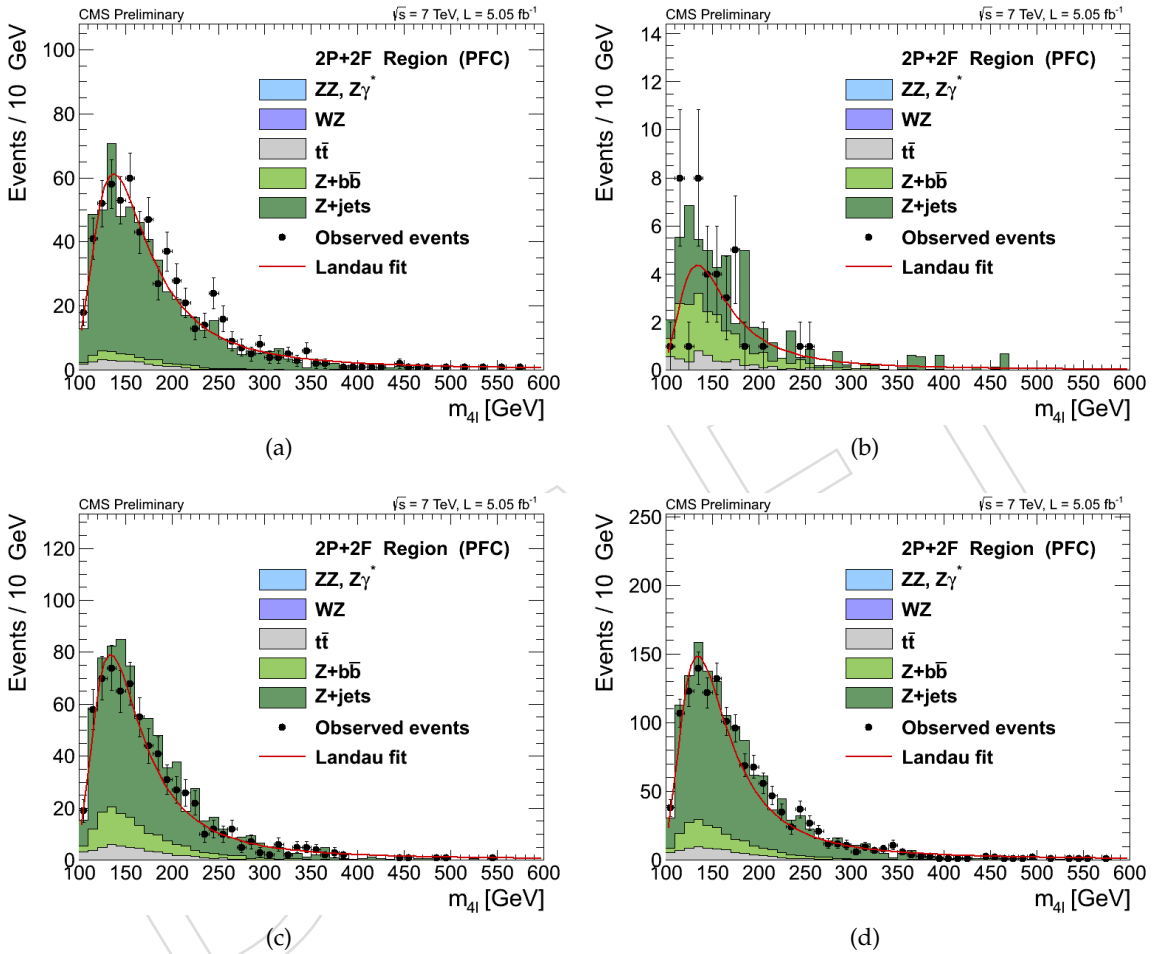


Figure 73: Invariant mass distribution of events in the control region 2P+2F for $4e$ (a), 4μ (b), $2e2\mu$ (c), and cumulative 4ℓ final states. The distributions are fitted with the Landau function. The distributions correspond to 5.05fb^{-1} of 7 TeV data.

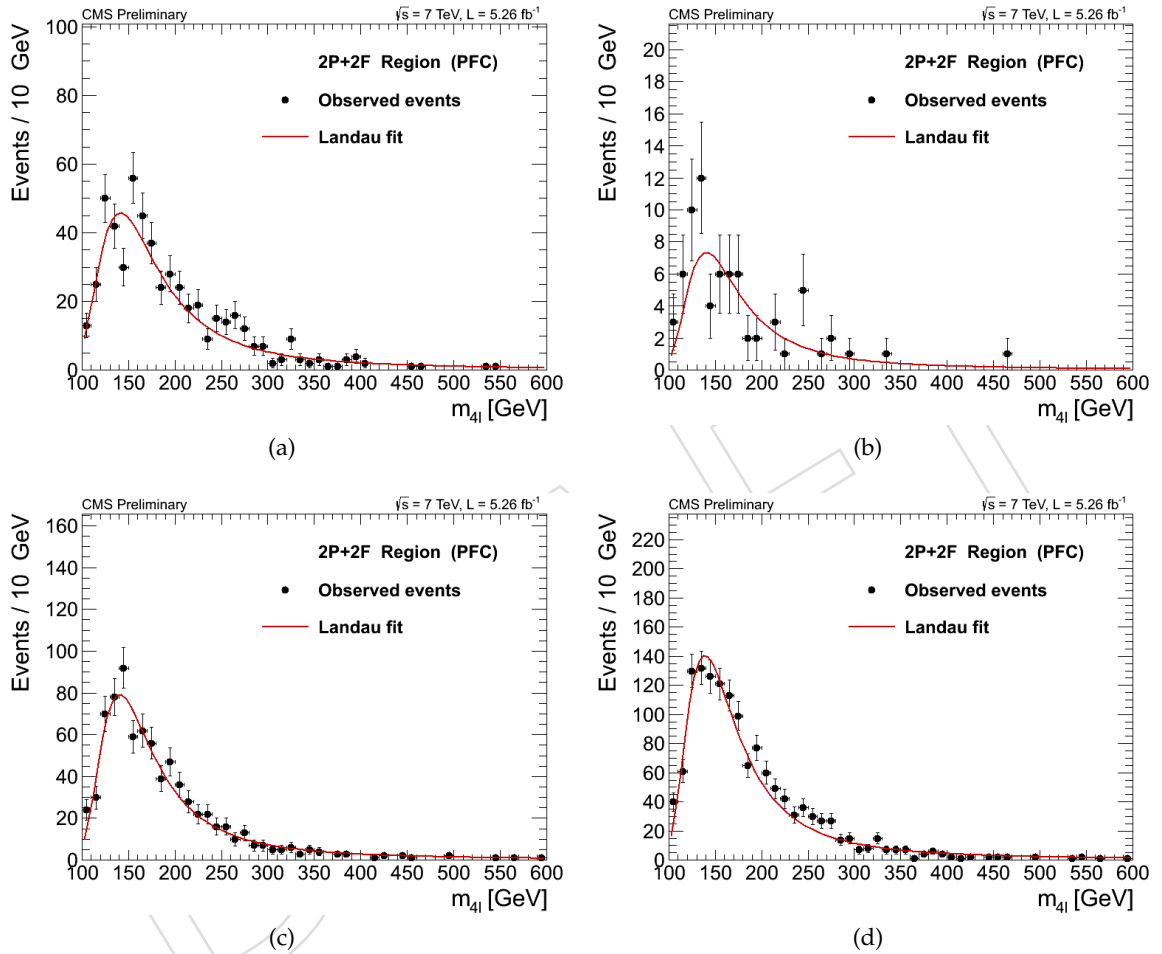


Figure 74: Invariant mass distribution of events in the control region 2P+2F for $4e$ (a), 4μ (b), $2e2\mu$ (c), and cumulative 4ℓ final states. The distributions are fitted with the Landau function. The distributions correspond to 5.26 fb^{-1} of 8 TeV data.

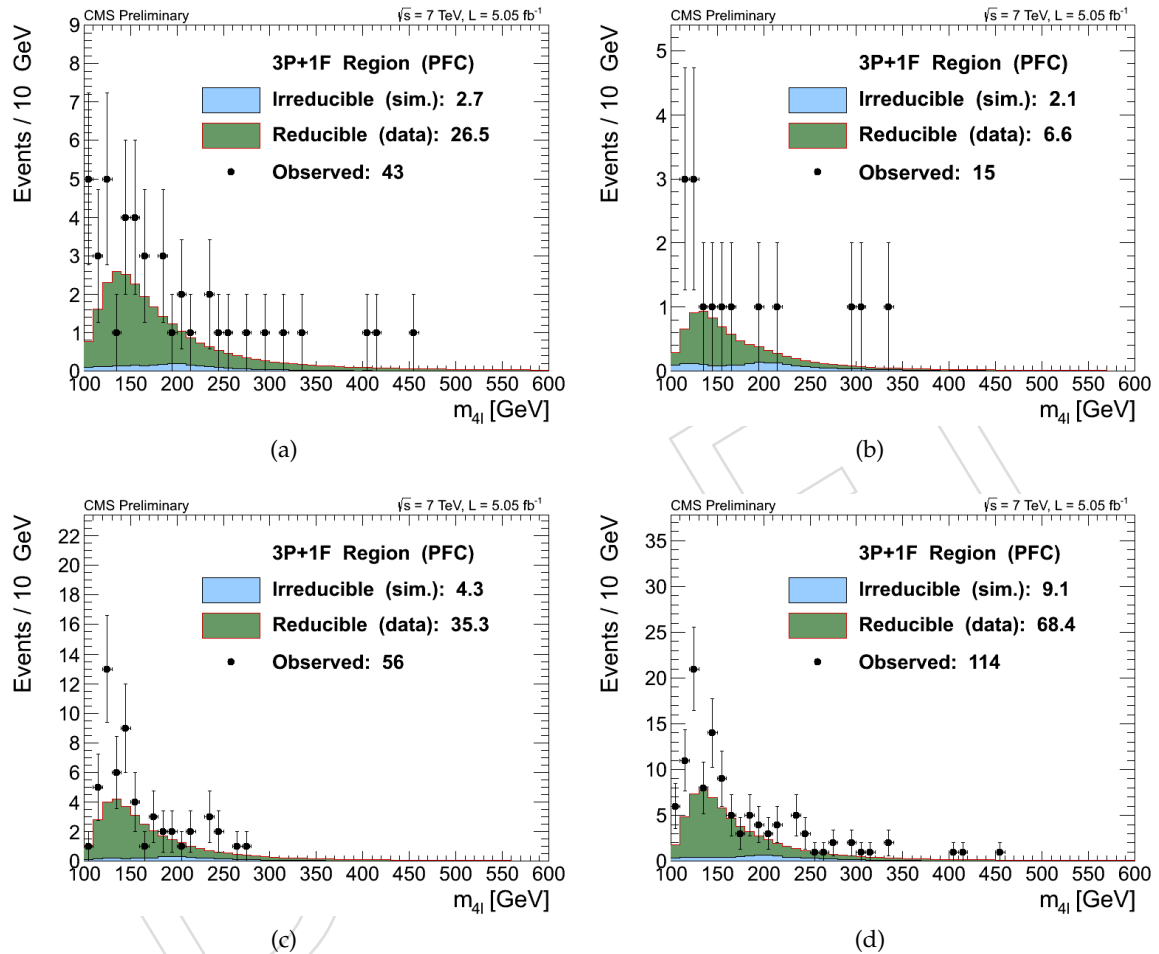


Figure 75: Invariant mass distribution of events in the control region 3P+1F for $4e$ (a), 4μ (b), $2e2\mu$ (c), and cumulative 4ℓ final states. The distribution of the estimated contribution from the reducible background events in this region is stacked on the distribution of irreducible backgrounds taken from simulation (e.g. $ZZ \rightarrow 4\ell$).

1635 **11.1.2.2 Method AA** The second method used to control the reducible background allows to
1636 have an inclusive measurement of the all the main reducible backgrounds at the same time.

1637 The control sample is obtained as subsets of the events that satisfy the first step of the selection (*First Z*
1638 step, see section 7), requiring an additional pair of *loose leptons* of same sign (to avoid signal contamination)
1639 and same flavour (SS-SF: $e^\pm e^\pm, \mu^\pm \mu^\pm$). The SS-SF leptons are requested to pass SIP_{3D} cut while no
1640 identification or isolation requirements are imposed. The reconstructed invariant mass of the SS-SF lepto-
1641 nts has to satisfy the baseline or the high-mass selections and the reconstructed four-lepton invariant
1642 mass is required to satisfy $m_{4\ell} > 100$ GeV/ c^2 . From this set of events the inclusive number of reducible
1643 background in the signal region is obtained taking into account the probability for the two additional
1644 leptons to pass the isolation and identification analysis cuts obtained from a fake rate measurement.

1645 **Extraction to the signal region**

Starting from the control sample previously described, the final reducible background prediction in the signal region is given by the following expression:

$$N_{\text{expect}}^{Z+X} = N^{\text{DATA}} \times (\frac{\text{OS}}{\text{SS}})^{\text{MC}} \times \epsilon_1(p_T, \eta) \times \epsilon_2(p_T, \eta) \quad (29)$$

1646 where:

- 1647 • N^{DATA} is the number of events in the control region,
- 1648 • $(\frac{\text{OS}}{\text{SS}})^{\text{MC}}$ is a correction factor between opposite sign and same sign control samples,
- 1649 • $\epsilon_i(p_T, \eta)$ is the fake rate probability for each of additional pair of *loose leptons* ($i = 1, 2$) in
1650 function of p_T and η .

DRAFT

1651 **SS vs OS**

1652 Figures 76 and 77 are showing the comparison between data and MC of samples selected with SS-SF
 1653 and OS-SF samples for all three channels for both 7 and 8 TeV data. A reasonable agreement is achieved
 1654 between data and MC for the 7 TeV. For 8 TeV, the lack of MC statistics prevents to draw any meaningful
 1655 conclusions. The differences in rates (taken from MC, with ZZ contribution subtracted) between OS and
 1656 SS samples are used to compute the correction factor in equation 29 for the final data-driven estimation.
 1657 They are estimated as 0.93(1.28,0.94) for the $4e(4\mu, 2e2\mu)$ final states with 7 TeV samples. Due to lack of
 1658 statistics for the 8 TeV MonteCarlo samples, the same factors are applied to the 8 TeV analysis.

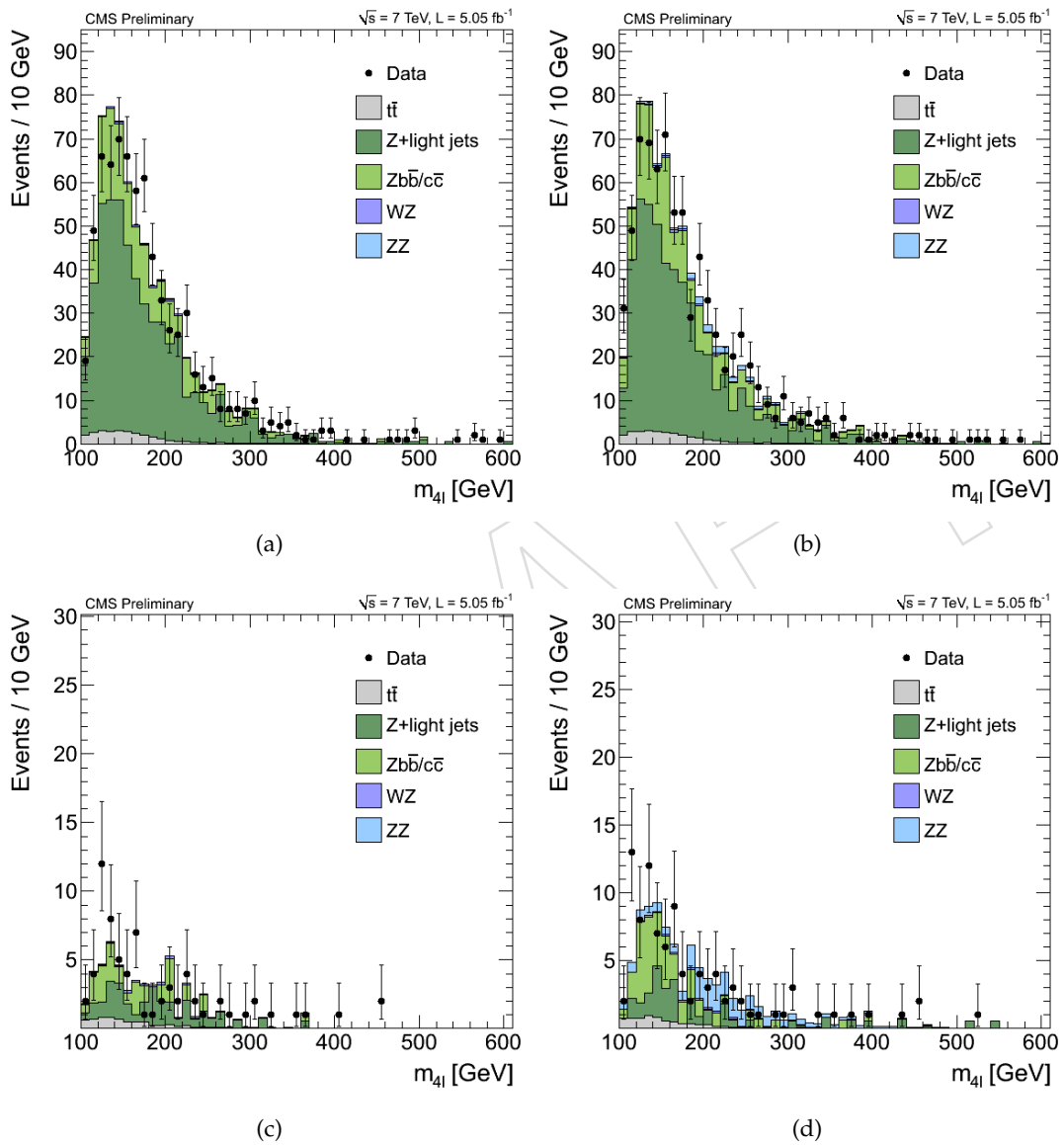


Figure 76: DATA-MC comparison of the SS-SF (on the left) and OS-SF (on the right) samples in the $Z+X$ background control samples. (a) and (b) $4e$, (c) and (d) 4μ . The distributions correspond to 5.05 fb^{-1} of 7 TeV data.

1659 **Cross checks**

1660 A full MC closure test was performed. Unfortunately, due to lack of statistics in MC samples after, only
 1661 the $2e2\mu$ channel was tested. Fake rate was computed and parameterized using MC samples, the same
 1662 way as in the DATA. Estimated reducible background extracted using formula 29 were compared to the

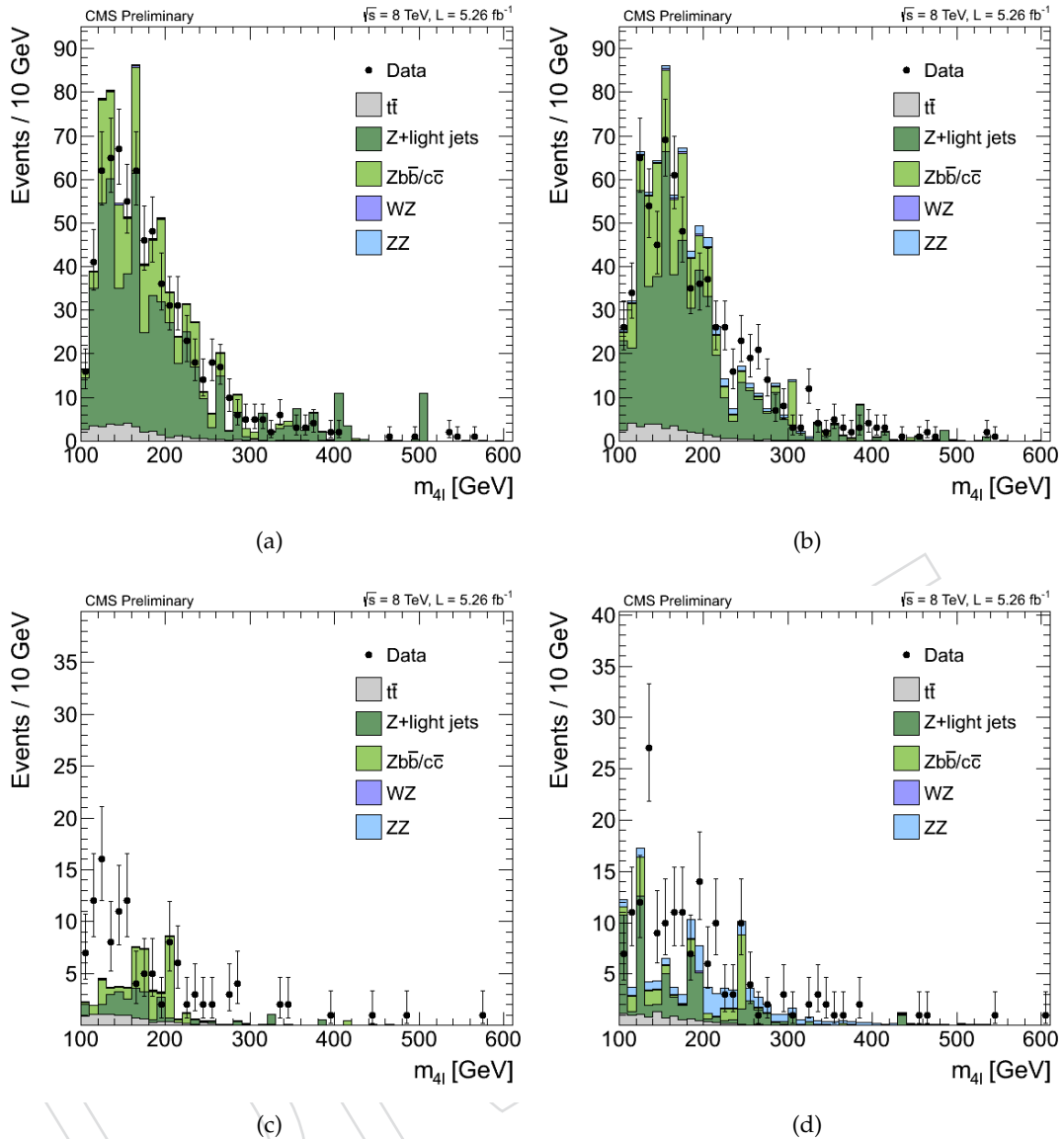


Figure 77: DATA-MC comparison of the SS-SF (on the left) and OS-SF (on the right) samples in the $Z+X$ background control samples. (a) and (b) $4e$, (c) and (d) 4μ . The distributions correspond to 5.26 fb^{-1} of 8 TeV data.

1663 rates estimated applying the full selection on MC samples. The two methods agree fairly, given the large
 1664 statistical errors.

1665 Results on DATA

1666 With the 5.05 fb^{-1} of collected integrated luminosity at 7 TeV and 5.23 fb^{-1} at 8 TeV , the number of
 1667 events from $Z+X$ expected and the relative systematics and statistical errors in the signal region in a
 1668 mass range from $m_1 = 100 \text{ GeV}/c^2$ to $m_2 = 600 \text{ GeV}/c^2$ for the baseline, and high-mass selections are
 1669 listed in table 21 and 22. The statistical error quoted represents the number of events in the control
 1670 region, while the systematics one is extracting varying the fake rates by ± 1 sigma and inflated by 10%
 1671 according to the WZ underestimation.

Table 21: The number of events from $Z+X$ expected and the relative systematics and statistical errors in the signal region in a mass range from $m_1 = 100 \text{ GeV}/c^2$ to $m_2 = 600 \text{ GeV}/c^2$, for baseline analysis and for 7 TeV data.

	baseline (full range)
$N^{Z+X \rightarrow 4e}$	$2.0 \pm 0.1 \text{ (5.0\%)} \text{ (stat., 737 events) } \pm 1.0 \text{ (50.0\%)} \text{ (syst.)}$
$N^{Z+X \rightarrow 4\mu}$	$0.9 \pm 0.1 \text{ (10.0\%)} \text{ (stat., 70 events) } \pm 0.5 \text{ (55.5\%)} \text{ (syst.)}$
$N^{Z+X \rightarrow 2e2\mu}$	$2.9 \pm 0.1 \text{ (3.4\%)} \text{ (stat., 1005 events) } \pm 1.4 \text{ (48\%)} \text{ (syst.)}$

Table 22: The number of events from $Z+X$ expected and the relative systematics and statistical errors in the signal region in a mass range from $m_1 = 100 \text{ GeV}/c^2$ to $m_2 = 600 \text{ GeV}/c^2$, for baseline and for 8 TeV data.

	baseline (full range)
$N^{Z+X \rightarrow 4e}$	$1.9 \pm 0.1 \text{ (5.0\%)} \text{ (stat., 692 events) } \pm 0.9 \text{ (47\%)} \text{ (syst.)}$
$N^{Z+X \rightarrow 4\mu}$	$1.5 \pm 0.1 \text{ (7.0\%)} \text{ (stat., 118 events) } \pm 0.7 \text{ (47\%)} \text{ (syst.)}$
$N^{Z+X \rightarrow 2e2\mu}$	$3.2 \pm 0.1 \text{ (3.0\%)} \text{ (stat., 980 events) } \pm 1.6 \text{ (50\%)} \text{ (syst.)}$

1672 11.2 Reducible Backgrounds Uncertainties

1673 One of the important aspects of the reducible background prediction method is the assessment of the
 1674 statistical and systematic uncertainties. There are several sources of uncertainties:

- 1675 • Statistical uncertainty due to the limited size of the samples in the control regions where we
 1676 measure and where we apply the fake ratio method,
- 1677 • Different compositions of reducible background processes ($DY, t\bar{t}, WZ, Z\gamma^{(*)}$) in the region
 1678 where we measure and where we apply the fake ratio method,
- 1679 • Choice of the functional form for the m_{4l} shape that is used to extrapolate from the full range
 1680 of the invariant m_{4l} mass to the range of interest.

1681 The systematic uncertainties will be estimated using three different approaches:

- 1682 • Estimate the systematic uncertainty for the fake ratios from MC and propagate it to the final
 1683 prediction taking into account also the associated statistical uncertainties,
- 1684 • Estimate the systematic uncertainty for the prediction method using the MC closure test,
- 1685 • Estimate directly the systematic uncertainty for the prediction method using the “orthogonal”
 1686 4l data samples with the “wrong combination of charge and flavour”.

1687 11.2.1 Statistics in 4l Control Sample

1688 The limited size of the samples in the control regions where we measure and where we apply the fake
 1689 ratios is the source of the statistical uncertainties of the method. The dominating statistical uncertainty
 1690 is driven by the number of events in the control region and is typically in the range of 5-10%.

1691 11.2.2 Sensitivity of Fake Ratios to Background Composition

1692 Compositions of reducible background processes ($DY, t\bar{t}, WZ, Z\gamma^{(*)}$) in the region where we measure
 1693 and where we apply the fake ratio method are typically not the same. This is the main source of the
 1694 systematic uncertainty of the fake ratio method.

1695 This uncertainty can be estimated by measuring the fake ratios for individual background processes in
 1696 the $Z + 1L$ region in simulation. The weighted average of these individual fake ratios is the fake ratio
 1697 that we measure in this sample (in simulation). The exact composition of the background processes in
 1698 the 2P+2F region where we plan to apply the fake ratios can be determined from simulation, and one
 1699 can reweigh the individual fake ratios according to the 2P+2F composition. The difference between the
 1700 reweighed fake ratio and the average one can be used as a measure of the uncertainty on the measure-
 1701 ment of the fake ratios. The fake ratios for individual processes, the average fake ratio and the reweighed
 1702 fake ratio determined by simulation are shown in table below.

Table 23: The fake ratios for individual background processes, the average fake ratio and the fake ratio reweighed according to the composition of backgrounds in 2P+2F region. **!!FIXME!!**
Add the numbers from simulation in the table and write-up the conclusion...

Sample	DY	Zbb	ttbar	average	reweighed	uncertainty
electron fake ratio	-	-	-	0.023 ± 0.001	-	??% (< 40% in 2011)
muon fake ratio	-	-	-	0.072 ± 0.002	-	??% (< 40% in 2011)

1703 11.2.3 Closure Test (in Data and/or Simulation)

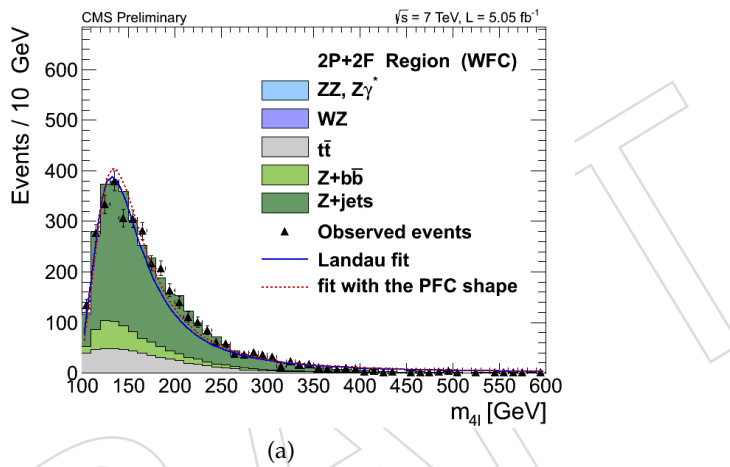
1704 A way to validate the reducible backgrounds prediction method and to estimate its associated systematic
 1705 uncertainty is to apply the same method in the subset of four-lepton events which satisfy the Higgs
 1706 selection criteria but leptons have “wrong combination of charges and flavours” (WFC). These samples
 1707 are expected to be free of the signal.

1708 The distribution of four-lepton invariant mass for data events in the WFC 2P+2F control region is shown
 1709 in Figure 78. The distribution is shown for the cumulative 4ℓ final state. The shape of the observed mass
 1710 distribution is fitted using the Landau function convoluted with the 4th order polynomial, as in the case

of selection with “proper combination of lepton charges and flavours” (PFC) defined in the previous section.

The distribution of four-lepton invariant mass for the 4ℓ final state events in the WFC Signal region is shown for 7TeV data in Figure 79 (left). The figure also shows distribution of the expected number of reducible background events in this region stacked on the distribution of irreducible backgrounds taken from simulation ($ZZ \rightarrow 4\ell$). The expected number of reducible background events is computed by the method A outlined above.

A reasonably good agreement between the predicted and the observed number of events in the WFC 3P+1F control region (Figure 79) is a validation of the method by measurements performed in data. The difference between the predicted and the observed number of events in the WFC Signal region can be used as a direct measure of the uncertainty of the method. Taking into account low statistical accuracy, the uncertainty is estimated to be less than 50%. The estimation of the uncertainty is dominated by the limited statistics (30% statistical uncertainty) and is expected to improve with the increase of the integrated luminosity.



(a)

Figure 78: Invariant mass distribution of events in the WFC 2P+2F control region for $4e$ (a), 4μ (b), $2e2\mu$ (c), and cumulative 4ℓ final states. The distributions are fitted with the Landau function convoluted with the 4th order polynomial (see text for details). The fit with the shape used in the PFC 2P+2F control region is overlaid on top. The difference between the two shapes can be used as a measure of the uncertainty on the shape of the fitting function.

11.2.4 Choice of Functional Form for M4L Shape

The functional form for the m_{4l} shape that is used to extrapolate from the full range of the invariant m_{4l} mass to the range of interest is also one source of the systematic uncertainty. In order to estimate this uncertainty we have looked at the differences between the shapes of predicted background distributions for all three channels. The envelope of differences between these shapes of distributions is used as a measure of the uncertainty of the shape. The uncertainty is estimated to be up to 10 - 15%. Since the difference of the shapes slowly varies with m_{4l} , it is taken as a constant term and is practically absorbed in the much larger uncertainty on the predicted yield of backgrounds (see previous chapter). The shapes of predicted background m_{4l} distributions for $4e$ and 4μ channels are shown in Figure 80.

11.3 Summary

Two methods for the prediction of the contribution of reducible background processes in the signal region are presented with associated uncertainties in the previous two section. The Table 24 below shows the summary of the results of both methods. As the final estimate of this contribution, we take the mean value of the results of the two methods, while as the uncertainty of the result we quote the one

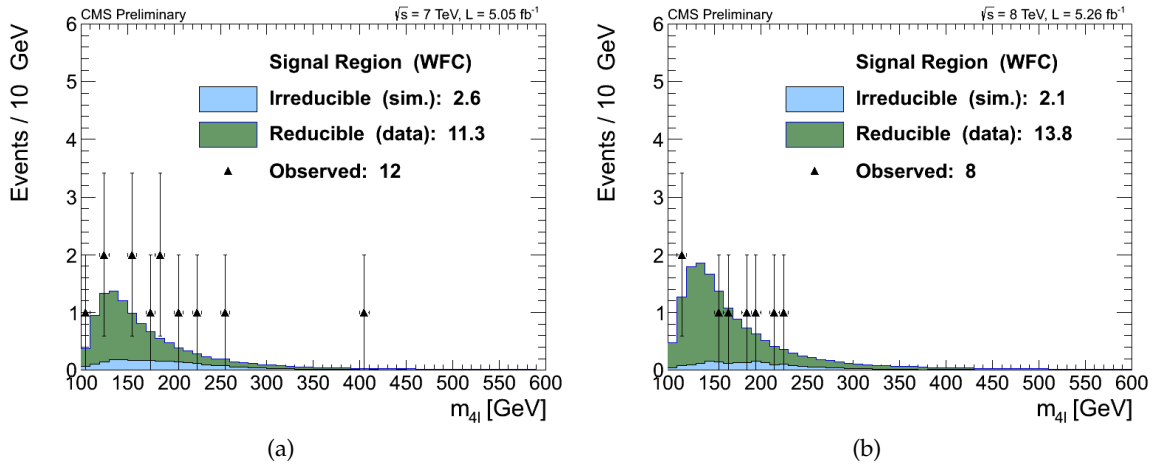


Figure 79: Results of the prediction method applied in the 4l data sample with the “wrong combination of charge and flavour” (as defined in the text above). Figures show the “closure” test in the signal region for the 7TeV data (left) and 8 TeV data (right). The difference between the predicted and the observed number of events in the WFC Signal region is used as a measure of the uncertainty of the prediction method A.

1739 that covers the uncertainties of both methods (using the symmetric log-normal distribution). Figure 81
 1740 is a visual representation of the predictions of individual methods and the combined results.

Table 24: The summary of the results of two methods for the prediction of the contribution of reducible background processes in the signal region. The arithmetic mean value of the results of the two methods is taken as the final estimate of this contribution, while the uncertainty of the result is the one that covers the uncertainties of both methods. The table shows symmetric individual uncertainties for two methods, while in the combination and statistical analysis these are treated with the (a)symmetric log-normal distribution. The quoted predictions correspond to the 5.05fb^{-1} of 7 TeV data and the 5.26fb^{-1} of 8 TeV data.

	7 TeV	4e	4 μ	2e2 μ
Method A	$1.2 \pm 0.0_{\text{stat.}} \pm 0.6_{\text{syst.}}$	$1.1 \pm 0.1_{\text{stat.}} \pm 0.5_{\text{syst.}}$	$2.4 \pm 0.1_{\text{stat.}} \pm 1.2_{\text{syst.}}$	
Method AA	$2.0 \pm 0.1_{\text{stat.}} \pm 1.0_{\text{syst.}}$	$0.9 \pm 0.1_{\text{stat.}} \pm 0.5_{\text{syst.}}$	$2.9 \pm 0.1_{\text{stat.}} \pm 1.4_{\text{syst.}}$	
Combined central value	1.6	1.0	2.6	
Combined κ_{min}	0.4	0.4	0.5	
Combined κ_{max}	1.9	1.6	1.6	
	8 TeV	4e	4 μ	2e2 μ
Method A	$0.9 \pm 0.1_{\text{stat.}} \pm 0.5_{\text{syst.}}$	$0.9 \pm 0.1_{\text{stat.}} \pm 0.5_{\text{syst.}}$	$1.6 \pm 0.1_{\text{stat.}} \pm 0.8_{\text{syst.}}$	
Method AA	$1.9 \pm 0.1_{\text{stat.}} \pm 0.9_{\text{syst.}}$	$1.5 \pm 0.1_{\text{stat.}} \pm 0.7_{\text{syst.}}$	$3.2 \pm 0.1_{\text{stat.}} \pm 1.6_{\text{syst.}}$	
Combined central value	1.4	1.2	2.4	
Combined κ_{min}	0.3	0.4	0.3	
Combined κ_{max}	1.9	1.8	2.0	

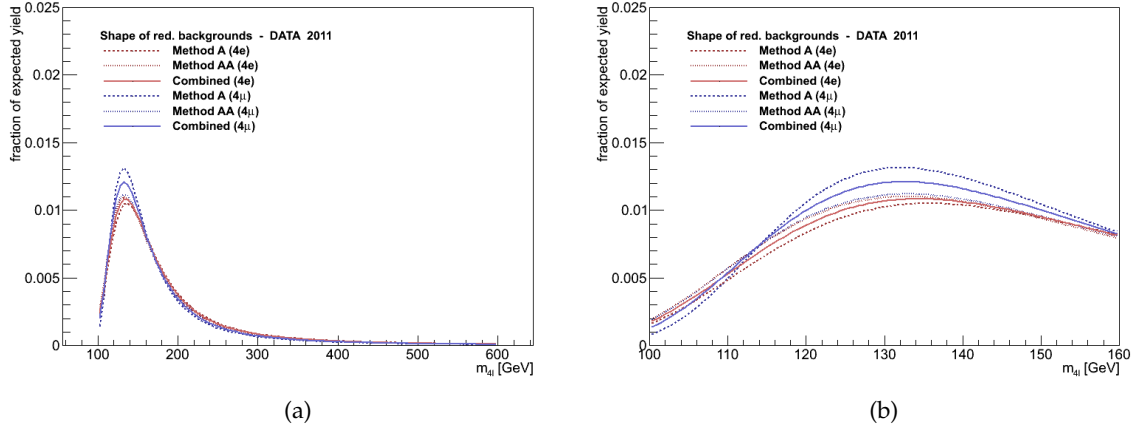


Figure 80: The shapes of predicted background m_{4l} distributions for $4e$ and 4μ channels. The envelope of differences between the shapes of distributions can be used as a measure of the uncertainty of the shape. The uncertainty is estimated to be in the range 10 - 15% and is absorbed in the much larger uncertainty on the predicted yield of backgrounds.

Table 25: The summary of the parameters of the predicted shape of reducible background processes in the signal region for 7 TeV (upper part) and 8 TeV of data (lower part). The estimated uncertainty on the shape is found to be below 10-15% and is included in the uncertainties quoted above (as discussed in the text).

	7 TeV	n_0	m	c
4e	0.054	146.0	19.4	
2e2mu	0.059	145.2	17.8	
4mu	0.054	137.7	19.8	
	8 TeV	n_0	m	c
4e	0.050	146.9	21.3	
2e2mu	0.054	142.6	19.8	
4mu	0.052	138.4	20.8	

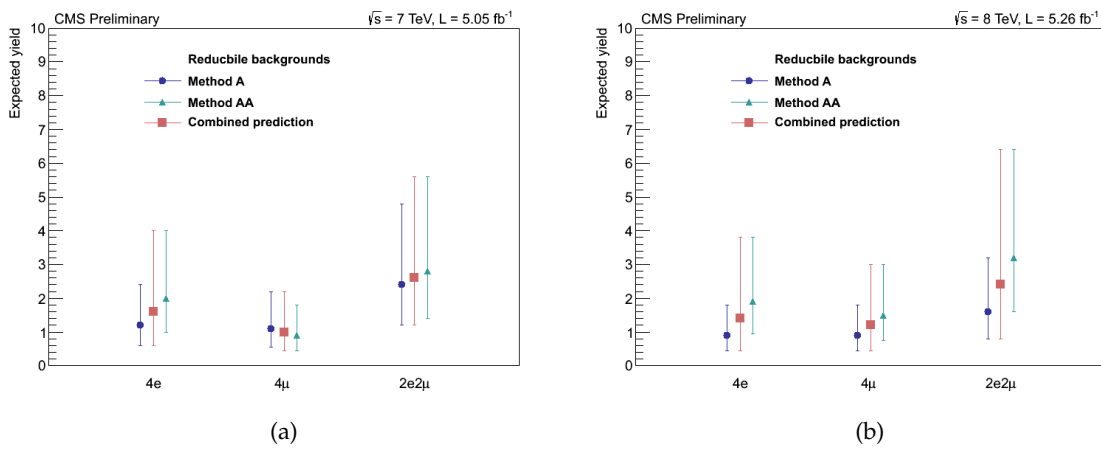


Figure 81: The visual representation of the predictions of individual methods and the combined results of two methods. The final estimate is taken as the geometrical mean of the two extreme values allowed by the two methods. The uncertainty of the result is the one that covers the uncertainties of both methods (symmetric log-normal distribution).

1741 12 Kinematic Discriminant (MELA)

1742 12.1 Introduction of the methodology

1743 Kinematics of the Higgs decay to ZZ final state has been extensively studied in the literature in appli-
 1744 cation to the studies of the Higgs boson or new exotic boson properties, see for example Refs. [92–103].
 1745 Only recently a complete set of angular observables was introduced in Ref. [101] and it was suggested
 1746 that it may also help in background rejection. This approach was recently introduced in the analysis of
 1747 the decay $H \rightarrow ZZ \rightarrow 2\ell 2q$ [104] on CMS and we adopt a similar methodology in $H \rightarrow ZZ \rightarrow 4\ell$. In this
 1748 approach, the signal-to-background probability is created using analytical or empirical multi-dimension
 1749 likelihood for an event to be signal or background. Signal and background analytical parameterizations
 1750 are taken from Refs. [101] and [103], respectively. In the following, we introduce the methodology
 1751 in more detail with the analytical MELA approach (Matrix Element Likelihood Approach). As cross-
 1752 checks, kinematics has also been studied with Boosted Decision Trees, Bayesian Neural Networks, and
 1753 numerical Matrix Element, as discussed in Appendixes.

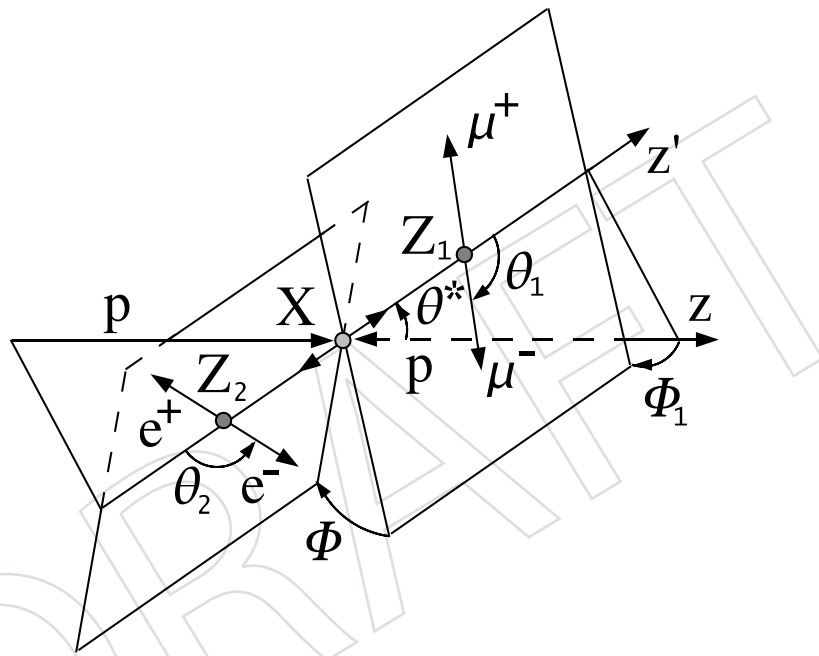


Figure 82: Left: Illustration of a particle X production and decay $ab \rightarrow X \rightarrow Z_1 Z_2 \rightarrow 4\ell$ with the two production angles θ^* and Φ_1 shown in the X rest frame and three decay angles θ_1 , θ_2 , and Φ shown in the P_i rest frames [101].

1754 In Fig. 82 we illustrate the angular distribution in the production and decay chain $ab \rightarrow X \rightarrow ZZ \rightarrow 4\ell$.
 1755 The angular distribution can be expressed as a function of three helicity angles θ_1 , θ_2 , and Φ , and two
 1756 production angles θ^* and Φ_1 . The full kinematics in the production and decay of an X resonance $ab \rightarrow$
 1757 $X \rightarrow Z_1 Z_2 \rightarrow 4\ell$ can be described with the help of the following 12 observables (reflecting all degrees of
 1758 freedom with four lepton momenta):

- 1759 • three resonance masses (including the off-shell cases): $m_{4\ell}$, m_1 , m_2 ;
- 1760 • five production and decay angles defined in Fig. 82 as $\vec{\Omega} = \{\theta^*, \Phi_1, \theta_1, \theta_2, \Phi\}$;
- 1761 • longitudinal boost of the resonance, expressed as rapidity Y ;
- 1762 • transverse momentum of the resonance p_T and its azimuthal angle;
- 1763 • one arbitrary azimuthal angle Φ^* reflecting the overall orientation of the system.

1764 The 2011 baseline analysis of the $H \rightarrow ZZ \rightarrow 4\ell$ channel employed cuts on the two $Z^{(*)}$ invariant

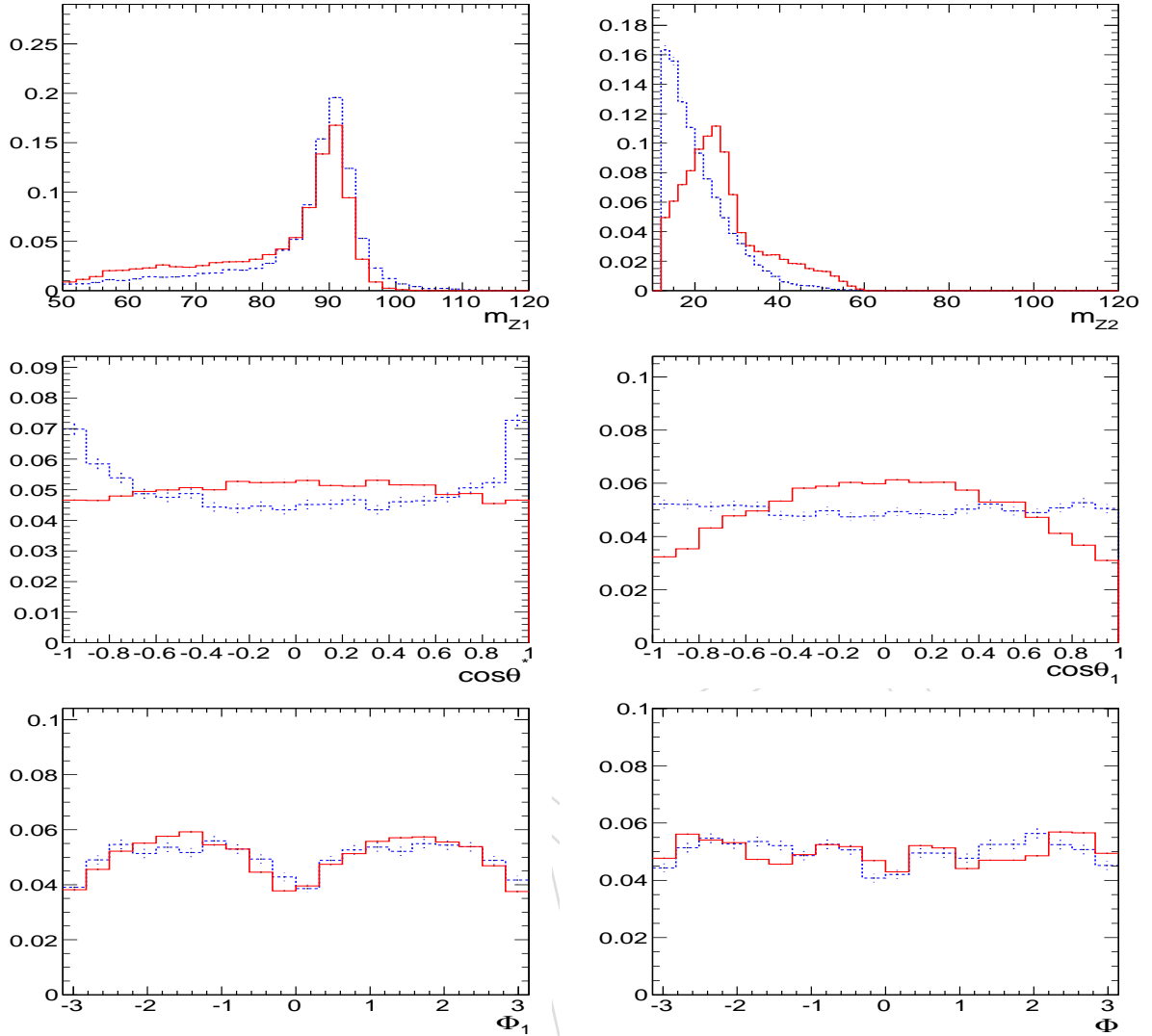


Figure 83: Distribution of Higgs signal events with $m_H = 120$ GeV (solid red) and background ZZ events (dashed blue) in the range $100 < m_{4\ell} < 135$ GeV. Top-left: m_1 ; top-right: m_2 ; middle-left: $\cos \theta^*$; middle-right: $\cos \theta_{1,2}$ (both angles have the same distribution); bottom-left: Φ_1 ; bottom-right: Φ .

masses m_1 and m_2 with the shape-based fit of the $m_{4\ell}$ distribution. In the current approach, we expand information used and construct a kinematic discriminant KD from the seven mass and angular observables $KD = F\{m_1, m_2, \theta^*, \Phi_1, \theta_1, \theta_2, \Phi\}$ and perform a 2D shape fit with the two observables ($m_{4\ell}, KD$). In Figs. 83 and 84 we show separation power between signal and background for each individual observable. The KD discriminant combines this power in a single observable using full correlation of all input observables in the most optimal way. In this approach we remove from consideration those observables which depend on QCD kinematics, such as Y , p_T , and its azimuthal angle, and keep only observables coming from well-understood electro-weak Quantum Mechanics of the processes of either Higgs or continuum ZZ production. In particular, these seven observables are independent from the Higgs production mechanism, as long as we consider the SM Higgs boson. The same seven observables are also the key input to measuring the new boson properties, such as spin and CP quantum numbers, should a new boson be discovered.

It has been noted that Y and p_T distributions are different for processes dominated by gluon fusion

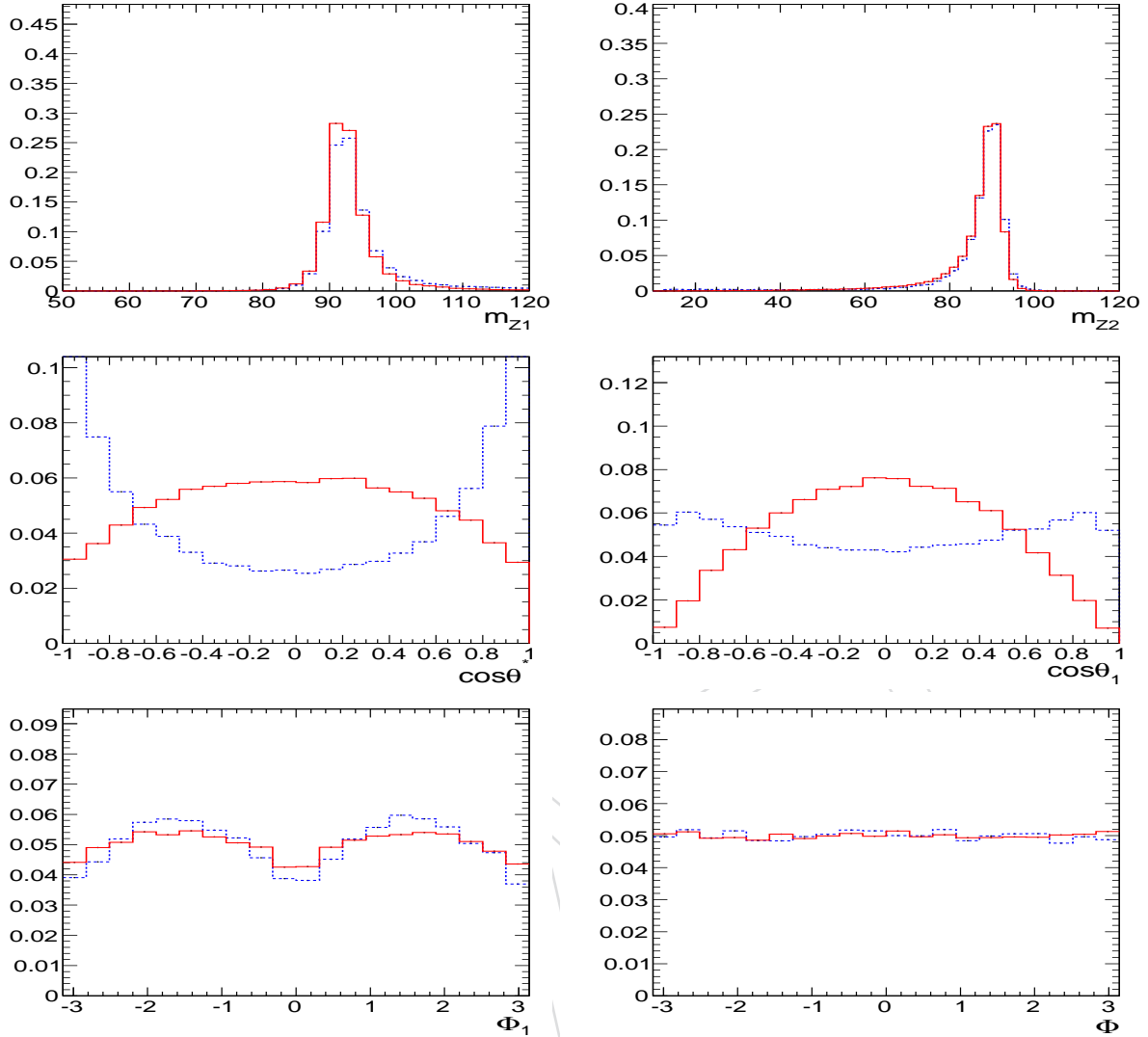


Figure 84: Distribution of Higgs signal events with $m_H = 400$ GeV (solid red) and background ZZ events (dashed blue) in the range $300 < m_{4\ell} < 500$ GeV. Top-left: m_1 ; top-right: m_2 ; middle-left: $\cos \theta^*$; middle-right: $\cos \theta_{1,2}$ (both angles have the same distribution); bottom-left: Φ_1 ; bottom-right: Φ .

(signal) and $q\bar{q}$ production (background), due to larger longitudinal boost of the $q\bar{q}$ system and larger Initial State Radiation (QCD ISR) in gluon fusion. However, these observables are fully driven by QCD effects and require further validation. Therefore, they are not used in the current analysis.

12.2 Construction of the MELA discriminant

Construction of the kinematic discriminant KD in the MELA approach (Matrix Element Likelihood Approach) relies on probability for an event with a set of observables $(m_{4\ell}, m_1, m_2, \vec{\Omega})$ to come either from signal or background

$$\mathcal{P}_{\text{sig}}(m_1, m_2, \vec{\Omega} | m_{4\ell}) \quad (30)$$

$$\mathcal{P}_{\text{bkg}}(m_1, m_2, \vec{\Omega} | m_{4\ell}) \quad (31)$$

where probabilities are normalized with respect to the seven observables while treating $m_{4\ell}$ as a conditional parameter. These probabilities are calculated analytically and are quoted in Ref. [101] for signal and in Ref. [103] for continuum ZZ background. Then the discriminant is constructed as follows

$$\text{KD} = \frac{\mathcal{P}_{\text{sig}}}{\mathcal{P}_{\text{sig}} + \mathcal{P}_{\text{bkg}}} = \left[1 + \frac{\mathcal{P}_{\text{bkg}}(m_1, m_2, \vec{\Omega} | m_{4\ell})}{\mathcal{P}_{\text{sig}}(m_1, m_2, \vec{\Omega} | m_{4\ell})} \right]^{-1} \quad (32)$$

There are several considerations in the above construction. This discriminant is continuously distributed between 0 and 1, with signal being closer to 1 and background closer to 0. The signal probability is parameterized as a function of $m_{4\ell}$ instead of m_H . This allows continuous selection of the data-sample independent of the m_H hypothesis. Both signal and background probabilities are normalized for any given value of $m_{4\ell}$, which removes unnecessary correlation of KD with $m_{4\ell}$ and makes further fit implementation more robust. Parameterization is performed for ideal distributions, not including the detector effects, and therefore does not require any training. This is still an optimal approach because detector acceptance effects are identical for signal and background and would cancel in the ratio in Eq. (32). From statistical considerations the above construction of the KD is the most optimal given the input under consideration. The input to the KD construction can be carefully controlled, certain observables can be integrated out or included depending on the level of confidence in the input.

There are also different approaches for $m_{4\ell}$ above and below the $2m_Z$ threshold. The signal and background probabilities include the phase-space and the Z resonance propagator terms in the form $m_i^3 / [(m_i^2 - m_Z^2)^2 + m_Z^2 \Gamma_Z^2]$ which cancel in the signal-to-background ratio above threshold. Therefore, the KD above the threshold becomes a function of only five angles. In other words, there is no separation power in the m_1 and m_2 observables above threshold, as can be seen in Fig. 84. However, below threshold di-lepton invariant mass m_2 distribution for the off-shell Z becomes broad, see Fig. 83 for example, and we use the full propagator terms for signal. For background below threshold, analytical parameterization is substituted with a correlated template distribution illustrated in Fig. 85. This is done to simplify parameterization below threshold (analytical one is to be used for testing). We use the value of 180 GeV as a boundary between the two ranges below and above the threshold.

The background template distribution in Fig. 85 includes the most important correlations of five angles and two masses m_1 and m_2 as a function of $m_{4\ell}$ as well as of the two masses m_1 and m_2 with respect to each other. For example, for a given value of $m_{4\ell}$ there is a kinematic constraint $(m_1 + m_2) \leq m_{4\ell}$. We also use the convention $m_1 > m_2$ without any loss of information, which explains the triangular shape in Fig. 85.

The resulting MELA KD distributions for signal and background are shown in Fig. 86 in three different mass ranges. Good agreement is found between data and background MC. Overall, significant separation between signal and background is evident from the MELA KD distributions.

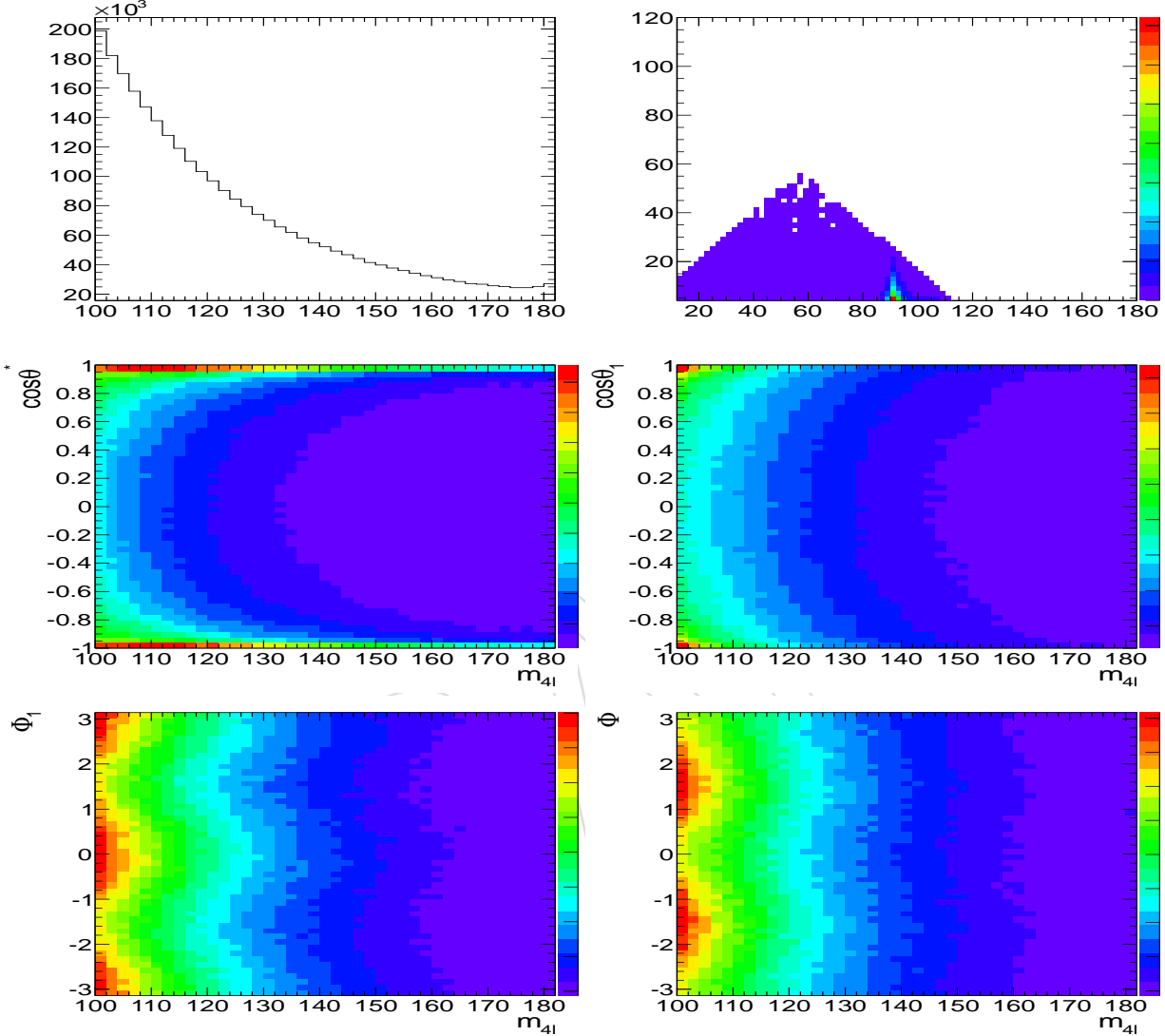


Figure 85: Parameterization of continuum ZZ background probability distribution \mathcal{P}_{bkg} using generator-level POWHEG events in the mass range [100,180] GeV. Top-left: $m_{4\ell}$ distribution. Top-right: m_2 vs m_1 distribution in a narrow slice of $m_{4\ell}$ around 125 GeV. Middle-left: $\cos \theta^*$ vs $m_{4\ell}$ distribution. Middle-right: $\cos \theta_{1,2}$ vs $m_{4\ell}$ distribution. Bottom-left: Φ_1 vs $m_{4\ell}$ distribution. Bottom-right: Φ vs $m_{4\ell}$ distribution.

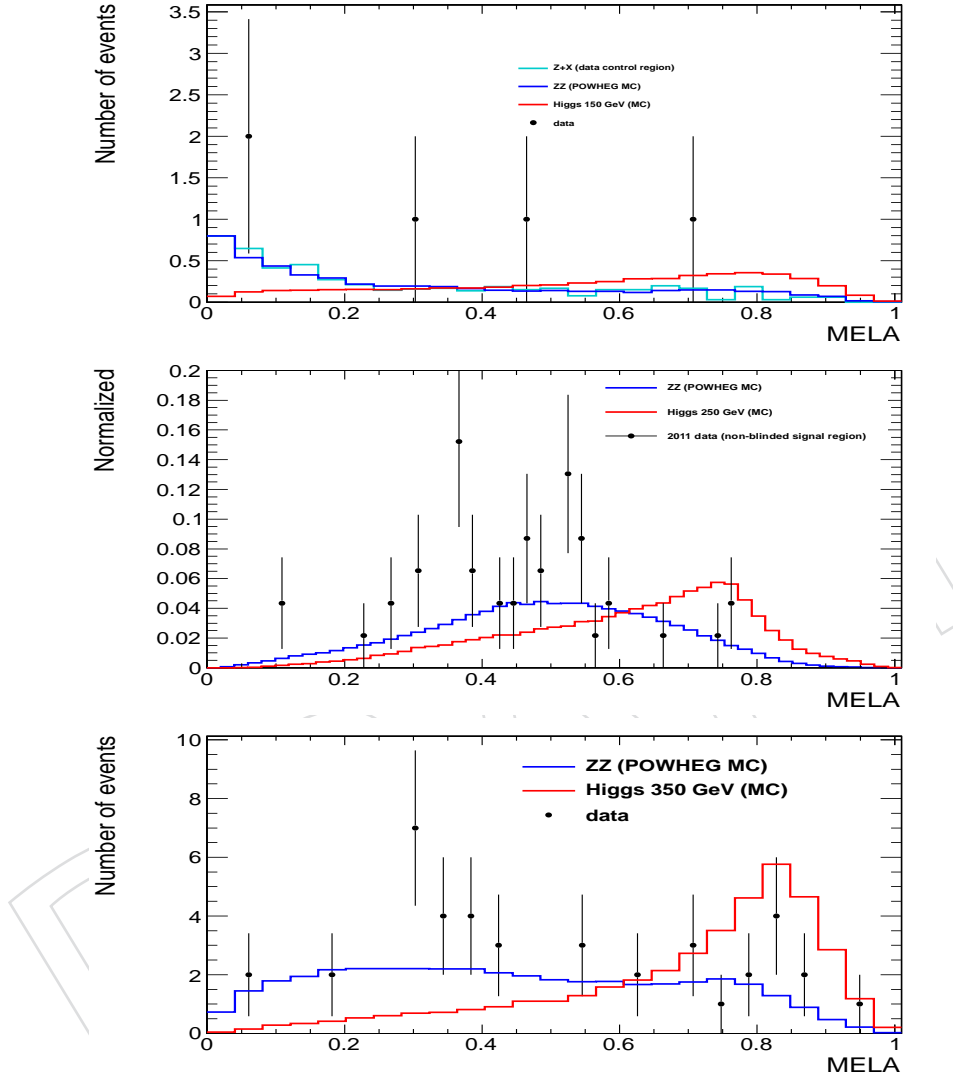


Figure 86: The KD distributions for signal and background in three mass ranges: $140 < m_{4\ell} < 160$ GeV (top), $200 < m_{4\ell} < 300$ GeV (middle), and $250 < m_{4\ell} < 450$ GeV (bottom). The signal (red solid histogram) is shown for $m_H = 150, 250$, and 350 GeV, respectively. The ZZ continuum background is shown as blue solid histogram. The top plot also shows $Z + X$ background estimated from data control region.

1817 12.3 Parameterization of the MELA discriminant

1818 While the MELA parameterization is performed using the ideal distributions in Eq. (32), the resulting
 1819 observable KD is a certain number for each event candidate. This observable is parameterized using
 1820 MC samples (with full CMS simulation and with data-to-MC corrections applied) for the Quantum
 1821 Mechanical processes that we model well, such as signal and ZZ background, and using data control
 1822 samples for instrumental and reducible background, such as $Z + X$. It is important to note that we use
 1823 only invariant masses and angles in the sequential process with ZZ system production and decay, which
 1824 is under good control from basic Quantum Mechanics and electroweak couplings, no QCD effects are
 1825 included. The KD observable is no more complex than the di-lepton invariant mass for example, and it
 1826 is even more reliable than p_T of the objects, which in turn depend on QCD effects in production.

1827 The KD distributions are somewhat affected by interference of identical leptons in the final states $ZZ \rightarrow$
 1828 $e^+e^-e^+e^-$ and $\mu^+\mu^-\mu^+\mu^-$, but not in $2e2\mu$. First of all, this effect is only relevant at low masses, be-
 1829 low the ZZ threshold, where at least one of the Z bosons is off-shell and therefore the phase-space for
 1830 interference increases. The background simulation of continuum ZZ background already includes inter-
 1831 ference effects and this is taken into account when KD distributions are parameterized for background.
 1832 The signal POWHEG+Pythia simulation of $H \rightarrow ZZ$ signal does not include such interference effect and
 1833 we use Prophecy event generator to calculate the difference. This is shown in Fig. 87, where this effect
 1834 is visible only at the low mass and essentially disappears at around $m_H = 160$ GeV. We perform a linear
 1835 fit of the ratio and apply mass-dependent re-scaling algorithm to MC simulation when KD distribution
 1836 is parameterized for signal. This mass-dependence is shown in Fig. 88.

1837 The KD distributions depend on the value of the $m_{4\ell}$, due to kinematics dependence on the mass. There-
 1838 fore, any further analysis of the data which includes KD must also include its full correlation with $m_{4\ell}$.
 1839 Below $2m_Z$ threshold, the dominant background is $q\bar{q} \rightarrow ZZ$ with a secondary contribution of $Z + X$
 1840 background. Above $2m_Z$ threshold, the dominant background is also $q\bar{q} \rightarrow ZZ$ with a secondary contribu-
 1841 tion of $gg \rightarrow ZZ$ background. For the signal, $q\bar{q} \rightarrow ZZ$ and $gg \rightarrow ZZ$ background, the ideal angular
 1842 and mass distributions come from basic quantum mechanics given the EWK couplings and are modeled
 1843 well by MC (apart from interference effect in signal, as corrected and discussed above).

1844 Detector effects may alter the KD distribution due to mis-modeling of lepton efficiency and resolutions.
 1845 Our estimates showed that those have very small effects on KD distributions because, as opposed to
 1846 $m_{4\ell}$, there is no distinct peak and smearing of broad distribution is a small effect. In Fig. 89, we show
 1847 an example of the shape variation due to extreme variation of MC efficiency by changing the Tag-and-
 1848 Probe corrections from those obtained from data to flat ones (typically this variation is larger than the
 1849 errors). In Fig. 90, we show an example of the shape variation due to extreme variation of MC resolution
 1850 in the $H \rightarrow ZZ \rightarrow 4e$ channel. Therefore, we ignore such detector effects in systematic uncertainties for
 1851 the KD, they are significantly smaller than statistical effects in the data to be analyzed.

1852 In Fig. 91 we show comparison of the KD distributions in several slices of $m_{4\ell}$ and in the full $m_{4\ell}$ range
 1853 below threshold for data control sample for $Z + X$ background, MC control sample for $Z + X$ background,
 1854 for MC POWHEG simulation of $q\bar{q} \rightarrow ZZ$ background. Two important conclusions could be drawn. First,
 1855 there is a good agreement between the $Z + X$ background parameterization in data and MC, which
 1856 gives us confidence in the $Z + X$ background estimation. Second, data-driven $Z + X$ background dis-
 1857 tributions and continuum $q\bar{q} \rightarrow ZZ$ distribution are in good agreement. Therefore, a joint background
 1858 parameterization can be used, with any potential difference observed in these plots treated as system-
 1859 atic uncertainty. In order to include systematics in the analysis, we create alternative KD distributions
 1860 according to the linear fit slope and its error by re-scaling the distributions according to that slope (with
 1861 error on the slope added), as shown in Fig. 92. It is also observed that the shape of the KD changes
 1862 somewhat as a function of $m_{4\ell}$, but its main feature remains, background peaks towards zero while
 1863 signal peaks towards one.

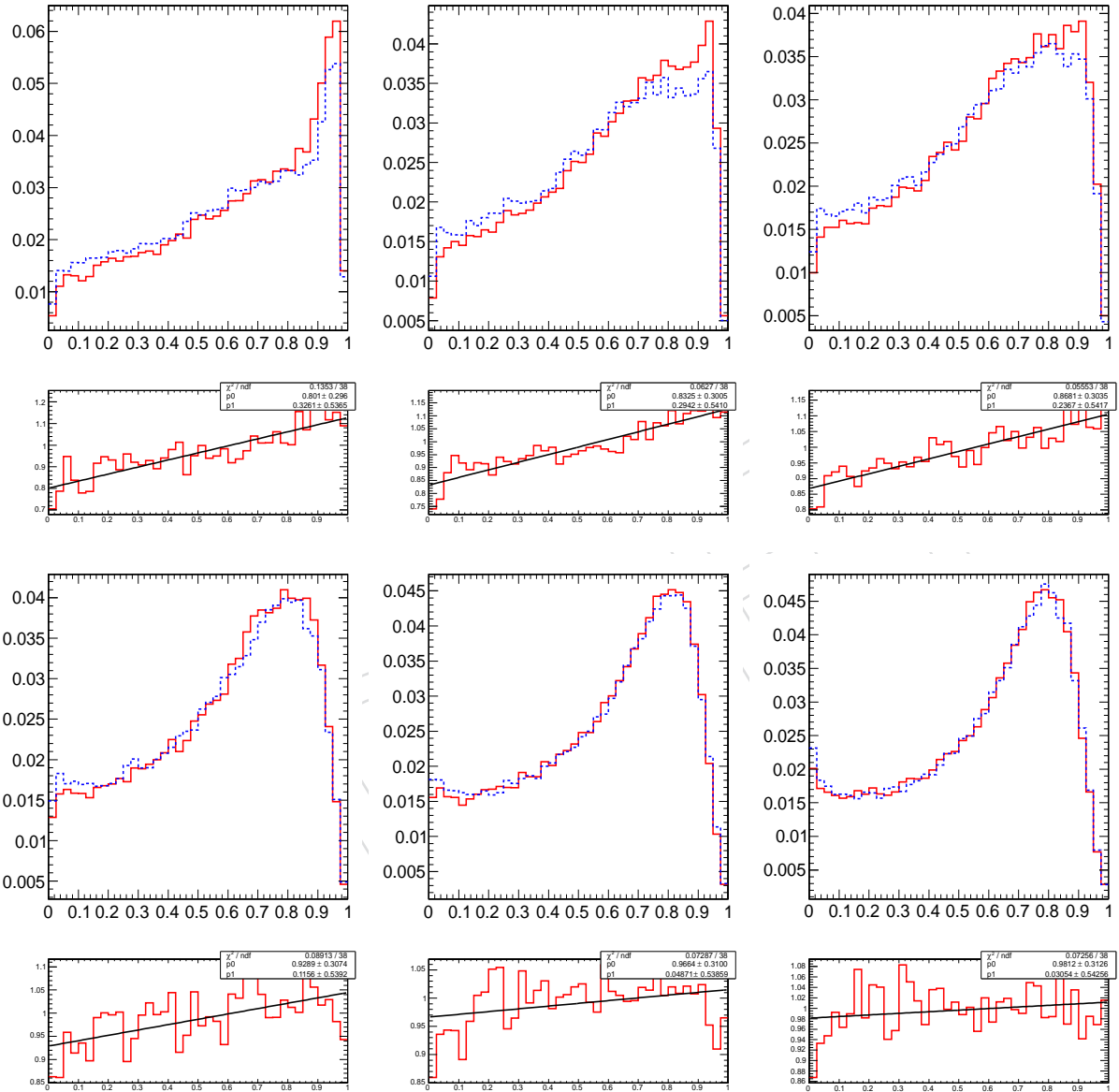


Figure 87: Distribution of signal MELA KD with and without interference effects and the ratio. Several m_H hypotheses are shown, top row: 120, 125, 130 GeV, bottom row: 140, 150, 160 GeV.

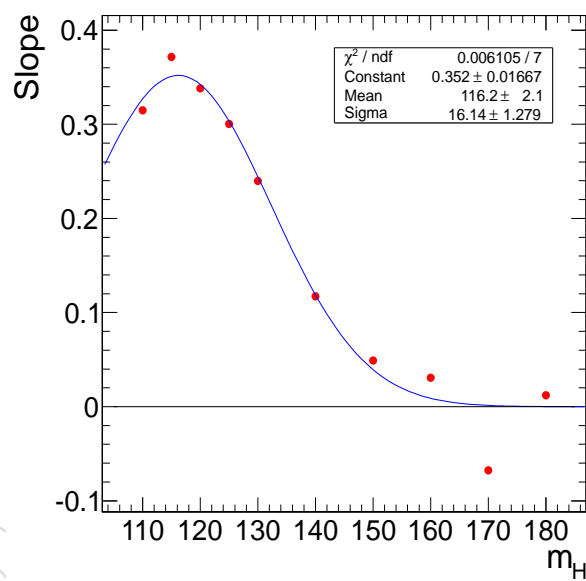


Figure 88: Slope of the correction to interference effect shown in Fig. 87 as a function of m_H .

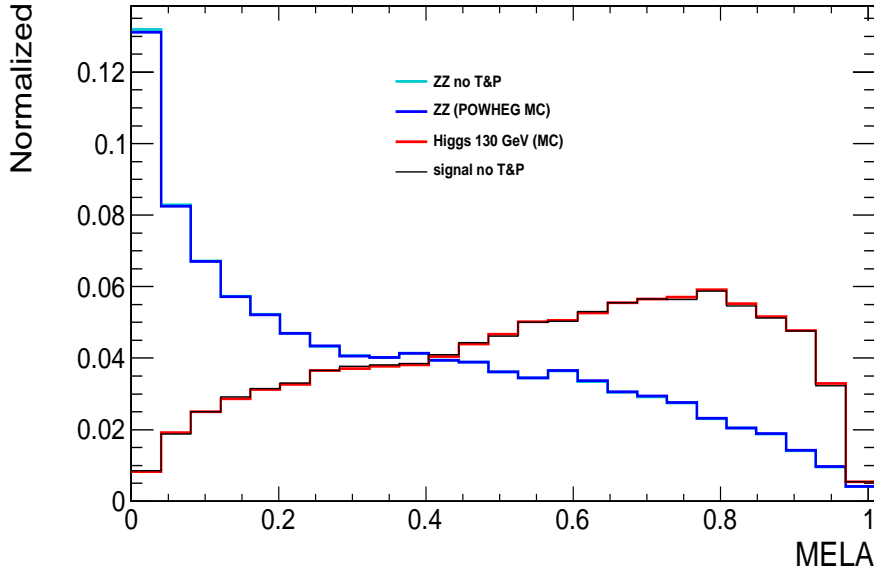


Figure 89: Distribution of the MELA KD for ZZ background and 130 GeV Higgs signal in MC, for events below $2m_Z$ threshold (background peaks towards 0 and signal peaks towards 1). For both signal and background two very close distributions are shown: with and without the Tag-and-Probe corrections for data-MC differences.

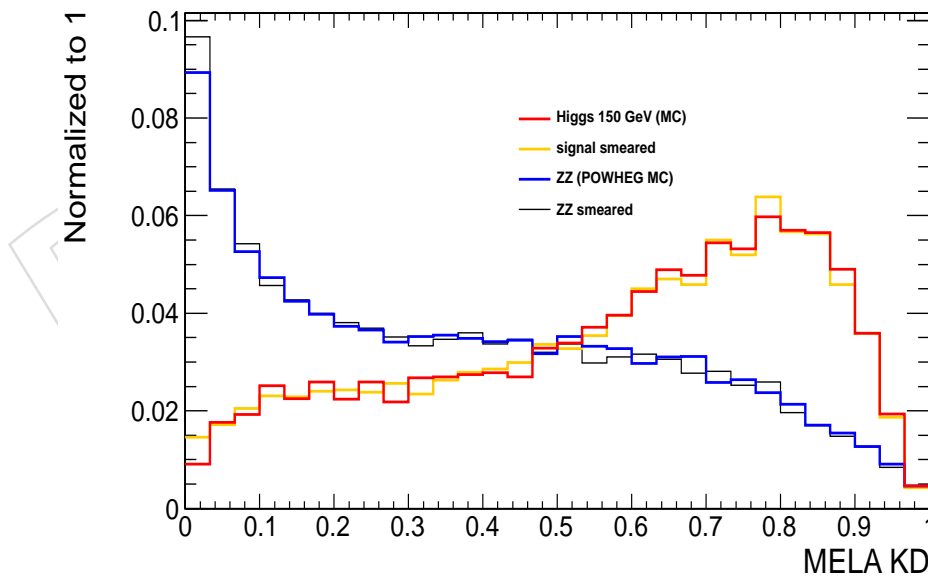


Figure 90: Distribution of the MELA KD for ZZ background and 150 GeV Higgs signal in MC, for events below $2m_Z$ threshold (background peaks towards 0 and signal peaks towards 1). For both signal and background two very close distributions are shown: with and without smearing of electron energy resolution, which is equal to uncertainty on this resolution. Only $H \rightarrow ZZ \rightarrow 4e$ channel is considered here, to show the largest effect.

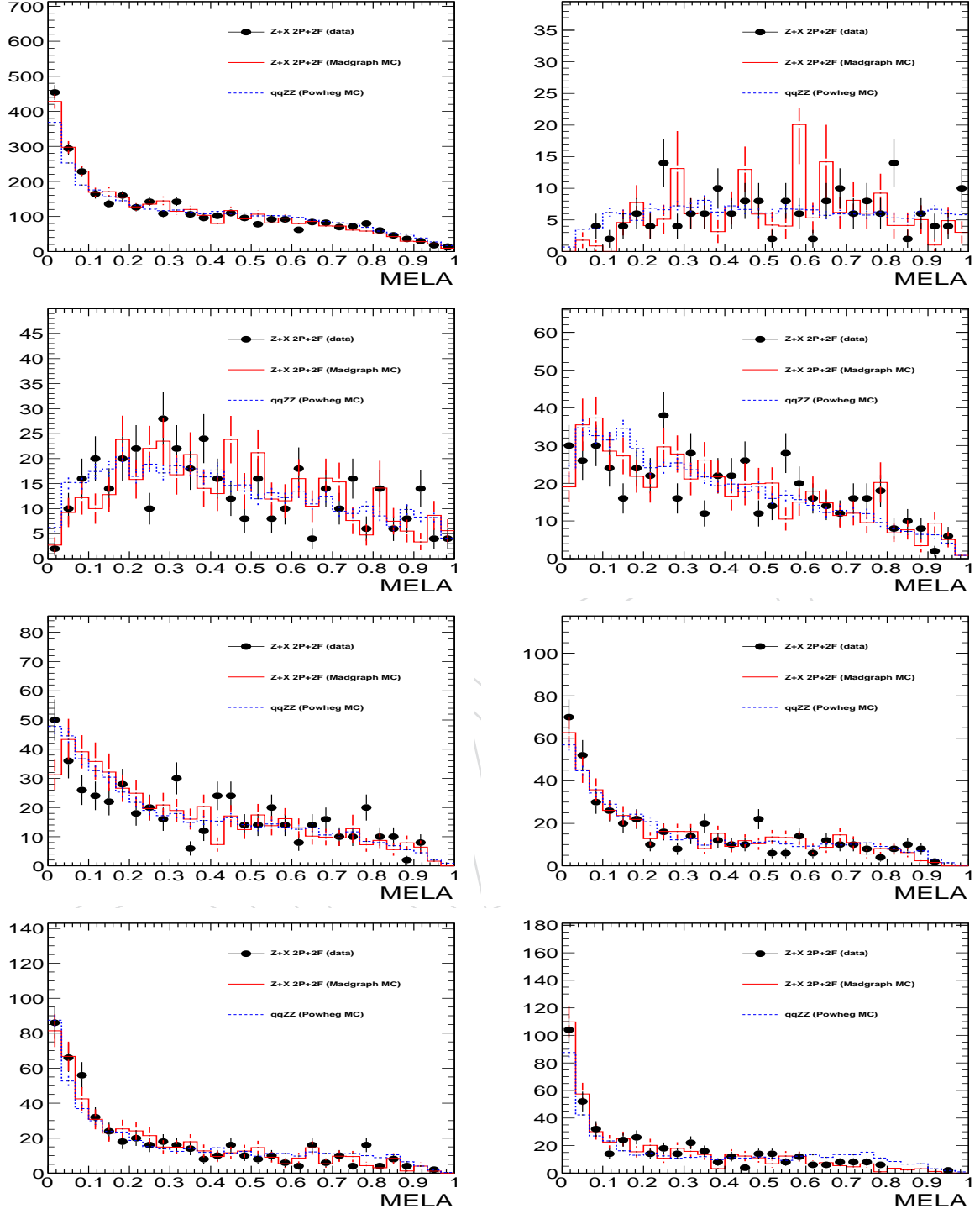


Figure 91: Parameterization of background MELA KD in several $m_{4\ell}$ ranges (in GeV). Top row: [100,180] in left, [100,110] in right; second row: [110,120] in left, [120,130] in right; third row: [130,140] in left, [140,150] in right; bottom row: [150,160] in left, [160,170] in right. Points show data control sample for $Z + X$ background, red solid histogram shows MC control sample for $Z + X$ background, blue dashed histogram shows MC POWHEG simulation of ZZ background.

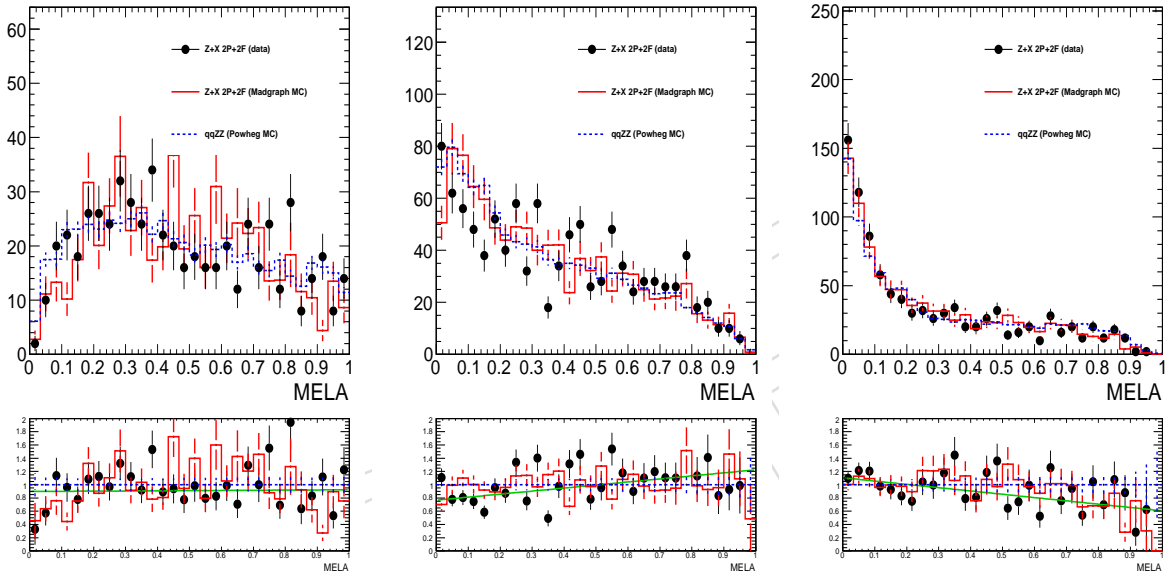


Figure 92: Parameterization of background MELA KD in several $m_{4\ell}$ ranges (in GeV). Left: [100,120]; middle: [120,140]; right: [140,160]. Points show data control sample for $Z + X$ background, red solid histogram shows MC control sample for $Z + X$ background, blue dashed histogram shows MC POWHEG simulation of ZZ background. Bottom plots show the ratio between the $Z + X$ background and ZZ background distributions.

1864 13 Summary of Selection and Systematic Uncertainties

1865 In this Section we summarize the input to the statistical analysis discussed in Section 14, expected and
 1866 observed yields, their uncertainties, and distributions of events in most critical observables. Discussion
 1867 of the shape models is presented elsewhere.

1868 13.1 Event yields and errors

1869 The number of candidates observed in 2011 and 2012 data, as well as the estimated background in the
 1870 signal region, are reported in Tables 28 and 27 for the baseline selection.

Table 26: The number of event candidates observed in 2011 data for 5.05 fb^{-1} , compared to the mean expected background and signal rates for each final state for $100 < m_{4\ell} < 800 \text{ GeV}$. For the Z +X background, the estimations are based on data.

Channel	4e	4μ	$2e2\mu$
ZZ background	14.88 ± 1.69	22.53 ± 2.23	35.83 ± 3.65
Z+X	$1.6^{+1.44}_{-0.96}$	$1.0^{+0.6}_{-0.6}$	$2.6^{+1.56}_{-1.3}$
All background expected	$16.48^{+2.22}_{-1.94}$	$23.53^{+2.31}_{-2.31}$	$38.43^{+3.97}_{-3.88}$
$m_H = 120 \text{ GeV}$	0.37 ± 0.06	0.73 ± 0.09	0.89 ± 0.12
$m_H = 125 \text{ GeV}$	0.66 ± 0.11	1.21 ± 0.15	1.57 ± 0.21
$m_H = 126 \text{ GeV}$	0.73 ± 0.12	1.32 ± 0.16	1.73 ± 0.23
$m_H = 130 \text{ GeV}$	1.03 ± 0.17	1.8 ± 0.21	2.45 ± 0.32
$m_H = 200 \text{ GeV}$	3.92 ± 0.5	5.62 ± 0.63	9.52 ± 1.11
$m_H = 350 \text{ GeV}$	2.18 ± 0.33	3.01 ± 0.42	5.28 ± 0.75
$m_H = 500 \text{ GeV}$	0.75 ± 0.18	1.02 ± 0.23	1.8 ± 0.41
Observed	14	20	43

1871 13.2 Distributions of events

1872 The reconstructed four-lepton invariant mass distribution is shown in Figure 114 for the full dataset,
 1873 where different mass ranges, including the mass below 100 GeV (not used for analysis). These distribu-
 1874 tions are also shown in Figs. 94 and 95 but splitted by channel, and for 7 and 8 TeV data separately. The
 1875 reconstructed di-lepton invariant mass and MELA KD distributions are shown in Figure 96. The SM
 1876 background distributions are obtained combining the rate normalization from data-driven meth-
 1877 ods and knowledge on shapes taken from the MC samples.

1878 The correlation between the four-lepton reconstructed mass and KD, or the reconstructed mass of the
 1879 second or first lepton pair are shown in Figs. 97.

Table 27: The number of event candidates observed in 2012 data 5.26 fb^{-1} , compared to the mean expected background and signal rates for each final state for $100 < m_{4\ell} < 800 \text{ GeV}$. For the Z +X background, the estimations are based on data.

Channel	4e	4μ	2e2 μ
ZZ background	14.4 ± 1.74	26.48 ± 2.85	39.62 ± 4.37
Z+X	$1.4^{+1.26}_{-0.98}$	$1.2^{+0.96}_{-0.72}$	$2.4^{+2.4}_{-1.68}$
All background expected	$15.8^{+2.15}_{-2.0}$	$27.68^{+3.01}_{-2.94}$	$42.02^{+4.99}_{-4.68}$
$m_H = 120 \text{ GeV}$	0.4 ± 0.06	0.92 ± 0.11	1.05 ± 0.13
$m_H = 125 \text{ GeV}$	0.71 ± 0.11	1.54 ± 0.17	1.87 ± 0.24
$m_H = 126 \text{ GeV}$	0.78 ± 0.12	1.68 ± 0.19	2.07 ± 0.26
$m_H = 130 \text{ GeV}$	1.11 ± 0.17	2.29 ± 0.26	2.94 ± 0.37
$m_H = 200 \text{ GeV}$	4.43 ± 0.55	7.63 ± 0.84	12.11 ± 1.37
$m_H = 350 \text{ GeV}$	2.61 ± 0.37	4.45 ± 0.58	7.37 ± 0.97
$m_H = 500 \text{ GeV}$	0.93 ± 0.21	1.56 ± 0.34	2.59 ± 0.57
Observed	18	27	50

Table 28: The number of event candidates observed, compared to the mean expected background and signal rates for each final state. For the Z +X background, the estimations are based on data. The results are given integrated over the full mass measurement range for the Higgs boson search from 100 to 800 GeV and for 2011 and 2012 data combined.

Channel	4e	4μ	2e2 μ
ZZ background	29.27 ± 3.43	49.01 ± 5.08	75.45 ± 8.02
Z+X	$3.0^{+2.7}_{-1.94}$	$2.2^{+1.56}_{-1.32}$	$5.0^{+3.96}_{-2.98}$
All background expected	$32.27^{+4.37}_{-3.94}$	$51.21^{+5.31}_{-5.25}$	$80.45^{+8.96}_{-8.56}$
$m_H = 120 \text{ GeV}$	0.77 ± 0.12	1.64 ± 0.19	1.94 ± 0.25
$m_H = 125 \text{ GeV}$	1.36 ± 0.22	2.74 ± 0.32	3.44 ± 0.44
$m_H = 126 \text{ GeV}$	1.51 ± 0.24	2.99 ± 0.35	3.81 ± 0.49
$m_H = 130 \text{ GeV}$	2.14 ± 0.34	4.08 ± 0.47	5.39 ± 0.69
$m_H = 200 \text{ GeV}$	8.34 ± 1.06	13.25 ± 1.47	21.63 ± 2.48
$m_H = 350 \text{ GeV}$	4.79 ± 0.7	7.46 ± 0.99	12.65 ± 1.72
$m_H = 500 \text{ GeV}$	1.68 ± 0.39	2.58 ± 0.57	4.39 ± 0.98
Observed	32	47	93

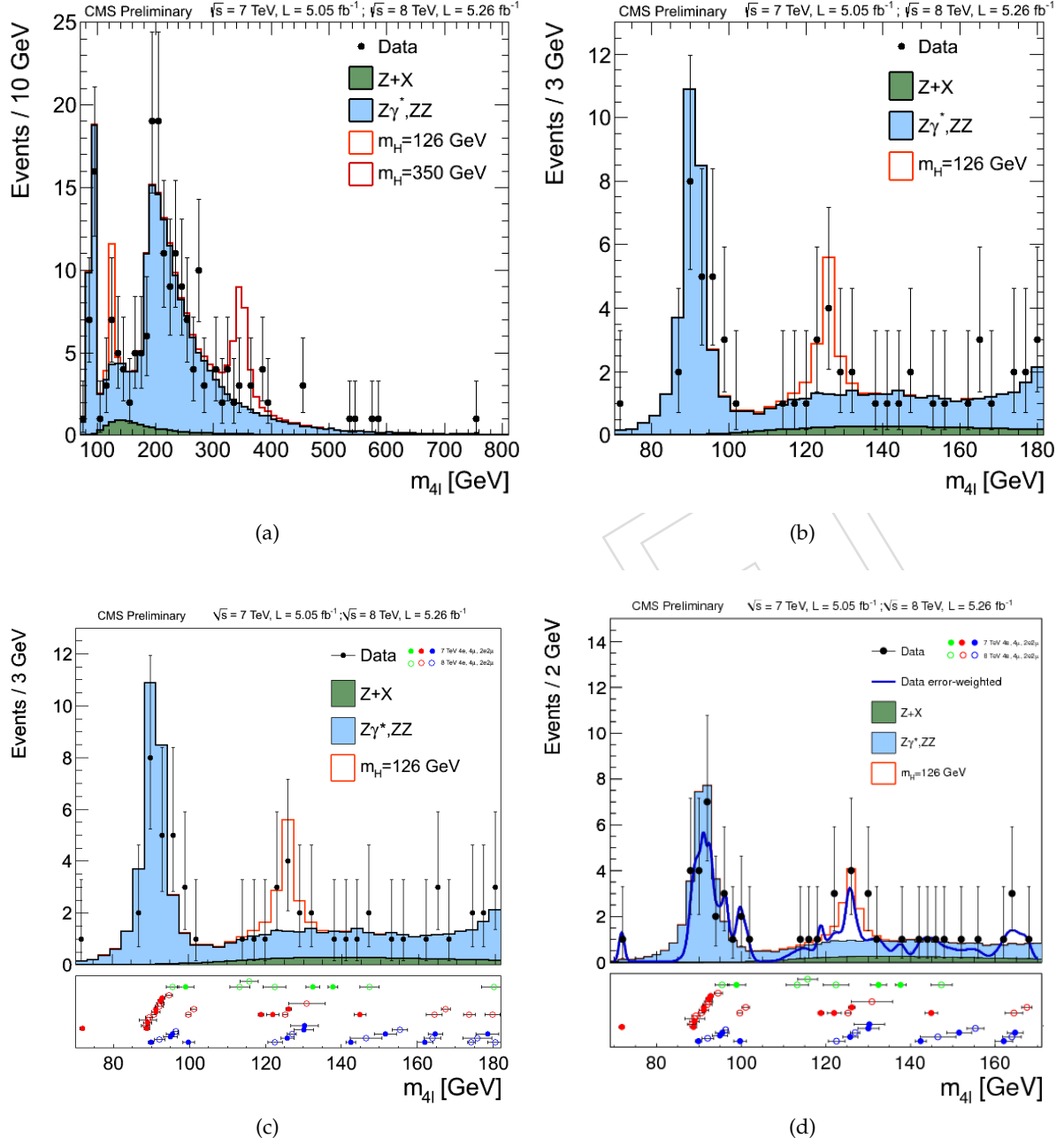


Figure 93: Distribution of the four-lepton reconstructed mass. Region $m_{4\ell} < 100$ GeV is shown but not used in analysis. The sample correspond to an integrated luminosity of $\mathcal{L} = 5.05 \text{ fb}^{-1}$ of 2011 data and $\mathcal{L} = 5.26 \text{ fb}^{-1}$ of 2012 data. The bottom plots show per-event-errors on the mass (left) and a sum of Gaussian distributions where each event observed in data is represented by a unit-area Gaussian.

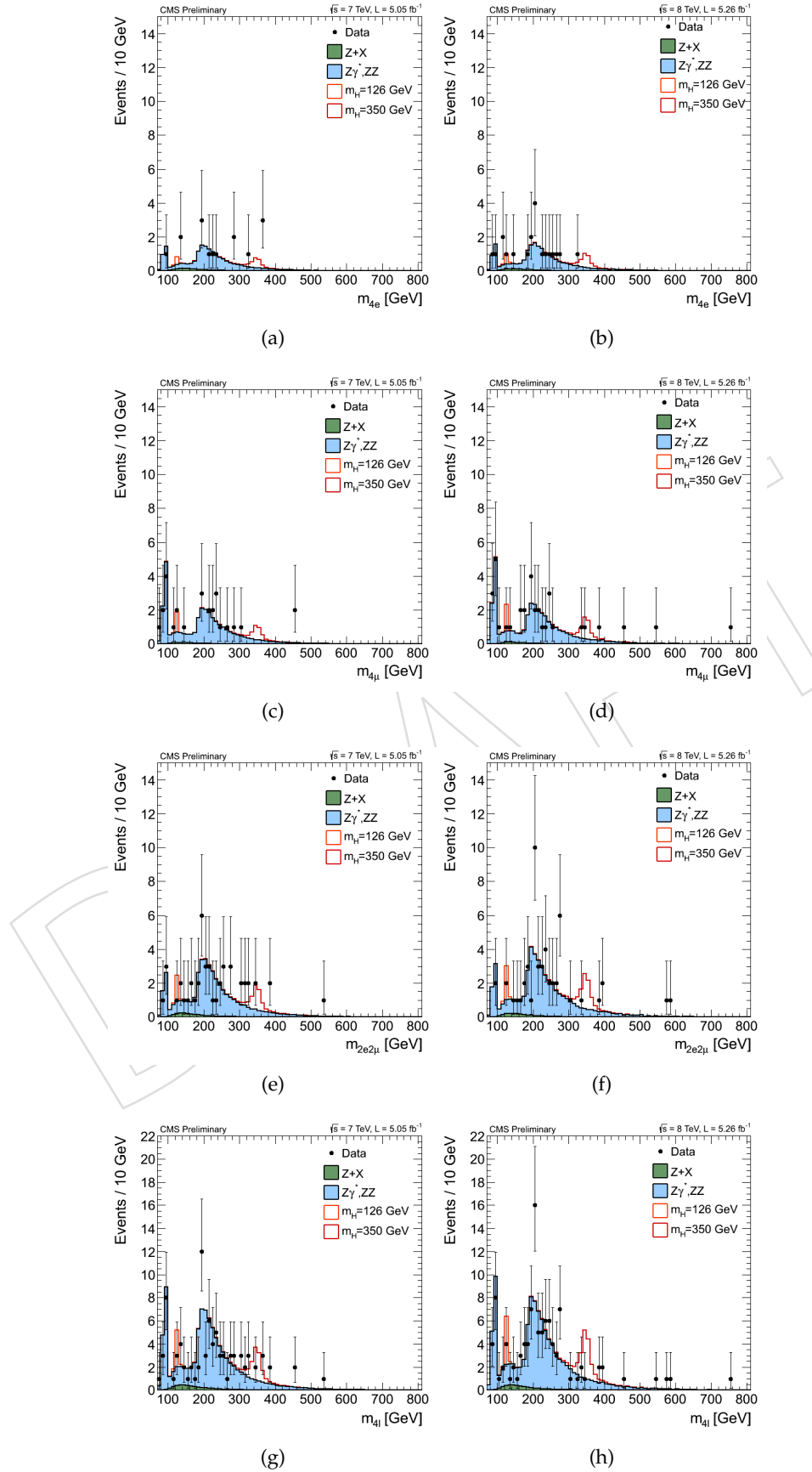


Figure 94: Distribution of the four-lepton reconstructed mass in several sub-channels: $4e$ (top), 4μ (middle top), $2e2\mu$ (middle bottom), for all channels combined (bottom) and for 7 TeV (left) and 8 TeV (right).

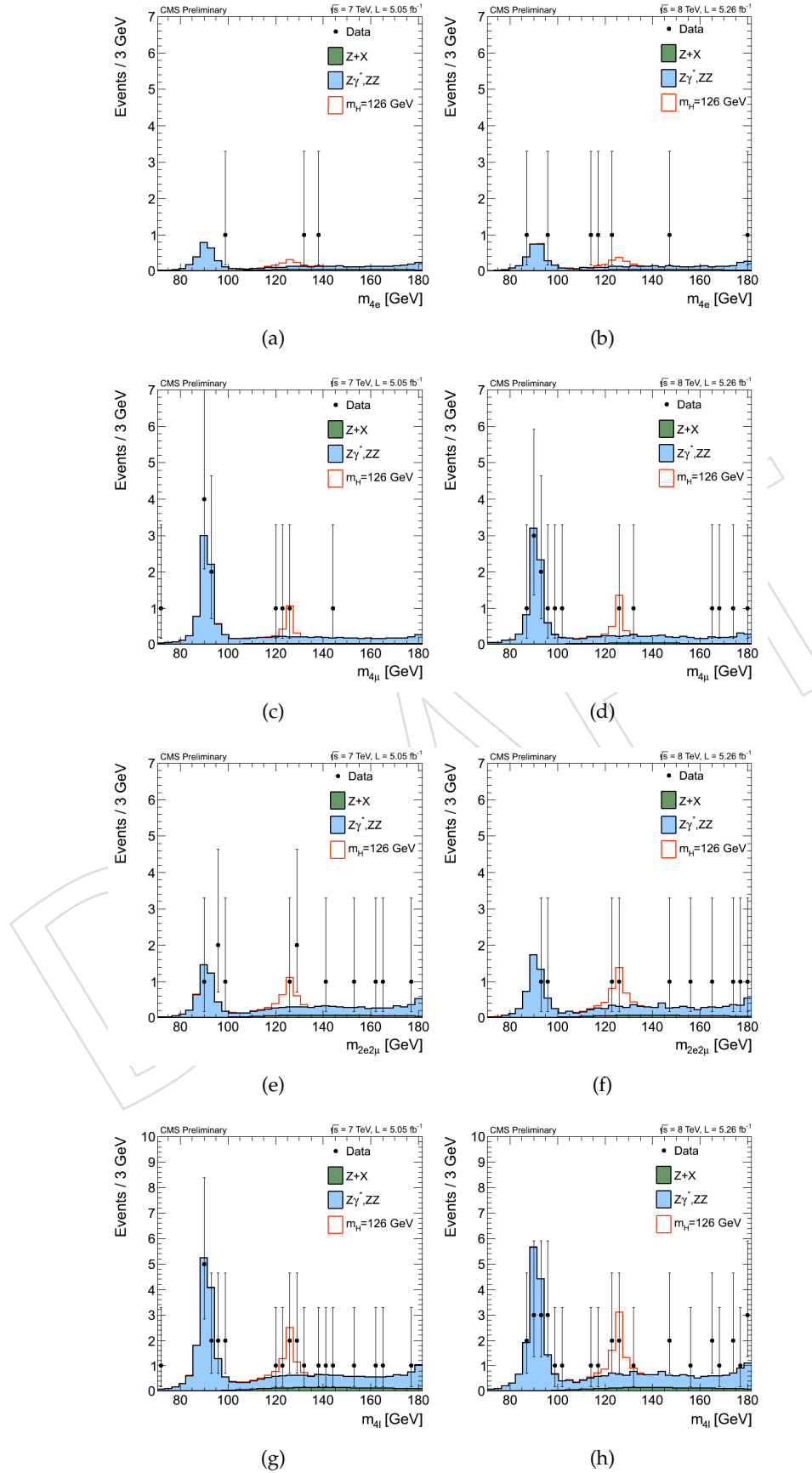


Figure 95: Distribution of the four-lepton reconstructed mass in the low-mass range in several sub-channels: $4e$ (top), 4μ (middle top), $2e2\mu$ (middle bottom), for all channels combined (bottom) and for 7 TeV (left) and 8 TeV (right).

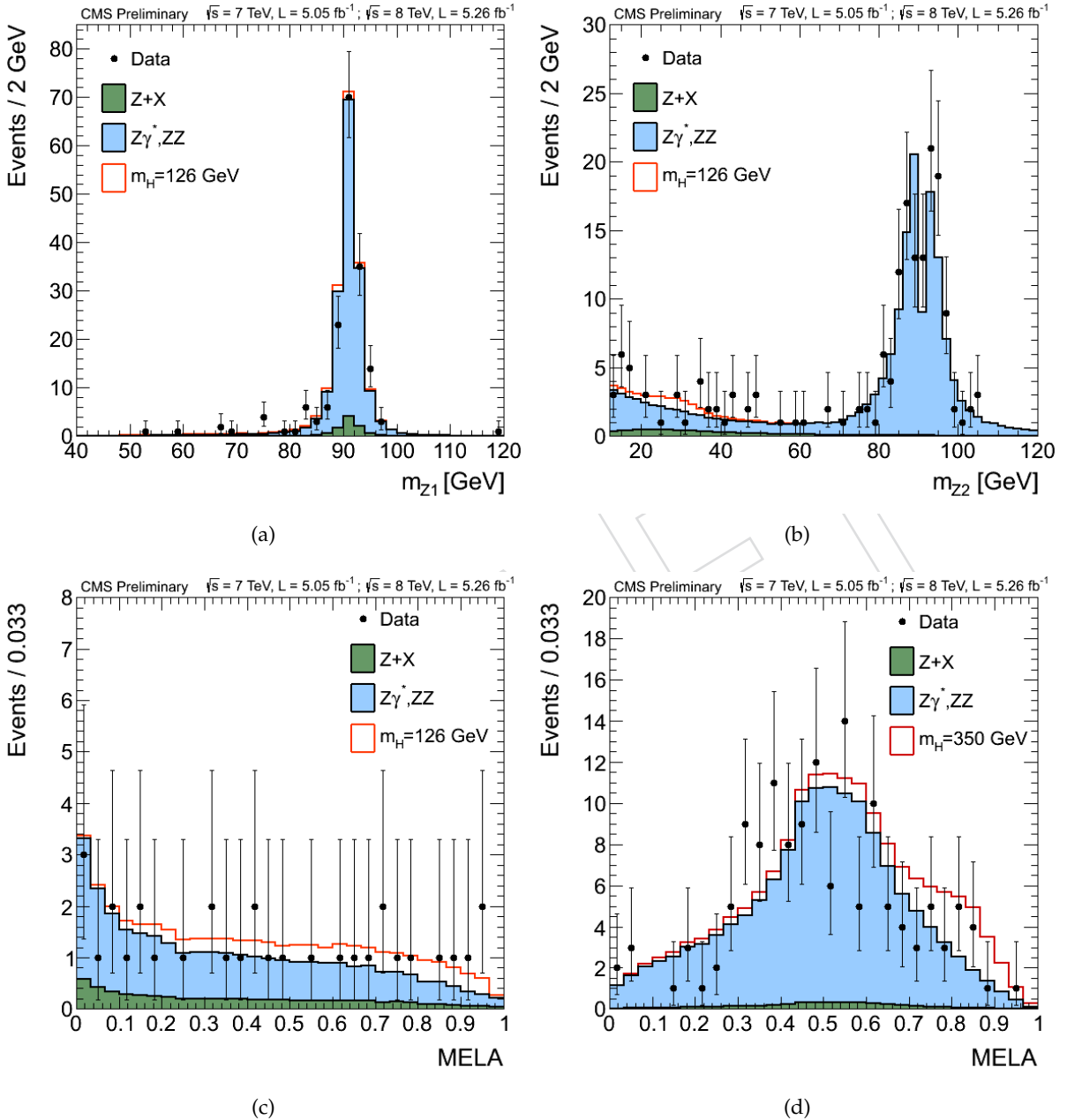


Figure 96: Distribution of Z_1 (top left) and Z_2 (top right) invariant mass, MELA KD in the mass range (100 - $180 \text{ GeV}/c^2$) on the bottom left and in the mass range (180 - $800 \text{ GeV}/c^2$) on the bottom right. The samples correspond to an integrated luminosity of $\mathcal{L} = 5.05 \text{ fb}^{-1}$ for the 7 TeV data, and 5.26 fb^{-1} for the 8 TeV data.

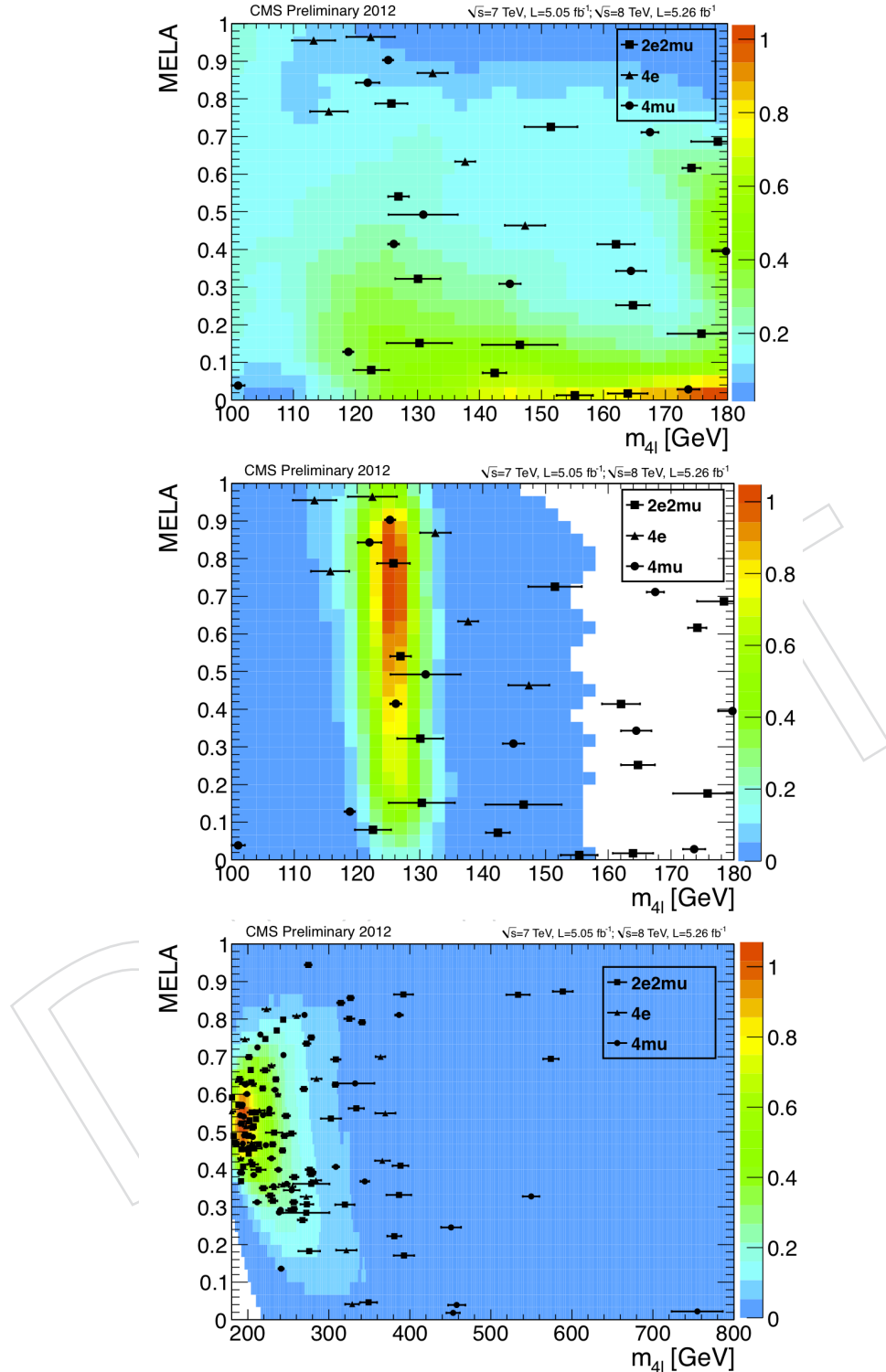


Figure 97: Distribution of the MELA KD versus the four-lepton reconstructed mass $m_{4\ell}$ for 2011 and 2012 data combined. Circles are 4μ events, triangles $4e$ events and squares $2e2\mu$ events. Event-by-event errors is attached to each event. Top plot: low-mass range with contours for background expectation. Middle plot: low-mass range with contours for signal expectation with $m_H = 126$ GeV. Bottom plot: high-mass range with contours for background expectation.

1880 13.3 FSR performances

1881 The FSR recovery algorithm affects eight events selected in 2011 and 2012 data. The properties of the
 1882 selected events are included in table ??.

$m_{4\ell}$	$m_{4\ell+\gamma}$	$p_T(\gamma)$	$\min(\ell, \gamma)$	Z affected
269.9	259.9	9.74	0.275	Z_1
126.1	114.8	7.67	0.308	Z_1
241.1	217.2	20.0	0.027	Z_1
197.9	193.0	4.04	0.072	Z_1
201.0	169.1	11.03	0.044	Z_1
333.9	312.9	8.21	0.0	Z_2
204.4	202.3	2.23	0.067	Z_2
122.5	113.6	4.48	0.053	Z_2

Table 29: Properties of the events with identified FSR photons in the processed dataset

1883 The observed FSR rate is $5 \pm 2\%$ and the overall efficiency gain $1.9 \pm 0.1\%$ both consistent with expec-
 1884 tation.

1885 In three of the FSR events, Z_2 is affected and this happens mainly at high four-lepton mass where Z_2 is
 1886 on-shell except one event at 122.5 GeV. The fact that the Z_2 is affected is a good indication that it could
 1887 be also a background event since the FSR rate in non-isolated objects is much higher.

1888 Figure 98 shows the complete spectrum before and after FSR is applied as well as the ratio of events
 1889 per bin before and after applying the FSR algorithm. The $Z \rightarrow 4\ell$ peak and the excess at 125 GeV are
 1890 enhanced by the FSR algorithm while the ZZ turn on becomes steeper.

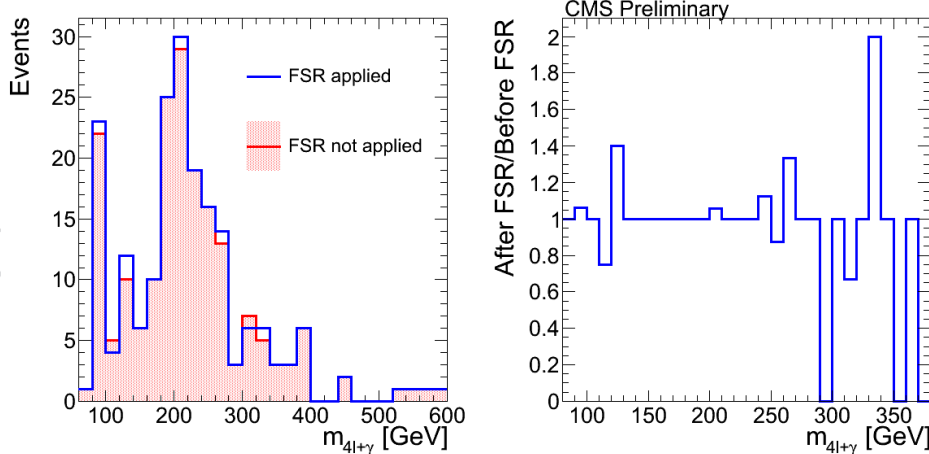


Figure 98: Invariant mass of the final selected events before and after FSR recovery (left) and ratio (right)

1891 13.4 Differences with respect to the 2011 PRL analysis

- 1892 In this section we describe the differences in the events selected by current analysis with respect to the
 1893 2011 PRL analysis. The main differences between the two selections are the isolation with the use of the
 1894 PF isolation (cone of $\Delta R = 0.4$) in the current analysis, and the lepton identification with in particular
 1895 the use of the multivariate analysis for the electron identification.
- 1896 In Table 30 the number of events selected in current 7 TeV analysis and in the PRL analysis is given, in
 1897 the full mass range. Out of 6 events that were in the PRL and are not in the current analysis 5 of them
 1898 failed isolation and one failed the electron ID.

	4e	4μ	2e2 μ	total
Current analysis	14	20	43	77
PRL analysis	12	21	37	70
PRL not Current	2	3	1	6
Current not PRL	4	2	7	13

Table 30: Number of events selected in the current 7 TeV analysis with respect to the number of events selected in the PRL analysis.

1899 Migrations of events in the previously blinded mass region between 110 and 140 GeV have been studied
 1900 in details and the reasons for migrations are summarized in the table 31. In addition to the events from
 1901 the table 30 one μ event migrated from $m_{4l} = 114.8$ GeV in PRL analysis to the $m_{4l} = 126.1$ due to the
 1902 application of the FSR recovery algorithm, which is now the part of the analysis. More details about
 1903 specific events are given in the events dump in the Appendix D.

Channel	Current	PRL	m_{4l} (GeV)	reason for migration
4μ	NO	YES	118.9	Failed isolation, mainly due to a PF photon at $\delta R = 0.34$
4μ	NO	YES	119.0	Failed isolation, several PF charged hadrons within $\Delta R < 0.3$
4e	NO	YES	125.7	Failed electron ID
4μ	YES	NO	122.0	$p_T > 20, 10$ GeV requested now to any two leptons (in the PRL it was requested for leptons from Z_1)
4μ	YES	YES	$114.8 \rightarrow 126.1$	FSR recovery

Table 31: Migration of events in the blinded region between the current analysis and the 2011 PRL analysis.

13.5 Summary of systematic uncertainties

The summary of systematic uncertainties for the analysis parts on 2011 and 2012 collected data is provided in the Tab. 32, 33, 34, 35. All systematic uncertainties are correlated between 7 and 8 TeV samples except uncertainty on luminosity. Log-normal uncertainty on Z+jets normalization is correlated between 7 and 8 TeV samples, but it is correlated between different final states (i.e. it is correlated for 4e 7 TeV and 4e 8 TeV, but it is not correlated for example for 4e and 4mu). Uncertainties affecting muons and electrons are correlated to any other channel that contains those objects and are given combined and per event. Uncertainties on MELA template shapes are introduced through alternative shapes which are representing 1 sigma errors.

Table 32: Simulated samples for 7 TeV: Summary of the magnitude of theoretical and phenomenological systematic uncertainties in percent for $H \rightarrow ZZ \rightarrow 4\ell$ and $ZZ \rightarrow 4\ell$. Errors are common to all 4ℓ channels. Last three lines are parametric uncertainties on the shape of the HZZ4L signal Crystal Ball (mean, sigma and tail parameter).

Source of uncertainties	Error for different processes						
	ggH	VBF	WH	ZH	ttH	ZZ	ggZZ
gg partonic luminosity	7.5-10				0-10		10
$qq/q\bar{q}$ partonic luminosity		2.2-4.7	0-4.5	0-5.0		5	
QCD scale uncert. for $gg \rightarrow H$	8.7-10						
QCD scale uncert. for VBF qqH		0-1.5					
QCD scale uncert. for VH			0-0.75	0-1.3			
QCD scale uncert. for ttH					0-8.3		
4ℓ -acceptance for $gg \rightarrow H$	negl.	negl.	negl.	negl.	negl.		
Wide Higgs uncertainties			$1 + 1.5 \times (m_H/1\text{TeV})^3$				
Uncertainty on $BR(H \rightarrow 4\ell)$	2	2	2	2	2		
QCD scale uncert. for $ZZ(\text{NLO})$						2.6-6.7	
QCD scale uncert. for $gg \rightarrow ZZ$							24-44
CB mean, parametric			0.4				
CB sigma, parametric			20				
CB tail parameter, parametric			5.0				

Table 33: Simulated samples for 8 TeV: Summary of the magnitude of theoretical and phenomenological systematic uncertainties in percent for $H \rightarrow ZZ \rightarrow 4\ell$ and $ZZ \rightarrow 4\ell$. Errors are common to all 4ℓ channels. Last three lines are parametric uncertainties on the shape of the HZZ4L signal Crystal Ball (related to scale and resolution uncertainties mean, sigma, and tail parameter).

Source of uncertainties	Error for different processes						
	ggH	VBF	WH	ZH	ttH	ZZ	ggZZ
gg partonic luminosity	7.2-9.2				0-9.8		10
$q\bar{q}/q\bar{q}$ partonic luminosity		1.2-1.8	0-4.5	0-5.0		5	
QCD scale uncert. for $gg \rightarrow H$	5.5-7.9						
QCD scale uncert. for VBF $q\bar{q}H$		0.1-0.2					
QCD scale uncert. for VH			0-0.6	0-1.5			
QCD scale uncert. for ttH					0-8.8		
4ℓ -acceptance for $gg \rightarrow H$	negl.	negl.	negl.	negl.	negl.		
Wide Higgs uncertainties			1 + $1.5 \times (m_H/1\text{TeV})^3$				
Uncertainty on $BR(H \rightarrow 4\ell)$	2	2	2	2	2		
QCD scale uncert. for $ZZ(\text{NLO})$						2.6-6.7	
QCD scale uncert. for $gg \rightarrow ZZ$							24-44
CB mean, parametric			0.4				
CB sigma, parametric			20				
CB tail parameter, parametric			5.0				

Table 34: 7 and 8 TeV samples: Summary of the magnitude of instrumental systematic uncertainties in percent for $H \rightarrow ZZ \rightarrow 4\ell$ and $ZZ \rightarrow 4\ell$. The instrumental systematic uncertainties for all five Higgs boson production mechanisms are assumed to be same, similarly on $ZZ \rightarrow 4\ell$ (NLO) and $gg \rightarrow ZZ \rightarrow 4\ell$.

Source of uncertainties	Error for different processes					
	$H \rightarrow ZZ \rightarrow 4\ell$		$ZZ/ggZZ \rightarrow 4\ell$			
	$4e$	4μ	$2e2\mu$	$4e$	4μ	$2e2\mu$
Luminosity	2.2 (5 for 8 TeV)					
Trigger	1.5%					
electron reco/ID/isolation (4e)	6.2-11					
muon reco/ID/isolation (4mu)	1.9					

Table 35: 7 and 8 TeV samples: Summary of the magnitude of systematic uncertainties (asymmetric) in percent for the reducible 4ℓ backgrounds (for 8 TeV in parenthesis). There are several uncertainties (as described earlier in the paper). Below we give the combined uncertainty.

$4e$	4μ	$2e2\mu$
-40..+90 (-30..+90)	-	-
-	-40..+60 (-40..+80)	-
-	-	-50..+60 (-30..+100)

14 Statistical Analysis

14.1 Methodology using 2D distributions ($m_{4\ell}$, KD)

1915 The ($m_{4\ell}$, KD) unbinned distributions of the selected events are split into six categories based on three
 1916 final states (4μ , $4e$, $2\mu 2e$) and two running periods (7 and 8 TeV). These events are examined for 183
 1917 hypothetical Higgs boson masses m_H in a range between 110 GeV and 600 GeV, where the mass steps
 1918 are optimized to account for the expected width, Γ , and resolution for measurement of m_H [105]. For
 1919 each mass hypothesis, we perform a simultaneous likelihood fit of the six two-dimensional ($m_{4\ell}$, KD)
 1920 distributions using the statistical approaches discussed in Ref. [105]. As a cross-check, we have also
 1921 studied one-dimensional $m_{4\ell}$ distributions and found consistent, but systematically higher median ex-
 1922 pected limits. We adopt the modified frequentist construction CL_s [105–107] as the primary method
 1923 for reporting limits. As a complementary method to the frequentist paradigm, we use the Bayesian
 1924 approach [108] and find consistent results.

1925 The probability distribution of $\mathcal{P}^{1D}(m_{4\ell})$ for the background is parameterized with empirical functions
 1926 using MC simulation for ZZ background and data control regions for Z + X background. The recon-
 1927 structed signal $m_{4\ell}$ distributions are described with a relativistic Breit-Wigner parametrization convo-
 1928 luted with a two-sided Crystal-Ball function [109]. The correlated two-dimensional ($m_{4\ell}$, KD) distribu-
 1929 tion is described by the two-dimensional probability distribution $\mathcal{P}(m_{4\ell}, \text{KD})$ for signal and background
 1930 as follows

$$\mathcal{P}_{\text{sig}}(m_{4\ell}, \text{KD}) = \mathcal{P}_{\text{sig}}^{1D}(m_{4\ell}) \times \mathcal{T}_{\text{sig}}(m_{4\ell}, \text{KD}) \quad (33)$$

$$\mathcal{P}_{\text{bkg}}(m_{4\ell}, \text{KD}) = \mathcal{P}_{\text{bkg}}^{1D}(m_{4\ell}) \times \mathcal{T}_{\text{bkg}}(m_{4\ell}, \text{KD}) \quad (34)$$

1931 where $\mathcal{P}_{\text{sig}}^{1D}(m_{4\ell})$ and $\mathcal{P}_{\text{bkg}}^{1D}(m_{4\ell})$ are the analytical 1D distributions used in 1D fits. The 2D distributions
 1932 $\mathcal{T}_{\text{sig}}(m_{4\ell}, \text{KD})$ and $\mathcal{T}_{\text{bkg}}(m_{4\ell}, \text{KD})$ are templates, or 2D histograms, which are normalized in the KD di-
 1933 rection at any given value of $m_{4\ell}$. This ensures that projections of the 2D functions in Eqs. (33) and (34)
 1934 on $m_{4\ell}$ are identical to analytical $\mathcal{P}_{\text{sig}}^{1D}(m_{4\ell})$ and $\mathcal{P}_{\text{bkg}}^{1D}(m_{4\ell})$ distributions. The templates are created from
 1935 simulated samples and are shown in Fig. 99 and 100 for low and high mass ranges, respectively.

1936 At the low mass, different electron and muon p_T thresholds and efficiencies affect kinematics. Therefore,
 1937 KD distributions may be different between $4e$, 4μ , and $2e2\mu$ channels. We keep templates different at
 1938 low mass. However, at high mass low p_T thresholds do not affect kinematics (angles only) much and
 1939 we have a joint template distributions for the three channels. We also combine 7 TeV and 8 TeV samples,
 1940 since kinematics is the same in both cases. Still, due to limited statistics in the background MC samples
 1941 available, population of events in the bins of templates may be limited, or even zero, at high mass (in the
 1942 tail of the $m_{4\ell}$ distribution). We apply a smoothing procedure such that when the number of simulated
 1943 events entering the bin is low, the bin value is averaged over the range of 3×3 bins for $m_{4\ell} < 180$ GeV,
 1944 5×5 for $180 < m_{4\ell} < 300$ GeV (with the exception of KD near zero), 7×7 for $m_{4\ell} > 300$ GeV. There is
 1945 an overall protection that no template bin should have zero probability.

1946 As it was shown earlier, both $q\bar{q} \rightarrow ZZ$ and Z + X background can be described by the same tem-
 1947 plates and any small potential difference is covered by systematics, which is taken to be 100% correlated
 1948 between different channels and LHC run periods.

14.2 Limits

1950 In Fig. 101 we show expected limits obtained with a fit of the ($m_{4\ell}$, KD) distribution. In Fig. 102 results
 1951 for 7 TeV and 8 TeV data are shown separately.

14.3 Significance of excesses

1953 In Fig. 103 we show the significance of the local fluctuation with respect to the Standard Model expec-
 1954 tation. These significances are shown separately for 7 and 8 TeV data in Fig. 104 and for the comparisin
 1955 between 1D and 2D fits in Fig. 105.

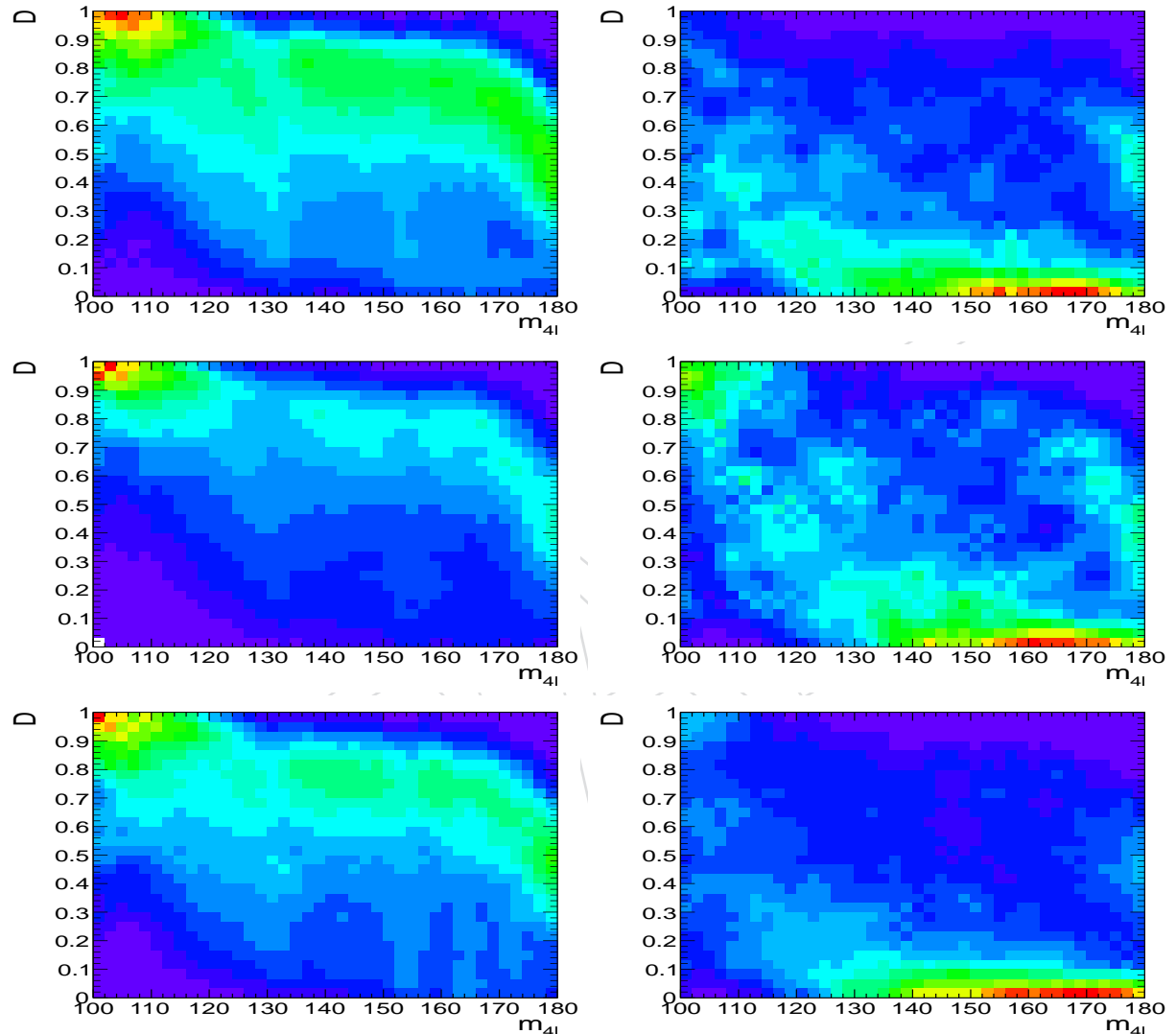


Figure 99: Parameterization signal and $q\bar{q} \rightarrow ZZ$ background template distributions $\mathcal{T}_{\text{sig}}(m_{4\ell}, \text{KD})$ (left) and $\mathcal{T}_{\text{bkg}}(m_{4\ell}, \text{KD})$ (right) from Eqs. (33) and (34) in three channels: $2e2\mu$ (top), $4e$ (middle), and 4μ (bottom).

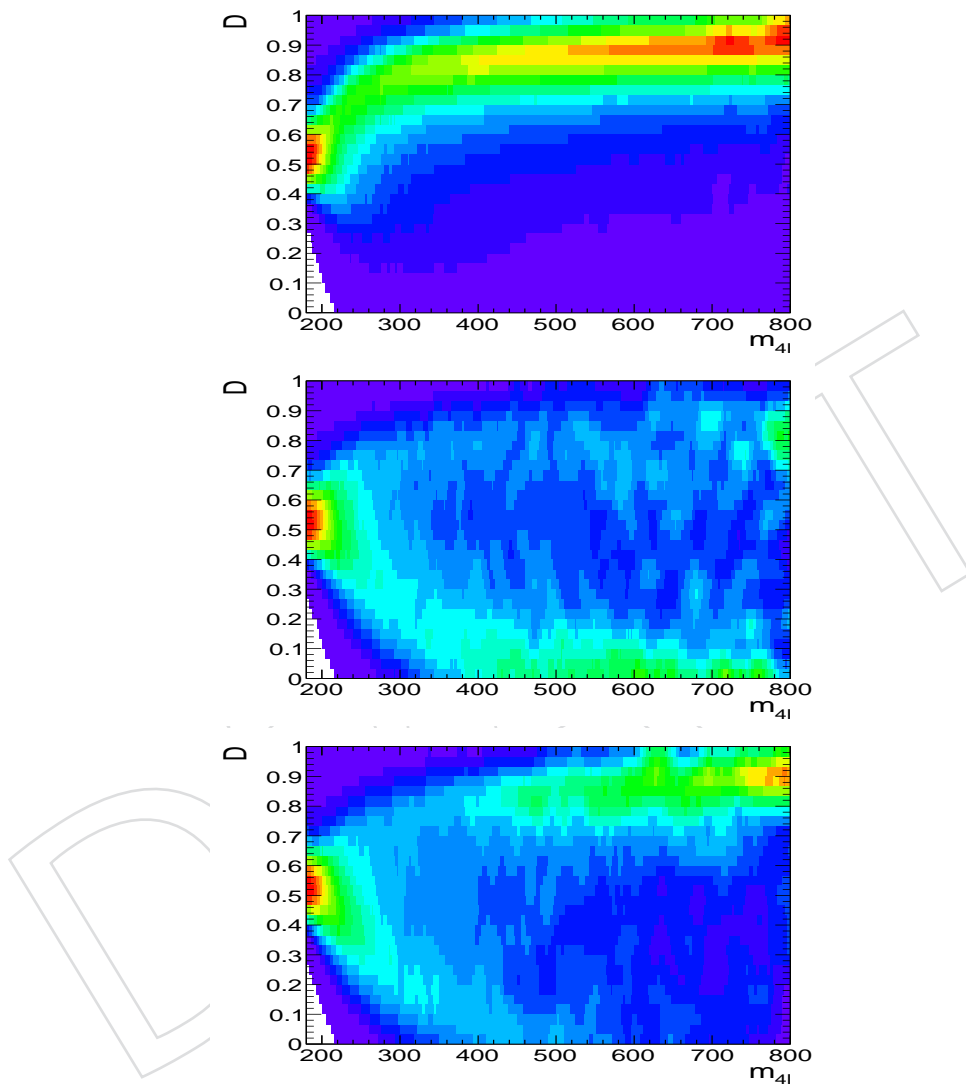


Figure 100: Parameterization of template distributions $\mathcal{T}(m_{4\ell}, \text{KD})$ for signal (top), $q\bar{q} \rightarrow ZZ$ background (middle), and $gg \rightarrow ZZ$ background (bottom).

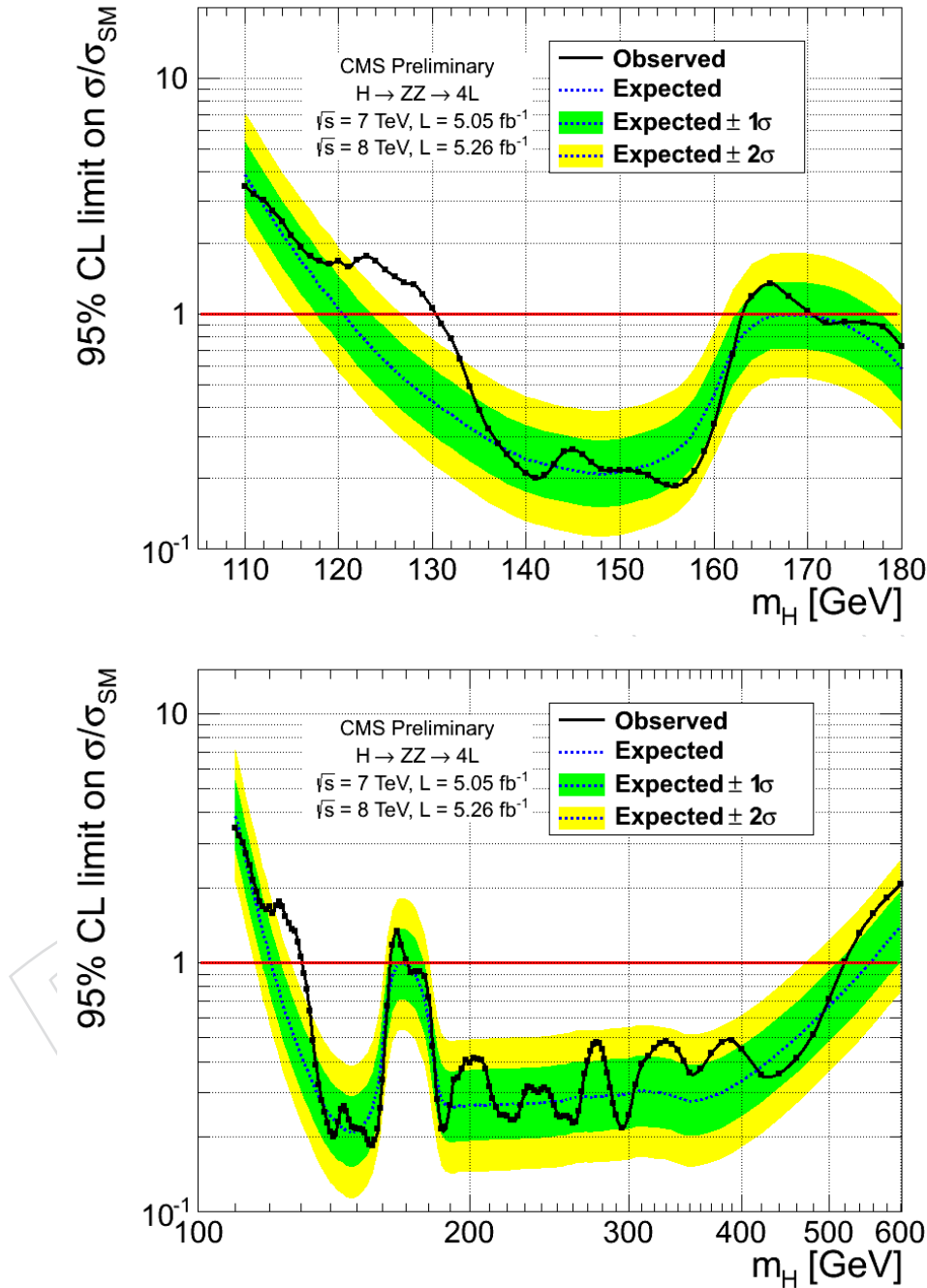


Figure 101: Observed and expected 95% CL upper limit on the ratio of the production cross section to the SM expectation with the 2D fit. 2011 and 2012 data-samples are used. The 68% and 95% ranges of expectation for the background-only model are also shown with green and yellow bands, respectively. Top plot: lower mass range only, bottom plot: full mass range.

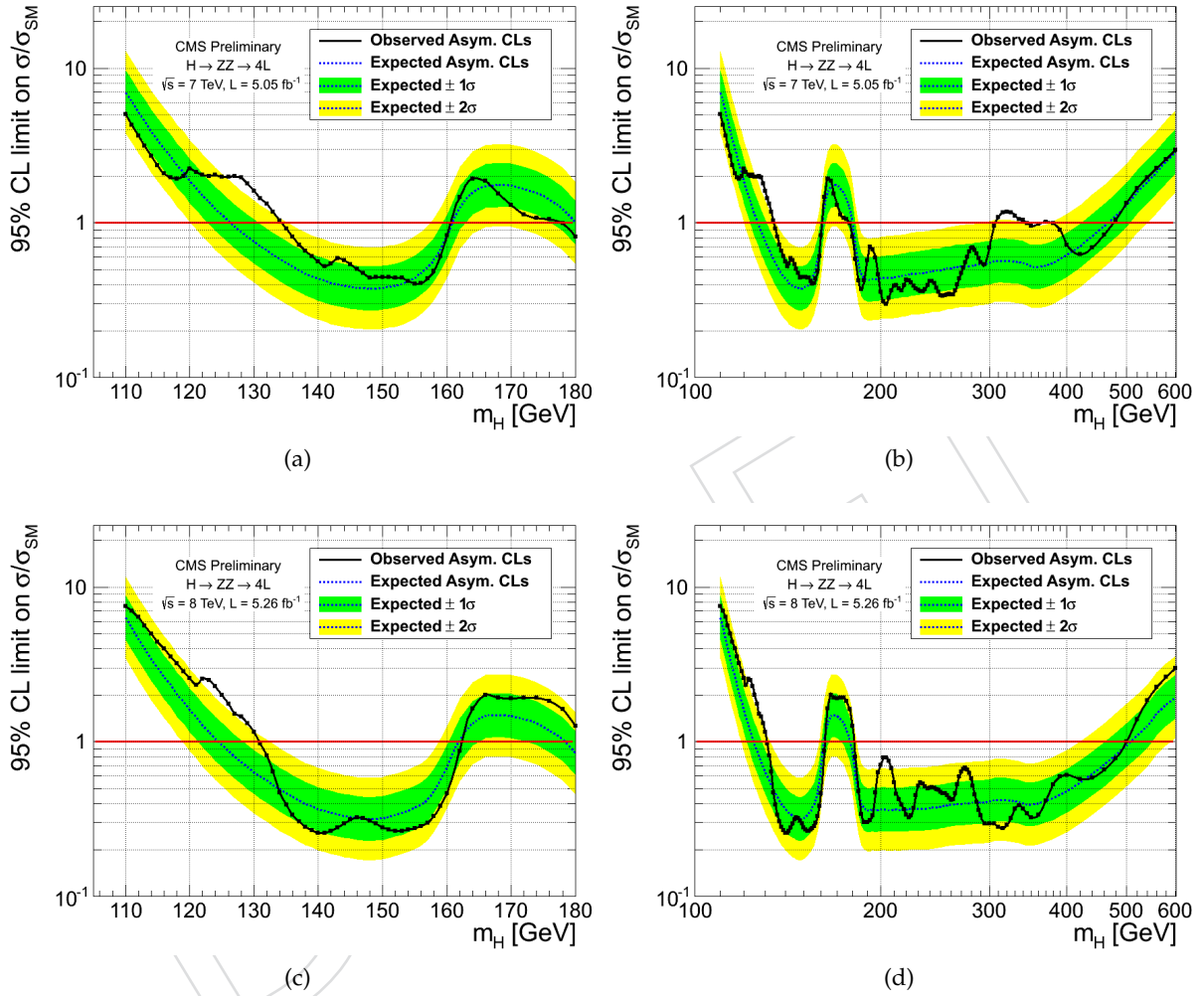


Figure 102: Observed and expected 95% CL upper limit on the ratio of the production cross section to the SM expectation with the 2D fit. The 68% and 95% ranges of expectation for the background-only model are also shown with green and yellow bands, respectively. Left plots: low mass range only, right plots: full mass range. Top plots: 7 TeV data, bottom plots: 8 TeV data.

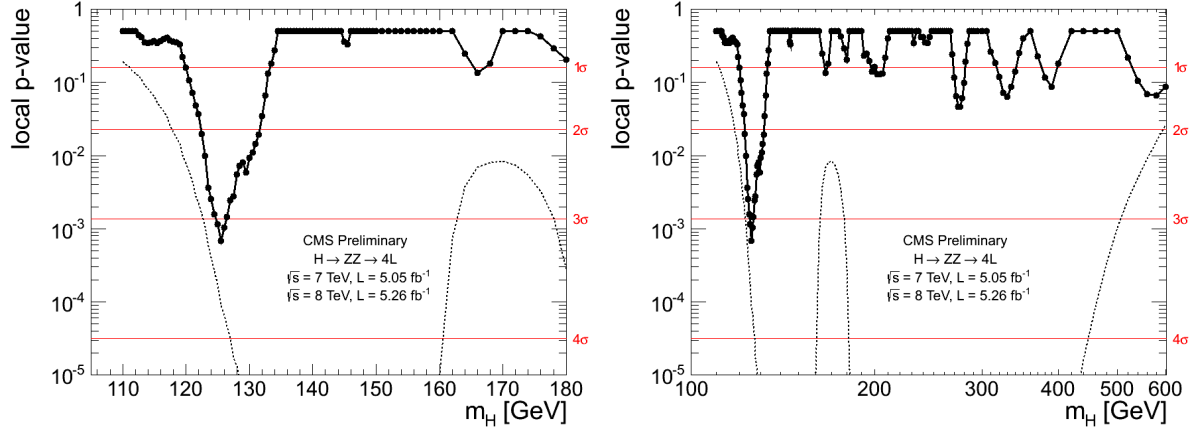


Figure 103: Significance of the local fluctuations with respect to the standard model expectation as a function of the Higgs boson mass for an integrated luminosity of 5.05 fb^{-1} at 7 TeV and 5.26 fb^{-1} at 8 TeV in the low mass range ($110\text{-}180 \text{ GeV}/c^2$) on the left and in the mass range ($110\text{-}600 \text{ GeV}/c^2$) on the right. Dashed line shows mean expected significance of the SM Higgs signal for a given mass hypothesis.

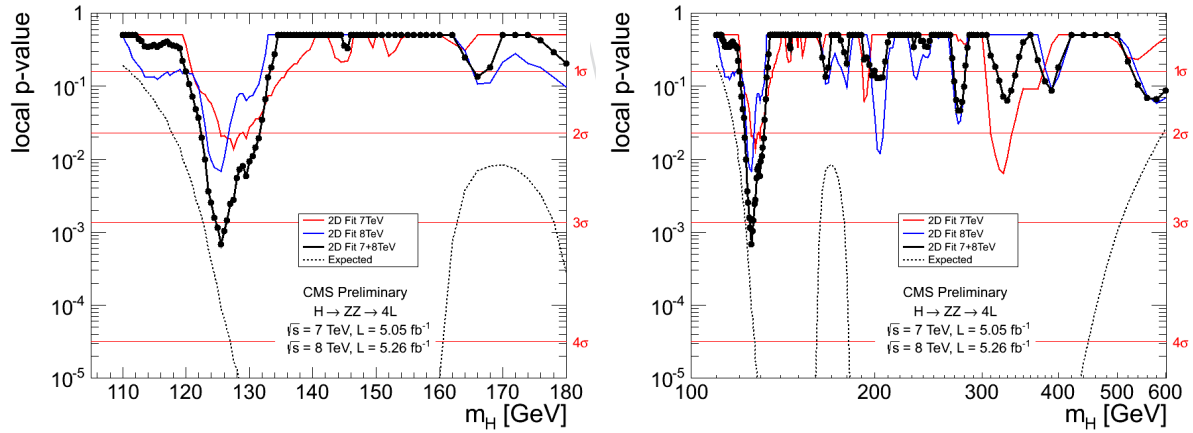


Figure 104: Significance of the local fluctuations with respect to the standard model expectation as a function of the Higgs boson mass for an integrated luminosity of 5.05 fb^{-1} at 7 TeV (red), 5.26 fb^{-1} at 8 TeV (blue) and the full dataset combined (black), in the low mass range ($110\text{-}180 \text{ GeV}/c^2$) on the left and in the mass range ($110\text{-}600 \text{ GeV}/c^2$) on the right. Dashed line shows mean expected significance of the SM Higgs signal for a given mass hypothesis.

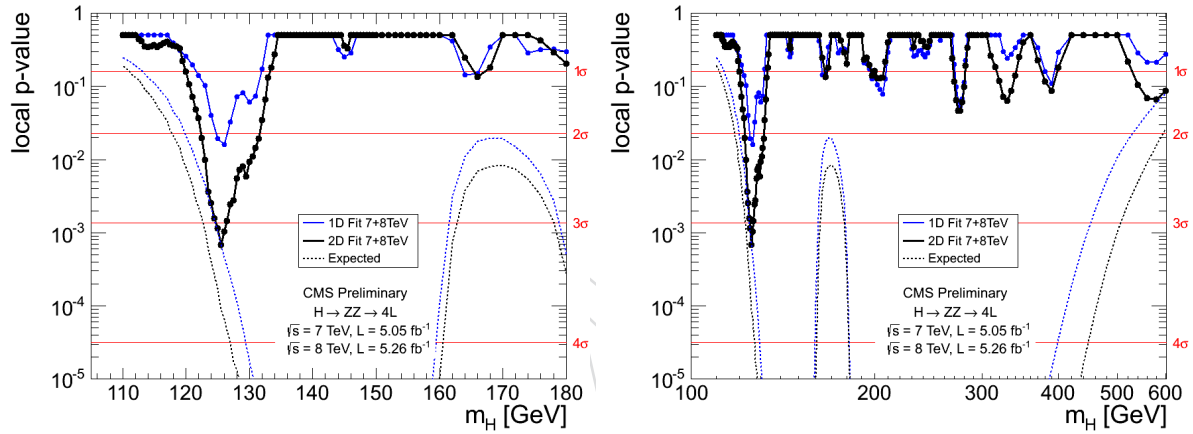


Figure 105: Significance of the local fluctuations with respect to the standard model expectation as a function of the Higgs boson mass for an integrated luminosity of 5.05 fb^{-1} at 7 TeV and 5.26 fb^{-1} at 8 TeV with a 1D (blue) and 2D (black) analysis, in the mass range (110-180 GeV/c^2) on the left and in the mass range (110-600 GeV/c^2) on the right. Dashed line shows mean expected significance of the SM Higgs signal for a given mass hypothesis.

1956 14.4 Approach to Higgs Boson Mass Measurements

1957 Thanks to excellent mass resolution of HZZ4L, it will play a leading role in determination of Higgs boson
 1958 mass once it's observed on LHC. This will be done via likelihood scanning over the space of Higgs boson
 1959 mass m_H vs. signal strength μ , which requires m_H to be included in the likelihood function.

1960 In order to construct a likelihood function which is m_H dependent, one need to parameterize all inputs
 1961 information against m_H . The following information are parameterized: Higgs cross section branching
 1962 ratio, Higgs signal selection efficiency, Signal shape CB function parameters CBmean, CBsigma,
 1963 CBalpha, and CBn. At low mass region (< 150 GeV), the Higgs decay width is negligible comparing
 1964 to experimental detector resolution, so no convolution with Breit Wigner is used. All uncertainties (including
 1965 uncertainties on normalization and CB mean, sigma, alpha) are the same among mass points.

1966 We perform a likelihood scanning on 2011+2012 analysis, the result is shown on figure 106. At each point
 1967 (m_H, μ), the likelihood is minimized w.r.t. all nuisance parameters. The global minimum is located at
 1968 $m_H = 126$ GeV and $\mu = 0.9$. The 68% and 95% confidence level contours are also shown on the plots.

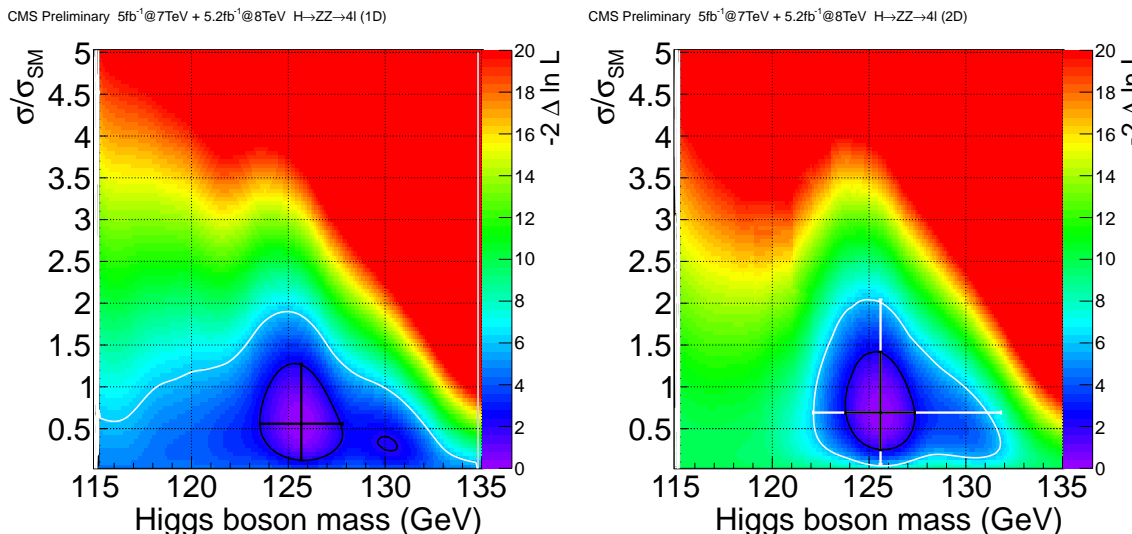


Figure 106: Likelihood scan on Higgs mass vs. signal strength. The two crosses in white and black are the 1 sigma and 2 sigma uncertainties from MINOS fit. The two ellipses correspond to 68% and 95% CL contours. Left plot: 1D fit, right plot: 2D fit (with MELA KD).

1969 14.5 Approach to Higgs Boson Spin and Property Measurements

1970 If a new resonance is observed on LHC, it will be crucial to determine the spin and quantum numbers
 1971 of the new particle and its couplings to Standard Model fields as accurately as possible. The full-case
 1972 study has been presented in Ref. [101] and CMS internal study in Ref. [110]. Here we adopt a simplified
 1973 version of that approach following the MELA methodology in Section 12, where instead of signal-to-
 1974 background probability ratio we construct probability ratio for two signal hypotheses. The discriminant
 1975 for signal hypothesis testing is constructed as follows

$$KD^H = \frac{\mathcal{P}_{\text{sig1}}}{\mathcal{P}_{\text{sig1}} + \mathcal{P}_{\text{sig2}}} = \left[1 + \frac{\mathcal{P}_{\text{sig2}}(m_1, m_2, \vec{\Omega} | m_{4\ell})}{\mathcal{P}_{\text{sig1}}(m_1, m_2, \vec{\Omega} | m_{4\ell})} \right]^{-1} \quad (35)$$

1976 where the probabilities for two signal hypotheses "sig1" and "sig2" (for example scalar and pseudo-
 1977 scalar Higgs, or a spin-2 particle with minimal set of couplings to vector bosons) are calculated analyti-
 1978 cally and are quoted in Ref. [101].

1979 Here we illustrate the power of the above approach with the example of a narrow resonance at 125 GeV
 1980 with two hypotheses scalar ($J^P = 0^+$) and pseudo-scalar ($J^P = 0^-$) Higgs. The alternative hypotheses

1981 of a resonance are produced with the generator from Ref. [101] (JHU generator). Similarly to discussion
 1982 in Section 12, the seven observables $\{m_1, m_2, \vec{\Omega}\}$ appear different for resonances with different quantum
 1983 numbers, as shown in Fig. 107 with generated samples.

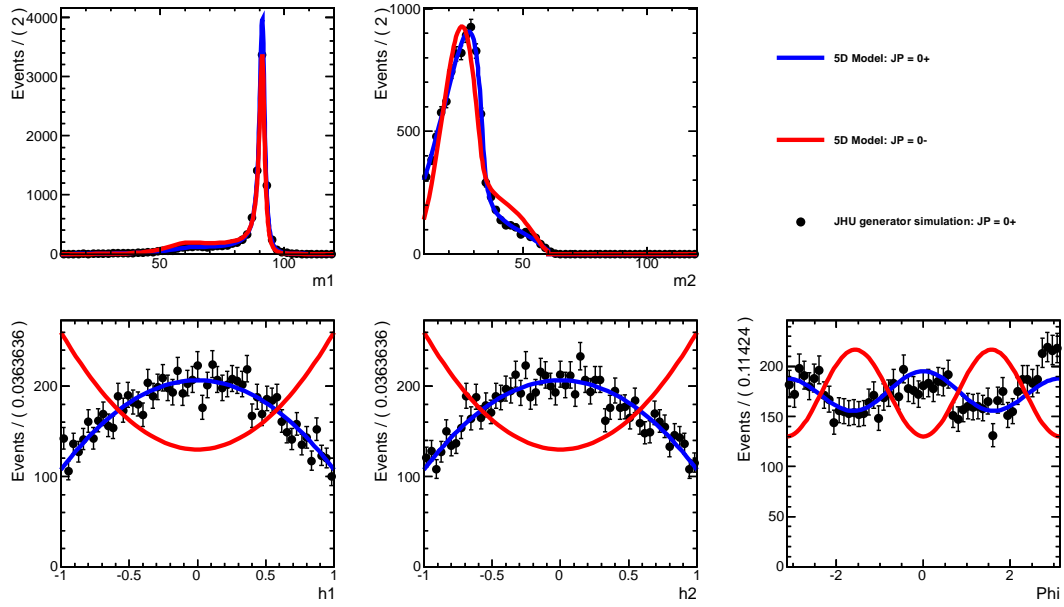


Figure 107: Distribution of the observables in the top row: m_1 , m_2 (where $m_1 > m_2$), bottom row: $\cos \theta_1$, $\cos \theta_2$, and Φ generated for $m_X = 125$ GeV with the JHU generator and projections of the ideal angular distributions. Two resonance hypotheses are shown: $J^P = 0^+$ and 0^- .

1984 We perform further statistical analysis of the generated samples with signal and background yields
 1985 expected with 20/fb of data (about 14 events for $m_H = 125$ GeV). The analysis used the 2D distribution
 1986 ($KD^H, m_{4\ell}$) in the same way as for signal-to-background separation. Ideally the fit should include all
 1987 three observables with KD as well, but for simplicity we omit it here. In the future this could be done
 1988 either with a 3D fit, or with a cut on KD and fit of the 2D distribution ($KD^H, m_{4\ell}$). We follow the
 1989 methodology of Ref. [101] and construct the parameter $2 \ln(\mathcal{L}_1 / \mathcal{L}_2)$ with the likelihood \mathcal{L} evaluated for
 1990 two models. The separation between the two hypotheses depends on the Higgs mass and is about 2.1σ
 1991 for $m_H = 125$ GeV, see Fig. 108. In other words, the hypotheses of the scalar ($J^P = 0^+$) and pseudo-scalar
 1992 ($J^P = 0^-$) Higgs can be separated already at 95% CL with the signal observation with significance of a
 1993 little over 3σ . Separation of other hypotheses (such as spin-two) can follow easily in a similar manner.

1994 Distributions of the pseudoMELA discriminant (for scalar-to-pseudoscalar separation) are shown in
 1995 Fig. 109. These distributions are shown for mass around 125 GeV and for signal and background. We
 1996 also show distributions of the graviMELA discriminant optimized for separation of $J^P = 0^+$ and 2^+
 1997 (minimal couplings) hypotheses. However, separation of the latter hypotheses seems to be limited and
 1998 further studies are pending inclusion of the full CMSSW MC samples.

1999 Technical implementation with the CMS Higgs combination tools is shown in Fig. 110. In this fit, instead
 2000 of the 2D fit of ($MELA, m_{4\ell}$) distribution, we fit (pseudoMELA, $m_{4\ell}$) distribution. The observed value
 2001 is indicated by an arrow and corresponds to a toy MC experiment. With the current 7 TeV (5.05/fb)
 2002 and 8 TeV (3.68/fb) dataset, the expected significance is 2.9σ and the average hypothesis separation
 2003 significance is 1.6σ . In any particular experiment separation from either 0^+ or 0^- hypothesis may vary
 2004 depending on statistical distribution of events. All systematic uncertainties included in the nominal
 2005 analysis are incorporated in the hypothesis separation analysis as well. Since instead of the MELA
 2006 observable we now use pseudoMELA, we have explicitly checked that all the same effects apply here
 2007 as well. For example the shape of pseudoMELA for $Z + X$ background could be well modeled by the
 2008 $q\bar{q} \rightarrow ZZ$, as shown in Fig. 111. Any residual systematic effects are small and are accounted in the same

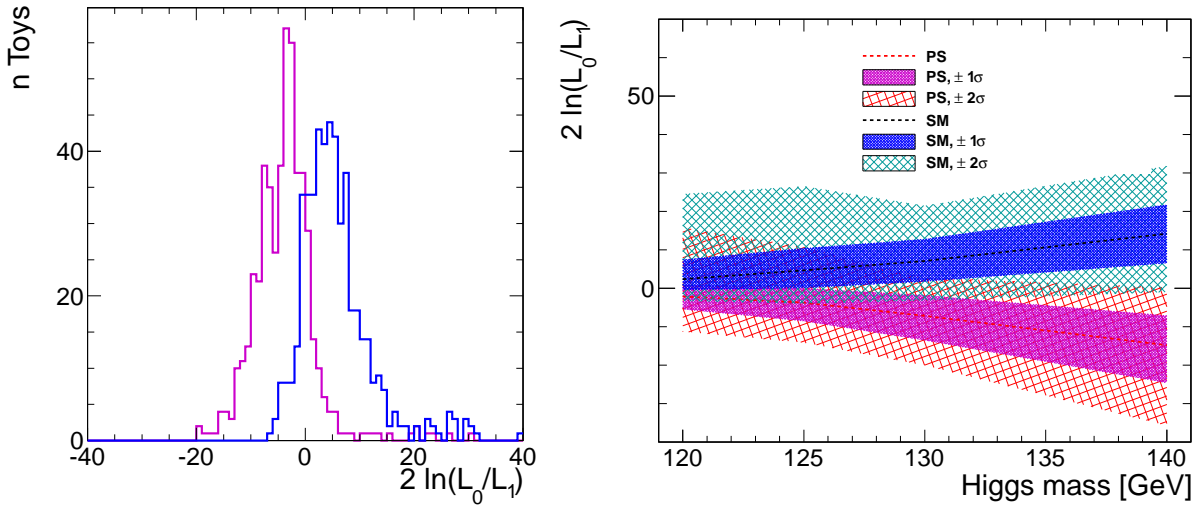


Figure 108: Left: Distribution of $2 \ln(L_1/L_2)$ with the likelihood \mathcal{L} evaluated for two models and shown for 500 generated experiments with the MC events generated according to model one (0^+) and model two (0^-). Right: Expected $2 \ln(L_1/L_2)$ distributions with 68% (solid) and 95% (hatched) coverage for the two hypotheses (0^+ and 0^-) shown on the left, as a function of the scalar boson mass.

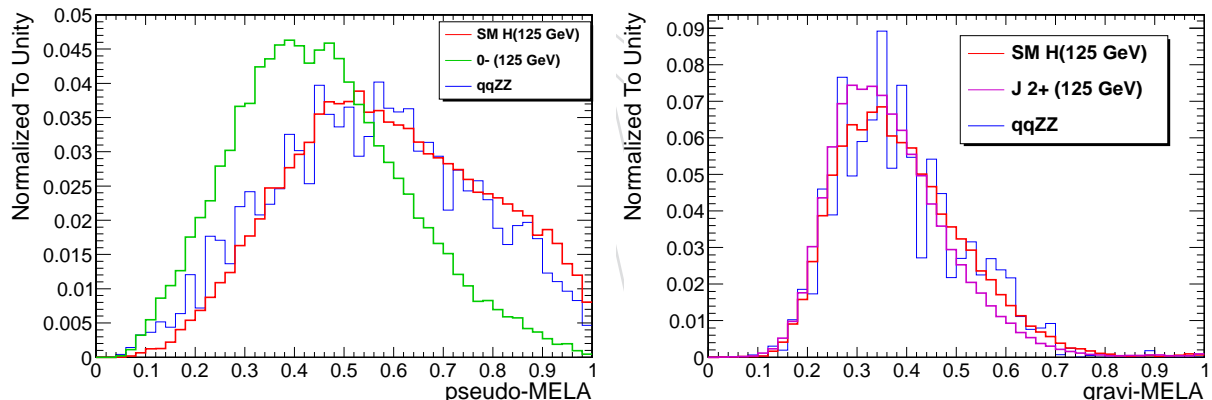


Figure 109: Distributions of the pseudoMELA discriminant (for scalar-to-pseudoscalar separation, left) and graviMELA discriminant (for scalar-to-spin-two separation, right). The distributions are shown for mass around 125 GeV and for signal (0^+ red, 0^- green, 2^+ KK graviton magenta) and background (blue). All MC distributions are shown for the full CMSSW simulation, except for KK graviton model which is shown with fast track parameter smearing and acceptance effects (CMSSW samples are pending).

2009 way as in the fit with the MELA observable.

2010 While the expected separation between the two hypotheses with present statistics is 1.6 standard deviations, the actual observed separation is shown in Fig. 110 (left). Observed consistency with pseudoscalar
2011 is 1.1σ and observed consistency with the SM Higgs is 0.4σ . MC studies indicate that with additional 15
2012 fb^{-1} of data we expect separation of 2.6σ . and with additional 25 fb^{-1} of data we expect separation of
2013 3.1σ .
2014

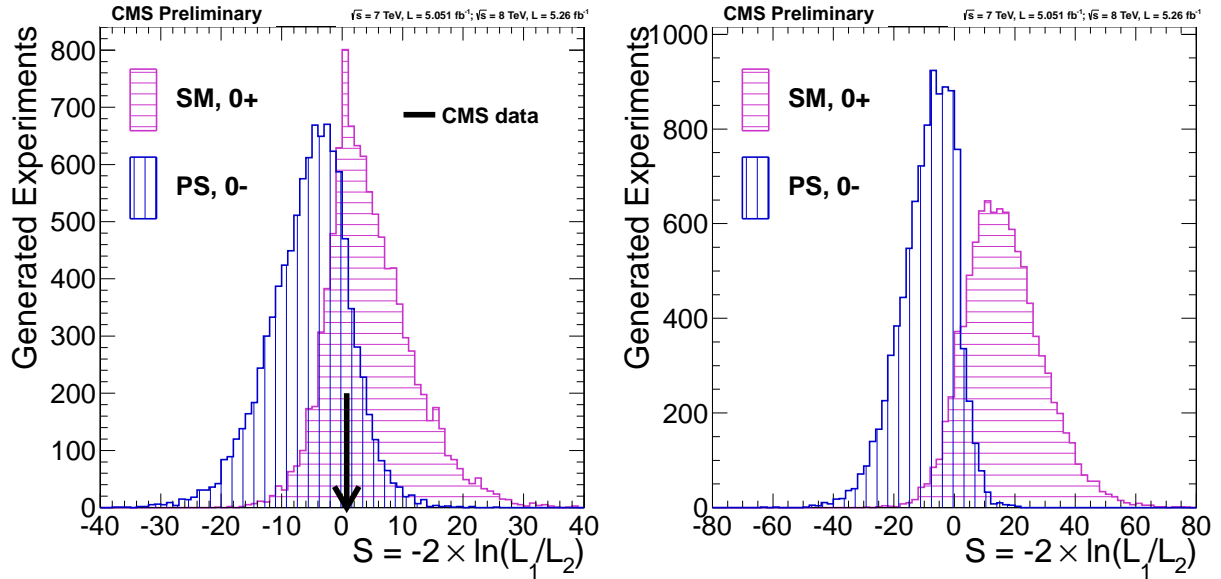


Figure 110: Distribution of $-2\ln(\mathcal{L}_1/\mathcal{L}_2)$ for two signal types (0^+ black, 0^- red) for $m_H = 126$ GeV. The observed value is indicated by an arrow. Left plot: current data-sample, right plot: expectation with additional 15 fb^{-1} of data.

2015 In Fig. 112 we show distribution of pseudoMELA for pseudoscalar, scalar signal, and background, and
2016 for observed events in the signal region $121 < m_{4\ell} < 131$ GeV and MELA > 0.5 . For comparison, in
2017 Fig. 113 we show distribution of MELA for scalar signal and background and for observed events in the
2018 signal region $121 < m_{4\ell} < 131$ GeV.

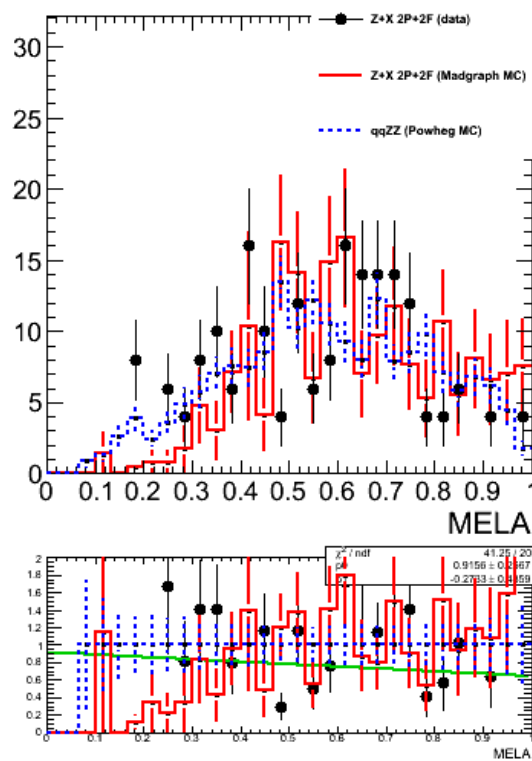


Figure 111: Distribution of pseudoMELA for $Z + X$ background in the control sample for data (data points), MC (red histogram) and for $q\bar{q} \rightarrow ZZ$ MC (blue dashed histogram) in the mass range $120 < m_{4\ell} < 130$ GeV.

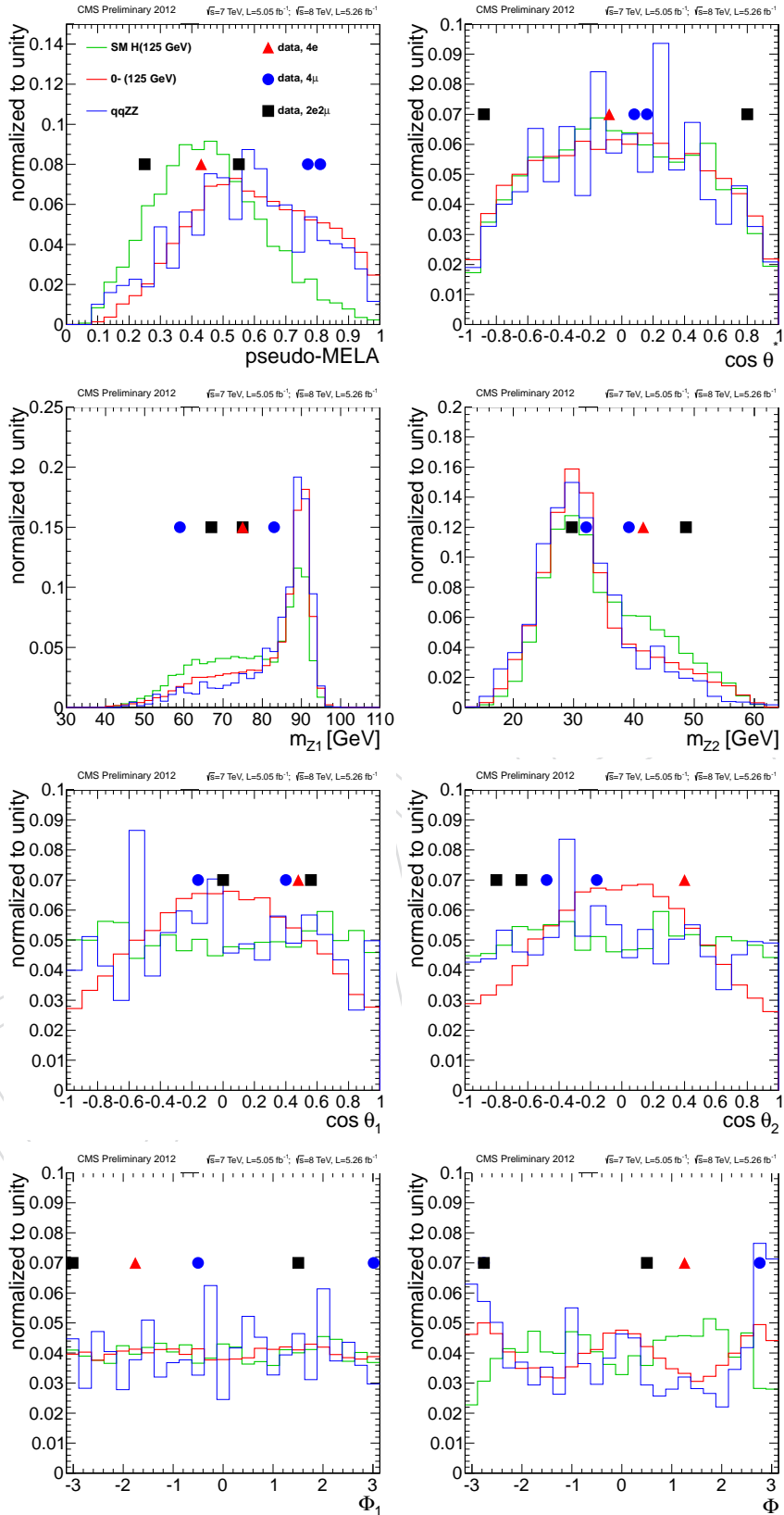


Figure 112: Distribution of pseudoMELA for pseudoscalar, scalar signal, and background, and for observed events in the signal region $121 < m_{4\ell} < 131 \text{ GeV}$ and $\text{MELA} > 0.5$.

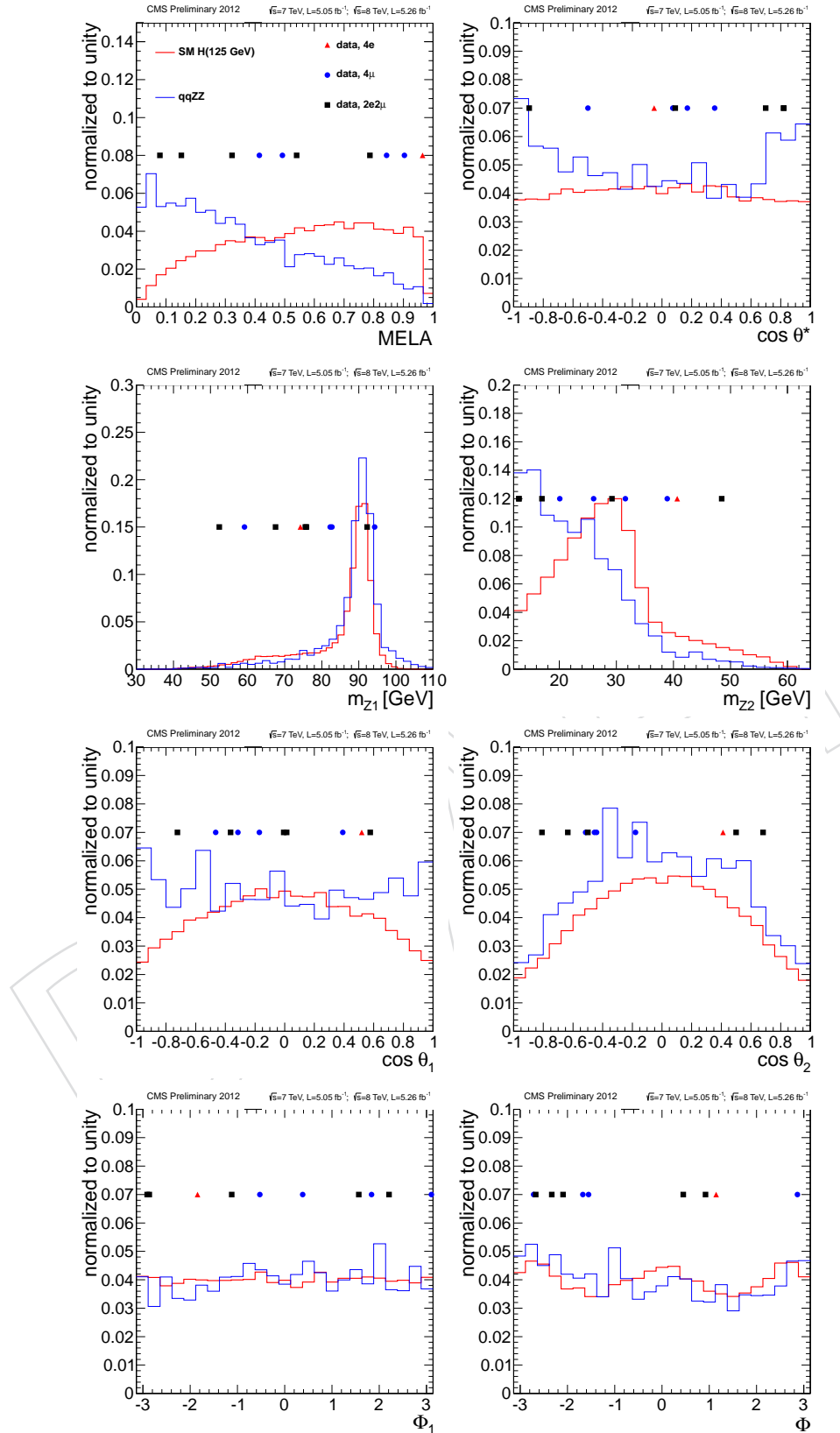


Figure 113: Distribution of MELA for scalar signal and background and for observed events in the signal region $121 < m_{4\ell} < 131$ GeV.

14.6 Measurement of ZZ cross section

- 2019 The reference cross section is obtained from MCFM. Renormalization and factorization scales are set at
 2020 $\mu_R = \mu_F = m_Z$ and we use MSTW08 PDF. The signal acceptance is evaluated using MC and the data-
 2021 to-MC correction factors are evaluated using data-to-MC correction factors for each individual leptons
 2022 obtained using tag-and-probe method.
- 2024 The requirements on p_T and η for the particles in the final state reduces the full possible phase space of
 2025 the $ZZ \rightarrow 4l$ measurement by factor of 0.56–0.59 for the $4e$, 4μ and $2e2\mu$ and by factor of 0.18–0.21 for
 2026 the $2\ell2\tau$ final states.
- 2027 Table 37 presents the number of observed events as well as the number of expected signal and the
 2028 number of estimated background events in the signal region.

Table 36: Acceptances, uncertainty 4%, and efficiencies, uncertainty 5%.

Channel	4e	4μ	$2e2\mu$	$2\ell2\tau$
Acceptance	57.8%	54.4%	56.3%	24.5%
Efficiency	0.53%	0.80%	0.66	0.12%

- 2029 Table 37 presents the number of observed events as well as the number of expected signal and the
 2030 number of estimated background events in the signal region.

Table 37: The number of event candidates observed, compared to the mean expected background and signal rates for each final state. For the $Z + X$ background, the estimations are based on data.

Channel	4e	4μ	$2e2\mu$	$2\ell2\tau$
ZZ	11.61 ± 1.38	20.28 ± 2.21	32.35 ± 3.49	6.51 ± 0.84
Z+X	0.41 ± 0.21	0.44 ± 0.26	0.52 ± 0.41	5.61 ± 1.35
Total	12.02 ± 1.40	20.72 ± 2.23	32.87 ± 3.51	12.12 ± 1.59
Observed	14	19	38	13

- 2031 We observe 71 candidates compared to an expectation of 65.6 ± 4.4 events from SM among which 1.4
 2032 from background processes in the $4e$, 4μ and $2e2\mu$ channels, and 13 candidates for an expectation of
 2033 12.1 ± 1.6 events from SM among which 5.6 from background processes in the $2\ell2\tau$ channels. The
 2034 reconstructed four-lepton invariant mass distribution is shown in Fig. 114 for the sum of the $4e$, 4μ and
 2035 $2e2\mu$, and the sum of all the $2\ell2\tau$ channels. Data are compared to expectations from the SM backgrounds.
 2036 The shape of the background is taken from the MC simulation, with each component normalized to the
 2037 corresponding estimated value from Table 37. The reconstructed masses in $2\ell2\tau$ states are shifted with
 2038 respect to the generated values by $\approx 30\%$ due to the undetected neutrinos in τ decays. Bottom plots in
 2039 Fig. 114 represent correlation between reconstructed masses of Z_1 and Z_2 .

- 2040 To include all final states in the cross section calculation a simultaneous constrained fit on the number
 2041 of observed events in all decay channels is performed. It allows for combining many decay modes with
 2042 very few or no events observed and background compatible with the signal expectation. The likelihood
 2043 is written as a combination of individual channel likelihoods for the signal and background hypothesis:

$$\mathcal{L}(r) = \prod_i \mathcal{L}_i(N_i^{obs}, r, S_i, B_i, \nu_S, \nu_B), \quad (36)$$

- 2044 where r is the signal strength, N_i^{obs} is the number of observed events in channel i , S_i the number of
 2045 expected signal events, B_i the number of expected background events, ν_S and ν_B are the statistical and
 2046 systematical uncertainties in form of scaling nuisance parameters. Each tau decay mode is treated as a
 2047 separated channel.

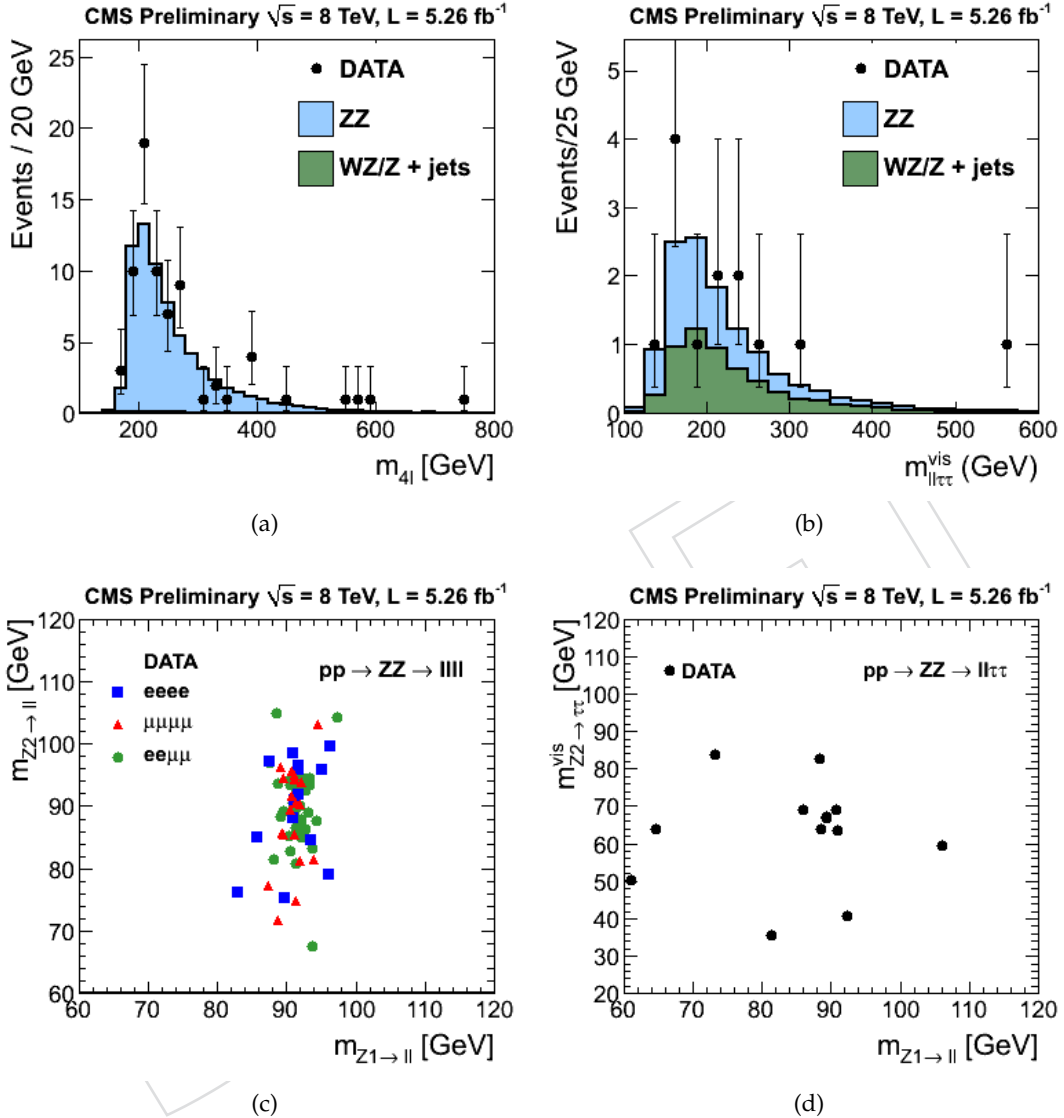


Figure 114: Distribution of the four-lepton reconstructed mass for the sum of the $4e, 4\mu$ and $2e2\mu$, and sum of the $2\ell 2\tau$ channels. Points represent the data, shaded histograms represent the expected ZZ signal and reducible background. The background shapes are taken from MC simulation and are normalized to the values obtained using control data samples, as described in the text. Bottom plots represent correlation between reconstructed masses of Z_1 and Z_2 .

2048 The resulting cross section is measured to be $\sigma(pp \rightarrow ZZ) = 8.4 \pm 1.0(stat.) \pm 0.7(sys.) \pm 0.4(lumi.)\text{ pb}$
 2049 to be compared to the theoretical value of $7.7 \pm 0.6\text{ pb}$ calculated with MCFM [21]. at NLO $qqZZ$ and LO
 2050 $gg \rightarrow ZZ$.

2051 The resulting signal strengths for the combined 4ℓ and $2\ell 2\tau$ are $r = 1.08784 - 0.143374/\sqrt{+0.160848}$ with
 2052 both statistical and systematical uncertainties included, and $r = 1.08675 - 0.123191/\sqrt{+0.132786}$ with
 2053 the statistical uncertainties only.

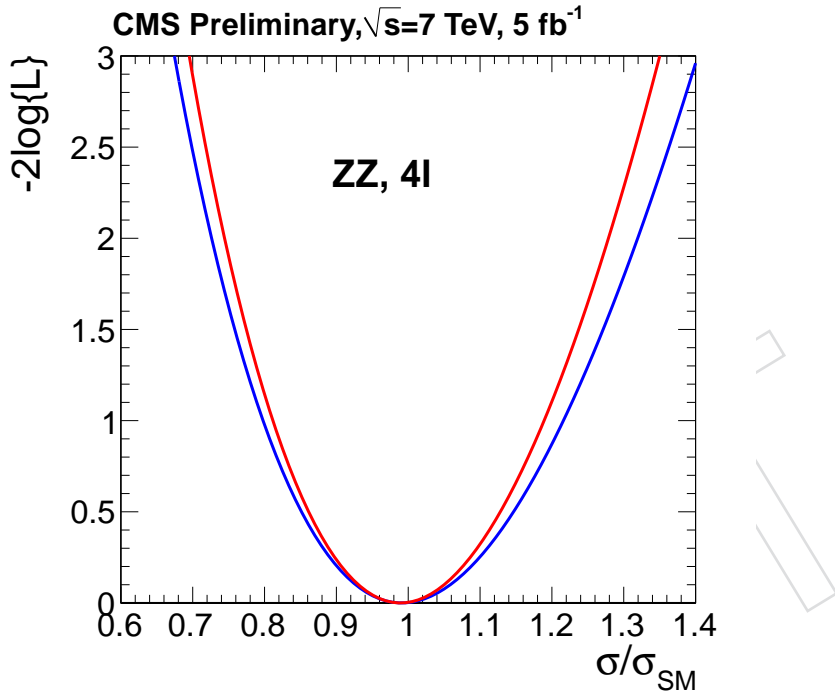


Figure 115: Measurement of the cross section using 4ℓ and $2\ell 2\tau$ channels combined. Red line represents the fit with statistical uncertainties only and the blue one with all uncertainties. This is a typical shape and width, will be updated as soon as we stop updating the luminosity.

2054 15 Summary and Conclusions

2055 In summary, a search for the standard model Higgs boson has been presented in the four-lepton decay
 2056 modes $H \rightarrow 4\ell$. The mass distributions measured with four-lepton invariant masses $m_{4\ell}$ or $m_{2\ell 2\tau} >$
 2057 100 GeV are found globally consistent with the expectation of standard model background expectation.
 2058 The measurements are interpreted by using for each event the information from the measured four-
 2059 lepton mass and a kinematic discriminant. Upper limits at 95% confidence level exclude the standard
 2060 model Higgs boson in the range 130–520 GeV. An excess of events is observed in the mass range $120 <$
 2061 $m_{4\ell} < 130$ GeV making the observed limits weaker than expected in the absence of a signal. These
 2062 events cluster in a peak around a mass $m_{4\ell} \simeq 126$ GeV, giving rise to a local excess with respect to the
 2063 background expectation, with a significance for the standard model Higgs boson hypothesis of 3.2σ .

2064 We have also performed the measurement of the ZZ production cross section and found results in agree-
 2065 ment with the predictions from the Standard model.

2066 References

- 2067 [1] S. L. Glashow, “Partial Symmetries of Weak Interactions”, *Nucl. Phys.* **22** (1961) 579–588,
 doi:[10.1016/0029-5582\(61\)90469-2](https://doi.org/10.1016/0029-5582(61)90469-2).
- 2069 [2] S. Weinberg, “A Model of Leptons”, *Phys. Rev. Lett.* **19** (1967) 1264–1266,
 doi:[10.1103/PhysRevLett.19.1264](https://doi.org/10.1103/PhysRevLett.19.1264).
- 2071 [3] A. Salam, “Elementary Particle Physics”, N. Svartholm ed., Almqvist and Wiksell, Stockholm (1968).
- 2072 [4] F. Englert and R. Brout, “Broken Symmetry and the Mass of Gauge Vector Mesons”,
 Phys.Rev.Lett. **13** (1964) 321–322, doi:[10.1103/PhysRevLett.13.321](https://doi.org/10.1103/PhysRevLett.13.321).
- 2074 [5] P. W. Higgs, “Broken symmetries, massless particles and gauge fields”, *Phys.Lett.* **12** (1964)
 132–133, doi:[10.1016/0031-9163\(64\)91136-9](https://doi.org/10.1016/0031-9163(64)91136-9).
- 2076 [6] P. W. Higgs, “Broken Symmetries and the Masses of Gauge Bosons”, *Phys.Rev.Lett.* **13** (1964)
 508–509, doi:[10.1103/PhysRevLett.13.508](https://doi.org/10.1103/PhysRevLett.13.508).
- 2078 [7] G. Guralnik, C. Hagen, and T. Kibble, “Global Conservation Laws and Massless Particles”,
 Phys.Rev.Lett. **13** (1964) 585–587, doi:[10.1103/PhysRevLett.13.585](https://doi.org/10.1103/PhysRevLett.13.585).
- 2080 [8] P. W. Higgs, “Spontaneous Symmetry Breakdown without Massless Bosons”, *Phys.Rev.* **145**
 (1966) 1156–1163, doi:[10.1103/PhysRev.145.1156](https://doi.org/10.1103/PhysRev.145.1156).
- 2082 [9] T. Kibble, “Symmetry breaking in nonAbelian gauge theories”, *Phys.Rev.* **155** (1967) 1554–1561,
 doi:[10.1103/PhysRev.155.1554](https://doi.org/10.1103/PhysRev.155.1554).
- 2084 [10] ATLAS Collaboration Collaboration, “Search for the Standard Model Higgs boson in the decay
 channel $H \rightarrow ZZ(*) \rightarrow 4l$ with 4.8 fb-1 of pp collision data at $\sqrt{s} = 7$ TeV with ATLAS”,
 Phys.Lett. **B710** (2012) 383–402, arXiv:[1202.1415](https://arxiv.org/abs/1202.1415).
- 2087 [11] CMS Collaboration Collaboration, “Search for the standard model Higgs boson in the decay
 channel H to ZZ to 4 leptons in pp collisions at $\sqrt{s} = 7$ TeV”, arXiv:[1202.1997](https://arxiv.org/abs/1202.1997).
- 2089 [12] ATLAS Collaboration Collaboration, “Combined search for the Standard Model Higgs boson
 using up to 4.9 fb-1 of pp collision data at $\sqrt{s} = 7$ TeV with the ATLAS detector at the LHC”,
 Phys.Lett. **B710** (2012) 49–66, arXiv:[1202.1408](https://arxiv.org/abs/1202.1408).
- 2092 [13] CMS Collaboration Collaboration, “Combined results of searches for the standard model Higgs
 boson in pp collisions at $\sqrt{s} = 7$ TeV”, *Phys.Lett.* **B710** (2012) 26–48, arXiv:[1202.1488](https://arxiv.org/abs/1202.1488).
- 2094 [14] LEP Working Group for Higgs boson searches, ALEPH Collaboration, DELPHI Collaboration, L3
 Collaboration, OPAL Collaboration Collaboration, “Search for the standard model Higgs boson
 at LEP”, *Phys.Lett.* **B565** (2003) 61–75, doi:[10.1016/S0370-2693\(03\)00614-2](https://doi.org/10.1016/S0370-2693(03)00614-2),
 arXiv:[hep-ex/0306033](https://arxiv.org/abs/hep-ex/0306033).

- [15] CDF and D0 Collaborations, "Combination of Tevatron Searches for the Standard Model Higgs Boson in the W^+W^- Decay Mode", *Phys. Rev. Lett.* **104** (2010) 061802, doi:10.1103/PhysRevLett.104.061802. a more recent, unpublished, limit is given in preprint arXiv:1103.3233.
- [16] ALEPH, CDF, D0, DELPHI, L3, OPAL, SLD Collaborations, the LEP Electroweak Working Group, the Tevatron Electroweak Working Group, and the SLD Electroweak and Heavy Flavour Groups, "Precision Electroweak Measurements and Constraints on the Standard Model", technical report, (2010).
- [17] ALEPH, CDF, D0, DELPHI, L3, OPAL, SLD Collaborations, the LEP Electroweak Working Group, the Tevatron Electroweak Working Group, and the SLD Electroweak and Heavy Flavour Groups, "Precision electroweak measurements on the Z resonance", *Phys. Rept.* **427** (2006) 257, doi:10.1016/j.physrep.2005.12.006, arXiv:hep-ex/0509008.
- [18] CMS Collaboration, "Search for the standard model Higgs boson in the $H \rightarrow ZZ$ to ll tau tau decay channel in pp collisions at $\sqrt{s}=7$ TeV", *JHEP* **1203** (2012) 081, arXiv:1202.3617.
- [19] CMS Collaboration, "The CMS experiment at the CERN LHC", *JINST* **3** (2008) S08004, doi:10.1088/1748-0221/3/08/S08004.
- [20] LHC Higgs Cross Section Working Group, "Handbook of LHC Higgs Cross Sections: 2. Differential Distributions", CERN Report CERN-2012-002, (2012).
- [21] C. W. John Campbell, Keith Ellis, "MCFM - Monte Carlo for FeMtobarn processes", (2011).
- [22] ATLAS Collaboration, "Measurement of the ZZ production cross section and limits on anomalous neutral triple gauge couplings in proton-proton collisions at $\sqrt{s} = 7$ TeV with the ATLAS detector", *Phys. Rev. Lett.* **108** (2012) 041804, doi:10.1103/PhysRevLett.108.041804, arXiv:1110.5016.
- [23] E. Gross and O. Vitells, "Trial factors or the look elsewhere effect in high energy physics", *Eur. Phys. J. C* **70** (2010) 525, doi:10.1140/epjc/s10052-010-1470-8, arXiv:1005.1891.
- [24] ATLAS and CMS Collaborations, "Procedure for the LHC Higgs boson search combination in Summer 2011", ATL-PHYS-PUB-2011-011, CMS NOTE-2011/005, (2011).
- [25] T. Junk, "Confidence level computation for combining searches with small statistics", *Nucl. Instrum. Meth. A* **434** (1999) 435, doi:10.1016/S0168-9002(99)00498-2, arXiv:hep-ex/9902006.
- [26] A. L. Read, "Modified frequentist analysis of search results (the CL_s method)", CERN Report CERN-OPEN-2000-005, (2000).
- [27] Marlow, D, "talk at the CMS GWM", <https://indico.cern.ch/getFile.py/access?contribId=2&resId=0&materialId=slides&confId=123724> (2011).
- [28] Pierini, M., "talk at the Joint PVT/PO Meeting", <https://twiki.cern.ch/twiki/bin/viewauth/CMS/PdwgMain> (2011).
- [29] LHC Higgs Cross Section Working Group, "Handbook of LHC Higgs Cross Sections: 1. Inclusive Observables", CERN Report CERN-2011-002, (2011).
- [30] T. Sjöstrand, S. Mrenna, and P. Z. Skands, "PYTHIA 6.4 Physics and Manual", *JHEP* **05** (2006) 026, doi:10.1088/1126-6708/2006/05/026, arXiv:hep-ph/0603175.
- [31] J. Alwall et al., "MadGraph/MadEvent v4: The New Web Generation", *JHEP* **09** (2007) 028, doi:10.1088/1126-6708/2007/09/028, arXiv:0706.2334.
- [32] S. Frixione, P. Nason, and C. Oleari, "Matching NLO QCD computations with Parton Shower simulations: the POWHEG method", *JHEP* **11** (2007) 070, doi:10.1088/1126-6708/2007/11/070, arXiv:0709.2092.

- [33] T. Binoth, N. Kauer, and P. Mertsch, "Gluon-induced QCD corrections to $pp \rightarrow ZZ \rightarrow \ell\bar{\ell}\ell'\bar{\ell}'$ ", in *Proceedings of the XVI Int. Workshop on Deep-Inelastic Scattering and Related Topics (DIS'07)*. 2008. arXiv:0807.0024. doi:10.3360/dis.2008.142.
- [34] C. Anastasiou, R. Boughezal, and F. Petriello, "Mixed QCD-electroweak corrections to Higgs boson production in gluon fusion", *JHEP* **04** (2009) 003, doi:10.1088/1126-6708/2009/04/003, arXiv:0811.3458.
- [35] D. de Florian and M. Grazzini, "Higgs production through gluon fusion: updated cross sections at the Tevatron and the LHC", *Phys. Lett. B* **674** (2009) 291, doi:10.1016/j.physletb.2009.03.033, arXiv:0901.2427.
- [36] S. Dawson, "Radiative corrections to Higgs boson production", *Nucl. Phys. B* **359** (1991) 283, doi:10.1016/0550-3213(91)90061-2.
- [37] M. Spira et al., "Higgs boson production at the LHC", *Nucl. Phys. B* **453** (1995) 17, doi:10.1016/0550-3213(95)00379-7, arXiv:hep-ph/9504378.
- [38] R. V. Harlander and W. B. Kilgore, "Next-to-next-to-leading order Higgs production at hadron colliders", *Phys. Rev. Lett.* **88** (2002) 201801, doi:10.1103/PhysRevLett.88.201801, arXiv:hep-ph/0201206.
- [39] C. Anastasiou and K. Melnikov, "Higgs boson production at hadron colliders in NNLO QCD", *Nucl. Phys. B* **646** (2002) 220, doi:10.1016/S0550-3213(02)00837-4, arXiv:hep-ph/0207004.
- [40] V. Ravindran, J. Smith, and W. L. van Neerven, "NNLO corrections to the total cross section for Higgs boson production in hadron-hadron collisions", *Nucl. Phys. B* **665** (2003) 325, doi:10.1016/S0550-3213(03)00457-7, arXiv:hep-ph/0302135.
- [41] S. Catani et al., "Soft-gluon resummation for Higgs boson production at hadron colliders", *JHEP* **07** (2003) 028, doi:10.1088/1126-6708/2003/07/028, arXiv:hep-ph/0306211.
- [42] S. Actis et al., "NLO Electroweak Corrections to Higgs Boson Production at Hadron Colliders", *Phys. Lett. B* **670** (2008) 12, doi:10.1016/j.physletb.2008.10.018, arXiv:0809.1301.
- [43] M. Ciccolini, A. Denner, and S. Dittmaier, "Strong and electroweak corrections to the production of Higgs + 2-jets via weak interactions at the LHC", *Phys. Rev. Lett.* **99** (2007) 161803, doi:10.1103/PhysRevLett.99.161803, arXiv:0707.0381.
- [44] M. Ciccolini, A. Denner, and S. Dittmaier, "Electroweak and QCD corrections to Higgs production via vector-boson fusion at the LHC", *Phys. Rev. D* **77** (2008) 013002, doi:10.1103/PhysRevD.77.013002, arXiv:0710.4749.
- [45] T. Figy, C. Oleari, and D. Zeppenfeld, "Next-to-leading order jet distributions for Higgs boson production via weak-boson fusion", *Phys. Rev. D* **68** (2003) 073005, doi:10.1103/PhysRevD.68.073005, arXiv:hep-ph/0306109.
- [46] K. Arnold et al., "VBFNLO: A parton level Monte Carlo for processes with electroweak bosons", *Comput. Phys. Commun.* **180** (2009) 1661, doi:10.1016/j.cpc.2009.03.006, arXiv:0811.4559.
- [47] P. Bolzoni et al., "Higgs production via vector-boson fusion at NNLO in QCD", *Phys. Rev. Lett.* **105** (2010) 011801, doi:10.1103/PhysRevLett.105.011801, arXiv:1003.4451.
- [48] A. Bredenstein et al., "Precise predictions for the Higgs-boson decay $H \rightarrow WW/ZZ \rightarrow 4$ leptons", *Phys. Rev. D* **74** (2006) 013004, doi:10.1103/PhysRevD.74.013004, arXiv:hep-ph/0604011.
- [49] A. Bredenstein et al., "Radiative corrections to the semileptonic and hadronic Higgs-boson decays $H \rightarrow WW/ZZ \rightarrow 4$ fermions", *JHEP* **02** (2007) 080, doi:10.1088/1126-6708/2007/02/080, arXiv:hep-ph/0611234.

- [50] A. Djouadi, J. Kalinowski, and M. Spira, "HDECAY: A program for Higgs boson decays in the standard model and its supersymmetric extension", *Comput. Phys. Commun.* **108** (1998) 56, doi:10.1016/S0010-4655(97)00123-9, arXiv:hep-ph/9704448.
- [51] S. Actis et al., "NNLO Computational Techniques: the Cases $H \rightarrow \gamma\gamma$ and $H \rightarrow gg$ ", *Nucl. Phys. B* **811** (2009) 182, doi:10.1016/j.nuclphysb.2008.11.024, arXiv:0809.3667.
- [52] G. Bozzi, S. Catani, D. de Florian et al., "Transverse-momentum resummation and the spectrum of the Higgs boson at the LHC", *Nucl. Phys. B* **737** (2006) 73, doi:10.1016/j.nuclphysb.2005.12.022, arXiv:hep-ph/0508068.
- [53] S. Baffioni et al., "Search strategy for the Higgs boson in the ZZ^(*) decay channel at $\sqrt{s} = 10$ TeV with the CMS experiment", *CMS AN* **2010/237** (2010).
- [54] M. Cacciari, S. Frixione, M. Mangano et al., "Updated predictions for the total production crosssections of top and of heavier quark pairs at the Tevatron and at the LHC", arXiv:0804.2800v3.
- [55] S. Baffioni et al., "Electron Reconstruction in CMS", *CMS Note* **2006/040** (2006).
- [56] S. Baffioni et al., "Electron Reconstruction in CMS", *CMS Analysis Note* **2009/164** (2009).
- [57] CMS Collaboration, "Electron reconstruction and identification at $\sqrt{s} = 7$ TeV", *CMS Physics Analysis Summary CMS-PAS-EGM-10-004* (2010).
- [58] CMS Collaboration, "Electron commissioning results at $\sqrt{s} = 7$ TeV", *CMS Detector Performance Summaries* **2011/003** (2011).
- [59] S. Baffioni et al., "Electron Charge Determination Commissioning from 7 TeV Data", *CMS AN* **2010/468** (2010).
- [60] S. Nourbakhsh et al., "Energy scale of CMS Electromagnetic Calorimeter with 2010 Data", *CMS Analysis Note* **2011/038** (2011).
- [61] R. Paramatti, "Private communication, AN in preparation", 2.
- [62] e/g POG, "Electron Selection Criteria in 2012", *CMS AN* **2012/201** (2012).
- [63] CMS Collaboration, "MUO-10-004: Performance of CMS muon reconstruction in pp collision events at $\sqrt{s} = 7$ TeV", technical report, (2010). In preparation to *JINST*.
- [64] R. Frühwirth, "Application of Kalman filtering to track and vertex fitting", *Nucl. Instrum. Meth. A* **262** (1987) 444, doi:10.1016/0168-9002(87)90887-4.
- [65] CMS Collaboration, "Performance of CMS muon reconstruction in cosmic-ray events", *JINST* **5** (2010) T03022, doi:10.1088/1748-0221/5/03/T03022, arXiv:0911.4994.
- [66] CMS Collaboration, "CMS Physics Technical Design Report, volume I: Detector performance and software", *CERN/LHCC* **2006-001** (2006).
- [67] CMS Collaboration, "Measurement of tracking efficiency", *CMS Physics Analysis Summary CMS-PAS-TRK-10-002* (2010).
- [68] CMS Collaboration, "Particle-flow event reconstruction in CMS and performance for jets, taus, and missing E_T ", *CMS Physics Analysis Summary CMS-PAS-PFT-09-001* (2009).
- [69] CMS Collaboration, "Commissioning of the particle-flow event reconstruction with leptons from J/Psi and W decays at 7 TeV", *CMS Physics Analysis Summary CMS-PAS-PFT-10-003* (2010).
- [70] M. Cacciari and G. P. Salam, "Pileup subtraction using jet areas", *Phys. Lett. B* **659** (2008) 119–126, doi:10.1016/j.physletb.2007.09.077, arXiv:0707.1378.
- [71] M. Cacciari, G. P. Salam, and G. Soyez, "The Catchment Area of Jets", *JHEP* **04** (2008) 005, doi:10.1088/1126-6708/2008/04/005, arXiv:0802.1188.
- [72] G. Daskalakis et al., "Measuring Electron Efficiencies at CMS with Early Data", *CMS Analysis Note* **2007/019** (2007).

- [73] CMS Collaboration, “Measurement of Tracking Efficiency”, *CMS Physics Analysis Summary CMS-PAS-TRK-10-002* (2010).
- [74] S. Baffioni et al., “Electron Efficiency Measurement from 7 TeV Data”, *CMS AN 2010/471* (2010).
- [75] K. Nakamura et al. (Particle Data Group), “The Review of Particle Physics”, *J. Phys. G* **37** (2010) 075021.
- [76] CMS, “Electron VBF Selection”, <https://twiki.cern.ch/twiki/bin/viewauth/CMS/VbtfEleID2011> (2011).
- [77] CMS, “Electron reconstruction efficiency measurement for 2011”, <https://twiki.cern.ch/twiki/bin/view/CMS/EgCommissioningAndPhysicsDeliverables> (2011).
- [78] CMS Collaboration, “TRK-10-001: Description and Performance of the CMS Track and Primary Vertex Reconstruction”, (2011). In preparation.
- [79] P. Avery, M. Chen, A. Drozdetskiy, A. Korytov, G. Mitselmakher, M. Snowball, “A complete model of the four-lepton invariant mass distributions for $H \rightarrow ZZ \rightarrow 4\ell$ and $ZZ \rightarrow 4\ell$ events”, (29 May, 2011). CMS AN-11-202.
- [80] LHC Higgs Cross Section Working Group, S. Dittmaier, C. Mariotti et al., “Handbook of LHC Higgs cross sections: 1. Inclusive observables”, *CERN-2011-002* (CERN, Geneva, 2011, All the numbers can be obtained at <https://twiki.cern.ch/twiki/bin/view/LHCPhysics/CrossSections>) arXiv:1101.0593.
- [81] ATLAS and CMS Collaborations Collaboration, “LHC Higgs Combination Working Group report”, *ATL-PHYS-PUB-2011-11, CMS NOTE-2011/005* (2011).
- [82] “Higgs Branching ratio errors”.
- [83] S. Alekhin et al., “The PDF4LHC working group interim report”, arXiv:hep-ph/1101.0536.
- [84] H. L. Lai, M. Guzzi, J. Huston, Z. Li, P. M. Nadolsky, J. Pumplin and C. P. Yuan, “New parton distributions for collider physics”, *Phys.Rev D* (2010), no. 82, 074024.
- [85] A. D. Martin, W. J. Stirling, R. S. Thorne and G. Watt, “Parton distributions for the LHC”, *Eur. Phys. J C* (2009), no. 63, 189.
- [86] R. D. Ball, L. Del Debbio, S. Forte, A. Guffanti, J. I. Latorre, J. Rojo and M. Ubiali, “A first unbiased global NLO determination of parton distributions and their uncertainties”, *Nucl. Phys B* (2010), no. 838, 136.
- [87] G. Bozzi, S. Catani, D. de Florian, and M. Grazzini, “The q_T spectrum of the Higgs boson at the LHC in QCD perturbation theory”, *Phys. Lett. B* (2003), no. 564, 65.
- [88] “LHC Higgs Cross Section Working Group web page”.
- [89]FIXME, “Tag-and-probe systematic errors”.
- [90] “Observation of Z to 4l production in pp collisions at 7 TeV”.
- [91] ATLAS Collaboration, “Measurement of hard double-partonic interactions in $W \rightarrow \ell\nu + 2$ jet events using the ATLAS detector at the LHC”, (2011). ATLAS-CONF-2011-160.
- [92] A. Soni and R. Xu, “Probing CP violation via Higgs decays to four leptons”, *Phys.Rev. D48* (1993) 5259–5263, doi:10.1103/PhysRevD.48.5259, arXiv:hep-ph/9301225.
- [93] V. D. Barger, K.-m. Cheung, A. Djouadi et al., “Higgs bosons: Intermediate mass range at e+ e- colliders”, *Phys.Rev. D49* (1994) 79–90, doi:10.1103/PhysRevD.49.79, arXiv:hep-ph/9306270.
- [94] S. Choi, . Miller, D.J., M. Muhlleitner et al., “Identifying the Higgs spin and parity in decays to Z pairs”, *Phys.Lett. B553* (2003) 61–71, doi:10.1016/S0370-2693(02)03191-X, arXiv:hep-ph/0210077.
- [95] B. Allanach, K. Odagiri, M. Palmer et al., “Exploring small extra dimensions at the large hadron collider”, *JHEP 0212* (2002) 039, arXiv:hep-ph/0211205.

- [96] C. Buszello, I. Fleck, P. Marquard et al., "Prospective analysis of spin- and CP-sensitive variables in $H \rightarrow ZZ \rightarrow l(1)^+l(1)^-l(2)^+l(2)^-$ at the LHC", *Eur.Phys.J.* **C32** (2004) 209–219, doi:10.1140/epjc/s2003-01392-0, arXiv:hep-ph/0212396.
- [97] R. M. Godbole, . Miller, D.J., and M. M. Muhlleitner, "Aspects of CP violation in the H ZZ coupling at the LHC", *JHEP* **0712** (2007) 031, doi:10.1088/1126-6708/2007/12/031, arXiv:0708.0458.
- [98] W.-Y. Keung, I. Low, and J. Shu, "Landau-Yang Theorem and Decays of a Z' Boson into Two Z Bosons", *Phys.Rev.Lett.* **101** (2008) 091802, doi:10.1103/PhysRevLett.101.091802, arXiv:0806.2864.
- [99] O. Antipin and A. Soni, "Towards establishing the spin of warped gravitons", *JHEP* **0810** (2008) 018, doi:10.1088/1126-6708/2008/10/018, arXiv:0806.3427.
- [100] K. Hagiwara, Q. Li, and K. Mawatari, "Jet angular correlation in vector-boson fusion processes at hadron colliders", *JHEP* **0907** (2009) 101, doi:10.1088/1126-6708/2009/07/101, arXiv:0905.4314.
- [101] Y. Gao, A. V. Gritsan, Z. Guo et al., "Spin determination of single-produced resonances at hadron colliders", *Phys.Rev.* **D81** (2010) 075022, doi:10.1103/PhysRevD.81.075022, arXiv:1001.3396.
- [102] A. De Rujula, J. Lykken, M. Pierini et al., "Higgs look-alikes at the LHC", *Phys.Rev.* **D82** (2010) 013003, doi:10.1103/PhysRevD.82.013003, arXiv:1001.5300.
- [103] J. S. Gainer, K. Kumar, I. Low et al., "Improving the sensitivity of Higgs boson searches in the golden channel", *JHEP* **1111** (2011) 027, doi:10.1007/JHEP11(2011)027, arXiv:1108.2274.
- [104] CMS Collaboration Collaboration, "Search for a Higgs boson in the decay channel H to ZZ(*) to q qbar l-l+ in pp collisions at sqrt(s) = 7 TeV", *JHEP* **1204** (2012) 036, arXiv:1202.1416.
- [105] ATLAS and CMS Collaborations, LHC Higgs Combination Group, "Procedure for the LHC Higgs boson search combination in Summer 2011", ATL-PHYS-PUB/CMS NOTE 2011-11, 2011/005, (2011).
- [106] T. Junk, "Confidence level computation for combining searches with small statistics", *Nucl. Instrum. Meth. A* **434** (1999) 435, doi:10.1016/S0168-9002(99)00498-2, arXiv:hep-ex/9902006.
- [107] A. Read, "Modified frequentist analysis of search results (the CL_s method)", Technical Report CERN-OPEN-2000-005, CERN, (2000).
- [108] Particle Data Group, "Review of particle physics", *J. Phys.* **G37** (2010) 075021, doi:10.1088/0954-3899/37/7A/075021.
- [109] M. Oreglia, "A study of the reactions psi-prime → gamma gamma psi". PhD thesis, Stanford University, 1980. SLAC-0236.
- [110] A. Bonato, A. Gritsan, Z. Guo et al., "Angular Analysis of Resonances $pp \rightarrow X \rightarrow ZZ$ ", *CMS Analysis Note* **2010-351**.

2319 **A Appendix #1 Event Properties**

DRAFT

Table 38: Observed events. 7 TeV.

type	$m_{4\ell}$	$dm_{4\ell}$	m_{Z_1}	m_{Z_2}	run	event
4μ	118.830	0.1233	90.32 ($\mu\mu$)	14.72 ($\mu\mu$)	167282	44166176
4μ	121.990	0.8124	59.16 ($\mu\mu$)	31.6 ($\mu\mu$)	178424	666626491
$2e2\mu$	125.790	0.7923	67.53 (ee)	48.5 ($\mu\mu$)	177782	72158025
4μ	126.140	0.4359	94.25 ($\mu\mu$)	25.99 ($\mu\mu$)	178421	87514902
$2e2\mu$	130.060	0.3172	75.57 (ee)	12.93 ($\mu\mu$)	176309	1340034258
$2e2\mu$	130.310	0.1762	92.27 (ee)	16.96 ($\mu\mu$)	172620	218903169
$4e$	132.460	0.8665	85.93 (ee)	43.03 (ee)	176201	562295642
$4e$	137.690	0.6336	91.9 (ee)	28.73 (ee)	163659	344708580
$2e2\mu$	142.430	0.0775	91.64 ($\mu\mu$)	14.85 (ee)	165970	275108397
4μ	144.910	0.2952	91.3 ($\mu\mu$)	34.83 ($\mu\mu$)	163817	155679852
$2e2\mu$	151.530	0.7133	85.8 (ee)	47.71 ($\mu\mu$)	178866	140063742
$2e2\mu$	162.040	0.4006	93.29 (ee)	42.16 ($\mu\mu$)	179452	1459855927
$2e2\mu$	164.740	0.2514	94.51 ($\mu\mu$)	66.79 (ee)	163334	286336207
$2e2\mu$	178.450	0.6437	89.65 ($\mu\mu$)	82.62 (ee)	178421	1450980155
$2e2\mu$	182.740	0.4895	90.58 (ee)	17 ($\mu\mu$)	176201	261184429
$2e2\mu$	185.920	0.4638	90.69 ($\mu\mu$)	92.45 (ee)	172401	3729470
$2e2\mu$	190.010	0.5973	90.44 ($\mu\mu$)	94.12 (ee)	173692	2722114329
$2e2\mu$	191.970	0.5235	91.33 (ee)	92.39 ($\mu\mu$)	166950	1491724484
$4e$	191.20	0.4425	91.4 (ee)	91.9 (ee)	171106	141954801
$2e2\mu$	191.720	0.3843	90.42 ($\mu\mu$)	93.93 (ee)	163334	129514273
$4e$	192.030	0.6408	92.87 (ee)	60.06 (ee)	178421	1610336854
$2e2\mu$	192.180	0.4647	94.85 (ee)	86.49 ($\mu\mu$)	177139	290826062
4μ	193.420	0.5774	90.58 ($\mu\mu$)	92.77 ($\mu\mu$)	176799	35688265
4μ	193.860	0.4508	89.77 ($\mu\mu$)	86.3 ($\mu\mu$)	176309	257489763
$2e2\mu$	194.350	0.4075	91.82 ($\mu\mu$)	88.71 (ee)	172949	1188043146
$4e$	196.480	0.5564	92.28 (ee)	89.66 (ee)	180076	79350642
$2e2\mu$	196.720	0.4952	87.14 ($\mu\mu$)	84.4 (ee)	178703	191352626
4μ	198.820	0.7356	92.15 ($\mu\mu$)	87.7 ($\mu\mu$)	172163	191231387
$2e2\mu$	204.670	0.5414	92.92 ($\mu\mu$)	96.31 (ee)	175921	495614354
$2e2\mu$	205.80	0.4218	91.75 ($\mu\mu$)	101.2 (ee)	176304	418052877
$2e2\mu$	208.10	0.4605	92.81 (ee)	82.35 ($\mu\mu$)	163795	30998576
$2e2\mu$	210.260	0.5339	94.08 (ee)	94.55 ($\mu\mu$)	179434	86225612
$2e2\mu$	210.290	0.5393	92.23 ($\mu\mu$)	97.59 (ee)	175974	7526662
4μ	211.640	0.3779	92.11 ($\mu\mu$)	15.09 ($\mu\mu$)	166438	862270386
$2e2\mu$	213.690	0.4849	90.27 ($\mu\mu$)	87.36 (ee)	179563	1409064222
$4e$	214.530	0.5548	95 (ee)	42.71 (ee)	166438	78213037
4μ	218.870	0.579	90.2 ($\mu\mu$)	88.93 ($\mu\mu$)	171369	160966858
$2e2\mu$	221.190	0.7387	91.49 (ee)	86.77 ($\mu\mu$)	178116	695859609
4μ	222.30	0.4843	90.42 ($\mu\mu$)	54.82 ($\mu\mu$)	167281	480301165
$4e$	223.070	0.7625	88.64 (ee)	87.44 (ee)	178162	10608364
4μ	226.830	0.5516	92.29 ($\mu\mu$)	92.3 ($\mu\mu$)	179476	30532070
4μ	231.940	0.3655	91.15 ($\mu\mu$)	37.15 ($\mu\mu$)	172952	559839432
$2e2\mu$	232.390	0.5295	95.75 (ee)	85.25 ($\mu\mu$)	175921	297753357
$4e$	232.480	0.3688	91.11 (ee)	89.23 (ee)	173659	389185367
4μ	237.880	0.3575	90.96 ($\mu\mu$)	91.74 ($\mu\mu$)	177790	657843813
4μ	238.530	0.225	90.97 ($\mu\mu$)	93.18 ($\mu\mu$)	166512	337493970
4μ	240.350	0.1172	93.01 ($\mu\mu$)	87.7 ($\mu\mu$)	177074	588602439
$2e2\mu$	243.680	0.7501	91.22 ($\mu\mu$)	92.56 (ee)	165633	394010457
$2e2\mu$	245.260	0.4611	91.63 (ee)	90.47 ($\mu\mu$)	178970	122998167
$2e2\mu$	252.730	0.2833	95.06 (ee)	80.53 ($\mu\mu$)	178708	573962528
$2e2\mu$	256.840	0.3148	88.17 (ee)	105.3 ($\mu\mu$)	166408	917379387
$2e2\mu$	257.320	0.4406	90.13 ($\mu\mu$)	92.3 (ee)	176886	1057019814
4μ	269.940	0.7742	89.93 ($\mu\mu$)	89.79 ($\mu\mu$)	178479	298608854

Table 39: Observed events. 7 TeV. Part 2.

type	$m_{4\ell}$	$dm_{4\ell}$	m_{Z_1}	m_{Z_2}	run	event
2e2 μ	2730	0.2989	89.47 ($\mu\mu$)	86.3 (ee)	178479	589085976
2e2 μ	278.480	0.3871	92.08 (ee)	86.56 ($\mu\mu$)	178100	326364918
2e2 μ	278.440	0.361	91.28 (ee)	94.22 ($\mu\mu$)	176207	256888239
4 μ	280.360	0.2626	91.62 ($\mu\mu$)	93.23 ($\mu\mu$)	177790	222240677
4e	284.930	0.584	90.83 (ee)	93.17 (ee)	173243	16706390
4e	284.250	0.3616	91.13 (ee)	93.31 (ee)	180250	591651181
4 μ	308.560	0.4104	87.7 ($\mu\mu$)	97.02 ($\mu\mu$)	172208	66033190
2e2 μ	308.630	0.6722	90.15 ($\mu\mu$)	86.71 (ee)	177222	339499459
2e2 μ	308.060	0.6004	92.4 ($\mu\mu$)	94.23 (ee)	175906	227517585
2e2 μ	314.90	0.7017	92.22 ($\mu\mu$)	88.86 (ee)	172868	933807102
2e2 μ	319.80	0.3101	89.37 ($\mu\mu$)	93.2 (ee)	178731	248562036
2e2 μ	325.310	0.8279	94.81 (ee)	102.7 ($\mu\mu$)	176468	215855118
2e2 μ	326.730	0.7832	90.19 ($\mu\mu$)	95.4 (ee)	167807	966824024
4e	328.790	0.03951	94.24 (ee)	96.71 (ee)	176548	403771114
2e2 μ	341.160	0.741	94.87 (ee)	95.42 ($\mu\mu$)	178116	709511403
2e2 μ	349.150	0.05378	89.81 ($\mu\mu$)	93.5 (ee)	178479	757111474
4e	363.860	0.7412	91.31 (ee)	81.69 (ee)	172799	10347106
4e	366.260	0.4012	90.35 (ee)	94.39 (ee)	177875	148667118
4e	369.890	0.5418	93.03 (ee)	87.25 (ee)	177318	270676815
2e2 μ	386.660	0.3274	92.71 (ee)	94.25 ($\mu\mu$)	178786	277942410
2e2 μ	388.560	0.3843	91.52 ($\mu\mu$)	86.85 (ee)	173657	65557571
4 μ	453.410	0.0197	91.65 ($\mu\mu$)	90.25 ($\mu\mu$)	180250	45096064
4 μ	457.920	0.03608	91.9 ($\mu\mu$)	85.04 ($\mu\mu$)	172802	107360878
2e2 μ	533.630	0.8794	93.72 ($\mu\mu$)	95.19 (ee)	176886	427567024

Table 40: Observed events. 8 TeV.

type	$m_{4\ell}$	$dm_{4\ell}$	m_{Z_1}	m_{Z_2}	run	event
4e	121.970	0.969	74.05 (ee)	40.49 (ee)	193575	400912970
4 μ	125.250	0.9146	82.72 ($\mu\mu$)	38.93 ($\mu\mu$)	191856	53791282
2e2 μ	126.940	0.4965	75.89 ($\mu\mu$)	29.24 (ee)	195099	137440354
2e2 μ	146.090	0.2024	85.76 (ee)	16.26 ($\mu\mu$)	194051	6362525
4e	147.230	0.4547	78.85 (ee)	20.32 (ee)	194076	340846024
2e2 μ	154.150	0.02328	94.55 (ee)	16.14 ($\mu\mu$)	195147	399538705
4 μ	164.460	0.3082	92.8 ($\mu\mu$)	29.12 ($\mu\mu$)	194644	78891305
4 μ	167.510	0.7306	91.3 ($\mu\mu$)	74.88 ($\mu\mu$)	191830	480555885
2e2 μ	175.510	0.1657	90.35 ($\mu\mu$)	49.28 (ee)	194115	521997420
2e2 μ	180.250	0.5909	89.94 (ee)	85.3 ($\mu\mu$)	193541	306664497
2e2 μ	184.360	0.469	88.84 (ee)	93.74 ($\mu\mu$)	194075	76117998
4 μ	190.560	0.5447	90.7 ($\mu\mu$)	91.72 ($\mu\mu$)	194224	400957190
4e	191.430	0.5338	90.84 (ee)	87.29 (ee)	194480	109881951
4e	197.750	0.5041	90.26 (ee)	99.01 (ee)	194119	168130224
4e	199.880	0.5246	85.81 (ee)	84.73 (ee)	194153	93572313
2e2 μ	200.890	0.4456	91.19 ($\mu\mu$)	90.4 (ee)	191226	1820521419
2e2 μ	201.940	0.615	93.44 ($\mu\mu$)	93.74 (ee)	193541	115301904
2e2 μ	201.040	0.3959	89.71 (ee)	94.37 ($\mu\mu$)	195304	393582426
4e	202.810	0.4162	90.87 (ee)	90.24 (ee)	191062	330091192
4e	203.110	0.4722	90.9 (ee)	96.02 (ee)	194480	863682922
2e2 μ	205.720	0.4469	88.47 (ee)	104.8 ($\mu\mu$)	194050	519488427
4 μ	206.150	0.4858	89.39 ($\mu\mu$)	85.75 ($\mu\mu$)	195304	128008670
4e	207.420	0.5885	91.65 (ee)	95.77 (ee)	195378	155753218
4 μ	207.350	0.4602	89.45 ($\mu\mu$)	85.41 ($\mu\mu$)	194897	146471772
2e2 μ	212.270	0.3922	91.45 (ee)	85.67 ($\mu\mu$)	195147	607057396
4 μ	215.430	0.7069	91.03 ($\mu\mu$)	94.41 ($\mu\mu$)	195251	147388276
2e2 μ	218.260	0.6124	92.19 ($\mu\mu$)	87.75 (ee)	194108	394007716
2e2 μ	227.80	0.3374	82.97 (ee)	34.59 ($\mu\mu$)	195378	906545322
4e	229.0	0.6326	91.47 (ee)	91.84 (ee)	194050	401484983
4 μ	229.320	0.3882	90.68 ($\mu\mu$)	95.71 ($\mu\mu$)	194704	372667387
2e2 μ	230.220	0.4594	90.55 ($\mu\mu$)	82.08 (ee)	194314	243501633
2e2 μ	231.20	0.4692	92.68 ($\mu\mu$)	86.18 (ee)	195165	306811048
4 μ	233.450	0.6738	94.52 ($\mu\mu$)	103.1 ($\mu\mu$)	195147	502821363
4e	241.610	0.3507	83 (ee)	75.51 (ee)	193336	432667035
4 μ	241.160	0.1417	81.02 ($\mu\mu$)	59.97 ($\mu\mu$)	194789	164079659
2e2 μ	242.390	0.4509	93.35 (ee)	83.19 ($\mu\mu$)	191226	979037526
2e2 μ	247.350	0.494	94.26 ($\mu\mu$)	87.61 (ee)	195378	372893489
4e	253.950	0.3837	87.43 (ee)	96.7 (ee)	195304	1069824602
4 μ	254.080	0.3439	90.94 ($\mu\mu$)	34.08 ($\mu\mu$)	195304	487153301
2e2 μ	257.250	0.2706	93.13 ($\mu\mu$)	89.17 (ee)	194790	38426260
4e	259.230	0.6267	96.21 (ee)	99.06 (ee)	194108	818802354
2e2 μ	266.160	0.1895	92.51 (ee)	94.63 ($\mu\mu$)	191226	1730707882
2e2 μ	271.640	0.741	88.34 ($\mu\mu$)	88.24 (ee)	194644	196674650
2e2 μ	278.060	0.7043	91.54 ($\mu\mu$)	89.31 (ee)	195147	567117841
2e2 μ	302.610	0.5313	91.03 (ee)	95.12 ($\mu\mu$)	195115	18955331
4e	321.550	0.1992	96.41 (ee)	78.58 (ee)	193621	393672516
2e2 μ	332.860	0.4818	83.13 (ee)	48.72 ($\mu\mu$)	194533	677674570
2e2 μ	392.30	0.1533	90.95 (ee)	86.5 ($\mu\mu$)	191277	617265349
2e2 μ	570.970	0.6323	90.26 (ee)	89.11 ($\mu\mu$)	195113	622426000

2320 **7 TeV Candidate** ($m_{4\ell} = 137.7 \text{ GeV}/c^2$, $\Delta m_{4\ell} = 1.25 \text{ GeV}/c^2$, $m_{Z_1} = 91.9 \text{ GeV}/c^2$, $m_{Z_2} = 28.8 \text{ GeV}/c^2$).

- 2321 • 4 electrons
 2322 • No extra electron nor muon
 2323 • No extra photon
 2324 • 2 extra tracks $p_T > 5 \text{ GeV}/c$
 2325 • 4 extra jets $p_T > 10 \text{ GeV}/c$
 2326 • MET (PF): 9.95 GeV
 2327 • 7 vertices in the event (all leptons come from the same primary vertex)

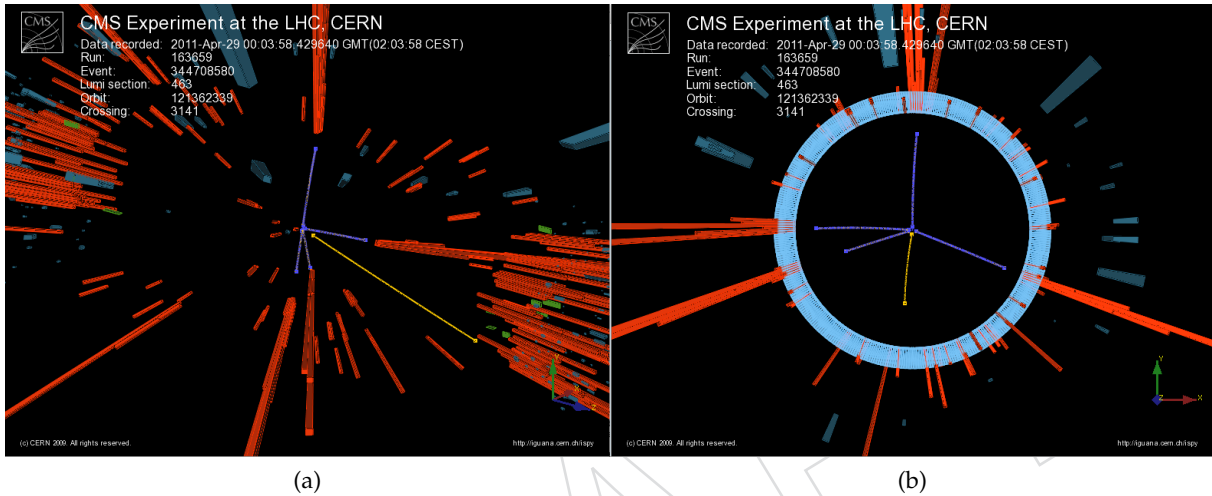


Figure 116: (a) 3D view and (b) R-Phi view of the event D (Run # 163659 - Event # 344708580). The four electrons (in blue) are all in the ECAL barrel. The electrons with $p_T = 26.8 \text{ GeV}/c$ and $13.8 \text{ GeV}/c$ at $\phi = 1.58$ and 3.07 rad respectively and constituting the Z2 candidate are showering with clear double cluster patterns. There are two other tracks with $p_T > 5 \text{ GeV}/c$ close to each other at $\phi \sim -1.7 \text{ rad}$ and in the forward region, well away from the electrons. One is reconstructed as a GSF track (in yellow) and has several nearby low p_T tracks, including a possible conversion leg. Possibly a tau jet.

2328 **7 TeV Candidate** ($m_{4\ell} = 118.8 \text{ GeV}/c^2$, $\Delta m_{4\ell} = 0.71 \text{ GeV}/c^2$, $m_{Z_1} = 90.3 \text{ GeV}/c^2$, $m_{Z_2} = 14.7 \text{ GeV}/c^2$).

- 2329 • 4 muons
- 2330 • No extra electron nor muon
- 2331 • No extra photon
- 2332 • No extra tracks $p_T > 5 \text{ GeV}/c$
- 2333 • 1 extra jets $p_T > 10 \text{ GeV}/c$ (central, $p_T = 18 \text{ GeV}/c$)
- 2334 • MET (PF): 16.3 GeV
- 2335 • 2 vertices in the event (all leptons come from the same primary vertex)

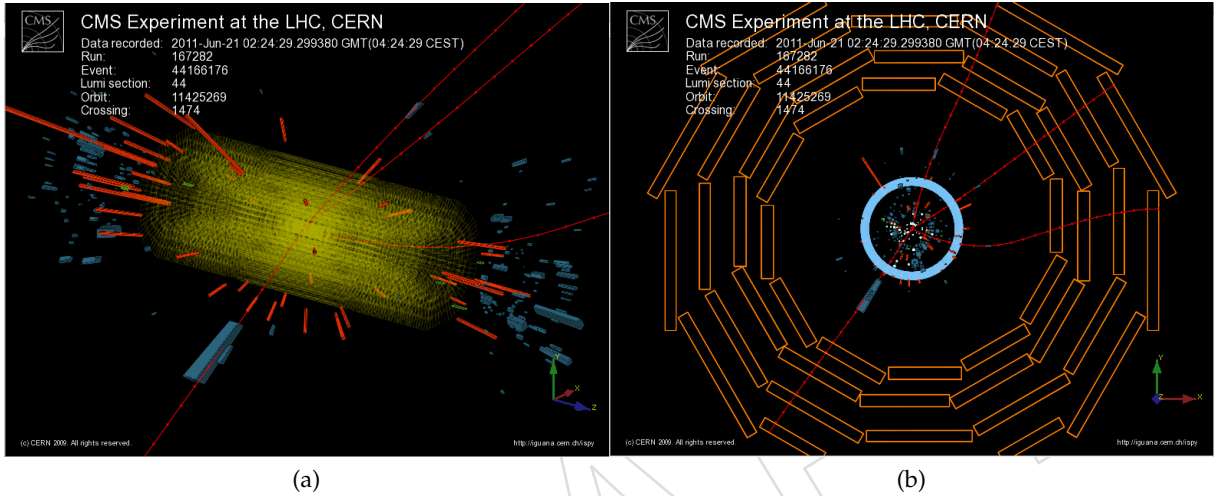


Figure 117: (a) 3D view and (b) R-Phi view of the event R-C (Run # 167282 - Event # 44166176). Very clean event with only two vertices. The two muons (constituting the Z1 candidate) are close to back-to-back in the transverse plane ($\phi = -2.13 \text{ rad}$ and $\phi = 0.54 \text{ rad}$). The Z2 candidate is constituted by the two lowest p_T muons, one of which is just above the threshold with a p_T of 5.2 GeV/c . Muons are in red.

2336 **7 TeV Candidate** ($m_{4\ell} = 130.3 \text{ GeV}/c^2$, $\Delta m_{4\ell} = 3.63 \text{ GeV}/c^2$, $m_{Z_1} = 92.3 \text{ GeV}/c^2$, $m_{Z_2} = 17.0 \text{ GeV}/c^2$).

- 2337 • 2 electrons - 2 muons
- 2338 • 1 extra electron ($p_T = 2.4 \text{ GeV}/c$)
- 2339 • No extra photon
- 2340 • No extra tracks $p_T > 5 \text{ GeV}/c$
- 2341 • No extra jets $p_T > 10 \text{ GeV}/c$
- 2342 • MET (PF): 9.0 GeV
- 2343 • 3 vertices in the event (all leptons come from the same primary vertex)

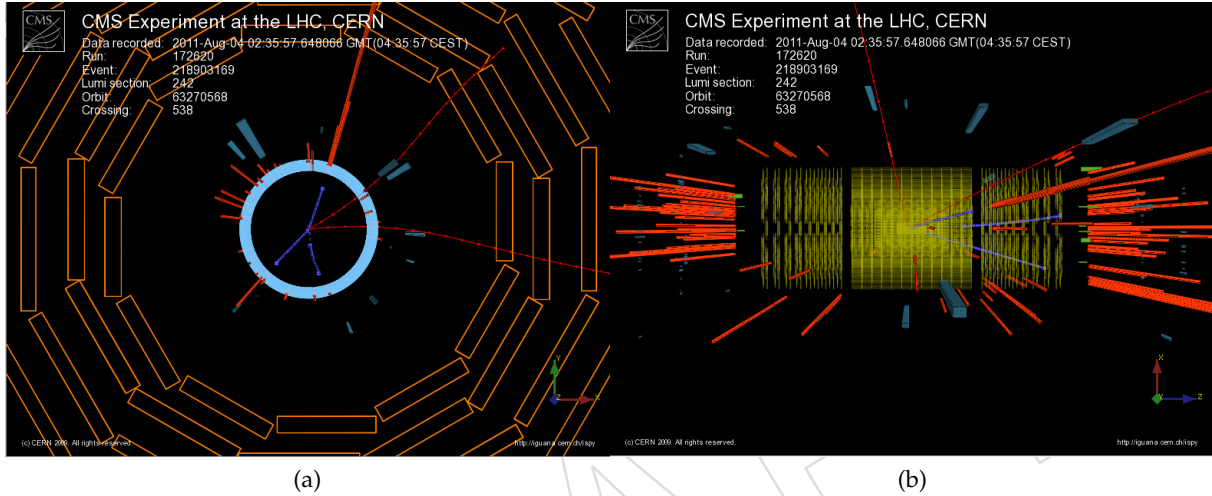


Figure 118: (a) R-Phi view and (b) R-Z view of the event R-D (Run # 172620 - Event # 218903169). The Z1 candidate is constituted by the two well isolated electrons (in blue) at $\phi = -2.32$ and 1.23 rad (back-to-back configuration). The leading electron is a 'crack' electron in the transition region between the ECAL barrel and the positive endcap. Its $\sigma_{ij\eta i\eta}$ is not very good due to this particular location, but the electron passes the ID thanks to the loose requirements applied. The other electron is a 'golden' in the ECAL barrel. The two muons (in red) constituting the low mass pair have p_T around $10 \text{ GeV}/c$. There is an extra reconstructed electron of very low p_T ($2.4 \text{ GeV}/c$) in the forward region ($\eta = 1.7$) and not starting from the primary vertex..

2344 **7 TeV Candidate** ($m_{4\ell} = 132.5 \text{ GeV}/c^2$, $\Delta m_{4\ell} = 1.9 \text{ GeV}/c^2$, $m_{Z_1} = 85.9 \text{ GeV}/c^2$, $m_{Z_2} = 43.0 \text{ GeV}/c^2$).

- 2345 • 4 leptons: 4 electrons
 2346 • No other track $p_T >> 5 \text{ GeV}$
 2347 • 1 jets $p_T > 10 \text{ GeV}$ ($p_T = 10.9 \text{ GeV}$, $\eta = 2.8$)
 2348 • No other photon nor muon
 2349 • pfMET: 30.5 GeV
 2350 • 10 vertices, the 4 leptons belong to the same primary vertex

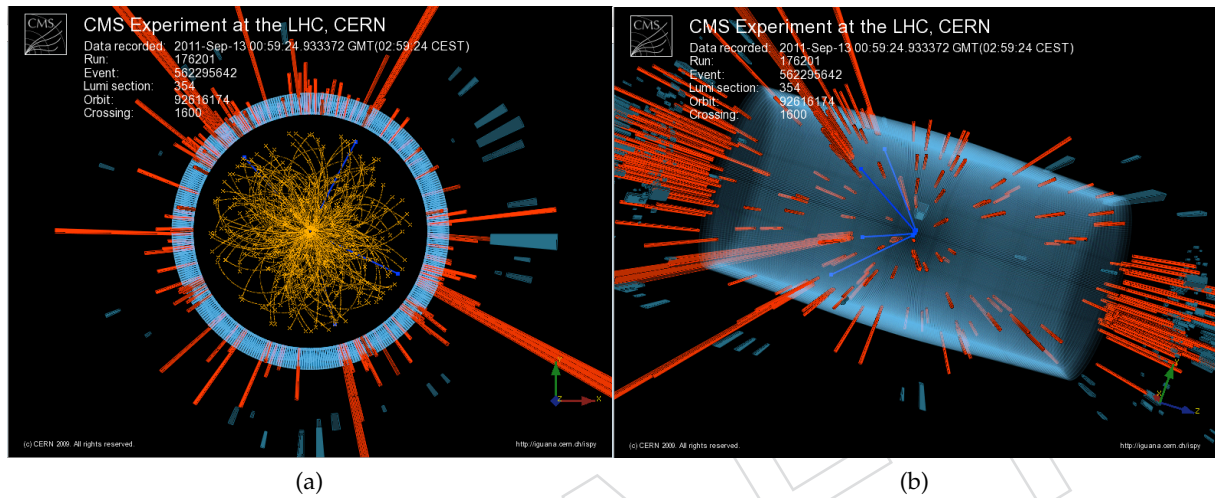


Figure 119: (a) R-Phi view and (b) 3D view of the event (Run # 176201 - Event # 562295642). All electrons are central. Two are showering with high fbrem, the two others are golden. The electrons are well isolated. ECAL rechit flags are good.

2351 **7 TeV Candidate** ($m_{4\ell} = 130.1 \text{ GeV}/c^2$, $\Delta m_{4\ell} = 2.52 \text{ GeV}/c^2$, $m_{Z_1} = 75.6 \text{ GeV}/c^2$, $m_{Z_2} = 12.9 \text{ GeV}/c^2$).

- 2352 • 2 electrons - 2 muons
 2353 • No extra electron nor muon
 2354 • 2 extra photons
 2355 • 3 extra tracks $p_T > 5 \text{ GeV}/c$
 2356 • 2 extra jets $p_T > 10 \text{ GeV}/c$
 2357 • MET (PF): 13.7 GeV
 2358 • 4 vertices in the event (all leptons come from the same primary vertex)

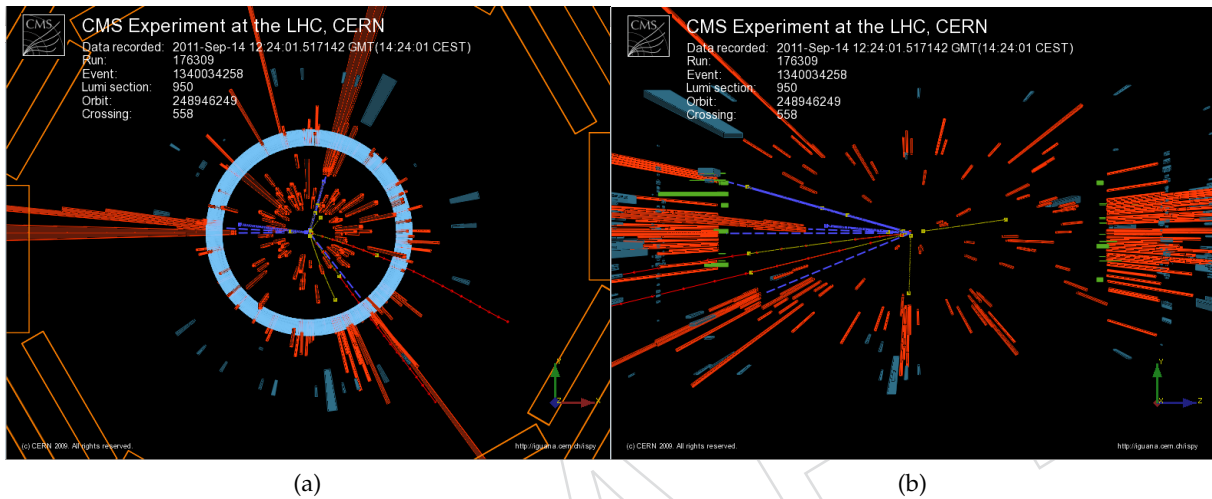


Figure 120: (a) R-Phi view and (b) R-Z view of the event R-F (Run # 176309 - Event # 1340034258). The leading electron (in blue) constituting the Z1 pair is a 'showering' in the negative ECAL endcap. The sub-leading electron is a 'crack' electron in a gap between two modules in the ECAL barrel. The two muons (in red) constituting the low mass pair are also in the negative η forward region. There are two extra isolated photons. In addition, there is an additional reconstructed photon very close to the electron at $\phi = 3.10$ which corresponds to a high energy bremsstrahlung radiated by the electron and whose energy is collected within the electron supercluster.

2359 **7 TeV Candidate** ($m_{4\ell} = 125.8 \text{ GeV}/c^2$, $\Delta m_{4\ell} = 1.79 \text{ GeV}/c^2$, $m_{Z_1} = 67.5 \text{ GeV}/c^2$, $m_{Z_2} = 48.5 \text{ GeV}/c^2$).

- 2360 • 2 electrons - 2 muons
 2361 • 1 extra electron ($p_T = 2.8 \text{ GeV}/c$)
 2362 • No extra photons
 2363 • No extra tracks $p_T > 5 \text{ GeV}/c$
 2364 • 6 extra jets $p_T > 10 \text{ GeV}/c$ (mostly $|\eta| > 2.5$)
 2365 • MET (PF): 3.2 GeV
 2366 • 12 vertices in the event (all leptons come from the same primary vertex)

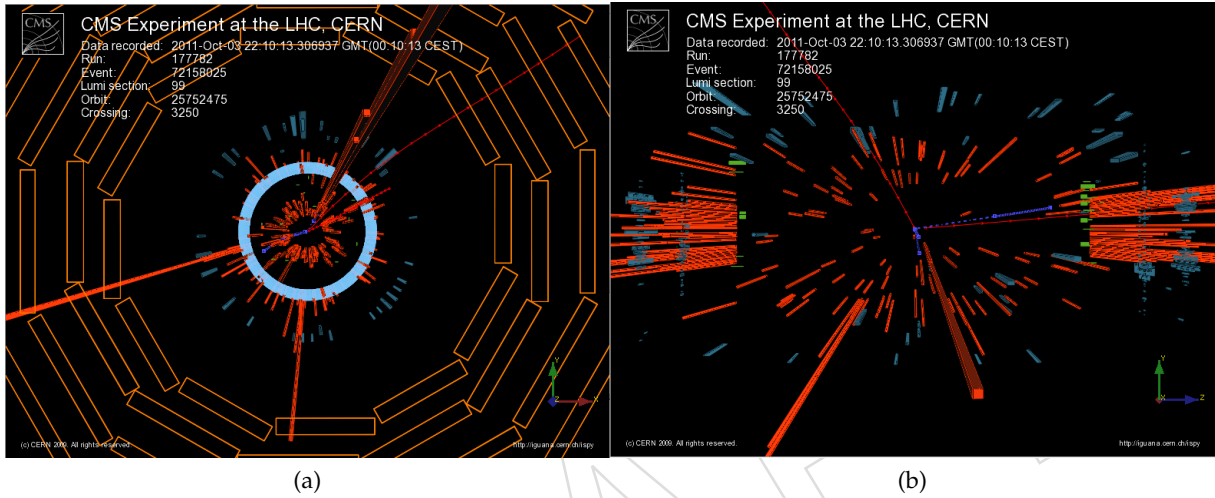


Figure 121: (a) R-Phi view and (b) R-Z view of the event AS (Run # 177782 - Event # 72158025). The leading electron of $28.2 \text{ GeV}/c$ constituting the Z1 candidate is very close to the acceptance border with $\eta = 2.438$. It is ECAL driven only and only starts in the TEC layers with one missing expected hit in the innermost layers. The sub-leading electron constituting the Z1 candidate has a rather high relative isolation and a SIP_{3D} close to the cut value. One of the two muons is also close to the acceptance border with an η of 2.35. Overall not a very nice candidate. Electrons are in blue and muons in red.

2367 **7 TeV Candidate** ($m_{4\ell} = 126.1 \text{ GeV}/c^2, \Delta m_{4\ell} = 0.77 \text{ GeV}/c^2, m_{Z_1} = 94.3 \text{ GeV}/c^2, m_{Z_2} = 26.0 \text{ GeV}/c^2$).

- 2368 • 4 muons
- 2369 • 1 extra electron ($p_T > 6.7 \text{ GeV}/c$) within a jet
- 2370 • 1 extra isolated SC with $E_T = 7.6 \text{ GeV}$, recovered through the FSR recovery algorithm
- 2371 • 6 extra tracks $p_T > 5 \text{ GeV}/c$ (one corresponding to the extra electron within the jet)
- 2372 • 18 extra jets $p_T > 10 \text{ GeV}/c$ (leading one with $\sim 27 \text{ GeV}/c$)
- 2373 • MET (PF): 11.6 GeV
- 2374 • 25 vertices in the event, 952 tracks (all leptons come from the same primary vertex)

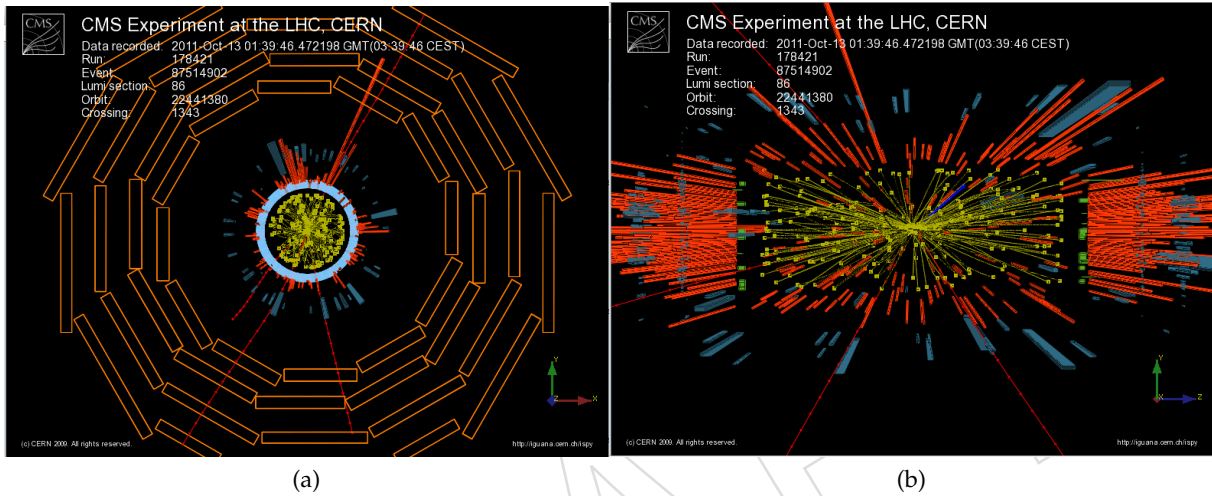


Figure 122: (a) R-Phi view and (b) R-Z view of the event AY (Run # 178421 -Event # 87514902). Very high vertex multiplicity (25 vertices, 952 tracks). All tracks with $p_T > 0.8 \text{ GeV}/c$ are shown in yellow on both views. There is one isolated extra SC of $E_T = 7.6 \text{ GeV}$, close to the muon at $\phi = 1.2 \text{ rad}$ ($\Delta dR = 0.34$). There is one extra electron of $6.7 \text{ GeV}/c$, well away from the four muons and clearly within a jet. The muons are in red.

2375 **7 TeV Candidate** ($m_{4\ell} = 122.0 \text{ GeV}/c^2$, $\Delta m_{4\ell} = 1.6 \text{ GeV}/c^2$, $m_{Z_1} = 59.2 \text{ GeV}/c^2$, $m_{Z_2} = 31.6 \text{ GeV}/c^2$).

- 2376 • 4 leptons: 4 muons
 2377 • No other track $p_T > 5 \text{ GeV}$
 2378 • No jets $p_T > 10 \text{ GeV}$
 2379 • No other photon nor muon
 2380 • pfMET: 12.7 GeV
 2381 • 5 vertices, the 4 leptons belong to the same primary vertex

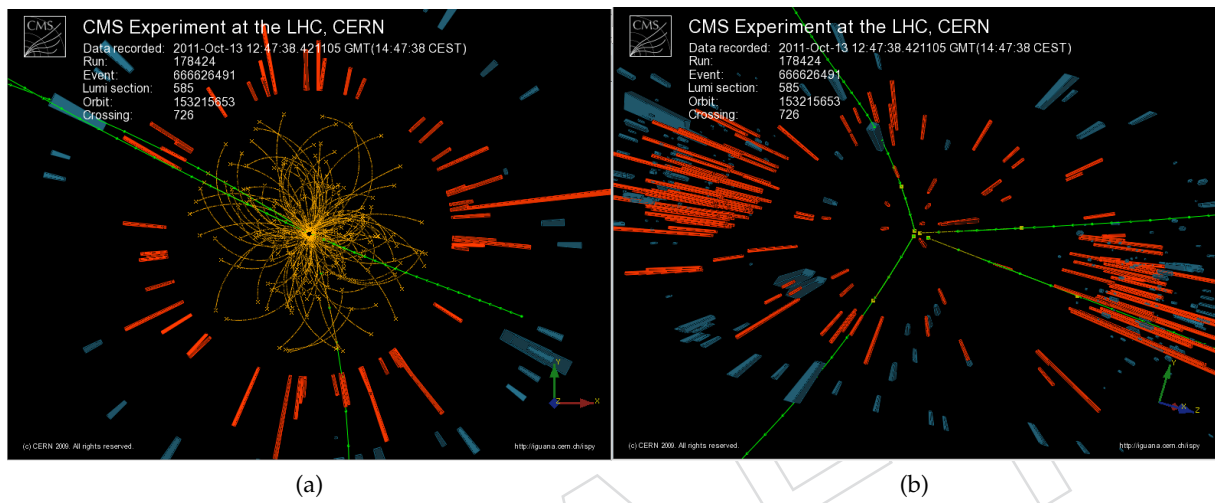


Figure 123: (a) R-Phi view and (b) 3D view of the event (Run # 178424 - Event # 666626491). Very clean event. Two muons are central, the two others are forward.

2382 **8 TeV Candidate** ($m_{4\ell} = 122.0 \text{ GeV}/c^2, \Delta m_{4\ell} = 3.0 \text{ GeV}/c^2, m_{Z_1} = 74.1 \text{ GeV}/c^2, m_{Z_2} = 40.5 \text{ GeV}/c^2$).

- 2383 • 4 electrons
 2384 • 2 other track $p_T > 5 \text{ GeV}$, well away from the electrons
 2385 • 5 jets $p_T > 10 \text{ GeV}$ (mostly forward, $p_T < 20 \text{ GeV}$)
 2386 • No extra photon
 2387 • pfMET: 22.0 GeV
 2388 • 11 vertices, the 4 leptons belong to the same primary vertex well separated from other vertices

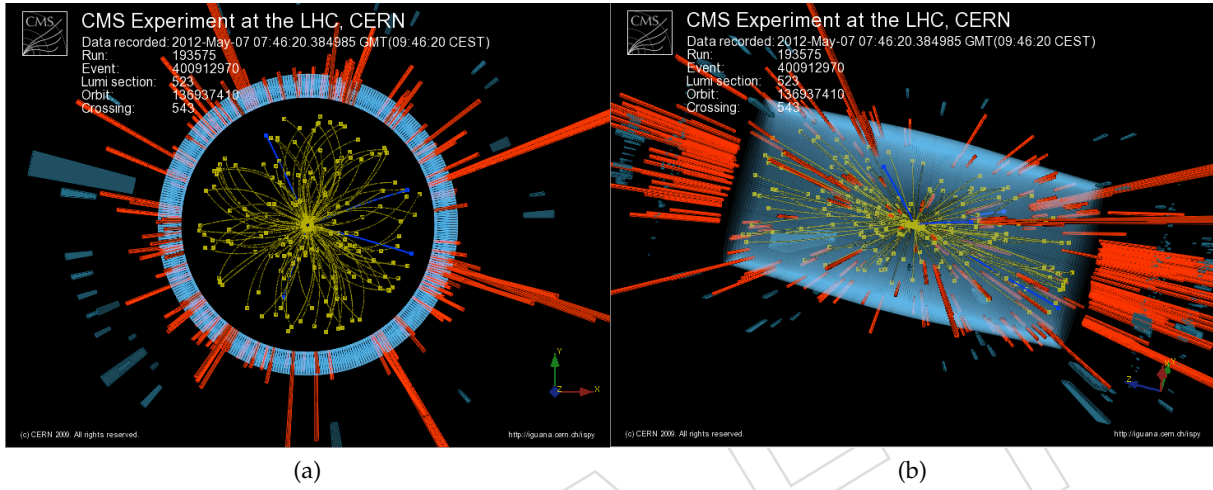


Figure 124: (a) R-Phi view and (b) 3D view of the event (Run # 193575 - Event # 400912970). Three electrons are central, one is in EE. There is one extra standalone muon of $p_T = 2.6 \text{ GeV}$, not reconstructed as global muon. One electron is golden, one is bigbrem, two are showering. Electron deta/dphi are excellent, fbrem is very low for all but for the bigbrem case. Id variable are good and mva (old one) is electron like for the 3 electrons that are reconstructed by PF. The showering electron of $p_T = 28.7 \text{ GeV}$ has 1 missing hit and is ecalDriven only. Charge estimates are all in agreement and the electrons are well isolated. ECAL rechit flags are good.

2389 **8 TeV Candidate** ($m_{4\ell} = 127.0 \text{ GeV}/c^2$, $\Delta m_{4\ell} = 1.2 \text{ GeV}/c^2$, $m_{Z_1} = 75.9 \text{ GeV}/c^2$, $m_{Z_2} = 29.2 \text{ GeV}/c^2$).

- 2390 • 4 leptons: 2 electrons 2 muons
 2391 • 3 other track $p_T > 4 \text{ GeV}$, well away from the electrons
 2392 • 8 jets $p_T > 10 \text{ GeV}$ ($p_T < 15 \text{ GeV}$)
 2393 • No extra photon
 2394 • pfMET: 16.4 GeV
 2395 • 19 vertices, the 4 leptons belong to the same primary vertex well separated from other vertices

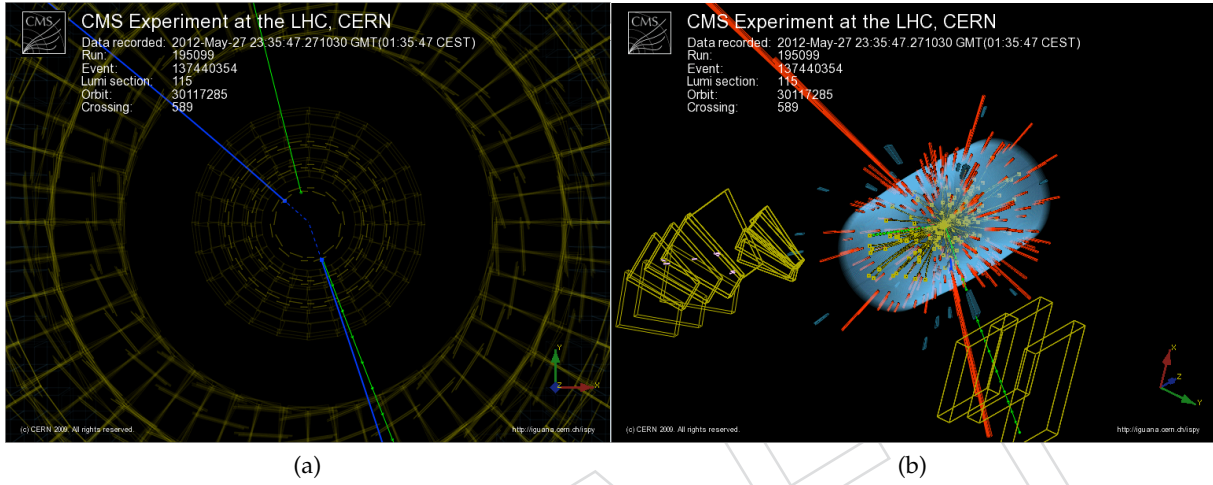


Figure 125: (a) R-Phi view and (b) 3D view of the event (Run # 195099 - Event # 137440354). One electron is golden (21.3), the other is showering (10.3), both are in EB. ID variables are very good, fbrem low for the golden and high for the showering case. Mva is very electron like. Both electrons are ecal and tracker driven. Charge estimates are all in agreement and the electrons are well isolated. ECAL rechit flags are good.

2396 **8 TeV Candidate** ($m_{4\ell} = 125.2 \text{ GeV}/c^2, \Delta m_{4\ell} = 0.7 \text{ GeV}/c^2, m_{Z_1} = 82.7 \text{ GeV}/c^2, m_{Z_2} = 38.9 \text{ GeV}/c^2$).

- 2397 • 4 leptons: 4 muons
 2398 • 2 other track $p_T > 5 \text{ GeV}$, well away from the muons
 2399 • 1 jets $p_T > 10 \text{ GeV}$ in the central region
 2400 • No other photon nor electron
 2401 • pfMET: 29.8 GeV
 2402 • 11 vertices, the 4 leptons belong to the same primary vertex well separated from other vertices

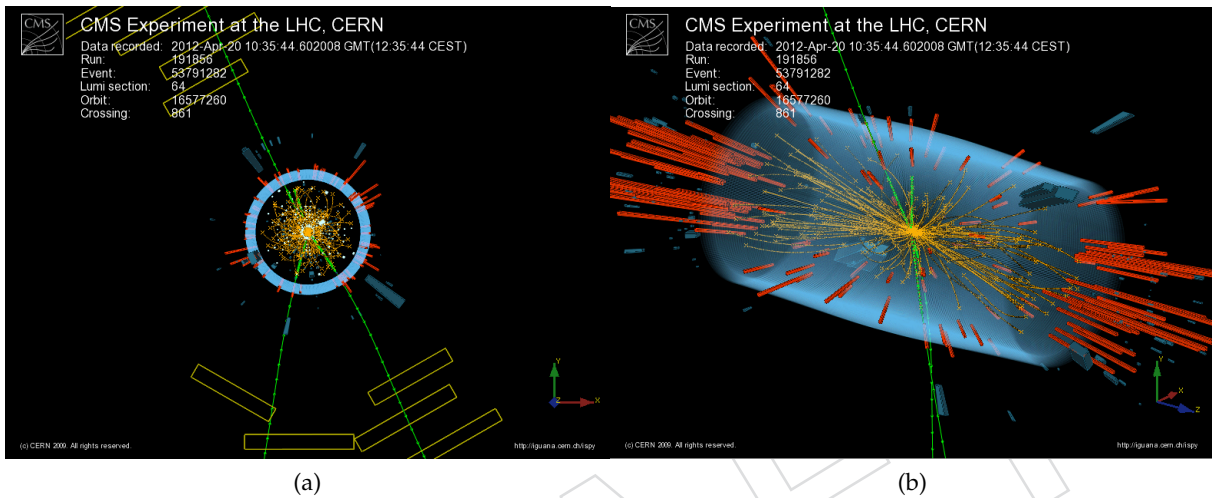


Figure 126: (a) R-Phi view and (b) 3D view of the event (Run # 191856 - Event # 53791282). All muons are central. One muon ($p_T = 22.3 \text{ GeV}$) is only tracker muon.

2403 **B Appendix #2 Control of lepton efficiencies from data, tables**

Table 41: Reconstruction efficiencies for single electrons, measured with the Tag and Probe technique on data, and data/MC discrepancy obtained applying the method on MC. All measurements are obtained using Z decays.

p_T Range (GeV/c)	$ \eta $ Coverage	Data	MC	Data/MC Ratio
10-20	0-1.479	1.000	1.000	1.000 ± 0.000 (stat.) ± 0.014 (sys.)
20-30	0-1.479	0.968	0.949	1.020 ± 0.005 (stat.) ± 0.010 (sys.)
30-40	0-1.479	0.980	0.977	1.002 ± 0.001 (stat.) ± 0.010 (sys.)
40-50	0-1.479	0.980	0.987	0.993 ± 0.001 (stat.) ± 0.010 (sys.)
>50	0-1.479	0.985	0.989	0.995 ± 0.002 (stat.) ± 0.010 (sys.)
10-20	1.479-2.5	0.843	0.842	1.001 ± 0.026 (stat.) ± 0.010 (sys.)
20-30	1.479-2.5	0.951	0.921	1.033 ± 0.008 (stat.) ± 0.010 (sys.)
30-40	1.479-2.5	0.945	0.946	0.999 ± 0.003 (stat.) ± 0.010 (sys.)
40-50	1.479-2.5	0.962	0.949	1.013 ± 0.002 (stat.) ± 0.010 (sys.)
>50	1.479-2.5	0.950	0.956	0.994 ± 0.005 (stat.) ± 0.010 (sys.)

DRAFT

Table 42: Identification, Isolation and IP efficiencies for single electrons, measured with the Tag and Probe technique on data, and data/MC discrepancy obtained applying the method on MC. All measurements are obtained using Z decays in 2011 data.

p_T Range (GeV/c)	$ \eta $ Coverage	Data (%)	MC (%)	Data/MC Ratio
7 - 10	0 - 1.4442	0.730	0.748	$0.976^{+0.019}_{-0.032}$ (syst.) ± 0.060 (stat.)
10-15	0 - 0.8	0.814	0.805	$1.012^{+0.022}_{-0.038}$ (syst.) ± 0.015 (stat.)
15-20	0 - 0.8	0.850	0.840	$1.012^{+0.022}_{-0.038}$ (syst.) ± 0.007 (stat.)
20-30	0 - 0.8	0.905	0.916	$0.989^{+0.017}_{-0.029}$ (syst.) ± 0.002 (stat.)
30-40	0 - 0.8	0.950	0.954	$0.996^{+0.010}_{-0.010}$ (syst.) ± 0.001 (stat.)
40-50	0 - 0.8	0.966	0.969	$0.997^{+0.010}_{-0.010}$ (syst.) ± 0.000 (stat.)
>50	0 - 0.8	0.972	0.972	$1.000^{+0.011}_{-0.012}$ (syst.) ± 0.001 (stat.)
10-15	0.8 - 1.4442	0.830	0.848	$0.970^{+0.018}_{-0.030}$ (syst.) ± 0.014 (stat.)
15-20	0.8 - 1.4442	0.868	0.858	$1.011^{+0.010}_{-0.010}$ (syst.) ± 0.007 (stat.)
20-30	0.8 - 1.4442	0.905	0.917	$0.987^{+0.022}_{-0.039}$ (syst.) ± 0.002 (stat.)
30-40	0.8 - 1.4442	0.945	0.948	$0.997^{+0.010}_{-0.010}$ (syst.) ± 0.001 (stat.)
40-50	0.8 - 1.4442	0.949	0.958	$0.991^{+0.010}_{-0.010}$ (syst.) ± 0.001 (stat.)
>50	0.8 - 1.4442	0.949	0.965	$0.984^{+0.011}_{-0.014}$ (syst.) ± 0.001 (stat.)
>7	1.4442 - 1.566	0.852	0.863	$0.987^{+0.049}_{-0.084}$ (syst.) ± 0.003 (stat.)
7 - 10	1.566 - 2.5	0.708	0.698	$1.015^{+0.021}_{-0.036}$ (syst.) ± 0.048 (stat.)
10-15	1.566 - 2	0.804	0.817	$0.975^{+0.026}_{-0.047}$ (syst.) ± 0.021 (stat.)
15-20	1.566 - 2	0.859	0.843	$1.019^{+0.010}_{-0.010}$ (syst.) ± 0.006 (stat.)
20-30	1.566 - 2	0.926	0.916	$1.011^{+0.014}_{-0.022}$ (syst.) ± 0.002 (stat.)
30-40	1.566 - 2	0.922	0.938	$0.983^{+0.013}_{-0.020}$ (syst.) ± 0.000 (stat.)
40-50	1.566 - 2	0.923	0.941	$0.980^{+0.010}_{-0.010}$ (syst.) ± 0.001 (stat.)
>50	1.566 - 2	0.938	0.952	$0.985^{+0.011}_{-0.013}$ (syst.) ± 0.000 (stat.)
10-15	2 - 2.5	0.814	0.809	$0.997^{+0.010}_{-0.012}$ (syst.) ± 0.021 (stat.)
15-20	2 - 2.5	0.834	0.838	$0.995^{+0.010}_{-0.010}$ (syst.) ± 0.006 (stat.)
20-30	2 - 2.5	0.898	0.919	$0.978^{+0.011}_{-0.014}$ (syst.) ± 0.003 (stat.)
30-40	2 - 2.5	0.899	0.916	$0.982^{+0.010}_{-0.010}$ (syst.) ± 0.002 (stat.)
40-50	2 - 2.5	0.931	0.914	$1.018^{+0.010}_{-0.010}$ (syst.) ± 0.002 (stat.)
>50	2 - 2.5	0.931	0.925	$1.006^{+0.013}_{-0.020}$ (syst.) ± 0.000 (stat.)

Table 43: Identification, Isolation and IP efficiencies for single electrons, measured with the Tag and Probe technique on data, and data/MC discrepancy obtained applying the method on MC. All measurements are obtained using Z decays in 2012 data.

7-10	0 - 1.479	0.670	0.673	$0.996^{+0.013}_{-0.020}$ (syst.) ± 0.084 (stat.)
10-15	0 - 1.479	0.841	0.803	$1.048^{+0.016}_{-0.025}$ (syst.) ± 0.022 (stat.)
15-20	0 - 1.479	0.802	0.835	$0.961^{+0.016}_{-0.027}$ (syst.) ± 0.011 (stat.)
20-30	0 - 1.479	0.863	0.911	$0.946^{+0.023}_{-0.040}$ (syst.) ± 0.003 (stat.)
30-40	0 - 1.479	0.923	0.946	$0.976^{+0.011}_{-0.014}$ (syst.) ± 0.001 (stat.)
40-50	0 - 1.479	0.944	0.959	$0.985^{+0.010}_{-0.010}$ (syst.) ± 0.001 (stat.)
>50	0 - 1.479	0.936	0.962	$0.973^{+0.011}_{-0.013}$ (syst.) ± 0.002 (stat.)
7-10	1.479 - 2.5	0.614	0.541	$1.136^{+0.034}_{-0.062}$ (syst.) ± 0.109 (stat.)
10-15	1.479 - 2.5	0.666	0.709	$0.939^{+0.031}_{-0.055}$ (syst.) ± 0.043 (stat.)
15-20	1.479 - 2.5	0.795	0.806	$0.987^{+0.029}_{-0.051}$ (syst.) ± 0.013 (stat.)
20-30	1.479 - 2.5	0.872	0.892	$0.977^{+0.018}_{-0.031}$ (syst.) ± 0.004 (stat.)
30-40	1.479 - 2.5	0.905	0.930	$0.973^{+0.010}_{-0.010}$ (syst.) ± 0.002 (stat.)
40-50	1.479 - 2.5	0.927	0.947	$0.979^{+0.010}_{-0.010}$ (syst.) ± 0.002 (stat.)
>50	1.479 - 2.5	0.916	0.950	$0.964^{+0.013}_{-0.018}$ (syst.) ± 0.004 (stat.)

Table 44: Efficiency for the requirement on the significance of the 3d impact parameter, measured using the tag-and-probe method for muons with $p_T < 20$ GeV and reconstructed as tracks in the inner tracker.

Region $ \eta $ range p_T range	Efficiencies for 2011 [%]			Efficiencies for 2012 [%]		
	data	sim.	ratio \pm stat.	data	sim.	ratio \pm stat.
+0.0, +1.2 5.0, 7.5	97.4	97.8	0.996 ± 0.007	100.0	96.1	1.041 ± 0.020
+0.0, +1.2 7.5, 10.0	98.2	99.3	0.989 ± 0.004	97.3	97.9	0.994 ± 0.029
+0.0, +1.2 10.0, 15.0	99.4	99.2	1.002 ± 0.005	95.8	98.9	0.969 ± 0.037
+0.0, +1.2 15.0, 20.0	100.0	99.9	1.001 ± 0.004	100.0	99.9	1.001 ± 0.013
+1.2, +2.4 5.0, 7.5	99.1	99.3	0.998 ± 0.013	98.6	98.5	1.001 ± 0.015
+1.2, +2.4 7.5, 10.0	99.0	99.6	0.993 ± 0.008	93.6	98.8	0.947 ± 0.056
+1.2, +2.4 10.0, 15.0	97.4	99.7	0.977 ± 0.011	100.0	99.3	1.007 ± 0.043
+1.2, +2.4 15.0, 20.0	100.0	99.8	1.002 ± 0.001	100.0	100.0	1.000 ± 0.001

Table 45: Efficiency for the requirement on the significance of the 3d impact parameter, measured using the tag-and-probe method for muons with $p_T > 20$ GeV and reconstructed as tracks in the inner tracker.

Region η range	Efficiencies for 2011A [%]			Efficiencies for 2011B [%]			Efficiencies for 2012 [%]		
	data	sim.	ratio ± stat.	data	sim.	ratio ± stat.	data	sim.	ratio ± stat.
-2.4, -2.1	99.5	99.6	0.999 ± 0.001	98.4	99.6	0.988 ± 0.003	98.8	99.2	0.995 ± 0.003
-2.1, -1.6	99.5	99.8	0.997 ± 0.001	98.2	99.8	0.984 ± 0.001	99.2	99.5	0.997 ± 0.002
-1.6, -1.2	99.9	99.9	1.000 ± 0.001	98.9	99.9	0.990 ± 0.001	99.8	99.8	1.001 ± 0.001
-1.2, -0.9	99.8	99.9	1.000 ± 0.001	99.6	99.9	0.998 ± 0.001	99.7	99.8	0.999 ± 0.001
-0.9, -0.6	99.8	99.9	0.999 ± 0.001	99.8	99.9	0.999 ± 0.001	99.7	99.8	1.000 ± 0.001
-0.6, -0.3	99.8	99.9	0.999 ± 0.001	99.8	99.9	0.999 ± 0.001	99.7	99.8	1.000 ± 0.001
-0.3, -0.2	99.4	99.5	0.999 ± 0.001	99.4	99.5	0.998 ± 0.001	99.0	99.0	1.000 ± 0.002
-0.2, +0.2	99.9	99.9	0.999 ± 0.001	99.8	99.9	0.999 ± 0.001	99.7	99.7	1.000 ± 0.001
+0.2, +0.3	99.3	99.4	0.999 ± 0.001	99.2	99.4	0.998 ± 0.001	98.6	99.1	0.995 ± 0.002
+0.3, +0.6	99.8	99.9	0.998 ± 0.001	99.9	99.9	1.000 ± 0.001	99.9	99.8	1.001 ± 0.001
+0.6, +0.9	99.8	99.9	0.999 ± 0.001	99.7	99.9	0.998 ± 0.001	99.6	99.8	0.998 ± 0.001
+0.9, +1.2	99.7	99.8	0.998 ± 0.001	99.6	99.8	0.998 ± 0.001	99.7	99.7	1.000 ± 0.001
+1.2, +1.6	99.7	99.8	0.999 ± 0.001	98.8	99.8	0.990 ± 0.001	99.9	99.6	1.003 ± 0.001
+1.6, +2.1	99.5	99.7	0.998 ± 0.001	98.2	99.7	0.985 ± 0.001	99.2	99.5	0.996 ± 0.002
+2.1, +2.4	99.3	99.4	0.999 ± 0.001	97.7	99.4	0.983 ± 0.003	98.7	99.2	0.995 ± 0.003

Table 46: Efficiency for the requirement on the significance of the 3d impact parameter, measured using the tag-and-probe method for muons with $p_T < 20$ GeV and passing the Particle Flow identification.

Region $ \eta $ range p_T range	Efficiencies for 2011 [%]			Efficiencies for 2012 [%]		
	data	sim.	ratio ± stat.	data	sim.	ratio ± stat.
+0.0, +1.2 5.0, 10.0	99.2	99.5	0.997 ± 0.009	95.6	100.0	0.956 ± 0.028
+0.0, +1.2 10.0, 15.0	99.5	99.6	0.999 ± 0.002	98.4	99.3	0.991 ± 0.007
+0.0, +1.2 15.0, 20.0	99.6	99.5	1.001 ± 0.001	99.4	99.7	0.996 ± 0.002
+1.2, +2.4 5.0, 10.0	97.6	99.0	0.986 ± 0.005	98.2	98.0	1.002 ± 0.014
+1.2, +2.4 10.0, 15.0	99.1	99.2	0.998 ± 0.001	98.7	99.5	0.992 ± 0.004
+1.2, +2.4 15.0, 20.0	98.9	99.3	0.996 ± 0.001	98.7	99.5	0.992 ± 0.001

Table 47: Efficiency for the requirement on the significance of the 3d impact parameter, measured using the tag-and-probe method for muons with $p_T > 20$ GeV and passing the Particle Flow identification.

Region η range	Efficiencies for 2011 [%]			Efficiencies for 2012 [%]		
	data	sim.	ratio \pm stat.	data	sim.	ratio \pm stat.
-2.4, -2.1	98.9	99.1	0.998 \pm 0.001	99.1	99.3	0.998 \pm 0.001
-2.1, -1.6	99.3	99.5	0.998 \pm 0.001	99.1	99.5	0.996 \pm 0.001
-1.6, -1.2	99.5	99.6	0.999 \pm 0.001	99.4	99.6	0.998 \pm 0.001
-1.2, -0.9	99.6	99.6	1.000 \pm 0.001	99.5	99.7	0.998 \pm 0.001
-0.9, -0.6	99.7	99.6	1.000 \pm 0.001	99.6	99.6	0.999 \pm 0.001
-0.6, -0.3	99.7	99.6	1.001 \pm 0.001	99.6	99.6	1.000 \pm 0.001
-0.3, -0.2	99.7	99.6	1.001 \pm 0.001	99.8	99.7	1.001 \pm 0.001
-0.2, +0.2	99.7	99.6	1.001 \pm 0.001	99.7	99.7	0.999 \pm 0.001
+0.2, +0.3	99.7	99.6	1.001 \pm 0.001	99.6	99.7	0.999 \pm 0.001
+0.3, +0.6	99.7	99.6	1.000 \pm 0.001	99.6	99.7	1.000 \pm 0.001
+0.6, +0.9	99.6	99.6	1.000 \pm 0.001	99.6	99.6	0.999 \pm 0.001
+0.9, +1.2	99.6	99.6	1.000 \pm 0.001	99.5	99.6	0.999 \pm 0.001
+1.2, +1.6	99.5	99.6	0.999 \pm 0.001	99.4	99.7	0.997 \pm 0.001
+1.6, +2.1	99.2	99.5	0.996 \pm 0.001	99.2	99.5	0.997 \pm 0.001
+2.1, +2.4	98.7	99.1	0.996 \pm 0.001	98.8	99.3	0.995 \pm 0.001

Table 48: Isolation efficiency measured using the tag-and-probe method for muons with $p_T < 20$ GeV and passing the Particle Flow identification and the 3d impact parameter requirements.

Region $ \eta $ range	p_T range	Efficiencies for 2011 [%]			Efficiencies for 2012 [%]		
		data	sim.	ratio \pm stat.	data	sim.	ratio \pm stat.
+0.0, +1.2	5.0, 10.0	87.7	89.7	0.978 \pm 0.020	86.0	88.4	0.973 \pm 0.064
+0.0, +1.2	10.0, 15.0	93.0	93.5	0.995 \pm 0.005	91.0	91.4	0.996 \pm 0.019
+0.0, +1.2	15.0, 20.0	95.2	95.0	1.002 \pm 0.002	93.2	94.7	0.984 \pm 0.007
+1.2, +2.4	5.0, 10.0	88.7	88.7	1.001 \pm 0.008	92.0	86.2	1.068 \pm 0.022
+1.2, +2.4	10.0, 15.0	94.3	94.2	1.002 \pm 0.003	93.7	94.6	0.991 \pm 0.008
+1.2, +2.4	15.0, 20.0	96.8	96.7	1.001 \pm 0.002	97.0	96.9	1.001 \pm 0.005

Table 49: Isolation efficiency measured using the tag-and-probe method for muons with $p_T > 20$ GeV and passing the Particle Flow identification and the 3d impact parameter requirements.

Region η range	Efficiencies for 2011 [%]			Efficiencies for 2012 [%]		
	data	sim.	ratio \pm stat.	data	sim.	ratio \pm stat.
-2.4, -2.1	99.5	99.4	1.001 \pm 0.001	99.5	99.4	1.001 \pm 0.001
-2.1, -1.6	99.5	99.6	1.000 \pm 0.001	99.7	99.6	1.001 \pm 0.001
-1.6, -1.2	99.5	99.5	1.000 \pm 0.001	99.6	99.7	0.999 \pm 0.001
-1.2, -0.9	99.5	99.4	1.000 \pm 0.001	99.5	99.6	0.999 \pm 0.001
-0.9, -0.6	99.5	99.5	1.000 \pm 0.001	99.5	99.6	0.999 \pm 0.001
-0.6, -0.3	99.4	99.4	1.000 \pm 0.001	99.4	99.5	0.999 \pm 0.001
-0.3, -0.2	99.5	99.4	1.000 \pm 0.001	99.4	99.3	1.001 \pm 0.001
-0.2, +0.2	99.4	99.4	1.000 \pm 0.001	99.4	99.4	1.000 \pm 0.001
+0.2, +0.3	99.5	99.4	1.000 \pm 0.001	99.5	99.6	0.999 \pm 0.001
+0.3, +0.6	99.5	99.4	1.000 \pm 0.001	99.4	99.4	1.000 \pm 0.001
+0.6, +0.9	99.4	99.5	1.000 \pm 0.001	99.5	99.7	0.998 \pm 0.001
+0.9, +1.2	99.5	99.5	1.000 \pm 0.001	99.6	99.4	1.001 \pm 0.001
+1.2, +1.6	99.5	99.5	1.000 \pm 0.001	99.5	99.6	0.999 \pm 0.001
+1.6, +2.1	99.5	99.5	0.999 \pm 0.001	99.5	99.6	1.000 \pm 0.001
+2.1, +2.4	99.3	99.4	0.999 \pm 0.001	99.6	99.4	1.002 \pm 0.001

Table 50: Muon trigger efficiency measured using the tag-and-probe method for muons with $p_T > 20$ GeV and passing the full offline selection, for the Run2011A period.

Region η range	Efficiencies for Mu17 leg [%]			Efficiencies for Mu8 leg [%]		
	data	sim.	ratio \pm stat.	data	sim.	ratio \pm stat.
-2.4, -2.1	88.2	91.1	0.969 \pm 0.002	90.5	91.5	0.989 \pm 0.002
-2.1, -1.6	92.1	94.3	0.977 \pm 0.001	92.8	94.4	0.983 \pm 0.001
-1.6, -1.2	96.0	97.1	0.990 \pm 0.001	96.2	97.1	0.991 \pm 0.001
-1.2, -0.9	96.2	97.5	0.986 \pm 0.001	96.4	97.6	0.988 \pm 0.001
-0.9, -0.6	96.0	97.6	0.983 \pm 0.001	96.1	97.6	0.984 \pm 0.001
-0.6, -0.3	97.9	98.8	0.991 \pm 0.001	98.0	98.8	0.992 \pm 0.001
-0.3, -0.2	87.9	91.6	0.959 \pm 0.002	88.1	91.7	0.961 \pm 0.002
-0.2, +0.2	97.4	98.3	0.991 \pm 0.001	97.5	98.3	0.991 \pm 0.001
+0.2, +0.3	87.3	90.6	0.963 \pm 0.002	87.4	90.7	0.964 \pm 0.002
+0.3, +0.6	97.5	98.7	0.988 \pm 0.001	97.6	98.7	0.988 \pm 0.001
+0.6, +0.9	96.2	97.3	0.989 \pm 0.001	96.3	97.4	0.990 \pm 0.001
+0.9, +1.2	96.1	97.4	0.986 \pm 0.001	96.3	97.6	0.987 \pm 0.001
+1.2, +1.6	95.5	96.7	0.988 \pm 0.001	95.8	96.8	0.989 \pm 0.001
+1.6, +2.1	92.6	93.2	0.993 \pm 0.001	93.3	93.4	1.000 \pm 0.001
+2.1, +2.4	88.5	89.9	0.984 \pm 0.002	90.6	90.5	1.001 \pm 0.002

Table 51: Muon trigger efficiency measured using the tag-and-probe method for muons with $p_T > 20$ GeV and passing the full offline selection, for the Run2011B period.

Region η range	Efficiencies for Mu17 leg [%]			Efficiencies for Mu8 leg [%]		
	data	sim.	ratio \pm stat.	data	sim.	ratio \pm stat.
-2.4, -2.1	84.8	91.1	0.931 \pm 0.003	87.3	91.5	0.954 \pm 0.003
-2.1, -1.6	89.7	94.3	0.951 \pm 0.001	90.4	94.4	0.958 \pm 0.001
-1.6, -1.2	95.2	97.1	0.980 \pm 0.001	95.4	97.1	0.982 \pm 0.001
-1.2, -0.9	95.6	97.5	0.980 \pm 0.002	95.8	97.6	0.982 \pm 0.001
-0.9, -0.6	95.8	97.6	0.981 \pm 0.001	95.9	97.6	0.982 \pm 0.001
-0.6, -0.3	97.5	98.8	0.987 \pm 0.001	97.6	98.8	0.987 \pm 0.001
-0.3, -0.2	86.8	91.6	0.947 \pm 0.003	86.8	91.7	0.947 \pm 0.003
-0.2, +0.2	97.0	98.3	0.986 \pm 0.001	97.0	98.3	0.986 \pm 0.001
+0.2, +0.3	87.0	90.6	0.960 \pm 0.003	87.0	90.7	0.960 \pm 0.003
+0.3, +0.6	97.3	98.7	0.986 \pm 0.001	97.3	98.7	0.986 \pm 0.001
+0.6, +0.9	96.0	97.3	0.986 \pm 0.001	96.1	97.4	0.987 \pm 0.001
+0.9, +1.2	95.4	97.4	0.979 \pm 0.001	95.6	97.6	0.980 \pm 0.003
+1.2, +1.6	94.7	96.7	0.979 \pm 0.001	95.0	96.8	0.981 \pm 0.001
+1.6, +2.1	90.6	93.2	0.972 \pm 0.001	91.5	93.4	0.980 \pm 0.002
+2.1, +2.4	84.2	89.9	0.936 \pm 0.003	86.6	90.5	0.957 \pm 0.003

Table 52: Muon trigger efficiency measured using the tag-and-probe method for muons with $p_T > 20$ GeV and passing the full offline selection, for the 2012 running period.

Region η range	Efficiencies for Mu17 leg [%]			Efficiencies for Mu8 leg [%]		
	data	sim.	ratio \pm stat.	data	sim.	ratio \pm stat.
-2.4, -2.1	89.4	90.7	0.985 \pm 0.004	94.2	93.9	1.003 \pm 0.003
-2.1, -1.6	89.3	91.9	0.972 \pm 0.003	94.1	95.2	0.988 \pm 0.002
-1.6, -1.2	91.6	92.7	0.987 \pm 0.002	97.9	98.2	0.996 \pm 0.001
-1.2, -0.9	93.1	94.8	0.982 \pm 0.002	97.7	98.5	0.993 \pm 0.001
-0.9, -0.6	95.8	97.4	0.984 \pm 0.002	97.3	98.5	0.988 \pm 0.001
-0.6, -0.3	97.9	98.5	0.994 \pm 0.001	98.9	99.4	0.996 \pm 0.001
-0.3, -0.2	85.8	91.6	0.936 \pm 0.005	88.2	93.2	0.946 \pm 0.004
-0.2, +0.2	96.8	97.7	0.990 \pm 0.001	98.0	98.6	0.994 \pm 0.001
+0.2, +0.3	86.3	89.7	0.962 \pm 0.005	88.5	91.4	0.968 \pm 0.005
+0.3, +0.6	97.9	98.7	0.992 \pm 0.001	98.9	99.4	0.995 \pm 0.001
+0.6, +0.9	96.5	97.2	0.993 \pm 0.001	97.8	98.2	0.995 \pm 0.001
+0.9, +1.2	93.1	94.2	0.988 \pm 0.002	97.8	98.1	0.998 \pm 0.001
+1.2, +1.6	90.2	93.0	0.970 \pm 0.003	97.0	97.8	0.991 \pm 0.001
+1.6, +2.1	92.9	93.2	0.997 \pm 0.002	96.5	96.4	1.001 \pm 0.002
+2.1, +2.4	89.6	90.7	0.988 \pm 0.004	94.0	93.8	1.002 \pm 0.003

C Appendix #3 Cross checks**C.1 Cross-check with a 1D fit of $m_{\ell\ell}$**

In Fig. 127 we show comparison of expected limits obtained with a 1D fit of the $m_{4\ell}$ distribution. Comparison to 2D fit is shown. The fact that 1D and 2D fit results show similar performance at around 200 GeV is expected. The fractions of longitudinal polarization of the bosons in Higgs decay changes sharply around 200 GeV, where it is initially similar to background, and then significant difference is accumulated as one goes to higher masses. This results in signal-to-background separation gain at higher masses. Below threshold kinematic difference includes di-lepton masses along with angles, and this is where the gain is in the range 10–15%, and this gain grows somewhat as one accumulates higher integrated luminosity.

DRAFT

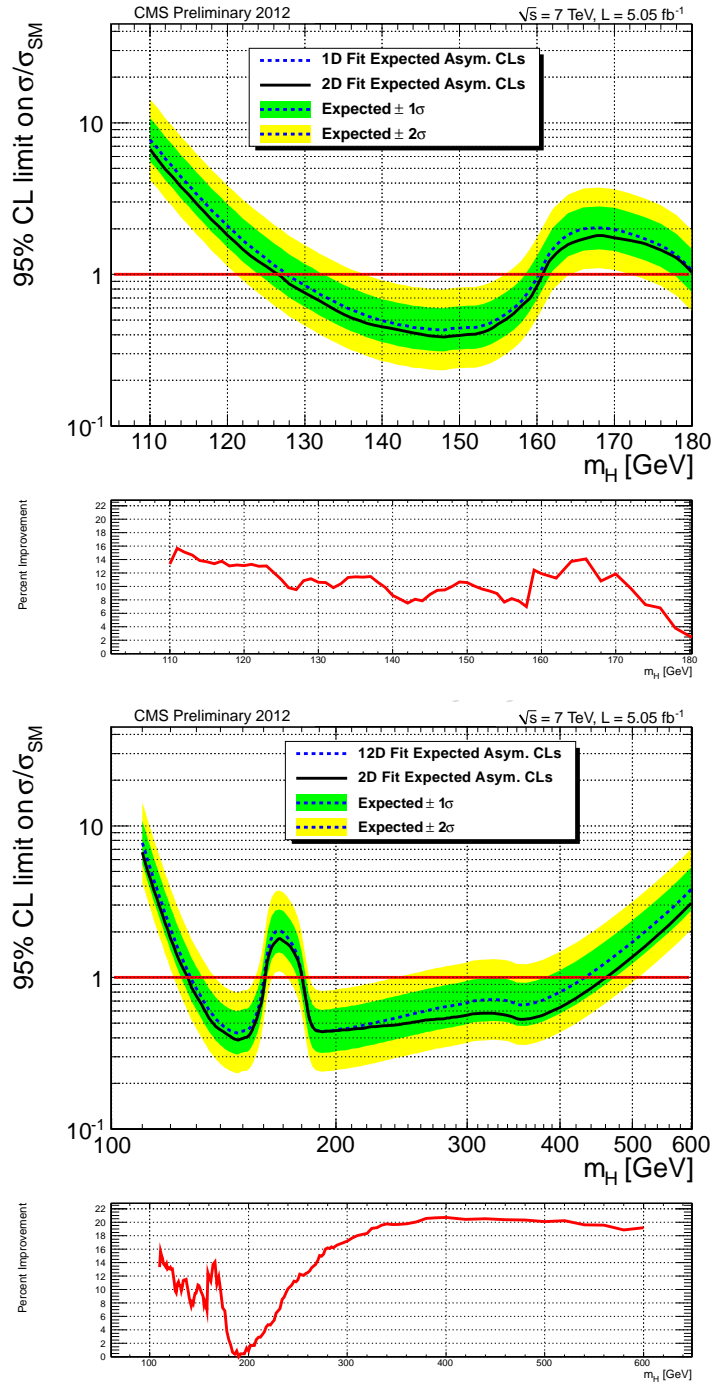


Figure 127: Expected 95% CL upper limit on the ratio of the production cross section to the SM expectation with the 1D fit of m_{4l} . The 68% and 95% ranges of expectation for the background-only model are also shown with green and yellow bands, respectively. Top plot: lower mass range only, bottom plot: full mass range. Comparison to 2D fit is shown: solid line and the ratio plots.

2414 C.2 Cross-check with a cut on KD and a 1D fit of $m_{\ell\ell}$

2415 In Fig. 128 we show comparison of expected limits obtained with a 1D fit of the $m_{4\ell}$ distribution with or
2416 without applying an additional cut on MELA KD.

DRAFT

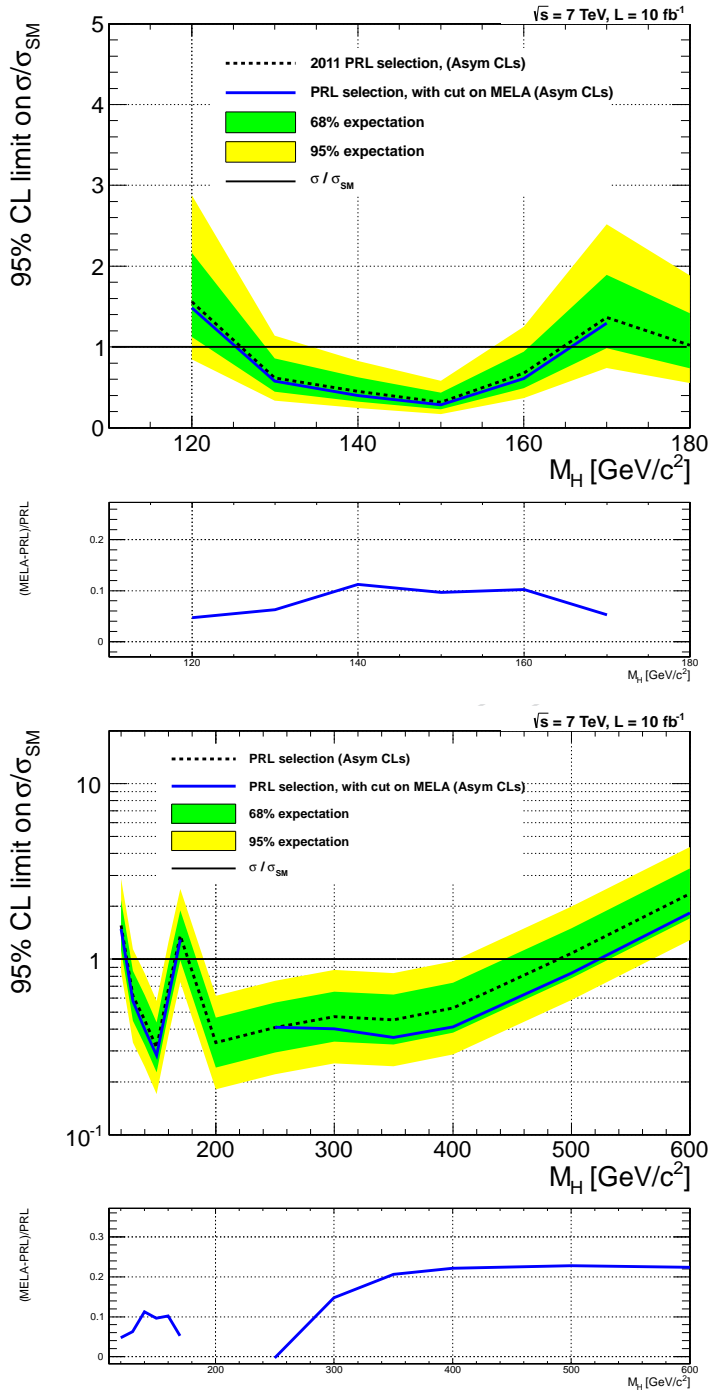


Figure 128: Expected 95% CL upper limit on the ratio of the production cross section to the SM expectation with the 1D fit with (solid) or without (dashed) applying an additional cut on MELA KD with $10/\text{fb}$ of data: KD > 0.1 at low mass and KD > 0.6 at high mass. The 68% and 95% ranges of expectation for the background-only model are also shown with green and yellow bands, respectively. Top plot: lower mass range only, bottom plot: full mass range. Also shown is the ratio of the two expectations.

²⁴¹⁷ **C.3 Cross-check without FSR recovery**

²⁴¹⁸ We also show comparison of expected results with two approaches, with and without FSR recovery, see
²⁴¹⁹ Fig 129. The gain is expected to be around 1–2%.

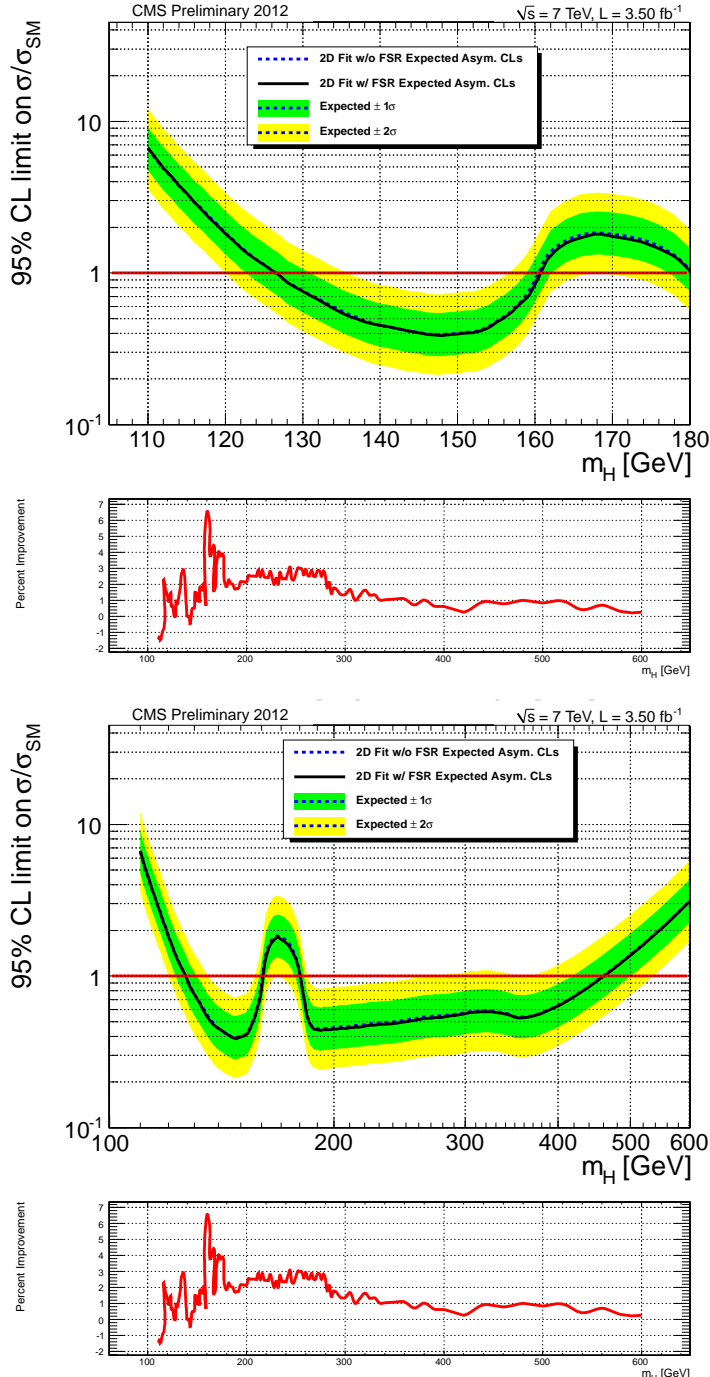


Figure 129: Expected 95% CL upper limit on the ratio of the production cross section to the SM expectation with the 2D with and without FSR recovery. Comparison of expected results with two approaches, with and without FSR recovery, shown as a ratio at the bottom.

2420 D Appendix #4 Some events from the PRL analysis not in the cur- 2421 rent analysis

2422 In this section we give more details about low mass events that were present in the PRL analysis but
2423 failed isolation or electron ID requirements in the current analysis.

```
Run= 167284 evt= 1038911933 ls= 1213
m4mu= 119.026 mZ1= 77.796 mZ2= 29.675
Other combination: mZ'1= 29.678 mZ'2= 18.693
pt_4l= 43.934 eta_4l= 1.337 y_4l 0.581 phi_4l= -0.675 N_vtx 6
loose = 1 baseline= 1 high-mass= 0
costhetal=-0.656 costhetastar=-0.465 Phi=-2.553 costhetastar=0.337 Phil=-0.771 Phi2=-2.959 rnd=0
rhoFJ: 11.261 Riso2= 0.340 iso2= 5.072 pt3= 15.656 SIP4= 0.711
PFMET= 19.989
10: -13 pt= 66.901 eta= 0.411 phi= -0.446 iso: 0.000 -0.083 -0.248 combRelIso= -0.005 SIP= 0.298
11: 13 pt= 20.986 eta= 1.324 phi= -2.805 iso: 0.000 -0.275 -0.248 combRelIso= -0.025 SIP= 0.711
12: -13 pt= 15.656 eta= 1.050 phi= 2.438 iso: 4.940 0.711 -0.248 combRelIso= 0.345 SIP= 0.245
13: 13 pt= 5.966 eta= -0.958 phi= -0.302 iso: 0.000 -0.195 -0.248 combRelIso= -0.074 SIP= 0.624
M_fit= 118.943 sigma= 0.868 constrVtxChi2= 0.631 ndf= 5.000 prob= 0.987
sigma_m4l = 0.943
      idx      pdgId      px       py       pz        E      pt       y
      1         23  40.543971 -35.806001  64.874540 114.833718  54.091434  0.640064
      2         23   -6.242688  8.353705 12.998990  34.034450 10.428593  0.402325
      3        -13  60.351167 -28.871124 28.247827 72.620631 66.901459  0.410595
      4        13  -19.807195 -6.934878 36.626714 42.213089 20.986126  1.323544
      5        -13 -11.938661 10.128693 19.633108 25.111594 15.656374  1.050072
      6        13   5.695973 -1.774988 -6.634118   8.922857  5.966128 -0.958254

### 2012 dump:

Dump for event 167284:1038911933 ls= 1213
mu Candidates: 4
e Candidates: 1
Muons:
 0 mu+ pt= 66.9015 eta= 0.410596 phi= -0.446207 isPFMuon=1 mvaIsoRings=0.990108 looseIso=0
combRelIso=-0.0049728 PFChargedHadIso=0.965755 PFNeutralHadIso=0 PFPhotonIso=0 combRelIsoPF=0.0144355
isMvaIsoRings=1 SIP=0.29833 dxy=0.000386278 dz=0.00056001 HLTMatch=1 ID=1 isGood=1
 1 mu- pt= 20.9861 eta= 1.32355 phi= -2.80481 isPFMuon=1 mvaIsoRings=0.982966 looseIso=0
combRelIso=-0.0247605 PFChargedHadIso=0 PFNeutralHadIso=0 PFPhotonIso=0.555498 combRelIsoPF=0
isMvaIsoRings=1 SIP=0.711185 dxy=8.39376e-05 dz=0.00330521 HLTMatch=1 ID=1 isGood=1
 2 mu+ pt= 15.6564 eta= 1.05009 phi= 2.43803 isPFMuon=1 mvaIsoRings=-0.699802 looseIso=0.315496
combRelIso=0.345709 PFChargedHadIso=7.27557 PFNeutralHadIso=0.941854 PFPhotonIso=4.53036
combRelIsoPF=0.727786 isMvaIsoRings=0 SIP=0.245351 dxy=1.52267e-05 dz=0.000936253 HLTMatch=0 ID=1
isGood=1
 3 mu- pt= 5.96613 eta= -0.958371 phi= -0.302084 isPFMuon=1 mvaIsoRings=0.42303 looseIso=0
combRelIso=-0.107712 PFChargedHadIso=0 PFNeutralHadIso=0 PFPhotonIso=0 combRelIsoPF=0 isMvaIsoRings=1
SIP=0.623918 dxy=0.00143083 dz=0.00283604 HLTMatch=0 ID=1 isGood=1

### Conclusion:
Event fails isolation for the 15.6 GeV muon: combRelIsoPF=0.727786.
The PRL iso (DR<0.3) is combRelIso=0.345709 (it was rather high also
in the PRL analysis)
```

Figure 130: Event dump for one PRL event that failed isolation in the current analysis.

```

Run= 167675 evt= 876658967 ls= 829
m4e= 125.661 mZ1= 92.314 mZ2= 27.221
Other combination: mZ'1= 65.276 mZ'2= 28.503
pt_4l= 16.093 eta_4l= 0.509 y_4l 0.067 phi_4l= -2.749 N_vtx 4
loose = 1 baseline= 1 high-mass= 0
costhetal=0.717 costhetar2=-0.939 Phi=2.269 costhetastar=-0.513 Phil=-0.901 Phi2=-1.367 rnd=1
rhoFJ: 3.845 Riso2= 0.044 iso2= 2.015 pt3= 23.593 SIP4= 2.309
PFMET= 35.583
10: 11 pt= 46.354 eta= -0.021 phi= 0.319 iso: 0.000 1.158 -0.081 combRelIso= 0.023 SIP= 2.309
11: -11 pt= 46.161 eta= -0.027 phi= -2.954 iso: 0.000 1.019 -0.081 combRelIso= 0.020 SIP= 1.066
12: -11 pt= 23.593 eta= 0.520 phi= -2.177 iso: 0.000 0.309 -0.081 combRelIso= 0.010 SIP= 2.068
13: 11 pt= 7.294 eta= -0.281 phi= 1.583 iso: 0.000 0.077 -0.081 combRelIso= -0.001 SIP= 0.707
M_fit= 124.089 sigma= 12.171 constrVtxChi2= 5.343 ndf= 5.000 prob= 0.375
sigma_m4l = 1.070
   idx      pdgId      px       py      | pz       E       pt      y
   1        23  -1.337118  5.940103  -2.192733  92.540807  6.088736  -0.023699
   2        23  -13.531469 -12.096516  10.737507 34.433824 18.150106  0.322571
   3       -11  -45.354003  -8.591954  -1.237587 46.177255 46.160667  -0.026807
   4        11  44.016885  14.532057  -0.955146 46.363555 46.353714  -0.020604
   5       -11  -13.440651 -19.389645 12.817239 26.849414 23.592571  0.519579
   6        11  -0.090817  7.293129  -2.079733  7.584409  7.293694  -0.281412

### 2012 dump:

Dump for event 167675:876658967 ls= 829
mu Candidates: 0
e Candidates: 4
Muons:
Electrons:
  0 e-  pt= 46.2258 eta= -0.0206041 phi= 0.31888 mvaIsoRings=0.95886 looseIso=0 combRelIso=0.0213989
  PFChargedHadIso=5.18661 PFNeutralHadIso=1.11992 PFPhotonIso=2.82003 combRelIsoPF=0.182441 isMvaIsoRings=1
  SIP=2.3089 dxy=0.0045029 dz=0.00965808 BDT=0.993481 isBDT=1 HLTMATCH=0 ID=1 isGood=1
  1 e+  pt= 45.3784 eta= -0.0268072 phi= -2.95437 mvaIsoRings=0.949382 looseIso=0 combRelIso=0.020817
  PFChargedHadIso=0 PFNeutralHadIso=0 PFPhotonIso=0.753603 combRelIsoPF=0.00133404 isMvaIsoRings=1
  SIP=1.06569 dxy=0.00286442 dz=0.00268396 BDT=0.996735 isBDT=1 HLTMATCH=0 ID=1 isGood=1
  2 e+  pt= 23.563 eta= 0.519579 phi= -2.17694 mvaIsoRings=0.97798 looseIso=0 combRelIso=0.00663693
  PFChargedHadIso=0 PFNeutralHadIso=0 PFPhotonIso=0.214036 combRelIsoPF=0 isMvaIsoRings=1 SIP=2.06752
  dxy=0.00937668 dz=0.0029255 BDT=0.992087 isBDT=1 HLTMATCH=0 ID=1 isGood=1
  3 e-  pt= 7.26713 eta= -0.281412 phi= 1.58325 mvaIsoRings=0.464426 looseIso=0 combRelIso=-0.000884496
  PFChargedHadIso=0 PFNeutralHadIso=0 PFPhotonIso=0 combRelIsoPF=0 isMvaIsoRings=1 SIP=0.707485
  dxy=0.00272074 dz=0.0022802 BDT=0.150701 isBDT=0 HLTMATCH=0 ID=0 isGood=0

### Conclusion: Event fails new ID for the 7.3 GeV electron (BDT=0.150701).

```

Figure 131: Event dump for one PRL event that failed isolation in the current analysis.

```

Run= 172822 evt= 2554393033 ls= 2004
m4mu= 118.937 m2l= 90.219 m22= 25.359
Other combination: mZ'1= 48.155 mZ'2= 24.117
pt_4l= 18.145 eta_4l= -1.571 y_4l= -0.340 phi_4l= 2.045 N_vtx 3
loose = 1 baseline= 1 high-mass= 0
costhetal=0.963 costhetal2=-0.279 Phi=-2.573 costhetastar=-0.399 Phil=-0.219 Phi2=2.792 rnd=1
rhoFJ: 2.582 Riso2= 0.279 iso2= 1.539 pt3= 5.652 SIP4= 1.392
PFMET= 8.771
10: 13 pt= 58.382 eta= -0.472 phi= 1.711 iso: 0.000 0.037 -0.057 combRelIso= -0.000 SIP= 0.442
11: -13 pt= 34.567 eta= -0.246 phi= -1.564 iso: 0.000 -0.191 -0.057 combRelIso= -0.007 SIP= 1.392
12: 13 pt= 5.652 eta= -1.666 phi= -0.769 iso: 0.000 0.505 -0.057 combRelIso= 0.079 SIP= 1.070
13: -13 pt= 5.448 eta= 1.354 phi= -2.520 iso: 0.000 0.293 0.797 combRelIso= 0.200 SIP= 0.399
M_fit= 118.814 sigma= 0.728 constrVtxChi2= 4.711 ndf= 5.000 prob= 0.452
sigma_m4l = 0.742
      idx pdgId      px      py      pz      E      pt      y
      1     23 -7.914754 23.244748 -37.171953 100.619161 24.555277 -0.387765
      2     23 -0.366684 -7.099514 -4.573577 26.730856 7.108977 -0.172797
      3    -13 0.226441 -34.566660 -18.603196 35.622064 34.567402 -0.246380
      4     13 -8.141195 57.811407 -28.568755 64.997098 58.381828 -0.471659
      5    -13 -4.429920 -3.170579  9.840277 11.248066 5.447639 1.353350
      6     13  4.063236 -3.928935 -14.413854 15.482790 5.652116 -1.665541

### 2012 dump:

Dump for event 172822:2554393033 ls= 2004
mu Candidates: 4
e Candidates: 0
Muons:
0 mu- pt= 58.382 eta= -0.472 phi= 1.711 isPFMuon=1.000 mvaIsoRings=0.988 looseIso=0.000 combRelIso=-0.000
PFChargedHadIso=0.000 PFNeutralHadIso=0.000 PFPhotonIso=0.000 combRelIsoPF=0.000 isMvaIsoRings=1.000
SIP=0.442 dxy=0.001 dz=0.001 HLTMatch=1.000 ID=1.000 isGood=1.000
1 mu+ pt= 34.567 eta= -0.246 phi= -1.564 isPFMuon=1.000 mvaIsoRings=0.989 looseIso=0.000 combRelIso=-0.007
PFChargedHadIso=0.207 PFNeutralHadIso=0.000 PFPhotonIso=0.000 combRelIsoPF=0.006 isMvaIsoRings=1.000
SIP=1.392 dxy=0.002 dz=0.000 HLTMatch=1.000 ID=1.000 isGood=1.000
2 mu- pt= 5.652 eta= -1.666 phi= -0.769 isPFMuon=1.000 mvaIsoRings=-0.504 looseIso=0.000 combRelIso=0.086
PFChargedHadIso=0.319 PFNeutralHadIso=0.000 PFPhotonIso=2.467 combRelIsoPF=0.441 isMvaIsoRings=1.000
SIP=1.070 dxy=0.003 dz=0.007 HLTMatch=0.000 ID=1.000 isGood=1.000
3 mu+ pt= 5.448 eta= 1.354 phi= -2.520 isPFMuon=1.000 mvaIsoRings=-0.278 looseIso=0.000 combRelIso=0.237
PFChargedHadIso=0.386 PFNeutralHadIso=0.000 PFPhotonIso=0.000 combRelIsoPF=0.071 isMvaIsoRings=1.000
SIP=0.399 dxy=0.002 dz=0.000 HLTMatch=0.000 ID=1.000 isGood=1.000

### Conclusion: The 5.65 GeV muon fails iso (combRelIsoPF=0.441).

```

Figure 132: Event dump for one PRL event that failed electron ID in the current analysis.